ABSTRACT

Title of dissertation: A STUDY OF TWO-LEVEL SYSTEM
DEFECTS IN DIELECTRIC FILMS
USING SUPERCONDUCING RESONATORS

Moe Khalil, Doctor of Philosophy, 2013

Directed by: Dr. Kevin D. Osborn
Laboratory for Physical Sciences

Professor Frederick C. Wellstood
Department of Physics

In this dissertation I describe measurements of dielectric loss at microwave frequencies due to two level systems (TLS) using superconducting resonators. Most measurements were performed in a dilution refrigerator at temperatures between 30 and 200 mK and all resonators discussed were fabricated with thin-film superconducting aluminum.

I derive the transmission through a non-ideal (mismatched) resonant circuit and find that in general the resonance line-shape is asymmetric. I describe an analysis method for extracting the internal quality factor (Q_i), the diameter correction method (DCM), and compare it to a commonly used phenomenological method, the ϕ rotation method (ϕRM). I analytically find that the ϕRM deterministically overestimates Q_i when the asymmetry of the resonance line-shape is high.

Four coplanar resonator geometries were studied, with frequencies spanning 5-7 GHz. They were all superconducting aluminum fabricated on sapphire and

silicon substrates. These include a quasi-lumped element resonator, a coplanar strip transmission line resonator, and two hybrid designs that contain both a coplanar strip and a quasi-lumped element. Measured Q_i's were as high as 2×10^5 for single photon excitations and there was no systematic variation in loss between quasi-lumped and coplanar strip resonance modes.

I also measured the microwave loss tangent of several atomic layer deposition (ALD) grown dielectrics and obtained secondary ion mass spectrometry (SIMS) measurements of the same films. I found that hydrogen defect concentrations were correlated with low temperature microwave loss. In amorphous films that showed excess hydrogen defects on the surface, two independent TLS distributions were required to fit the loss tangent, one for the surface and one for the bulk. In crystalline dielectrics where hydrogen contamination was uniform throughout the bulk, a single bulk TLS distribution was sufficient.

Finally, I measured the TLS loss in 250 nm thick HD-PECVD deposited silicon nitride ($\mathrm{SiN_x}$) while sweeping an independent applied bias electric field across the capacitor. With a strong microwave field and an increasing bias rate, the loss tangent changed from a low value, where saturation occurs on resonance near the steady state, to a larger value approximately equal to the linear-response loss tangent, where saturation appears to be avoided. This increase was explained with a new theory in which TLSs can experience Landau-Zener transitions as they're swept, where the maximum excitation probability is 1/2 at resonance. Data is found to scale if plotted as a function of the dimensionless sweep rate. The functional form of this loss tangent agrees well with the theory, and is predicted to hold for any amorphous dielectric. By fitting the measured loss tangent as a function of bias sweep rate to the theory, I was able to extract an average TLS dipole moment of 7.9 D and a TLS spectral spatial density of $P_0 = 4.9 \times 10^{43}\,\mathrm{J}^{-1}\mathrm{m}^{-3}$.

A STUDY OF TWO-LEVEL SYSTEM DEFECTS IN DIELECTRIC FILMS USING SUPERCONDUCING RESONATORS

by

Moe Shwan Khalil

Dissertation submitted to the Faculty of the Graduate School of the
University of Maryland, College Park in partial fulfillment
of the requirements for the degree of
Doctor of Philosophy
2013

Advisory Committee:
Professor Frederick C. Wellstood, Advisor/Chair
Dr. Kevin D. Osborn, Advisor/Principal Investigator
Professor Christopher J. Lobb
Dr. Ben Palmer
Professor Ichiro Takeuchi

Dedication

To my parents who worked so hard to give me opportunities that they never had.

Acknowledgments

I was very lucky to have not one but two great advisors in Dr. Kevin Osborn at the Laboratory for Physical Sciences (LPS) and Prof. Fred Wellstood at the University of Maryland. I cannot thank either of them enough. Kevin was always there in the lab happy to get his hands dirty and advise me early in my tenure but he also gave me the freedom to pursue my own research interests as I continued my research. The strength I gained from knowing that I always had his support cannot be overstated.

Fred's insight when making sense of puzzling phenomena was invaluable. The depth of his knowledge and the incredible intuition he possesses meant there wasn't a phenomenon that he couldn't come up with a plausible explanation for. I always knew that no matter how lost I felt I could go to him to have a sense of direction.

I'd also like to thank Prof. Chris Lobb, discussions with whom were always as entertaining as they were scientifically valuable. Chris brings a sense of joy to his work that he simply cannot hide.

I also have to thank Dr. Ben Palmer who was like a second advisor at LPS. Ben was always ready to discuss various experimental and analysis techniques. I was so impressed with his love experimental physics which drove him to be in the lab more than any other PI I've known.

I should also thank Prof. Ichiro Takeuchi who agreed to serve as the Dean's representative at my thesis defense.

I'd also like to thank my fellow group members, who aided me in more ways than I can possibly enumerate: Bahman Sarabi, Dr. Aruna Ramanayaka, Dr. Yaniv Rosen, Dr. Sergey Gladchenko, and Dr. Micah Stoutimore. I would be remiss if I didn't extend a special thanks to Micah. The countless discussions with him were enlightening when I was stuck and uplifting when I was frustrated, not to mention entertaining when I was not in the mood to do physics. I always knew when arguing with Micah that if I could convince him (rare), I was certain to be right.

I'm grateful to all of the postdocs and graduate students at LPS with which I had numerous interactions both scientific and otherwise: Sergey Novikov, Dr. Zachary Keane, Dr. Vitaley Zaretskey, Dr. Jennifer Robinson, Baladitya Suri, John Bavier, Anita Roychowdhury, Pavel Nagornykh, Dr. Mishkatul Bhattacharya, Dr. Nathan Siwak, Dr. Tomek Kott, and Dr. Zaeill Kim. My graduate experience would not have been nearly as rewarding or successful without each and every one of them. I should also thank Dr. Hanhee Paik who was Kevin's first postdoc. We overlapped in the group only briefly, but she taught me so much about low temperature experimental physics and processes fabrication.

I'm also very grateful to the cleanroom, machine shop, and LPS staff without whom my research wouldn't have been possible: Toby Olver, Steve Brown, Sean Flannery, Curt Walsh, John Sugrue, Don Crouse, Bill Donaldson, Paul Hannah, and Greg Latini.

I must also thank my friends how have made this experience so much sweeter. I can't name them all and will not try but you guys know who you are. You were there to celebrate with me during my accomplishments and to mourn with me during my failures. I can't imagine what the last six years would have been like without

each and every one of you.

Most of all I'd like to thank my family, in particular my brother Salwan Abdullah and my parents Bangean Abdullah and Zena Khalil. You were always there to support me during my trials and I will never be able to adequately express the strength I gained from knowing that I always had your full backing. You've been my safety net, giving me the courage to jump higher knowing that you'd always be there if I fall.

I'm grateful to so many and so I'm sure to have missed several of you. To anyone I may have missed, I'm sorry and thank you for all of your support.

Table of Contents

List of Figures

Chapter 1

Introduction

1.1 Quantum computing

1.1.1 Background

Quantum computing is a profound and potentially groundbreaking result of quantum mechanics. Since the genesis of the idea in 1982 [1] by Richard Feynman, physicists, engineers, and computer scientists have worked towards achieving this ambitious goal. This pursuit has led to new devices, new concepts, and a better and perhaps more intuitive understanding of some parts of quantum mechanics.

In 1982 [1] Feynman noted that there appear to be fundamental difficulties in simulating quantum mechanical systems with classical computers. This realization led him to the idea of a quantum computer for the purpose of simulating such systems. This is a very open ended and arguably the most rewarding ends for a quantum computer, with the potential to affect many fields of science. For example protein folding is ultimately a quantum mechanical process, the understanding of which could revolutionize medicine [2]. In addition, a quantum computer with an effective quantum simulator would have the potential to solve much of the problems facing quantum computing today and could make the design and construction of a quantum computer much simpler–it seems the universe is not without a sense of irony.

The Church-Turing thesis [3, 4] states that any algorithmic process can be simulated efficiently, meaning in polynomial time, with a probabilistic Turing machine. In other words one cannot write an algorithm that solves a problem more efficiently than a probabilistic Turing machine. In 1985 David Deutsch [5] showed that a quantum computer was not limited by the Church-Turing thesis and could efficiently solve a problem that has no efficient solution by a probabilistic Turing machine. In 1992 David Deutsch along with Richard Jozsa demonstrated an example of this with the Deutsch-Josza algorithm [6] which solved a proposed problem where one is attempting to determine the nature of a black box function. The idea is that you are given a function that acts on an n-bit number and is known to either be *constant*, meaning that it returns 1 (or 0) for all possible inputs, or *balanced*, meaning that it returns 0 for exactly half of all inputs and 1 for the other half. You are tasked with querying an oracle that evaluates the function until you determine whether the function is *constant* or *balanced*. In the worst, case a classical computer will require $2^{n-1} + 1$ queries to solve the problem but the Deutsch-Josza algorithm on a quantum computer can solve the problem with a single query by using a superposition of all 2^n possible inputs.

In 1994 Peter Shor discovered a quantum algorithm (Shor's algorithm) [7] that can factor numbers exponentially faster than classical algorithms. This again utilizes the principle of superposition to evaluate a function for what is classically multiple inputs. This is considered by many to be the most practical use for a quantum computer since modern RSA encryption is based on the inability to factor sufficiently large numbers in polynomial time. Then in 1995 Lov Grover proposed a quantum algorithm that can search an unsorted list with a quadratic speedup over classical algorithms. [8] While this did not give as dramatic a speedup as Shor's algorithm, the myriad of potential uses have many excited about its prospects. While the number of distinct quantum algorithms has been thus far limited, it is the opinion of many, myself included, that this is not a fundamental limit on quantum algorithms but rather an indication of the unintuitive nature of quantum computing and the relative novelty of the field. There is little doubt in my mind that given enough time, we will discover quantum algorithms that will revolutionize many aspects of life.

Another potential technique that could be used on a quantum computer is quantum annealing or adiabatic quantum computing. [9] Quantum annealing could be applied to the classically intractable problem of function optimization. While often finding a local minimum is relatively easy, there is no known classically efficient technique for finding a global minimum. Quantum annealing could effectively allow the solution to tunnel into its global minimum. Qualitatively this could be done by encoding a function into a potential that's turned on adiabatically. If the system is initialized in its ground state, it will remain there adiabatically as the potential is turned on.

The power of quantum computing comes from two fundamental properties of quantum mechanics. The first, which has already been mentioned, is the principal of quantum superposition. From linearity, a quantum mechanical system with two states can in general exist in a quantum superposition of both states. Thus a qubit unlike a classical bit can exists in a superposition of both the 0 state and the 1 state with some complex amplitude. The second unique property of quantum mechanics necessary for quantum computing is entanglement. Entanglement is a nonlocal property that allows the state of two quantum systems to be strongly correlated in a way that is not possible in classical mechanics.

1.1.2 Superconducting qubits

In principal any two-level-quantum-system, or more generally any quantum system where two levels can be isolated, can act as a qubit. The first realization of a qubit in a logic gate was in 1995 with a trapped beryllium ion, [10] where the internal energy levels of the atom were used as the qubit. In the late 1990's some attempted to utilize NMR technology to use nuclear magnetic spins as qubits [11] but this was met with limited success. The problem with these early techniques is that of scalability. Coupling to an atom can be difficult and the infrastructure required in scaling up to many qubits and eventually a quantum computer is not trivial.

At first sight, one might instead consider using a harmonic oscillator that has been cooled down to its quantum mechanical ground state and use single photon excitations to exchange quantum information. Superconducting LC microwave resonators are easy to build and can be cooled below their resonant frequency with existing dilution refrigerator technology. However, a harmonic oscillator has equally spaced energy levels and as a result an external drive field can't isolate individual energy levels. What we need is not a quantum spring (harmonic) but rather a quantum pendulum (anharmonic). This can be achieved with a Josephson junction [12], a thin insulating layer separating two superconducting metals which allows Cooper pairs to tunnel across. A Josephson junction is ideally lossless and gives superconducting circuits the non-linearity needed to isolate two energy levels. The first superconducting qubit was realized in 1999 [13] with a Cooper pair box, where the quantum states used for the qubit are zero/one excess Cooper pairs on a superconducting island.

The advantage of superconducting qubits is that it is easier to couple to them and for them to couple to each other. The disadvantage is that it is easier for the universe to couple to them as well, and in so doing decohere their quantum state. Figure 1.1(a) shows a simulation of a qubit's excited state probability while the qubit is being driven at the transition frequency. It is oscillating between the ground and the excited state due to absorption and stimulated emission of the microwave photons from the input drive. These are called Rabi oscillations after Isidor Isaac Rabi who first measured them in nuclear magnetic spins [14]. Figure 1.1(b) shows what happens when the drive is stopped. Rather than remaining in its current state the qubit decays into its grounds state exponentially with characteristic time T_1. This decay to the ground state as well as the decay in the Rabi oscillations is caused by coupling of the qubit to other degrees of freedom.

It is a major goal of research on superconducting quantum computing to increase these qubit lifetimes. Figure 1.2(a) [15] shows a loss tangent measurement of a linear superconducting resonator as a function of the microwave voltage across

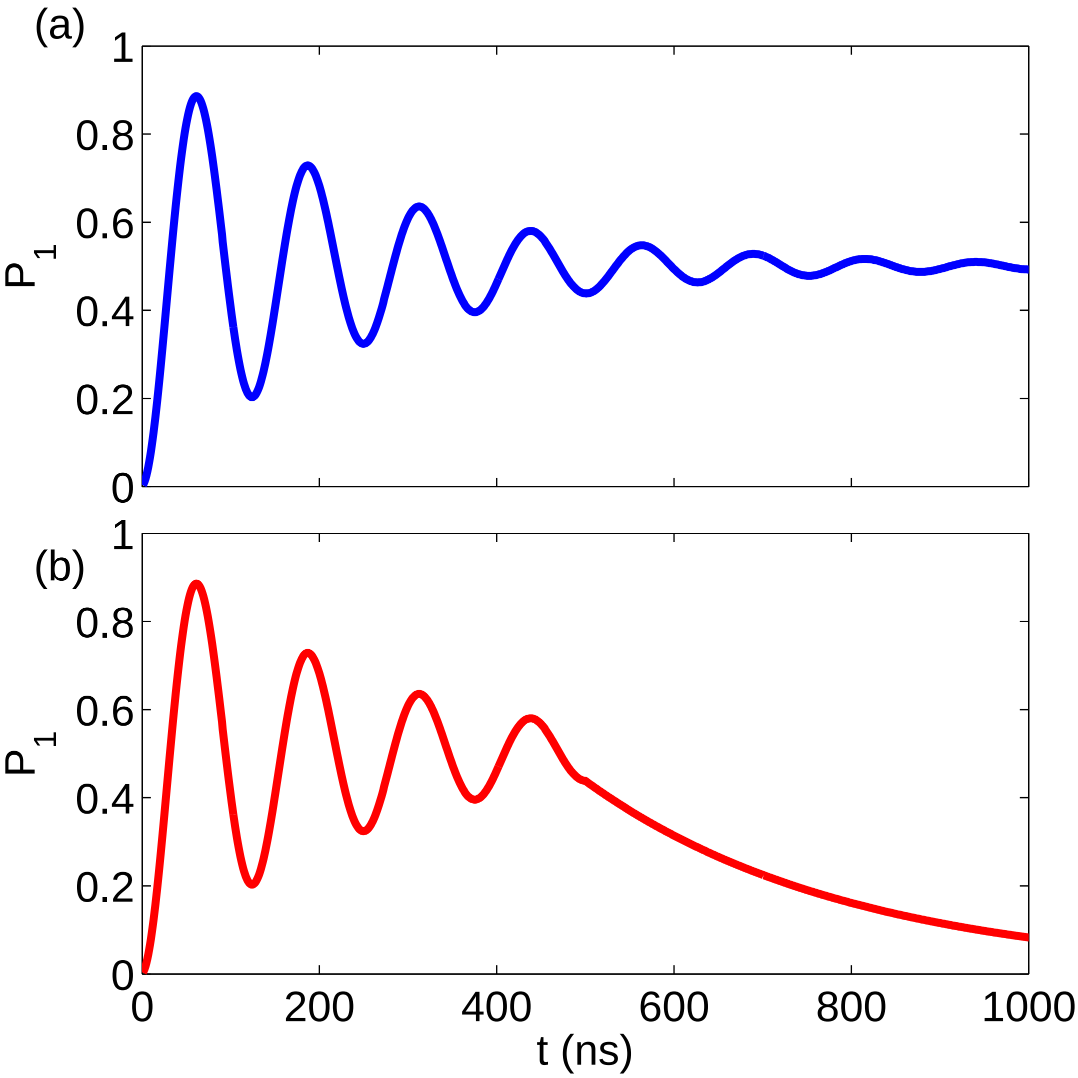

Figure 1.1: (a) Simulated Rabi oscillations for a qubit with $T_1 = 300ns$ and a $T_2 = 200ns$. (b) The drive is turned off at t=500 ns at which point the qubit decays into its ground state with the spontaneous emission time constant T_1

the capacitor for different dielectric materials. The functional form of the loss will be discussed in Chapter 2 but for now we note that silicon nitride has more than an order of magnitude less dielectric loss than silicon dioxide. Figure 1.2(b) (from Ref. [15]) shows Rabi oscillations for superconducting phase qubits where silicon nitride and silicon dioxide were used as wiring dielectrics; the qubits where silicon nitride was used clearly show longer coherence times. This result is evidence that coherence times in these superconducting qubits were limited by material losses. This work also shows that one can probe these losses not only with qubits which can be complicated to fabricate and measure, but also with simple linear resonators which are by comparison much easier to deal with. Thus understanding and improving dielectric loss in superconducting microwave resonators is a pathway to improving the performance of superconducting qubits.

1.1.3 Superconducting qubit readout

In addition to being useful in diagnosing sources of loss and decoherence, superconducting linear resonators are also useful in reading out qubits. This idea was the genesis of circuit cavity quantum electrodynamics in 2004 by the Schoelkopf group at Yale [16]. They demonstrated that by coupling a qubit to a linear resonator, the state of the qubit creates a dispersive shift in the resonance frequency of the resonator. Thus by measuring the resonance frequency of the linear resonator the state of the qubit can be determined.

When coupling a linear resonator to a qubit, the loss of the resonator can

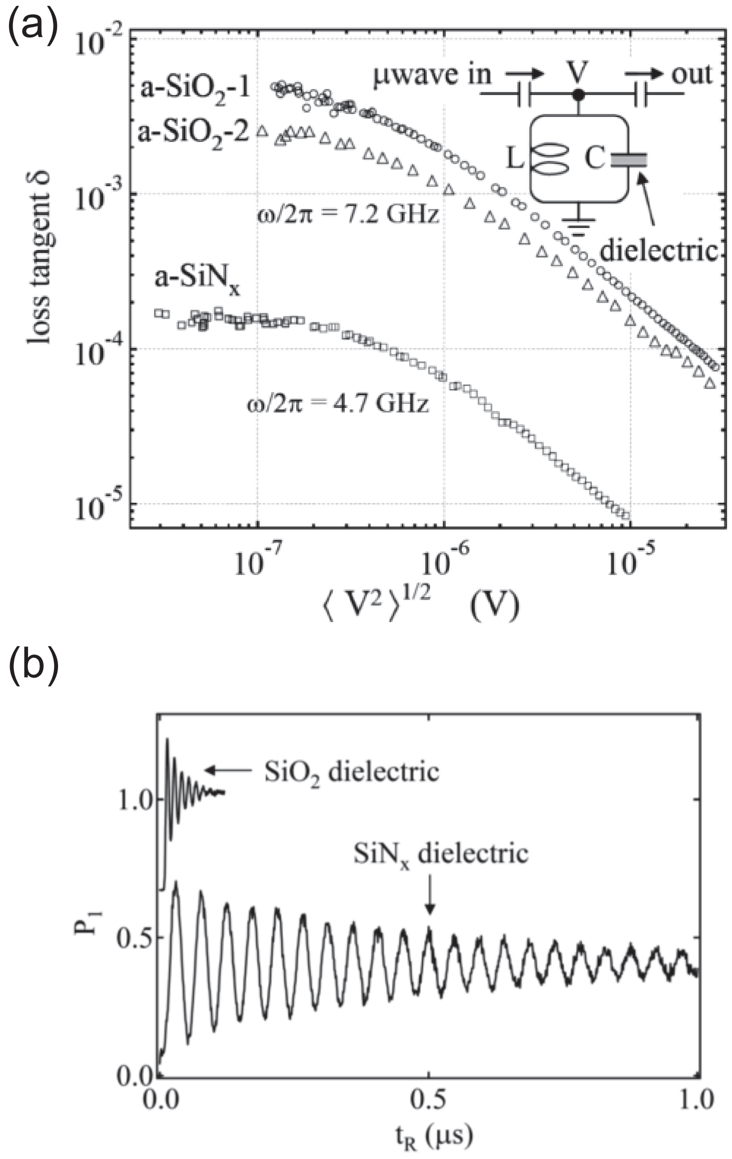

Figure 1.2: From Ref. [15] (a) Superconducting resonator loss tangent measurement for silicon nitride and silicon dioxide. Silicon nitride shows significantly lower loss (b) Rabi oscillations of phase qubit where the same silicon nitride and silicon dioxide are used as wiring dielectrics. Qubit made with the lower loss silicon nitride show longer coherence times indicating that qubit lifetimes are likely limited by dielectric loss.

limit the lifetime of the qubit. This was observed recently when the Yale group and eventually much of the community started using 3 dimensional cavities to measure their qubits [17]. The electromagnetic fields inside the 3-D cavities mostly reside in empty space. With little lossy dielectric, they exhibit much lower internal loss than planar LC resonators. Due to this improvement in the loss of the linear resonator, state of the art decay times were observed [17]. This presents another clear example where improvement in fabrication and understanding of linear resonators led to breakthroughs for non-linear superconducting qubits.

1.2 Microwave kinetic inductance detectors

While superconducting quantum computing is our underlying motivation for studying superconducting resonator loss, improved telescopes to better view the cosmos is no less romantic a pursuit. Superconducting microwave resonators are now used in some large array infrared telescopes; the resonators are in the form of microwave kinetic inductance detectors (MKIDs) that act as far-infrared photon detectors. [18] While visible light telescopes can give us beautiful pictures, seeing the universe in the far-infrared gives us information about “cold” objects such as planets, events inside interstellar gases and dust clouds where visible light is scattered, and distant galaxies with a high red shift. MKIDs are sensitive to far-infrared photons because an absorbed photon will break Cooper pairs and increase the kinetic inductance of the resonator. This decreases the resonance frequency and quality factor which can then be detected using standard microwave measurements. By understanding and reducing loss in superconducting resonators, we can potentially improve the sensitivity of MKIDs.

1.3 Other superconducting resonator applications

Superconducting resonators have several other applications that I have not mentioned. Niobium superconducting resonators have been used in particle accelerators [19] for years and have thus aided in understanding our universe at a more fundamental level. High-temperature superconducting microwave resonators have also been used for telecommunication purposes [20]. Superconducting resonators have recently even been used to read out nanomechanical resonators [21]. These applications as well as the yet unknown potential applications make the study of superconducting resonators, and the dielectric films that often cause their loss, an important one.

1.4 Overview of thesis

In this thesis, I discuss my research on thin-film superconducting resonators. My goal was to understand and improve their loss, usually by understanding the dielectric films that limit their loss. In Chapter 2, I discuss the two-level system model that has been used to explain dielectric loss and acoustic loss in amorphous films. In Chapter 3, I describe the experimental apparatus and details of the measurements performed as well as intricacies in the analysis of these measurements. In Chapter 4, I discuss the design and fabrication of four coplanar resonators on sapphire and silicon wafers. In Chapter 5, I discuss my results from the measurement of these four resonators. In Chapter 6, I discuss Atomic Layer Deposition (ALD) and its potential for growing thin dielectric films useful for superconducting quantum computing. In Chapter 6, I also propose using coplanar resonators as a test bed for ALD grown dielectrics. In Chapter 7, I describe measurements of several ALD grown dielectric films with coplanar resonators and analysis of their loss. In Chapter 8, I discuss a new experiment designed to electrically bias the defects in dielectric films in superconducting resonators. In Chapter 9, I discuss measurements of this experiment and analyze the results. Finally, in Chapter 10, I conclude with a summary of key results obtained and a discussion of possible future research.

Chapter 2

Two-level systems and dissipation

2.1 Background for undriven Two-level systems

In the early 1970's measurements of specific heat and thermal conductivity of different amorphous solids taken between 70 mK and 1 K [22] highlighted that there was a fundamental lack of understanding of low temperature thermal properties of amorphous solids. With this motivation, in 1972 Phillips [23] and Anderson [24] independently developed the standard tunneling two-level system (TLS) model to explain the experimental results. In this model each defect atoms can tunnel between two distinct local minima in a two-well potential. Needless to say this assumption of two wells is made to simplify the math and is in general not exactly true.

The microscopic identity of actual TLSs in real samples is typically unknown, but they can be modeled as ions hopping between two local minima (see Fig. 2.1(a)) i.e. by a particle of mass m in a double well potential (see Fig. 2.1(b)). For simplicity we assume that these are identical harmonic wells, with minima separated by distance d and shifted in energy by an asymmetry energy Δ. Since we are considering low-temperature properties, we restrict ourselves to the ground states of the two wells and solve the Schrodinger equation $H\psi = \mathcal{E}\psi$. We assume the state ψ obeys the *ansatz* $\psi = a\psi_l + b\psi_r$, where ψ_l and ψ_r are the normalized ground state wave functions for the left and right wells respectively, and the coefficients a and b

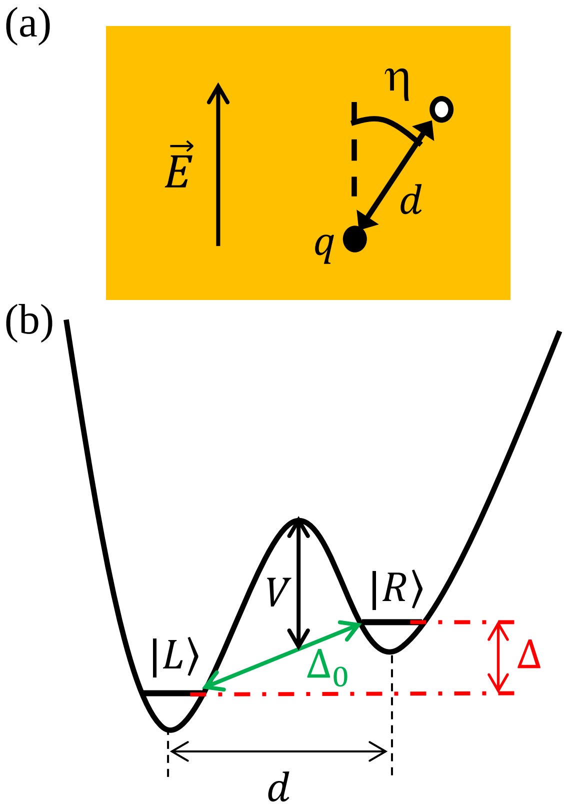

Figure 2.1: (a) Spatial representation of a TLS as a charged defect hopping between two positions a distance d apart that make angle η with respect to the applied electric field. (b) Spectral representation (potential energy description) of a TLS as a particle in a double well potential with asymmetry energy Δ, tunneling rate Δ_0, and barrier height V, where $(V >> \Delta, \Delta_0)$.

are assumed to be real. Multiplying Schrodinger's equation by ψ^* and solving for the energy eigenvalues we have

$$\mathcal{E} = \frac{\int \psi^* H \psi d^3x}{\int \psi^* \psi d^3x} = \frac{a^2 H_{ll} + b^2 H_{rr} + 2abH_{lr}}{a^2 + b^2 + 2abS}, \tag{2.1}$$

where H_{ll} and H_{rr} are the eigenvalues of the left and right well states, $H_{lr} = \int \psi_l^* H \psi_r d^3x$ is the exchange energy between the two states, and $S = \int \psi_l^* \psi_r d^3x$ is the overlap between them. We know that the true wave function ψ in the ground state will minimize $\mathcal{E}$. Thus the true eigenvalue is always smaller than or equal to the one calculated from the ansatz. Therefore we minimize $\mathcal{E}$ with respect to the coefficients a and b by solving for $\partial\mathcal{E}/\partial a = 0$ and $\partial\mathcal{E}/\partial b = 0$, resulting in

$$\frac{a}{b} = \frac{H_{lr} - \mathcal{E}S}{H_{ll} - \mathcal{E}}, \tag{2.2}$$

and

$$\frac{a}{b} = \frac{\mathcal{E} - H_{rr}}{H_{lr} - \mathcal{E}S}. \tag{2.3}$$

From Eqs. 2.2 and 2.3 we then obtain:

$$(H_{ll} - \mathcal{E})(H_{rr} - \mathcal{E}) - (H_{lr} - \mathcal{E}S)^2 \approx \mathcal{E}^2 + (H_{ll} - H_{rr})\mathcal{E} + H_{ll}H_{rr} - H_{lr}^2 = 0, \tag{2.4}$$

where we've assumed that the overlap between the left and right wavefunctions is small and have neglected the term $\mathcal{E}S$ in the second step. Choosing the average of the left and right ground states to be the zero energy gives $H_{rr,ll} = \hbar\Omega/2 \pm \Delta/2$, where Ω is the harmonic frequency of the left and right wells (defined by the curvature of the wells). Solving for the energy eigenvalues then gives

$$\mathcal{E}_{\pm} = \frac{1}{2}(\hbar\Omega \pm \sqrt{\Delta^2 + 4H_{lr}^2}). \tag{2.5}$$

The energy splitting between the two states is then

$$\mathcal{E} = \mathcal{E}_+ - \mathcal{E}_- = \sqrt{\Delta^2 + 4H_{lr}^2} = \sqrt{\Delta^2 + \Delta_0^2}, \tag{2.6}$$

where we have defined $\Delta_0 = 2H_{lr}$ for the exchange energy; $\Delta_0/\hbar$ is the tunneling rate. Thus the Hamiltonian in the left right basis is simply

$$H_0 = \frac{1}{2}\begin{pmatrix} \Delta & -\Delta_0 \\ -\Delta_0 & -\Delta \end{pmatrix}, \tag{2.7}$$

and diagonalizing it into the eigenbasis gives

$$\mathcal{H}_0 = \frac{1}{2}\begin{pmatrix} \mathcal{E} & 0 \\ 0 & -\mathcal{E} \end{pmatrix}. \tag{2.8}$$

It can be shown using the WKB approximation that the tunneling energy is $\Delta_0 \approx \hbar\Omega e^{-\lambda}$, where $\lambda \approx \sqrt{2mVd^2}/2\hbar$ [25]. Assuming a uniform distribution of barrier heights V it is easily shown that one expects uniform distribution in $\log \Delta_0$. That along with the assumption of a uniform distribution of Δ gives the standard distribution for the TLS barrier height and asymmetry

$$\frac{d^2N}{d\Delta d\Delta_0} = \frac{P_0}{\Delta_0}, \tag{2.9}$$

where P_0 is the TLS spectral and spatial density found to be of order 10^{44} $\mathrm{J}^{-1}\mathrm{m}^{-3}$ [25] for most amorphous dielectrics.

2.2 Two-level system loss

Charge TLS defects can couple to electric fields or strain fields. In this discussion we'll focus on electric field perturbation of TLSs but the results can be generalized to include strain fields.

An applied electric field $\vec{E}$ alters Δ and Δ_0 of a TLS via a perturbation Hamiltonian

$$H_S = \frac{1}{2}\begin{pmatrix} \delta\Delta & -\delta\Delta_0 \\ -\delta\Delta_0 & -\delta\Delta \end{pmatrix}. \tag{2.10}$$

Thus the total Hamiltonian in the left right basis is $H = H_0 + H_S$. Here we will make the assumption that the change in asymmetry $\delta\Delta$ is much bigger than the change in tunneling rate $\delta\Delta_0$. This is plausible because the electric field wavelength is in general much longer than the TLS length scales and thus we don't expect the barrier height and the separation of the wells to be affected by the application of a field, but we do expect the field to effect the EM environment of the TLSs, thus shifting their asymmetry energy, Δ. For small perturbations, we expect the asymmetry energy shift $\delta\Delta$ to vary linearly with the applied field,

$$\delta\Delta = 2\vec{p}\cdot\vec{E}, \tag{2.11}$$

where $\vec{p}$ is the dipole moment of the TLS and $\vec{E}$ is the applied electric field. Transforming the perturbation Hamiltonian into the eigenbasis of $\mathcal{H}_0$ gives [26]

$$\mathcal{H}_S = \frac{1}{\mathcal{E}}\begin{pmatrix} \Delta & \Delta_0 \\ \Delta_0 & -\Delta \end{pmatrix}(\vec{p}\cdot\vec{E}). \tag{2.12}$$

We note that this Hamiltonian for a TLS in an electric field is analogous to that of a spin 1/2 system in a magnetic field [27, 28],

$$\mathcal{H}^M = \mathcal{H}_0^M + \mathcal{H}_S^M = -\hbar\gamma\vec{B}\cdot\vec{S} = -\hbar\gamma(\vec{B}_0\cdot\vec{S}) - \hbar\gamma(\vec{B}'\cdot\vec{S}), \tag{2.13}$$

where γ is the gyromagnetic ratio, $\vec{B}_0$ is a static magnetic field representing the unperturbed Hamiltonian, $\vec{B}'$ is an oscillating magnetic field representing the perturbation Hamiltonian, and $\vec{S} = \vec{\sigma}/2$, where $\vec{\sigma}$ represents the Pauli matrices:

$$\sigma_x = \begin{pmatrix} 0 & 1 \\ 1 & 0 \end{pmatrix}, \ \sigma_y = \begin{pmatrix} 0 & -i \\ i & 0 \end{pmatrix}, \ \sigma_z = \begin{pmatrix} 1 & 0 \\ 0 & -1 \end{pmatrix}. \tag{2.14}$$

The two systems are identical once the following substitutions are made

$$-\hbar\gamma\vec{B}_0 = (0,0,\mathcal{E}) \quad \text{and} \quad -\hbar\gamma\vec{B}' = \left(2\frac{\Delta_0}{\mathcal{E}}\vec{p}\cdot\vec{E}, 0, 2\frac{\Delta}{\mathcal{E}}\vec{p}\cdot\vec{E}\right). \tag{2.15}$$

Without relaxation processes (infinite spin lifetimes), the dynamics of a free spin in a magnetic field are simply represented by

$$\frac{d}{dt}\vec{S}(t) = \gamma\vec{S}\times\vec{B}, \tag{2.16}$$

where $\vec{S}(t)$ is the spin operator.

In 1946 Felix Bloch derived the Bloch equations describing a spin 1/2 system with relaxation in the context of nuclear magnetic resonance (NMR) [29]

$$\begin{aligned} \frac{d}{dt}\langle S_x(t)\rangle &= \gamma\left(\langle S_y(t)\rangle B_z(t) - \langle S_z(t)\rangle B_y(t)\right) - \tfrac{\langle S_x(t)\rangle}{T_2} \\ \frac{d}{dt}\langle S_y(t)\rangle &= \gamma\left(\langle S_z(t)\rangle B_x(t) - \langle S_x(t)\rangle B_z(t)\right) - \tfrac{\langle S_y(t)\rangle}{T_2} \\ \frac{d}{dt}\langle S_z(t)\rangle &= \gamma\left(\langle S_x(t)\rangle B_y(t) - \langle S_y(t)\rangle B_x(t)\right) - \tfrac{\langle S_z(t)\rangle - S_z^0[B_z(t)]}{T_1}, \end{aligned} \tag{2.17}$$

where T_1 and T_2 are the longitudinal and transverse relaxation times, respectively, and $S_z^0[B_z(t)]$ is the equilibrium population difference between the two levels with field $B_z(t)$,

$$S_z^0[B_z(t)] = \frac{1}{2}\tanh\left(\frac{\hbar\gamma B_z(t)}{2kT}\right). \tag{2.18}$$

The Bloch equations are for an ensemble of spins, so $\langle\vec{S}(t)\rangle$ represents the average spin of the system. Thus to solve for the behavior of a TLS in an electric field, we need only solve the analogous Bloch equations for a spin in a magnetic field.

In the Bloch equations, the relaxation times, added in an ad hoc manner, are essential in understanding the loss in our system so let's briefly discuss their role. First, the longitudinal relaxation time T_1 is simply the characteristic timescale for a TLS to fall from the excited state to the ground state. It can be defined by the rate at which an ensemble of TLSs approaches their equilibrium state

$$\frac{dS_z}{dt} = -\frac{S_z - S_z^0}{T_1}, \tag{2.19}$$

where one can substitute polarization P for spin S when considering a TLS instead of a magnetic spin. It can be shown [27] that for an ensemble of TLSs

$$\frac{1}{T_1} = \left(\frac{\Delta_0}{\mathcal{E}}\right)^2 \frac{1}{T_{1,min}}, \tag{2.20}$$

where $T_{1,min}$ is a characteristic of the material. This inverse relationship between T_1 and the tunneling energy Δ_0 can be understood qualitatively. For lower tunneling rates, transitions between the two states are of course less common, naturally leading to a higher state lifetime T_1.

The transverse relaxation time T_2 is more subtle. Quantitatively it's the rate of decay of the off-diagonal terms of the TLS density matrix in the master equation (discussed in more detail in Chapter 8), or it's the rate at which a pure state approaches a mixed state. One can also think of it as the loss of quantum coherence, which includes both loss of phase information and loss of energy; this is why T_2 is also called the coherence time. Loss of phase information occurs on a time scale T_ϕ, the dephasing time. Thus T_2 incorporates T_1 relaxation as well as dephasing,

$$\frac{1}{T_2} = \frac{1}{2T_1} + \frac{1}{T_\phi}. \tag{2.21}$$

The correspondence between TLS behavior and the Bloch equations was recognized and used to solve the acoustic loss problem of a TLS in a strain field [28]. A year later this result was generalized to solve the electric loss problem [30]

$$\tan(\delta) = \frac{\pi P_0 |\vec{p}|^2}{3\epsilon} \frac{\tanh(\hbar\omega/2k_BT)}{\sqrt{1+\Omega_{R0}^2\tau^2}}, \tag{2.22}$$

where $f = \omega/2\pi$ is the measurement frequency, τ is a characteristic TLS lifetime that depends on the decoherence limit, and Ω_{R0} is the characteristic Rabi frequency of the TLS ensemble,

$$\Omega_{R0} = \frac{\vec{p}\cdot\vec{E}}{\hbar}. \tag{2.23}$$

Note that $\tau = \sqrt{T_{1,min}T_2/3}$ for constant coherence time T_2 and that the Rabi frequency for an individual TLS is

$$\Omega_R = \frac{\vec{p}\cdot\vec{E}}{\hbar}\frac{\Delta_0}{\mathcal{E}}. \tag{2.24}$$

To simplify the expression for the loss tangent we define the intrinsic loss tangent of a material

$$\tan\delta_0 = \frac{\pi P_0 |\vec{p}|^2}{3\epsilon}, \tag{2.25}$$

and the characteristic field

$$E_c = \frac{\hbar}{|\vec{p}|\tau}. \tag{2.26}$$

Thus the Eq. 2.22 becomes

$$\tan(\delta) = \tan(\delta_0)\frac{\tanh(\hbar\omega/2k_BT)}{\sqrt{1+(|\vec{E}|/E_c)^2}}. \tag{2.27}$$

A qualitative way to understand the functional form of the TLS loss is to think of the TLSs as a bath that absorbs and reemits photons through absorption and stimulated emission. For low excitation fields $|\vec{E}| \ll E_c$ the TLS bath is in its ground state and thus is able to absorb whatever energy is available to it, thus there's a constant loss tangent, $\tan\delta_0 \tanh(\hbar\omega/2k_BT)$, with no field dependence. In contrast when the field increases such that the Rabi frequency of the TLSs is faster than the decay rate, the TLSs become more and more likely to be in the excited state, and are just as likely to reemit a photon through stimulated emission as they are to absorb a photon. This leads to a reduction in loss tangent as $\sim 1/|\vec{E}|$ for high fields $|\vec{E}| \gg E_c$.

2.3 Loss in a qubit

Individual TLSs were first noticed as splittings in the spectrum of phase qubits [31] (see Fig. 2.2) and were initially believed to be TLSs causing critical current noise in the junction, but a year later were understood as TLSs coupling to the electric field of the qubit [15, 32]. I helped take a related resonator measurement of individual TLS with a device called a Josephson Junction Defect Spectrometer [33]. By solving for the Hamiltonian of a TLS in the junction dielectric of a phase qubit [15], it can be shown that the splitting size is given by

$$S = S_{max} \cos\eta \cos\theta, \tag{2.28}$$

where η is the angle between the TLS dipole and the field in the junction, $\theta = \arctan \Delta/\Delta_0$, and S_{max} is the maximum splitting size given by

$$S_{max} = 2\frac{|\vec{p}|}{x}\sqrt{\frac{\mathcal{E}}{2C}}, \tag{2.29}$$

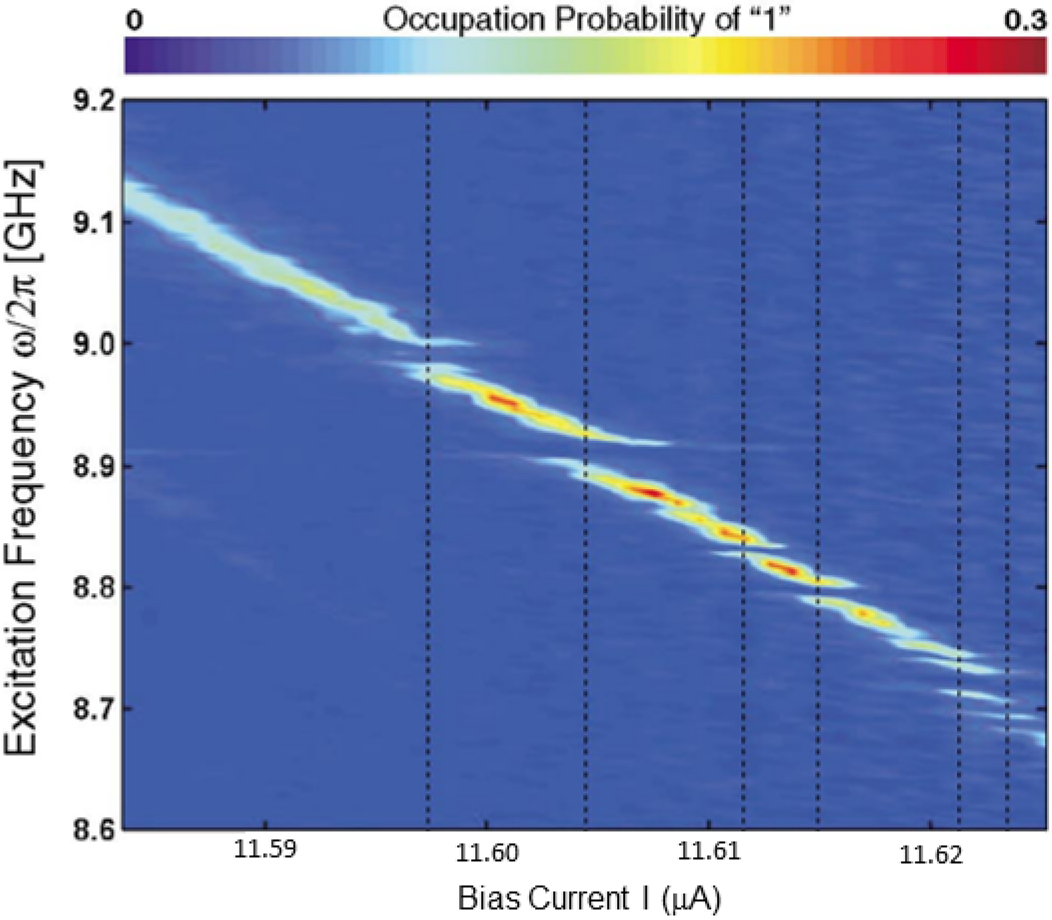

Figure 2.2: Splitting in the spectrum of phase qubit from Ref. [31] due to coupling to TLSs in the junction. The dotted lines mark the location of prominent splittings on the current bias axis.

where C is the capacitance of the qubit and x is the thickness of the junction. If we assume a surface density of TLSs for the junction, σ, as was done in Ref. [15] and the same uniform distribution of asymmetry energies Δ and logarithmic distribution of tunneling rates Δ_0 we arrive at this expression for the TLS density of states

$$\frac{d^2N}{dEd\theta} = \frac{\sigma A}{\cos\theta}, \tag{2.30}$$

where A is the junction area and we've changed the distribution variables from Δ and Δ_0 to E and θ. It can be shown that switching from θ to S and averaging over η yields the density

$$\frac{d^2N}{dEdS} = \sigma A \frac{\sqrt{1 - S^2/S_{max}^2}}{S}, \tag{2.31}$$

for $S < S_{max}$ and 0 otherwise [15].

Assuming that the qubit couples to a continuum of many TLSs, which is reasonable for large area junctions, we calculate the decay rate of the qubit from Fermi's golden rule

$$\Gamma_1 = \frac{2\pi}{\hbar}\int_0^{S_{max}} \frac{d^2N}{dEdS}(S/2)^2 dS \tag{2.32}$$

$$= (\pi/6)\sigma A S_{max}^2/\hbar \tag{2.33}$$

$$= \frac{\pi(\sigma/x)|\vec{p}|^2}{3\epsilon}\frac{E}{\hbar} \tag{2.34}$$

where we've substituted in Eq. 2.31 for the density of states and used the qubit-TLS interaction Hamiltonian,

$$H_{int} = i(S/2)(|1\rangle|g\rangle\langle 0|\langle e| - |0\rangle|e\rangle\langle 1|\langle g|) \tag{2.35}$$

where, $|g\rangle$ and $|e\rangle$ are the ground and excited states of the TLS and $|0\rangle$ and $|1\rangle$ are the ground and excited states of the qubit.

By comparing the qubit decay rate in Eq. 2.34 to the intrinsic loss tangent from TLSs in Eq. 2.25 it can be seen that the qubit decay rate is proportional to the low field limit of the dielectric loss tangent. Thus we need to minimize dielectric loss to optimize qubit lifetimes.

2.4 TLS micromechanism

TLSs have been germane to the study of low temperature properties of amorphous solids for over 40 years, however rarely has a TLS micromechanism been identified. One problem is that TLSs are so ubiquitous in low temperature solids that their effect can be due to many different types of structures. The amorphous nature of the materials inevitably creates variations in the environment, presenting a vast parameter space with which to form TLS defects, making the task of identifying such a defect very difficult.

Despite the difficulties there have been some successes in using density functional theory to identify potential TLS candidates. Holder *et al.* [34] found that in amorphous aluminum oxide ($\mathrm{AlO_x}$), hydrogen impurities are likely to fill aluminum cation vacancies and create an $\mathrm{OH^{-1}}$ rotors that can act as tunneling TLSs. Such defects were originally proposed by Phillips [26] as a leading TLS candidate. Some experiments have correlated low temperature TLS dielectric loss with room temperature defect spectroscopy of the material. Paik *et al.* [35] found that nitrogen rich silicon nitride ($\mathrm{SiN_x}$) films had a relatively high density of N-H bonds which were correlated with low temperature loss.

TLSs can also be found in crystals, and because crystals are relatively simple systems, it has been possible to identify the defects responsible for them. For example, it's been shown that lithium ion (Li^+) defects can replace potassium ions (K^+) in potassium chloride (KCl) and form tunneling TLSs [25]. It's also been found through thermal conductivity measurements that doping sodium fluoride (NaF) with hydroxide (OH^-) ions can create TLSs, suggesting an OH rotor defect model. Compared to crystalline systems, it seems likely that amorphous systems will tend to have many more types of TLSs. Thus a good starting point for research into loss in amorphous dielectrics is to find the leading TLS contributors to loss.

Chapter 3

Experimental setup and measurement technique

3.1 Dilution refrigerator setup

All measurements in this thesis were performed in a dilution refrigerator. A dilution refrigerator uses a mixture of He-3 and He-4 to reach millikelvin temperatures. The specific type of refrigerator I used was an Oxford Instrument Kelvinox model 400 dilution refrigerator which has a cooling power of 400 μW at 100 mK (see Fig. 3.1(a)). I typically reached a base temperature of about 30 mK, although there were instances when either vacuum leaks or insufficient heat sinking produced a higher base temperature.

For all of my measurements only two microwave lines were required (in measurements discussed in Chapters 8 and 9 an additional dc bias line was required). A schematic of the wiring setup in the refrigerator is shown in Fig. 3.1(b). Stainless steel UT85 coax cables (0.085" outer diameter) were used for the input lines for thermal isolation and copper nickel UT85 coax cables were used for the output lines for thermal isolation and reduced attenuation of the measurement signal. In addition to the attenuation in the lines themselves, 20 dB Midwest Microwave attenuators were used at the 1.5 K stage and the mixing chamber (base temperature) to eliminate thermal noise from higher temperatures. The output line had two PAMTECH circulators (CTH1409KS) terminated by 50 Ω at the mixing chamber and one at the

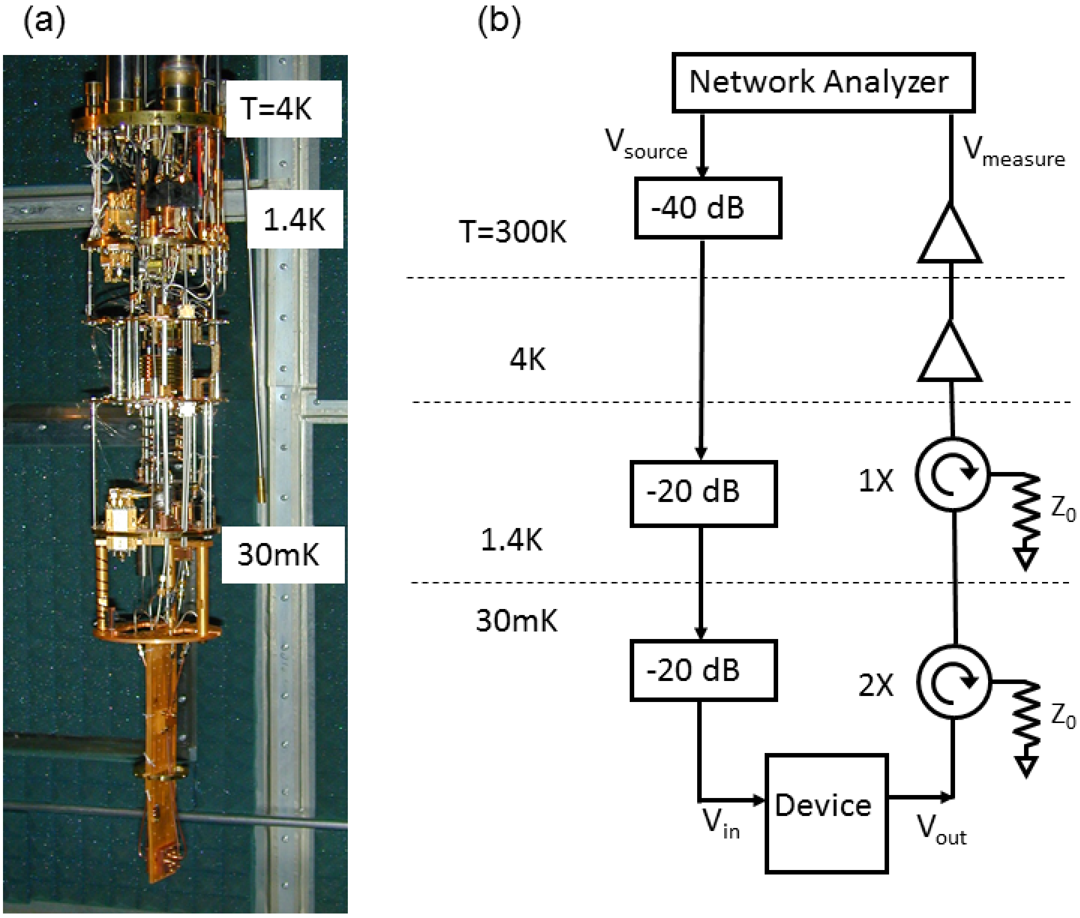

Figure 3.1: (a) Photograph of the inner vacuum chamber of the dilution refrigerator with the sample box mounted at the bottom. (b) Schematic of microwave wiring in the refrigerator.

1.5 K stage for microwave isolation between the sample and the amplifiers. Each provides 18 dB of isolation in the 4-8 GHz range. After the circulators there was a low noise, cryogenic HEMT amplifier, purchased from the Weinreb group in Caltech [36], in the 4 K helium bath followed by two additional room temperature amplifiers (see Fig. 3.1(b)).

3.2 Signal calibration

As shown in Fig. 3.1(b), an Agilent N5242A PNA-X network analyzer was used to perform device spectroscopy. Here I'll discuss the calibration of the system to convert from the applied network analyzer voltage to the voltage at the sample. This calibration is critical because as discussed in Chapter 2 TLS dielectric loss is power-dependent. Since stainless steel has little change in electrical conductivity with temperature, I performed the calibration of the input microwave lines at room temperature and assumed this was accurate at low temperatures.

First, to determine the attenuation of the input lines at room temperature, I used the network analyzer to measure the throughput S_{21} from the network analyzer to the input connection at the bottom of the mixing chamber where the device will be mounted. This was done for three input powers (see Fig. 3.2(a)). Three relatively high powers were used (-20, -10, and 0 dBm) to minimize the required averaging for sufficient signal to noise. I fit the three measurements of S_{21} to a line on a semi log plot (see Fig. 3.2(a)). I then averaged the slopes, and plotted the intercepts as a function of the input power (see Fig. 3.2(b)). The slope in Fig. 3.2(b) should ideally be unity but I fit to the slope in order to capture any nonlinearities in the system; the slope obtained was 0.981. The average slope with frequency from Fig. 3.2(a) (-3.53 dBm/GHz) was then combined with the slope with input power from Fig. 3.2(b) to obtain a calibration function for the power at the mixing chamber as a function of the frequency and the input power,

$$P_{device} = -3.53(\mathrm{dBm/GHz}) \times \mathrm{freq(GHz)} + 0.981 \times \mathrm{P_{NA}} - 57.04\ \mathrm{dBm}. \qquad (3.1)$$

Note that since the slopes with frequency from Fig. 3.2(a) are generally very close and the slope with power from Fig. 3.2(b) is generally close to 1, in principle a single power could be used to calibrate the lines. Three was chosen somewhat arbitrarily

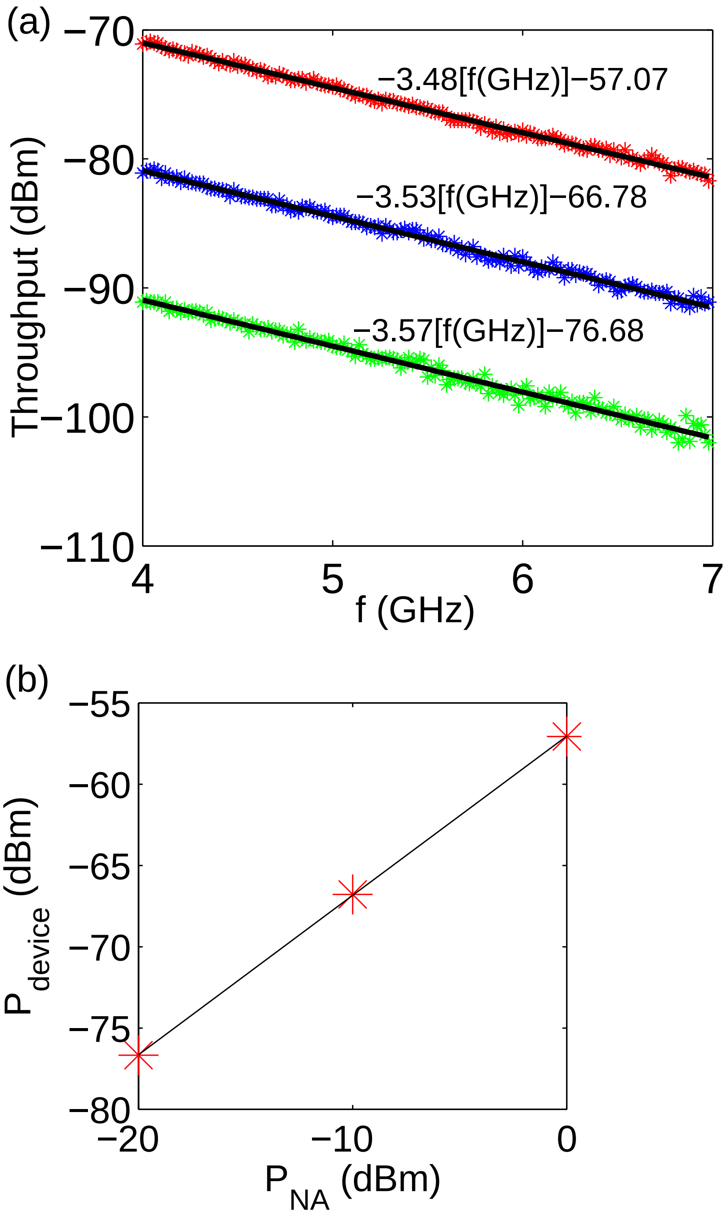

Figure 3.2: (a) Throughput calibration measurements of input microwave lines performed at room temperature with -20 (green), -10 (blue), and 0 (red) dBm at the Network analyzer. (b) Plot of the intercepts from the fits in (a).

to check and marginally improve the calibration.

From the 50 Ω characteristic impedance of the input lines and the input power at the device P_{device} we can calculate the input RMS voltage at the device

$$V_{device,RMS} = \sqrt{P_{device} \times 50\Omega}. \tag{3.2}$$

This input voltage will be used later to calculate the voltage across the resonators. The setup has two sets of input and output lines and I've shown here the calibration for only one. The calibration for the other input line is performed in an identical manner. The calibration equation for the other line analogous to Eq. 3.1 is

$$P_{device} = -3.51(\mathrm{dBm/GHz}) \times \mathrm{freq(GHz)} + 1.02 \times \mathrm{P_{NA}} - 58.03\ \mathrm{dBm}. \tag{3.3}$$

3.3 Resonance derivation

I measure a resonator's loss by coupling it to a coplanar waveguide (CPW) transmission line and measure the waveguide's throughput $S_{21} \equiv V_{out}/V_{in}$. I next present a derivation of S_{21} that is similar to the one originally derived for this project by Kevin Osborn. The throughput can be modeled by the circuit schematic shown in Fig. 3.3, where the resonator, composed of the inductor L and the capacitor $\hat{C}$, is coupled to a CPW. Both inductive and capacitive coupling is included through M and C_C respectively, and $\hat{C}$ is complex to account for dielectric losses. V_{in} and V_{out} are the input and output voltage amplitudes, and V is the voltage across the capacitor $\hat{C}$. For this model, I assume the transmission lines are perfectly coupled with the characteristic impedance Z_0 and L_1 is small ($L_1 << C_C Z_0^2$).

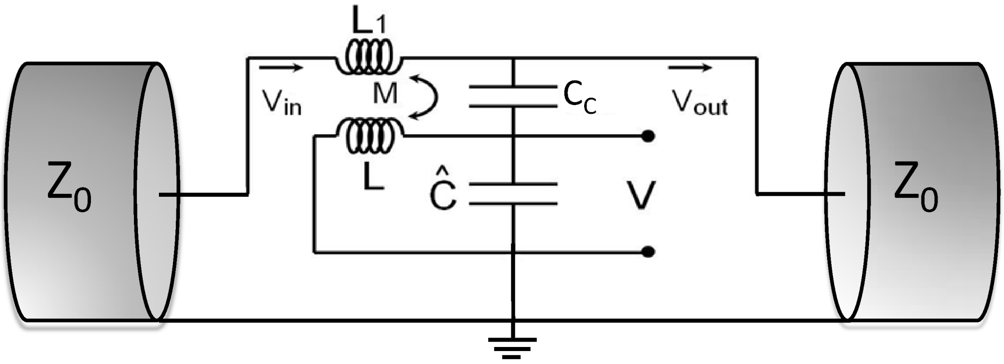

Figure 3.3: a schematic of the resonator measurement setup with both inductive and capacitive coupling.

Figure 3.3 can be redrawn as Fig. 3.4(a) and assuming low loss $\left(\mathbf{Im}\left\{\hat{C}\right\} << \mathbf{Re}\left\{\hat{C}\right\}\right)$, the complex capacitance can be split into a capacitor and a resistor as in Fig. 3.4(b), where $C = \mathbf{Re}\left\{\hat{C}\right\}$ and

$$R = \frac{1}{\omega \mathbf{Im}\left\{\hat{C}\right\}}. \tag{3.4}$$

To solve for the transmission through the CPW I write the following Kirchhoff's equations for the circuit in Fig. 3.4(b),

$$\begin{aligned} 2V_{in} - V_{out} &= I_1(Z_0 + i\omega L_1) - i\omega M I_L \\ V - V_{out} &= \frac{I_2}{i\omega C_C} \\ V_{out} &= (I_1 + I_2)Z_0 \\ V &= i\omega L I_L - i\omega M I_1 \\ V &= -\frac{I_2 + I_L}{i\omega \hat{C}}. \end{aligned} \tag{3.5}$$

Solving these equations we find an expression for the transmission S_{21} as a function

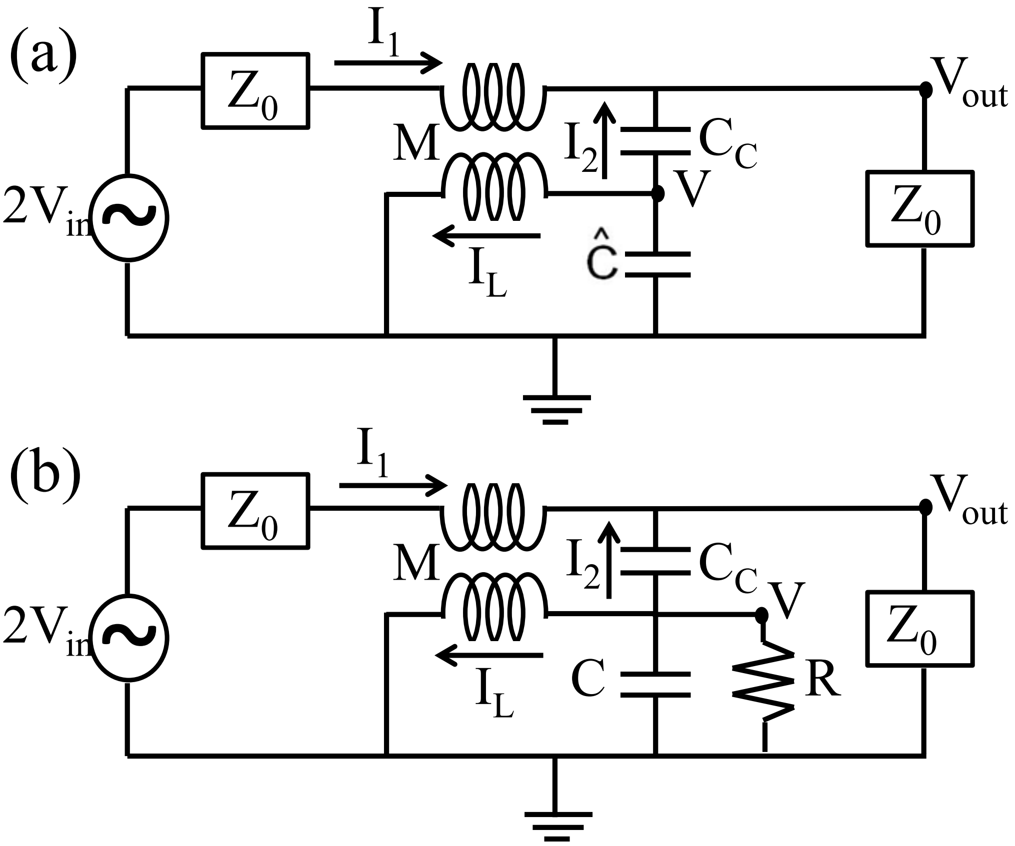

Figure 3.4: (a) Equivalent circuit to that shown in Fig. 3.3. (b) Equivalent circuit to (a) where $\hat{C}$ has been separated into its real (C) and imaginary $(1/\omega R)$ parts.

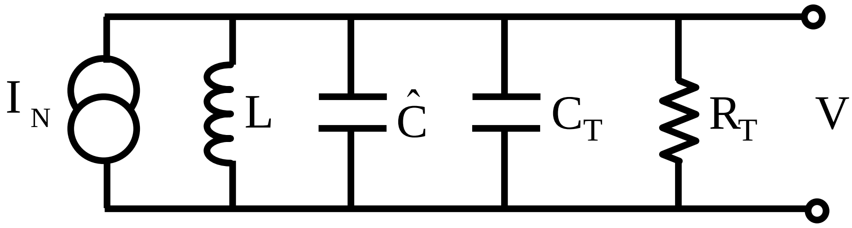

Figure 3.5: Norton equivalent circuit for resonator measurement where V is the voltage across the capacitor.

of the voltage across the capacitor:

$$S_{21} = \frac{V_{out}}{V_{in}} = 1 + \frac{V}{2V_{in}}\left(\frac{M}{L} + Z_0 i\omega C_C\right), \tag{3.6}$$

where some approximations have been used ($\omega C << 1/Z_0, \{\omega L_1, \omega M^2/L\} << Z_0$). Using Eqs. 3.5 again, this time to eliminate V_{out} we get the following independent equation:

$$-V\left(\frac{1}{i\omega L}+i\omega\hat{C}+\frac{i\omega C_C}{i\omega C_C Z_0+1}+\frac{1}{2Z_0}\left(\frac{M}{L}-\frac{i\omega C_C Z_0}{1+i\omega C_C Z_0}\right)^2\right)=\frac{V_{in}}{Z_0}\left(\frac{M}{L}-\frac{i\omega C_C Z_0}{1+i\omega C_C Z_0}\right). \tag{3.7}$$

To proceed, we note that Eq. 3.7 is of the form

$$I_N = V\left(\frac{1}{i\omega L} + i\omega\hat{C} + G_N\right), \tag{3.8}$$

where G_N and I_N are the Norton equivalent conductance and current respectively. The circuit in Fig. 3.4 thus has the Norton equivalent circuit shown in Fig. 3.5. From Eq. (3.7) we see that

$$I_N = -\frac{V_{in}}{Z_0}\left(\frac{M}{L} - \frac{i\omega C_C Z_0}{1+i\omega C_C Z_0}\right), \tag{3.9}$$

and

$$G_N = \frac{i\omega C_C}{i\omega C_C Z_0+1} + \frac{1}{2Z_0}\left(\frac{M}{L} - \frac{i\omega C_C Z_0}{1+i\omega C_C Z_0}\right)^2. \tag{3.10}$$

Since the real part of G_N loads the resonator measurement and the imaginary part shifts the resonance frequency, it is useful to separate G_N into its real (conductive) and imaginary (susceptive) components. We can now define $\mathbf{Re}\{G_N\} \equiv 1/R_T$, $\mathbf{Im}\{G_N\} \equiv \omega C_T$, $R_{eff}^{-1} \equiv R^{-1} + R_T^{-1}$, $Q \equiv R_{eff}\omega_0(C + C_T)$, and $\omega_0 = 1/\sqrt{L(C + C_T)}$. Expanding Eq. 3.10 around the small values M/L and $\omega C_C Z_0$ and keeping only the lowest order non-vanishing terms we find

$$C_T = C_C, \tag{3.11}$$

and

$$R_T^{-1} = \frac{1}{2Z_0}\left(\left(\frac{M}{L}\right)^2 + \omega^2 C_C^2 Z_0^2\right). \tag{3.12}$$

Equation (3.6) can then be rewritten as

$$S_{21} = 1 - \frac{R_{eff}/R_T}{1 + 2iQ\frac{\omega-\omega_0}{\omega_0}}, \tag{3.13}$$

where we've assumed that $\omega \approx \omega_0$. Next it is convenient to define the external quality factor $Q_e = R_T\omega_0(C + C_T)$, which effectively gives the resonator's coupling loss, allowing us to rewrite Eq. 3.13 as

$$S_{21} = 1 - \frac{Q/Q_e}{1 + 2iQ\frac{\omega-\omega_0}{\omega_0}}. \tag{3.14}$$

Equation 3.14 has the functional form of a Lorentzian with three free parameters (Q, Q_e, and ω_0) and can now in principle be used to fit transmission measurements to extract the resonance frequency as well as the total and external quality factors. Note that what we're generally most interested in is the loss tangent of the resonator $\tan\delta = \mathbf{Im}\left\{\hat{C}\right\}/\mathbf{Re}\left\{\hat{C}\right\}$. We can now use Eq. 3.4 to define the internal quality factor $Q_i = R\omega C = 1/\tan\delta$ such that

$$\frac{1}{Q_i} = \frac{1}{Q} - \frac{1}{Q_e}. \tag{3.15}$$

This relationship allows us to use extracted values of Q and Q_e to determine Q_i and thus the loss tangent of the resonator.

Note that the internal quality factor Q_i of the resonator is modeled here as the loss tangent of the dielectric, but in principle the loss can come from any internal loss mechanism in the device. When multiple loss mechanisms are active they add reciprocally as the internal and external quality factors do. For example if a resonator exhibited resistive loss (Q_{res}), radioactive loss (Q_{rad}), and dielectric loss ($Q_{\tan\delta}$), the total internal quality factor would be

$$\frac{1}{Q_i} = \frac{1}{Q_{rad}} + \frac{1}{Q_{res}} + \frac{1}{Q_{\tan\delta}}. \tag{3.16}$$

3.4 Determining the voltage across the resonator

In section 3.2 I discussed how I calibrated the microwave input lines to know what voltage I'm applying at the CPW. In section 3.3 I derived the output transmission through the CPW as a function of the resonator parameters. Here I combine these two results in order to calculate the voltage V across the resonator as a function of the resonator parameters. From Eq. 3.8 we can write the following expression for the voltage across the resonator,

$$V = \frac{I_N}{\frac{1}{i\omega L} + i\omega\hat{C} + G_N}. \tag{3.17}$$

The denominator can be split into its real and imaginary components using $i\omega\hat{C} = i\omega C + R^{-1}$ and $G_N = i\omega C_T + R_T^{-1}$. On resonance, the imaginary components of the denominator cancel leaving only real components, thus the voltage on resonance can be rewritten as

$$V(\omega = \omega_0) = \frac{I_N}{R^{-1} + R_T^{-1}} = I_N R_{eff}. \tag{3.18}$$

Substituting Eq. 3.9 in for I_N, Eq. 3.18 becomes

$$V(\omega = \omega_0) = -\frac{V_{in} R_{eff}}{Z_0}\left(\frac{M}{L} - \frac{i\omega C_C Z_0}{1 + i\omega C_C Z_0}\right), \tag{3.19}$$

and recognizing that we're interested in the RMS voltage across the resonator on resonance, we can rewrite Eq. 3.19 as

$$V_{RMS}(\omega = \omega_0) = \frac{R_{eff}}{Z_0}\left|\frac{M}{L} - \frac{i\omega C_C Z_0}{1 + i\omega C_C Z_0}\right| V_{in,RMS}. \tag{3.20}$$

Then using Eq. 4.5, this can be rewritten as

$$V_{RMS} = \frac{R_{eff}}{Z_0}\sqrt{\frac{2Z_0}{R_T}} V_{in,RMS}. \tag{3.21}$$

Finally using the definitions of Q and Q_e, we find the voltage on resonance is

$$V_{RMS}(\omega = \omega_0) = \sqrt{\frac{2}{Z_0 \omega_0 C Q_e}} Q V_{in,RMS}, \tag{3.22}$$

where we've assumed $C_C << C$.

We now have an expression for the voltage across the resonator in terms of extracted parameters (Q, Q_e, and ω_0) from throughput measurement fits to Eq. 3.14, the calibrated input voltage $V_{in,RMS}$ of the device from Eq. 3.2, and known design parameters of the resonator and the circuit (Z_0 and C). Note that a lumped element resonator was assumed for this derivation, and Chapter 4 contains further analysis for the situation where the resonator length is comparable to the resonance wavelength.

3.5 Asymmetric resonance line shapes

In section 3.3 we derived the Lorentzian line shape for a matched transmission line coupled to a resonator. However, as Fig. 3.6 shows non-ideal experimental setups can lead to asymmetry in the resonance line shape [37, 27, 35, 38, 39, 40, 41], corresponding to, as will be shown later in this section, a rotation of the resonance circle. This complicates the analysis and the interpretation of internal and external quality factors (Q_i and Q_e). Several methods for extracting the Q_i of a resonator have been used for different experimental setups [42, 43, 44, 45, 40]. However, these methods either require a single port reflective measurement [43, 44] (incompatible with most qubit measurements), full two-port characterization [42, 45] (typically unavailable for millikelvin measurements), or identifying and fitting to a second coupled mode [40] (a special case). The most widely used technique for analyzing millikelvin resonator measurements, prior to our publication of this work, the ϕ rotation method (ϕRM), simply adds an empirical rotation of the resonance circle before extracting the quality factor [35, 27, 38].

In this section I show how asymmetry in the resonance line shape can arise from coupling the resonator to mismatched input and output transmission lines as well as non-negligible transmission line series inductance (L_1), mutual inductance (M) or coupling capacitance (C_C). Based on this understanding of the origin of

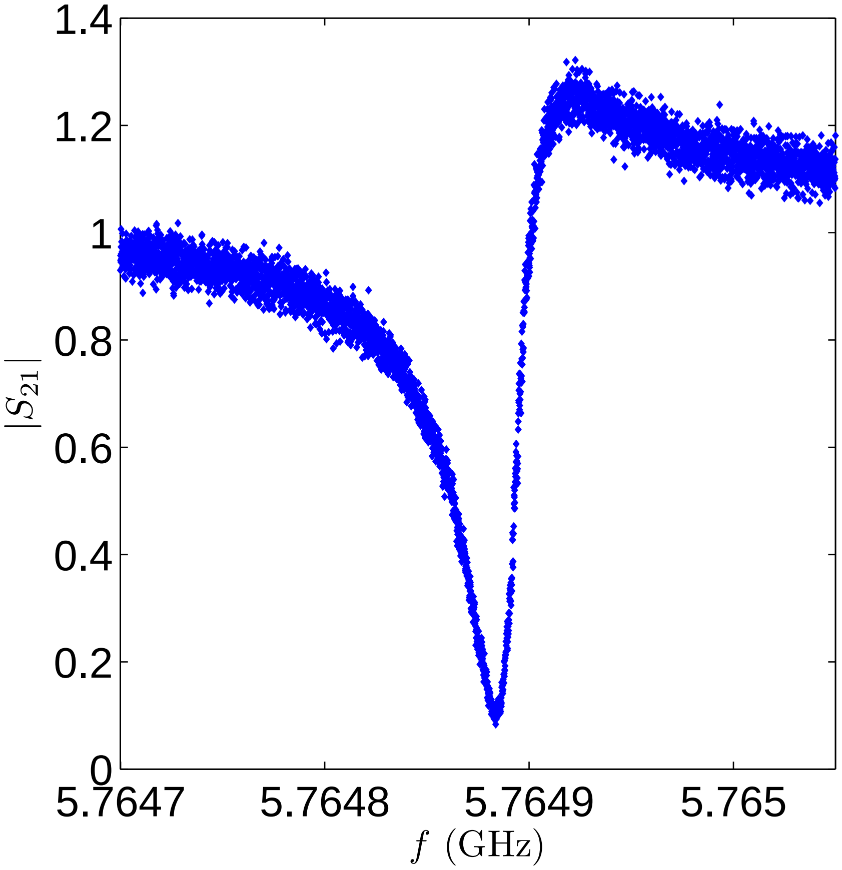

Figure 3.6: Resonance line shape of a coplanar superconducting aluminum QLL-CPS resonator taken at 30 mK (see Chapter 4). The line shape is clearly asymmetric and does not fit to Eq. 3.14.

the asymmetry, I'll derive the Diameter Correction Method (DCM) and use it to extract Q_i. I'll compare this to the conventional analysis method, the ϕ rotation method (ϕRM) [35, 27, 38], and show that there is a one-to-one mapping between the two methods but that the ϕRM systematically overestimates Q_i by an analytically quantifiable amount. Note, I do not address fitting techniques here but interested readers can find a comprehensive quantitative comparison of fitting techniques in Ref. [46].

3.5.1 Analysis of asymmetric resonance lineshape

Here I derive an expression for the resonance line shape of a resonator coupled to a transmission line. In contrast to section 3.3, here I assume mismatched transmission lines and non-negligible coupling components (see Fig. 3.7). Solving Kirchhoff's equations for this circuit yields a more general form of Eq. 3.6

$$S_{21} = (1+\hat{\epsilon})\left(1+\frac{V}{2V_{in}}\left(\frac{M}{L}+Z'_{in} i\omega C_C\right)\right), \tag{3.23}$$

where $1+\hat{\epsilon} \equiv 2/(1+(i\omega C_C + /Z_{out})\,Z'_{in})$, $Z'_{in} \equiv Z_{in} + i\omega L_1 - i\omega\frac{M^2}{L}$, and $|\hat{\epsilon}| << 1$. Solving Kirchhoff's equations and eliminating V_{out}, we get the independent equation:

$$\begin{aligned} -V\left(\frac{1}{i\omega L}\right. & \left. +i\omega\hat{C} + \frac{i\omega C_C}{i\omega C_C Z_{out}+1} + \frac{\left(\frac{M}{L}-\frac{i\omega C_C Z_{out}}{1+i\omega C_C Z_{out}}\right)^2}{Z'_{out}+Z_{in}+i\omega\left(L_1-\frac{M^2}{L}\right)}\right) \\ &= 2V_{in}\left(\frac{\frac{M}{L}-\frac{i\omega C_C Z_{out}}{1+i\omega C_C Z_{out}}}{Z'_{out}+Z_{in}+i\omega\left(L_1-\frac{M^2}{L}\right)}\right), \end{aligned} \tag{3.24}$$

where $Z'_{out} \equiv Z_{out}/(1+i\omega C_C Z_{out})$. Again we note that Eq. (3.24) is of the form $V\left(1/(i\omega L)+i\omega\hat{C}+G_N\right) = I_N$, where

$$I_N = -2V_{in}\left(\frac{\frac{M}{L}-\frac{i\omega C_C Z_{out}}{1+i\omega C_C Z_{out}}}{Z'_{out}+Z_{in}+i\omega\left(L_1-\frac{M^2}{L}\right)}\right), \tag{3.25}$$

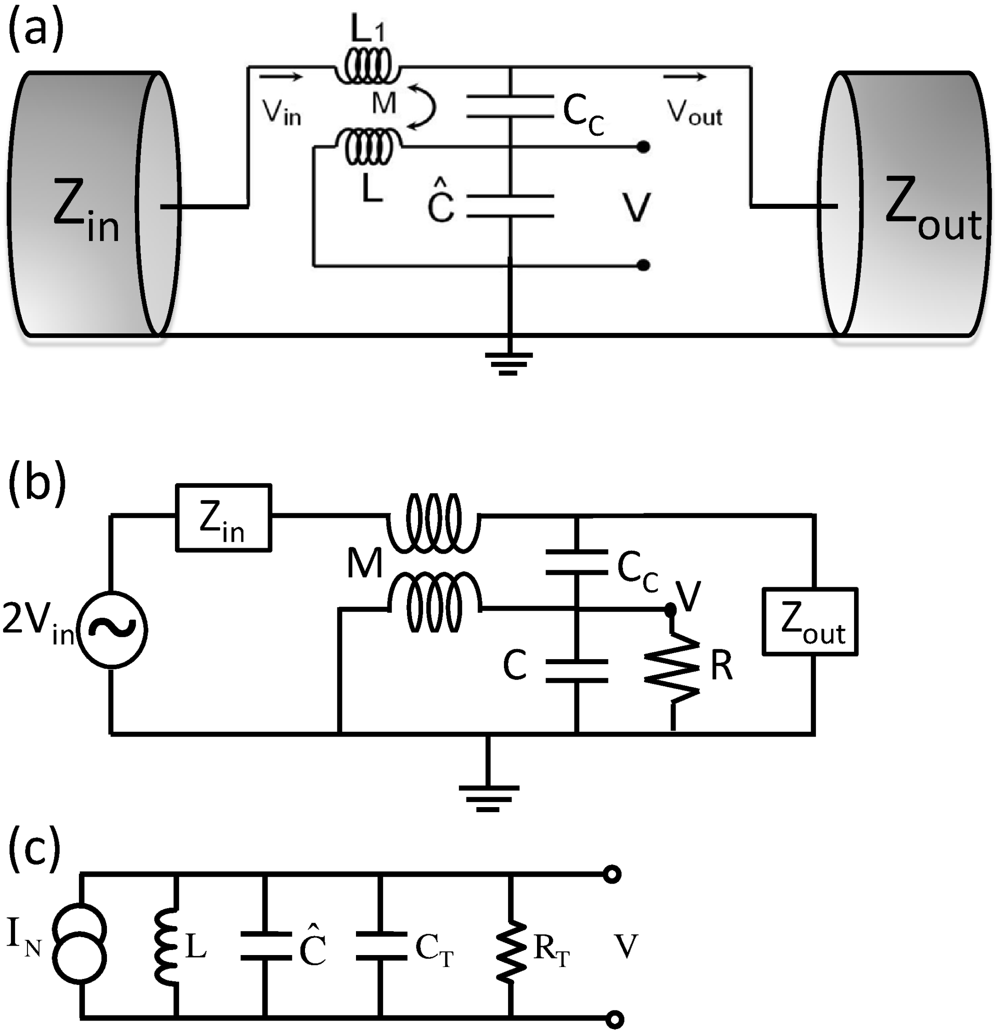

Figure 3.7: (a) Schematic of resonator measurement setup with inductive and capacitive coupling and mismatched input and output transmission lines. (b) equivalent circuit to (a), where $\hat{C}$ has been separated into its capacitive part (C) and its resistive parts ($1/\omega R$). (c) Norton equivalent circuit for resonator measurement where V is the voltage across the capacitor.

and,

$$G_N = \frac{i\omega C_C}{i\omega C_C Z_{out} + 1} + \frac{\left(\frac{M}{L} - \frac{i\omega C_C Z_{out}}{1+i\omega C_C Z_{out}}\right)^2}{Z'_{out} + Z_{in} + i\omega\left(L_1 - \frac{M^2}{L}\right)}. \tag{3.26}$$

Since the real part of G_N loads the resonator measurement and the imaginary part shifts the resonance frequency, it is useful to separate G_N into its real (conductive) and imaginary (susceptive) components. We can now make the same definitions as in section 3.3:

$$\mathbf{Re}\{G_N\} \equiv 1/R_T, \tag{3.27}$$

$$\mathbf{Im}\{G_N\} \equiv \omega C_T, \tag{3.28}$$

$$R_{eff}^{-1} \equiv R^{-1} + R_T^{-1}, \tag{3.29}$$

$$Q \equiv R_{eff}\omega_0(C + C_T), \tag{3.30}$$

$$\omega_0 = 1/\sqrt{L(C + C_T)}, \tag{3.31}$$

$$Q_i \equiv R\omega_0 C = \frac{\mathbf{Re}\{\hat{C}\}}{\mathbf{Im}\{\hat{C}\}} = \frac{1}{\tan\delta}, \tag{3.32}$$

and we add the definition

$$G' \equiv -\frac{I_N}{2V_{in}}\left(\frac{M}{L} + Z'_{in} i\omega C_C\right). \tag{3.33}$$

Then, Eq. (3.23) can be rewritten as

$$S_{21} = 1 - \frac{G' R_{eff}}{1 + 2iQ\frac{\omega - \omega_0}{\omega_0}}, \tag{3.34}$$

where I've dropped the $1 + \hat{\epsilon}$ multiplicative factor because it can be accounted for by assuming an arbitrary attenuation and phase shift. Note that a fundamental difference between section 3.3's derivation of Eq. 3.13 and this more general derivation of Eq. 3.34 is that here if higher order terms in the small parameters (M/L) and $\omega C_C Z_{out}$ are kept, $G' \neq R_T^{-1}$. Proceeding, I now rewrite Eq. (3.34) as

$$S_{21} = 1 - \frac{\left(G_D + R_T^{-1}\right) R_{eff}}{1 + 2iQ\frac{\omega-\omega_0}{\omega_0}}, \tag{3.35}$$

where I've defined

$$G_D \equiv G' - R_T^{-1}. \tag{3.36}$$

Expanding to third-order in M/L we find:

$$\begin{aligned} G_D &= i\omega C_C \frac{M}{L}\left(\frac{Z_{in} - Z_{out}}{Z_{in} + Z_{out}}\right) \\ &+ \frac{i}{\left(Z_{in} + Z_{out}\right)^2}\left(\left(\omega C_C\right)^2 Z_{out}^2 \left(L_1 - C_C Z_{in}^2\right) - \left(\frac{M}{L}\right)^2 \left(L_1 - C_C Z_{out}^2\right)\right), \end{aligned} \tag{3.37}$$

and note that G_D is purely imaginary.

At this point in the analysis it is useful to generalize the definition of the external quality factor

$$\hat{Q}_e^{-1} \equiv \frac{R_T^{-1} + G_D}{\omega_0 \left(C + C_T\right)}, \tag{3.38}$$

and recognize that since G_D is purely imaginary, combining Eqs. 3.38, 3.35, 3.29, 3.30, and 3.32 gives

$$Q_i^{-1} = Q^{-1} - \mathbf{Re}\left\{\hat{Q}_e^{-1}\right\}, \tag{3.39}$$

where I've assumed $C_T \ll C$. We can now rewrite Eq. 3.35 as

$$S_{21} = 1 - \frac{Q\hat{Q}_e^{-1}}{1 + 2iQ\frac{\omega-\omega_0}{\omega_0}}, \tag{3.40}$$

which adds another free parameter to the ideal throughput transmission of Eq. 3.14. This parameter accounts for asymmetry in the line shape. Note that the prefactor

$1+\hat{\epsilon}$ has been dropped from Eq. 3.40 because it only adds a constant phase and contributes a constant multiplicative factor to the amplitude which is convoluted with the amplification and attenuation of the signal.

I emphasize here that G_D is the term that creates the asymmetry in the line shape or equivalently a rotation of the resonance circle around the off resonance point. If G_D were zero then $\hat{Q}_e^{-1}$ would be real, reducing Eq. (3.40) to a symmetric Lorentzian line shape (Eq. 3.14). Equation (3.40) can also be written as

$$S_{21} = 1 - \frac{Q\left|\hat{Q}_e^{-1}\right| e^{i\phi}}{1 + 2iQ\frac{\omega-\omega_0}{\omega_0}}, \tag{3.41}$$

where $\hat{Q}_e^{-1}$ is represented in terms of its magnitude and phase ϕ. Another equivalent representation is

$$S_{21} = 1 - \frac{\frac{Q}{Q_e}\left(1 + 2iQ\frac{\delta\omega}{\omega_0}\right)}{1 + 2iQ\frac{\omega-\omega_0}{\omega_0}}, \tag{3.42}$$

where we've defined

$$\frac{1}{Q_e} \equiv \mathbf{Re}\left\{\hat{Q}_e^{-1}\right\}, \tag{3.43}$$

and $\delta\omega$ is the difference between the resonance frequency and the new rotated in-phase point on the resonance circle, ω_1 (see Fig. 3.8). The form of Eq. (3.42) can be understood by noting that S_{21} is real when $\omega = \delta\omega + \omega_0$.

Here I stress that Eqs. (3.40-3.42) are equivalent representations of the asymmetric line shape, each highlighting a different interpretation of the asymmetry. In Eq. (3.40) the asymmetry is quantified by $\mathbf{Im}\left\{\hat{Q}_e^{-1}\right\}$ and one can think of the asymmetry as coming from a complex loading of the resonator. In Eq. (3.41) the asymmetry is quantified by ϕ, where ϕ is the rotation angle of the resonance circle around the off-resonance point (see Fig. 3.8). And finally in Eq. (3.42) the asym-

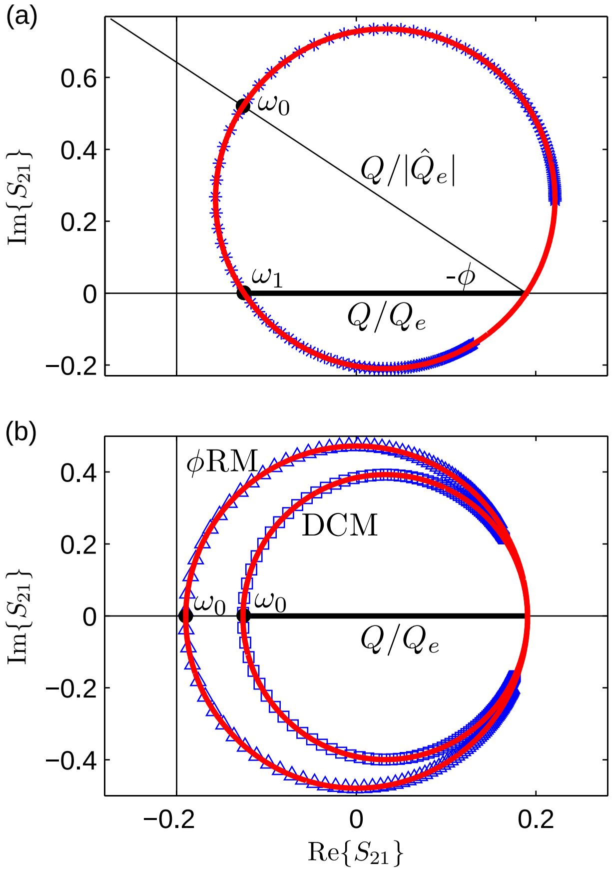

Figure 3.8: (a) Simulated transmission through mismatched coupling lines ($Z_{in} = 24.5\Omega$, $Z_{out} = 84.5\Omega$) plotted as $\mathrm{Im}\{S_{21}\}$ vs. $\mathrm{Re}\{S_{21}\}$ with a fit to a circle. The asymmetry is represented as a rotation of the resonance circle by the angle ϕ away from the real (in-phase) axis or equivalently as $\delta\omega = \omega_1 - \omega_0$, the frequency shift of the in-phase point on the resonance circle. (b) Shows the simulated transmission with asymmetry removed using both analysis techniques. The ϕRM ($\triangle$) only rotates the circle to the real axis while the DCM ($\square$) both rotates the circle and removes the factor of $1/\cos(\phi)$ increase to the diameter. The DCM shows that the invariant quantity is not, as the ϕRM assumes, the diameter of the circle (equal to $Q/|\hat{Q}_e|$ and Q/Q_e before and after the DCM transformation respectively) but rather the length of the real axis segment intersecting the circle (shown in bold and equal to Q/Q_e), where $1/Q_e \equiv \mathbf{Re}\left\{1/\hat{Q}_e\right\}$.

metry is quantified by $\delta\omega$, where $\delta\omega = \omega_1 - \omega_0$ is the frequency shift of the in-phase point on the resonance circle from ω_0 to ω_1 (see Fig. 3.8). Since the three representations are equivalent, there exists a one-to-one mapping between the three notations:

$$\phi = \arctan\left(\frac{\mathbf{Im}\{\hat{Q}_e^{-1}\}}{\mathbf{Re}\{\hat{Q}_e^{-1}\}}\right) = \arctan\left(2Q\frac{\delta\omega}{\omega_0}\right). \tag{3.44}$$

One method the, ϕ rotation method (ϕRM), has been used in the literature [35, 27, 38] to extract internal quality factors accounts for the asymmetry by simply adding an empirical ϕ rotation. Unfortunately this method incorrectly substitutes $\left|\hat{Q}_e^{-1}\right|$ for Q_e^{-1} and defines

$$\frac{1}{Q_{i,\ \phi RM}} = \frac{1}{Q} - \left|\frac{1}{\hat{Q}_e}\right|. \tag{3.45}$$

In effect the ϕRM accounts for the asymmetric line shape phenomenologically by adding the rotation, ϕ, without accounting for its origin and its impact on the interpretation of Q_i. It corresponds to rotating the resonance circle back an angle ϕ in the complex S_{21} plane, thereby putting ω_0 on the in-phase axis. The rotation of the ϕRM can best be seen by examining the difference between Fig. 3.8(a) and Fig. 3.8(b)(△).

The problem with the ϕRM is that simply rotating the resonance circle by angle ϕ does not take into account the fact that the asymmetry has also caused the circle to grow by a factor of $1/\cos(\phi)$, assuming the circle has been normalized to full transmission off resonance ($S_{21}(\omega << \omega_0) = S_{21}(\omega >> \omega_0) = 1$). I have shown here that instead of Eq. 3.45 one has

$$\frac{1}{Q_{i,\ DCM}} = \frac{1}{Q} - \frac{1}{Q_e}. \tag{3.46}$$

I call this the Diameter Correction Method (DCM) because in addition to rotating the circle by the asymmetry angle ϕ it also corrects the diameter by accounting for the complex Q_e. This can be seen by examining the transformation between Fig. 3.8(a) and Fig. 3.8(b)(□).

Another interpretation of the DCM is that the quantity that remains constant in the asymmetry transformation is not the diameter of the resonance circle, as the ϕRM assumes, but rather the distance between the in-phase axis intercepts, shown in bold in Fig. 3.8. That invariant length is the diameter of the circle for a symmetric resonance and becomes a chord of the circle as asymmetry is added, but remains equal to Q/Q_e, while the diameter grows as $Q/|\hat{Q}_e|$. The analytical discrepancy between the two methods can be determined by subtracting Eq. (3.46) from Eq. (3.45),

$$\frac{1}{Q_{i,\ DCM}} - \frac{1}{Q_{i,\ \phi RM}} = \left|\frac{1}{\hat{Q}_e}\right| (\cos(\phi) - 1)\,. \tag{3.47}$$

From Eq. (3.47) we see that the error in the ϕRM diverges for high asymmetry angle, $\phi \approx \pm\pi$, and for low Q_e (high coupling). Note that for $\phi = 0$, $\hat{Q}_e^{-1}$ is real and Eq. (3.46) reduces to Eq. (3.45) and therefore Eq. (3.47) goes to zero.

3.5.2 Analysis of S_{21} Simulations and Data

To test the ϕRM and the DCM, I simulated the transmission through resonant circuits using the numerical linear solver, Microwave Office. Simulations were run varying a range of parameters: Q_i, impedance mismatches, strength of both inductive and capacitive coupling and inductance L_1. The resonator capacitance and inductance were held at 0.3 pF and 2.5 nH, respectively, producing a resonance frequency that ranged from 5.717-5.802 GHz (resonance frequency varies with coupling capacitance). The simulated S_{21} data was then fit and analyzed using both methods. Figure 3.9 shows an example of a Microwave Office schematic from such a simulation. Microwave Office doesn't allow for variation of the port impedance (set to 50 Ω), so to vary Z_{in} and Z_{out} I used the built in coax transmission line element and calculated the effective input and output impedances by using the well-known equation for impedance of a loaded transmission line [47]

$$Z = Z_C \frac{Z_L + iZ_0 \tan \beta l}{Z_0 + iZ_L \tan \beta l}, \tag{3.48}$$

where Z is the effective input impedance, Z_L is the load impedance, Z_C is the characteristic transmission line impedance, l is the length of the transmission line, and $\beta = 2\pi/\lambda$ is the wavenumber. For an electrical length (βl) of 90°, the tangent term in Eq. 3.48 dominates, and the equation reduces to $Z = Z_C^2/Z_L$. The input and output impedances for the example shown in Fig. 3.9 are $Z_{in} = (30\ \Omega)^2/(50\ \Omega) = 18\ \Omega$ and $Z_{out} = (70\ \Omega)^2/(50\ \Omega) = 98\ \Omega$.

I typically modeled asymmetry by varying Z_{in}/Z_{out}. Asymmetry can also be created by increasing L_1. However, L_1 values in the nanohenries are required to create significant asymmetry, which is far too large to be physical in my setup. The impedance mismatches used are sometimes large, but after this work was published [41] a related study found that these large effective impedance mismatches are consistent with wire bonds made to the coplanar waveguides on the chip [48].

Figure 3.10 shows results from simulations and fits with the same simulated

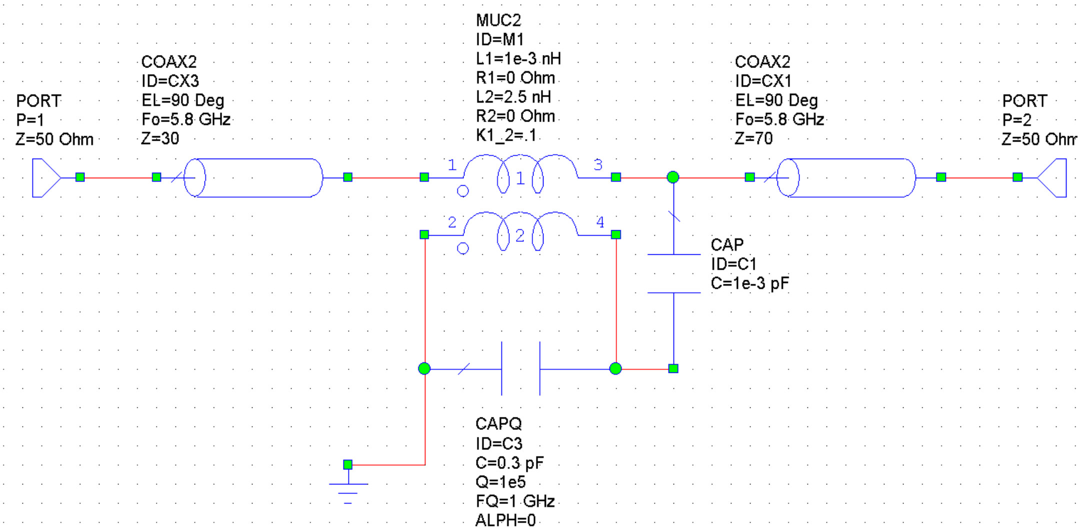

Figure 3.9: Schematic from the numerical linear solver Microwave Office showing a typical simulated resonance circuit.

quality factor, $Q_i = 10^5$ and a range of Z_{in}/Z_{out} values. The coupling line mismatch creates a clear asymmetry in the line shape which I quantified by extracting the asymmetry angle ϕ (see Fig. 3.10). In addition to the value of ϕ extracted from the fit, I also analytically determined the expected asymmetry using

$$\phi = \arctan\left(\frac{\mathbf{Im}\{G_D\}}{R_T^{-1}}\right), \tag{3.49}$$

which can be obtained from Eqs. 3.26, 3.27, and 3.37.

Two internal quality factors were extracted from these fits, one using the ϕRM and the other using the DCM. Figure 3.11 shows both extracted quality factors as well as the fit extracted asymmetry angle ϕ, plotted against the predicted ϕ from Eq. (3.49). Examination of Fig. 3.11 reveals that the DCM is more accurate than the ϕRM for large asymmetry ϕ, and that the two methods agree for small asymmetry.

I also compared both analysis techniques when asymmetry is held constant but Q_i is varied, which I will show later in this chapter corresponds to some experimen-

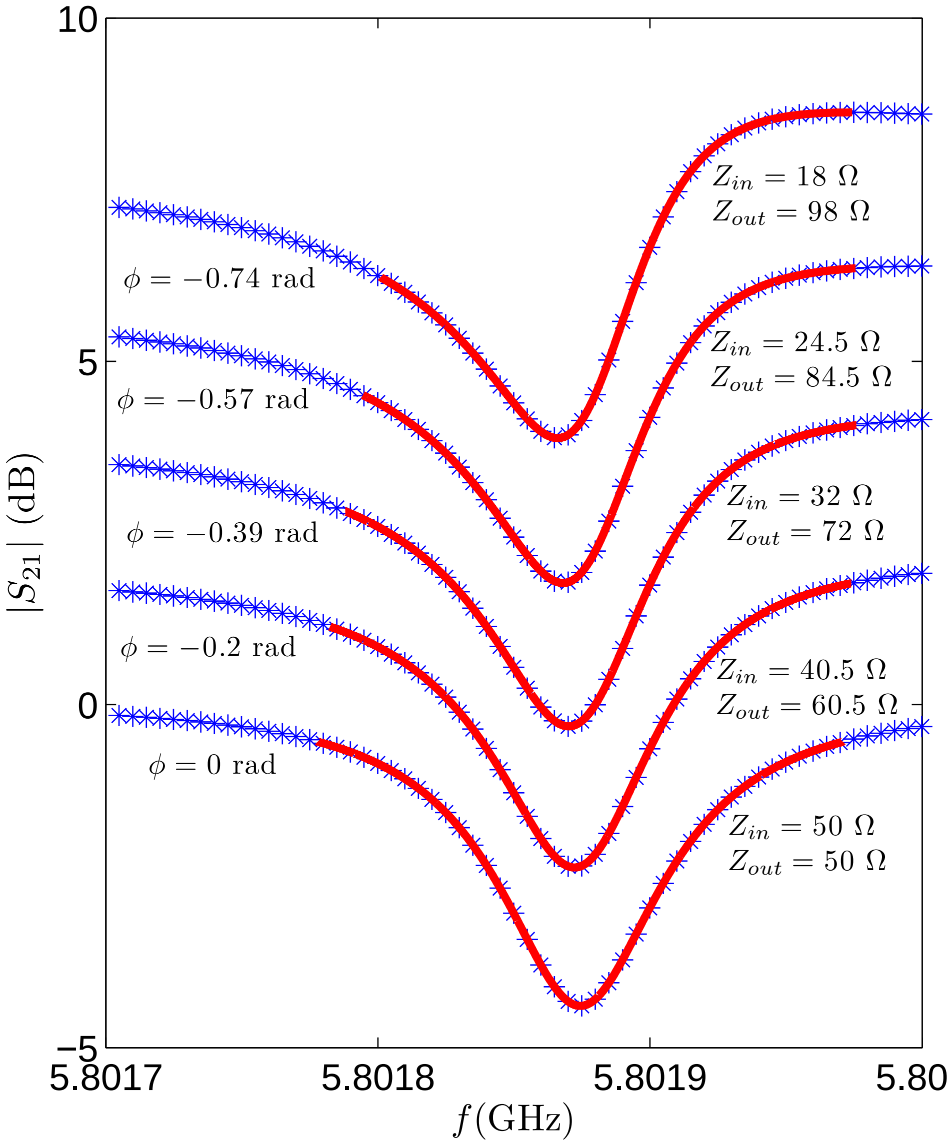

Figure 3.10: Plot of simulated S_{21} vs. freq f fit to symmetric and asymmetric resonance line shapes. Here the asymmetry was created using mismatched coupling lines (Z_{in} and Z_{out}). Asymmetry angles ϕ are extracted from the fits.

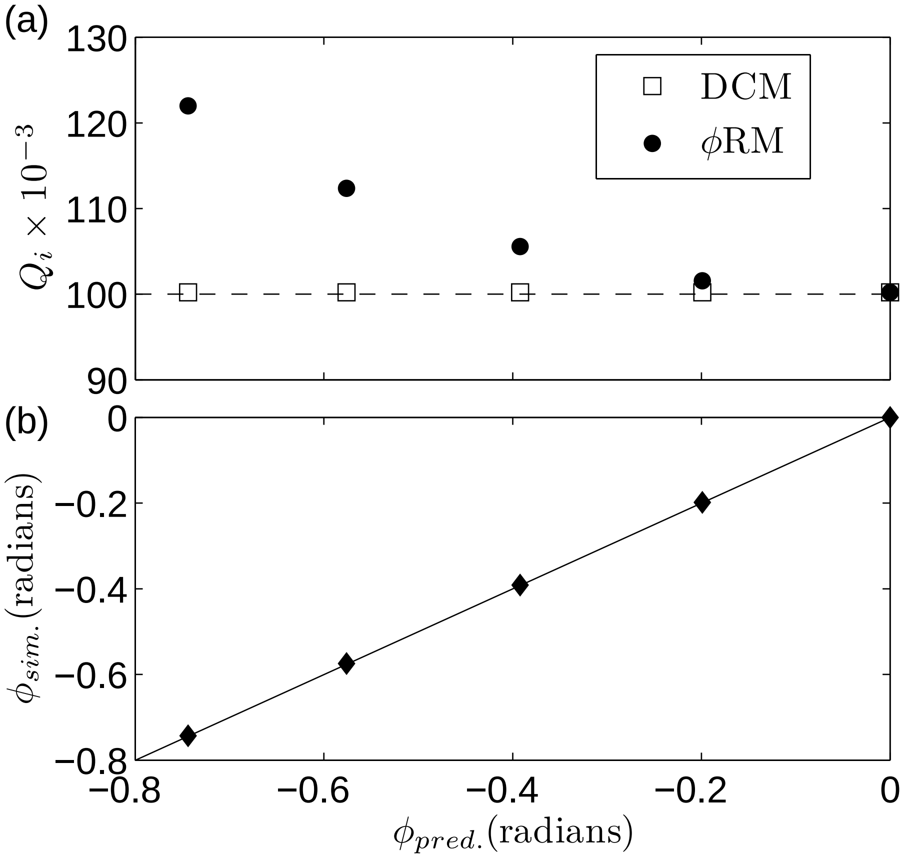

Figure 3.11: (a) Q_i extracted from fits to circuit simulations using ϕRM (●) and DCM (□) analysis techniques, as a function of predicted asymmetry angle $\phi_{pred.}$ calculated using Eq. (3.49). The dashed line indicates actual simulation Q_i. At low asymmetry the two methods agree. As asymmetry is increased, the ϕRM extracted Q_i deviates from the actual Q_i. (b) The fit extracted asymmetry angle, $\phi_{sim.}$ (⧫), as a function of predicted asymmetry angle, $\phi_{pred.}$. The solid line is the $\phi_{pred.} = \phi_{sim.}$ line. Good agreement of that line with the results (⧫) indicates that this method is accurate at predicting the asymmetry.

tal data sets. Figure 3.12 shows Q_i extracted using both analysis techniques plotted as a function of the actual (simulation set) Q_i for simulations with low and high asymmetry. For low asymmetry (matched ports) both analysis techniques yield the correct Q_i within the expected first-order error (C_C/C). However, for high asymmetry (mismatched ports), the ϕRM yields quality factors that are systematically too high. In addition, for sufficiently high Q_is, the ϕRM yields negative Q_is (this is why the asymmetric data analyzed by the ϕRM appears to stop at large Q_i in Fig. 3.12).

The occurrence of these unphysical, negative, Q_is in the ϕRM can be understood by examining the circle plots in Fig. 3.8. As discussed earlier when there is a large asymmetry, in addition to being rotated, the resonance circle grows by a factor of $1/\cos(\phi)$ (assuming full transmission off resonance). Since the ϕRM only rotates the circle back, it does not account for the increase in size, shown in Fig. 3.8(b). So if $Q \approx Q_e$ ($Q_i >> Q_e$), the circle diameter is larger than 1, almost crossing the y-axis. Rotating the circle using the ϕRM causes the circle to cross the y-axis and this yields a negative Q_i. In Fig. 3.8(b) the ϕRM analyzed simulation almost crosses the origin. This corresponds to the $Q_i = 8 \times 10^5$ simulation in Fig. 3.12; it is an example of a simulation data set with a Q_i and asymmetry not large enough to create a negative Q_i but still large enough to create a considerable discrepancy between $Q_{i,\ \phi RM}$ and $Q_{i,\ DCM}$.

To further evaluate both methods, I also analyzed the asymmetric data shown in Fig. 3.6. Figure 3.13 shows the fit used for that resonance line shape. In Fig. 3.14 I show the Q_i extracted using both techniques and the asymmetry angle ϕ. Figure 3.14

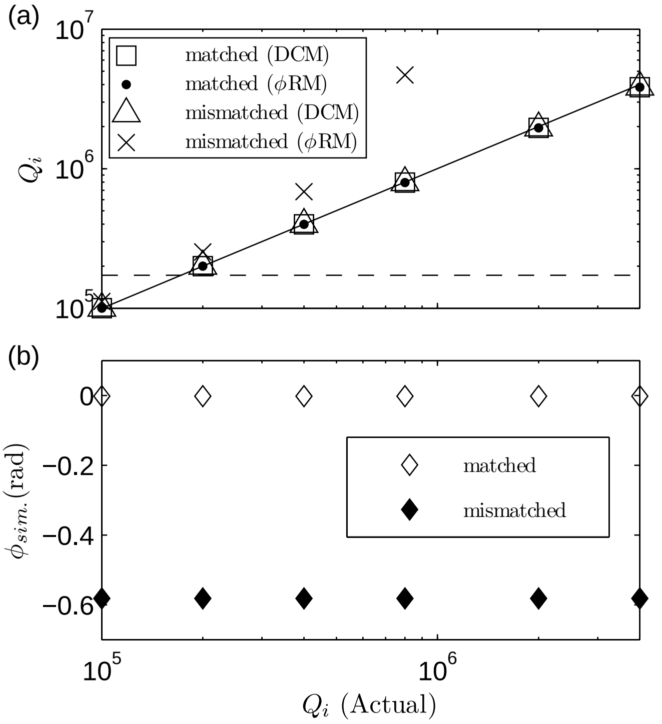

Figure 3.12: (a) Q_i extracted with both analysis techniques (ϕRM and DCM) as a function of the actual Q_i from two sets of simulations. The first set of simulations had high asymmetry (mismatched ports: $Z_{in} = 24.5\Omega$, $Z_{out} = 84.5\Omega$) and the second had low asymmetry (matched ports: $Z_{in} = Z_{out} = 50\Omega$). Solid line is actual Q_i equal to extracted Q_i line and dashed line indicates the coupling (Q_e). Both analysis techniques work well with low asymmetry but only the DCM works with high asymmetry at large Q_i. At low simulation internal quality factors ($Q_i = 10^5$) the DCM extracted internal quality factors ($Q_i = 1.002 \times 10^5$) with less than 1% deviation from the actual value in both low and high asymmetry simulations and at high simulation internal quality factors ($Q_i = 4 \times 10^6$) the DCM extracted internal quality factors ($Q_i = 3.85 \times 10^6$) with less than 4% deviation from the actual value for both low and high asymmetry simulations. The deviation at high internal quality factors is limited numerically by the fit and is not a limit of the method. (b) The fit extracted asymmetry angle $\phi_{sim.}$ for both low (♢) and high (♦) asymmetry simulations plotted against the actual simulation Q_i.

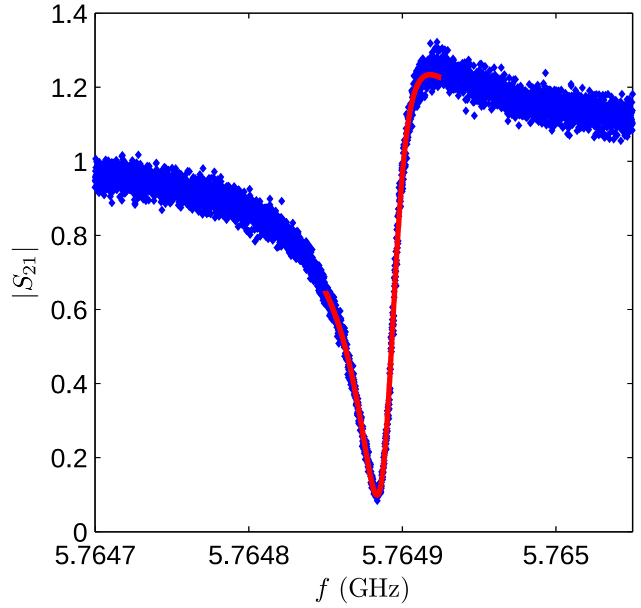

Figure 3.13: The resonance line shape from Fig. 3.6 fit with the derived asymmetric resonance line shape (Eq. 3.40).

is similar to the high asymmetry simulations shown in Fig. 3.12. As expected from Eq. (3.37), the asymmetry ϕ is independent of Q_i for both the real device measurements and the simulated data. Note also the last two data points for the ϕRM in Fig. 3.14 are negative (and off the plot) in the same manner that the last points in the simulated data of Fig. 3.12 are negative.

Another way to test the analysis techniques is by varying Q_e while keeping Q_i constant. In Fig. 3.15 I show the results form a set of simulations where I increased Q_e by lowering the capacitive coupling. As expected, for low asymmetry (matched ports) both analysis techniques do a good job of extracting $Q_i = 10^5$. However, for high asymmetry (mismatched ports) the ϕRM overestimates Q_i by a decreasing amount as Q_e/Q_i increases. Interestingly, in the ϕRM, as Q_e increases,

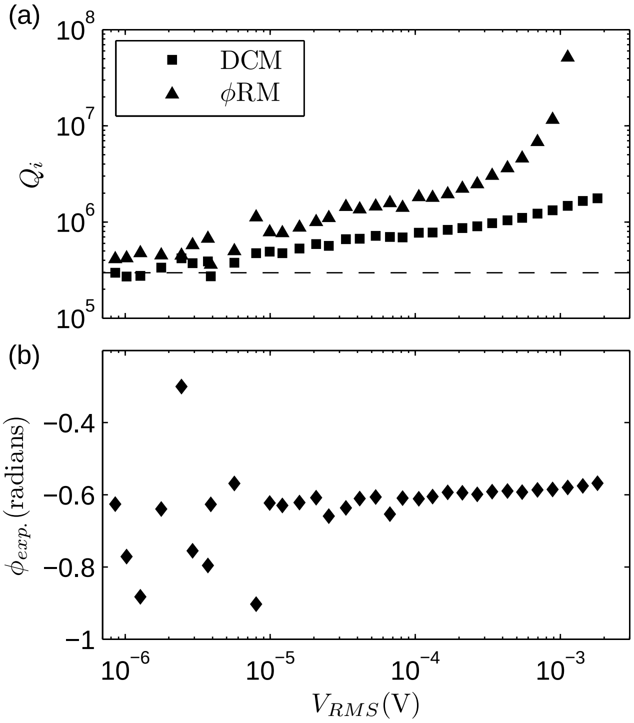

Figure 3.14: Extracted results from the same resonator that produced the data shown in Fig. 3.6 and Fig. 3.13. (a) Q_i, extracted using two analysis techniques, ϕRM (▲) and DCM (■), as a function of voltage across the resonator, V_{RMS}. As with simulated results in Fig. 3.12, the ϕRM systematically extracts higher Q_is or unphysical negative Q_is. The dashed line indicates the fit extracted external quality factor Q_e. (b) The fit extracted asymmetry angle $\phi_{exp.}$ (♦) plotted against V_{RMS}. Again similar to the simulated results in Fig. 3.12, $\phi_{exp.}$ is independent of Q_i, which is varying with V_{RMS}.

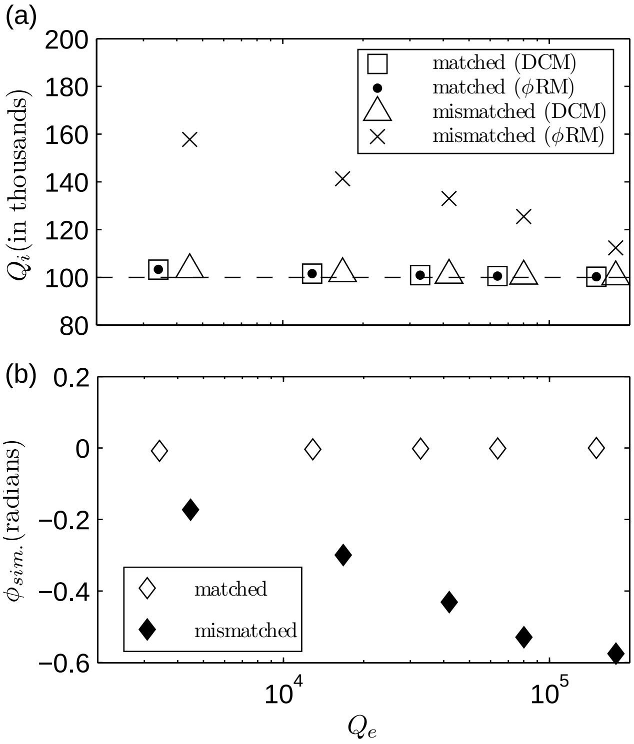

Figure 3.15: (a) Q_i extracted using DCM and ϕRM techniques from two sets of simulations plotted as a function of Q_e. One set has high asymmetry (mismatched ports: $Z_{in} = 24.5\ \Omega$, $Z_{out} = 84.5\ \Omega$) and one has low asymmetry (matched ports: $Z_{in} = Z_{out} = 50\Omega$). Q_e is varied by varying the coupling capacitance (1-10 fF), with a constant mutual inductance (5 pH). The dashed line indicates the actual Q_i of the simulations. With increasing Q_e the inaccuracy of the ϕRM is diluted due to the decreasing weight of Q_e in the analysis. (b) Plot of extracted asymmetry angles vs. Q_e for the two simulations with low (◇) and high (◆) asymmetry.

the extracted Q_i approaches the real value, although the asymmetry ϕ is increasing. This is because as Q_e increases the ϕRM is less sensitive to the asymmetry. This behavior is captured in Eq. (3.47), which shows that as Q_e increases, the difference between the two analysis methods vanishes. In fact for $Q_e >> Q_i$, the asymmetry becomes completely irrelevant and the two techniques converge.

3.6 Conclusion

In summary, in this chapter I first described the dilution refrigerator I used for cooling samples to 30 mK. I next discussed the input microwave lines and how I calibrated the voltage at the sample and the voltage across the resonance capacitor, based on the resonance line shape. Some resonance line shapes were found to be asymmetric so I derived an analytical resonance line shape based on circuit parameters and found that for non-ideal conditions the line shape is asymmetric. Based on this analysis I (with the help of my advisor Kevin Osborn) developed a technique (DCM) for extracting accurate values for internal quality factors Q_i from asymmetric resonator measurements using only transmission data. By analyzing simulated resonator measurements, I found that the DCM was superior at extracting accurate internal quality factors in contrast to the conventional ϕRM technique found in the literature. I found that in the limit where the asymmetry is low, the two methods agreed, but when the asymmetry is high, particularly when $Q_i >> Q_e$, the DCM accurately determines Q_i while the ϕRM systematically overestimates it. I also found that sufficiently high asymmetry and coupling, the ϕRM gives an unphysical negative Q_i. Finally, I showed that the two methods can produce different results on real data taken on a coplanar superconducting aluminum resonator with high asymmetry.

Chapter 4

Coplanar resonators

4.1 Resonator Design

4.1.1 Design Procedure

In this section I discuss how I designed, simulated and fabricated thin-film coplanar aluminum resonators on sapphire and silicon substrates. All resonators were designed based on simulations done with Microwave Office. Microwave Office is a finite element numerical E&M solver that accepts material parameters (e.g. conductivity, dielectric constant, loss tangent, ...) and boundary conditions on the enclosing box. Figure 9.2(a) shows a typical view of a resonator design (details of the design to be discussed later in this section) in Microwave Office. The metal (green in Fig. 9.2(a)) is modeled as a perfect conductor and the dielectric constant of the substrate is set to 10.7 since it's been found that this closely approximates the effective dielectric constant of the sapphire wafers we use.

As seen in Fig. 9.2(a), two ports are used to measure throughput of the coplanar waveguide (CPW) transmission line. Figure 9.2(b) shows the simulated throughput S_{21} of the resonant circuit of Fig. 9.2(a). From fits to S_{21}, I can extract the design value for Q_e, the coupling of the CPW to the resonator. Another method to determine Q_e for a design is to set the loss in the resonator and just record the

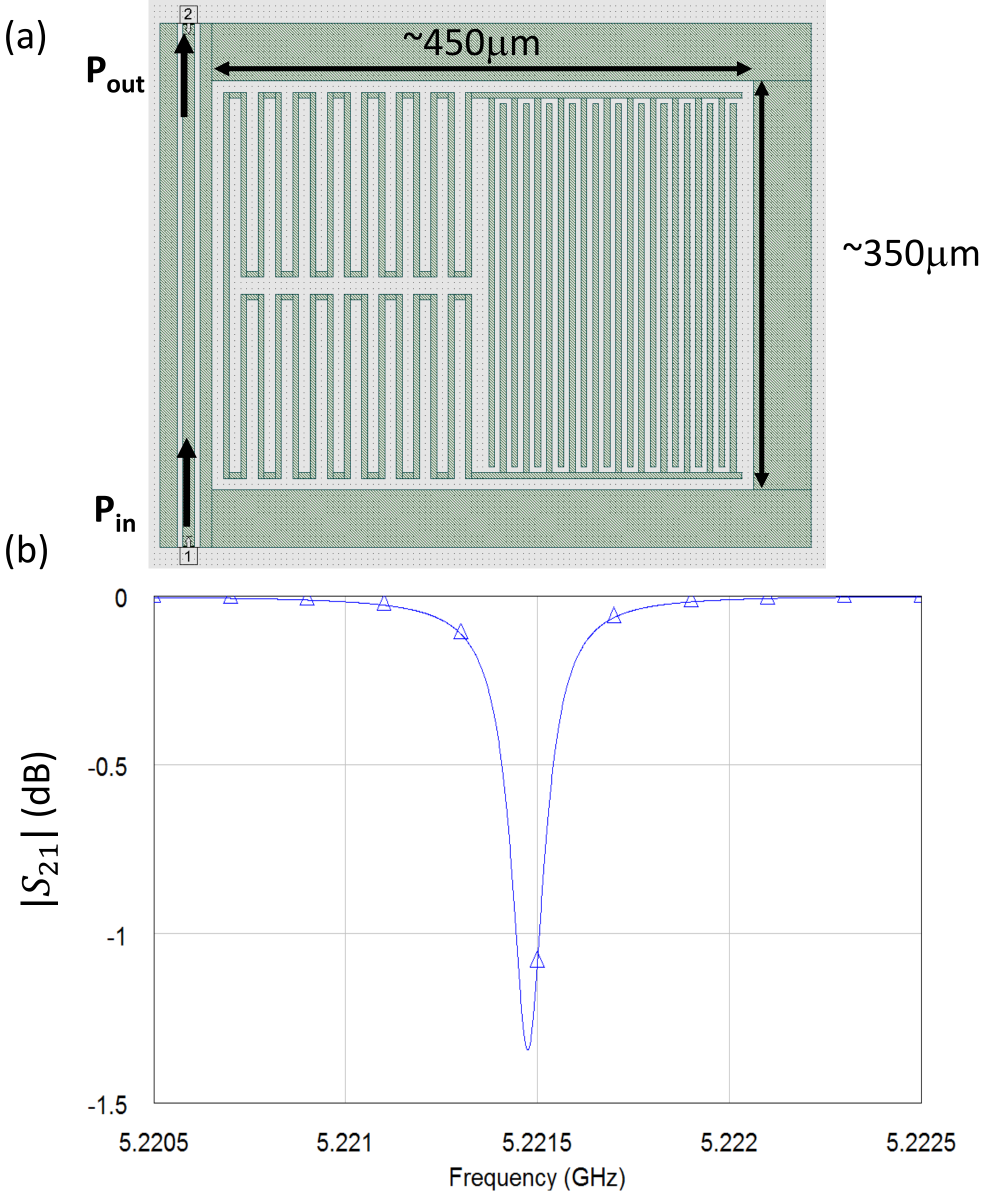

Figure 4.1: (a) Microwave Office layout of coplanar resonator. Green is prefect conductor and white is dielectric. Line width is 5 μm. (b) Microwave Office simulation of transmission from port 1 to port 2 (S_{21}) as a function of frequency. On resonance the CPW couples to the resonator and lower transmission is observed.

minimum throughput transmission (on resonance). By setting the loss you know the Q_i which allows you to determine Q_e since on resonance Eq. 3.14 reduces to $S_{21} = 1 - \frac{Q}{Q_e}$ and solving for Q_e gives

$$Q_e = Q_i \left(\frac{S_{21}}{1 - S_{21}} \right). \tag{4.1}$$

Perhaps the most useful thing about using Microwave Office to design resonators is that it allows for precise tuning of the resonance frequencies. Using a sapphire dielectric constant of 10.7, I found the Microwave Office estimation of the resonance frequency of coplanar resonators is off by less than 1% from the measured resonance frequency values.

Once the resonator designs were determined, the next step was to transfer all of the resonator designs onto one layout in the design software, Cadence. Since I use a notch type measurement that only affects the transmission of the CPW near resonance, I could multiplex several resonators (in this case 4) on a single CPW.

4.1.2 Designing and simulating resonators to analyze geometry dependence

Coplanar resonators have been ubiquitous in superconducting quantum computing, but most previous research has focused on quasi-one-dimensional cavity resonators, such as 1/2-wavelength or 1/4 wavelength CPW transmission line resonators [16, 49, 50]. Lumped element devices (where dimensions are much shorter than a wavelength) are less popular but have been used as part of qubits [51, 52], and in Josephson junction resonators [53, 33]. The interest in coupling quasi-lumped element resonators to qubits is that the lack harmonic modes in lumped element resonators reduces loss from the Purcell effect [54]. When coupling to a qubit, it's also been found that the symmetry of the qubit must be considered, since the type of coupling may affect coherence [55].

With this in mind I designed four resonators with frequencies between 5 and 7 GHz. The resonators had both quasi-lumped and quasi-one-dimensional cavity (transmission line) elements, in order to study the transmission between the two regimes. All the resonators were designed with a symmetric shape to induce inductive, rather than capacitive, coupling.

Figure 4.2 shows optical images of the four resonators. Device QL is a quasi-lumped element resonator, composed of a meandering quasi-lumped inductor (QLL) and a quasi-lumped interdigital capacitor (IDC) (see Fig. 4.2(a)) with an inductance and a capacitance of approximately 2 nH and 0.3 pF respectively. Device CPS is a 4.5 mm long shorted $\lambda/4$ coplanar strip (CPS) resonator, shown in Fig. 4.2(b). Unlike in the QL resonator the electric field in the CPS resonator is distributed along the entire length of the resonator rather than being confined to an IDC. The other two resonators have both a lumped and distributed element (see Fig. 4.2(c, d)). The four resonators were embedded in the ground plane of the same 50 Ω CPW and were inductively coupled to the waveguide (see Fig. 4.3).

To understand the behavior of the resonators when they are driven, note that the point connecting the two nominally symmetric halves of each resonator is a current anti-node and a voltage node, and the sides of each resonator far from the coplanar waveguide are voltage anti-nodes. The fundamental resonance frequency

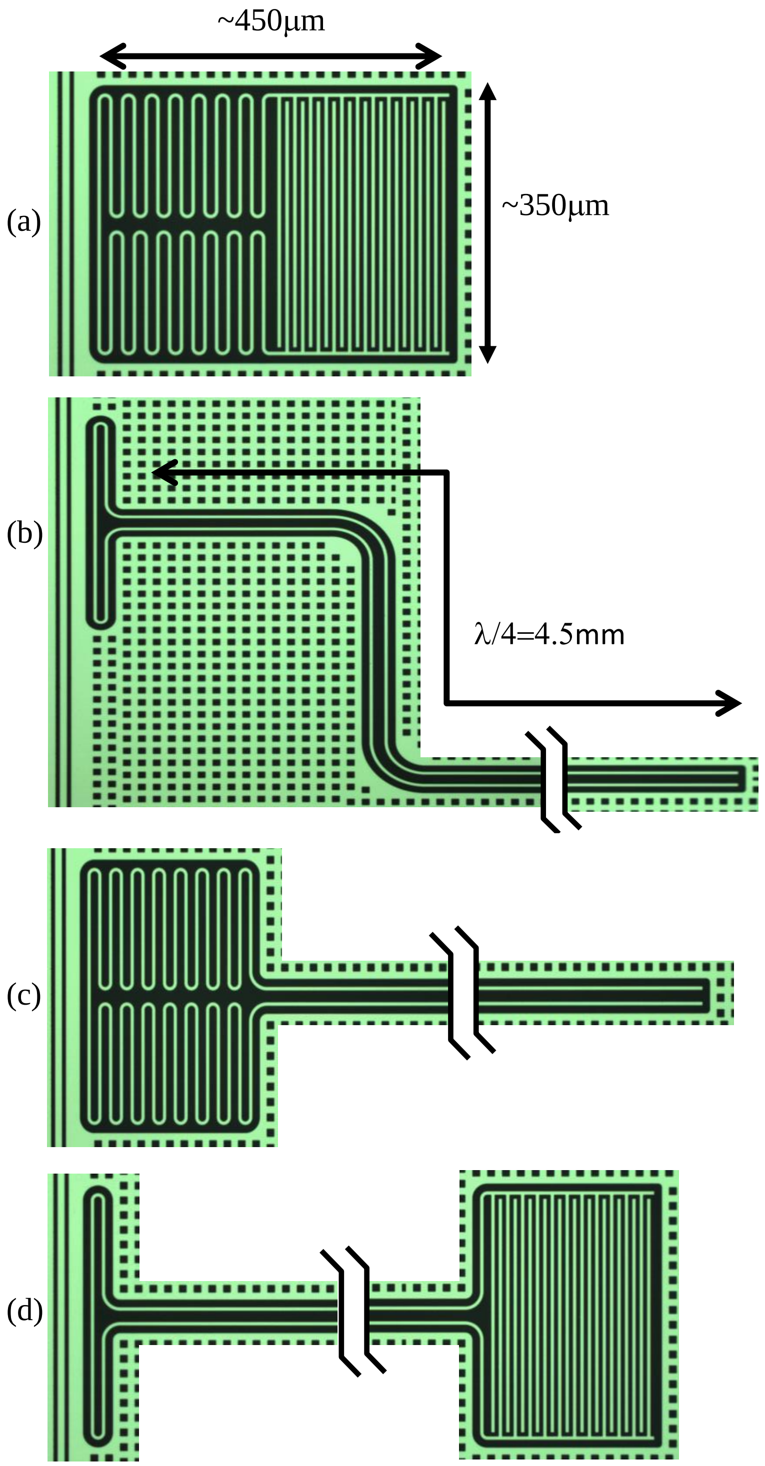

Figure 4.2: Optical images of four resonators (green is aluminum metal and black is sapphire substrate). (a) Quasi-lumped resonator (QL) at 5.46 GHz. (b) Coplanar strip resonator (CPS) at 6.44 GHz. (c) Quasi-lumped inductor with a CPS resonator (QLL-CPS) at 5.76 GHz. (d) Quasi-lumped capacitor with a coplanar strip resonator (QLC-CPS) at 6.01 GHz.

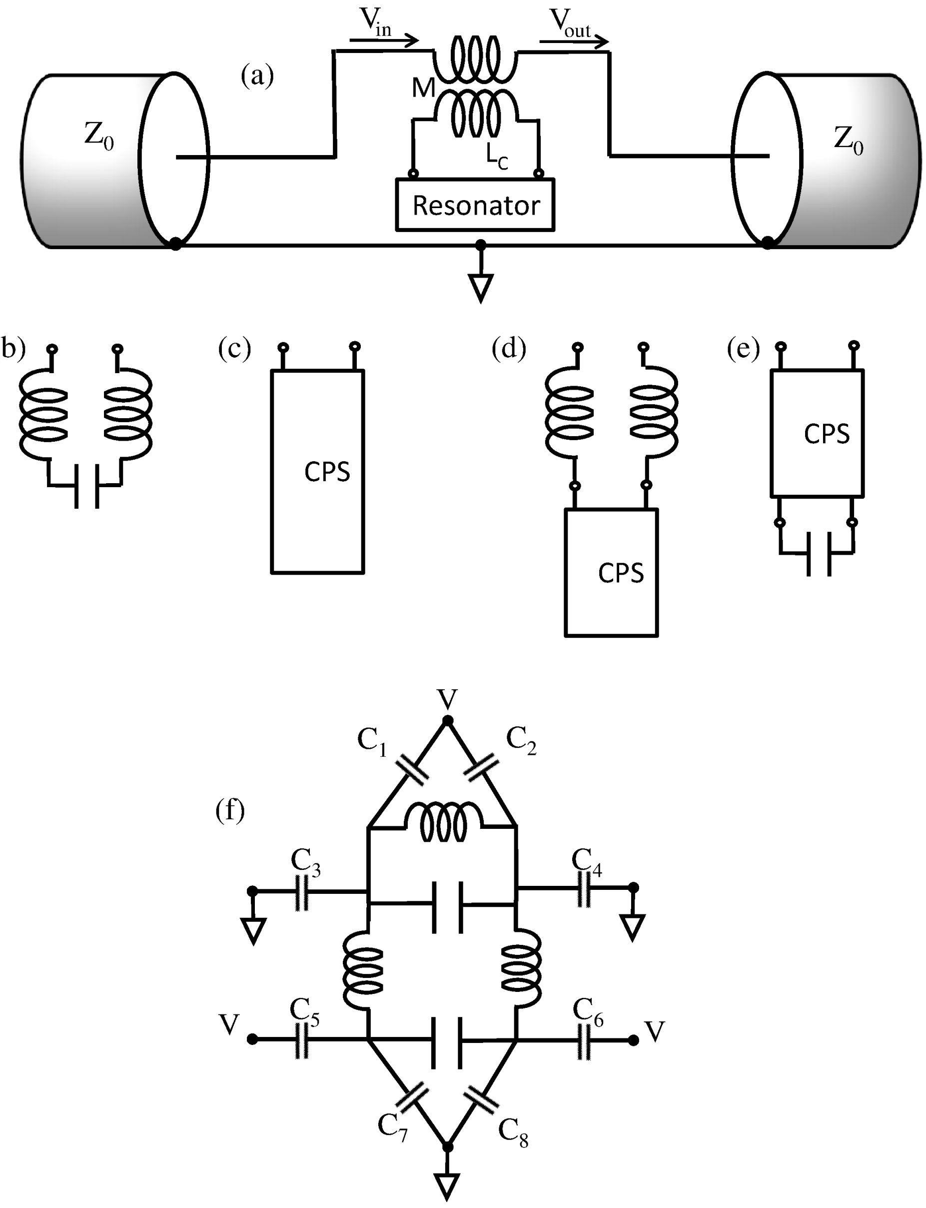

Figure 4.3: (a) Schematic drawing of an arbitrary resonator inductively coupled to a coplanar waveguide. (b-e) Schematic drawing of each of the four types of resonators: (b) QL, (c) CPS, (d) QLL-CPS, and (e) QLC-CPS. (f) Circuit schematic of capacitive coupling to a resonator. Due to the symmetry of these resonators $C_1 = C_2$, $C_3 = C_4$, $C_5 = C_6$, and $C_7 = C_8$, capacitive coupling cannot excite an antisymmetric resonance and only inductive coupling remains.

is voltage antisymmetric in all four resonators. The effective capacitive coupling between the CPW and the resonators for this mode is weak, due to the design and layout of the structures.

The fact that the capacitive coupling is weak can be understood from the nearly symmetric shape of these structures, which implies the capacitances to either side of the resonators are approximately equal. Since the lowest frequency mode is antisymmetric, we expect only inductive coupling between the resonators and the CPW. As another example, Fig. 4.3(f) shows a circuit schematic, where a capacitive network couples voltage V to a resonator. With a symmetric design, $C_1 = C_2$, $C_3 = C_4$, $C_5 = C_6$, and $C_7 = C_8$, the voltage V cannot excite antisymmetric modes.

In order to confirm that the QL resonator showed lumped element behavior, I used Microwave Office to simulate the current amplitude (see Fig. 4.4(a)) and electric field amplitude (see Fig. 4.4(b)) on resonance. As can clearly be seen in Fig. 4.4, the simulations show nearly uniform current amplitude in the meandering inductor and nearly uniform electric field amplitude in the IDC, while the meandering inductor shows nearly no electric field and the IDC shows nearly no current. This is indicative of quasi-lumped behavior in this device with the meandering inductor giving nearly no capacitance and the IDC giving nearly no inductance.

Since the CPS resonator is effectively a one-dimensional cavity, we should expect to see higher order modes at each harmonic of the resonator. However, if the QL resonator is truly lumped, we wouldn't expect to see any higher order modes. To test this, I used Microwave Office to simulate the spectrum of the CPS and the QL resonators from 2 to 40 GHz (see Fig. 4.5). As shown in Fig. 4.5(a), the CPS

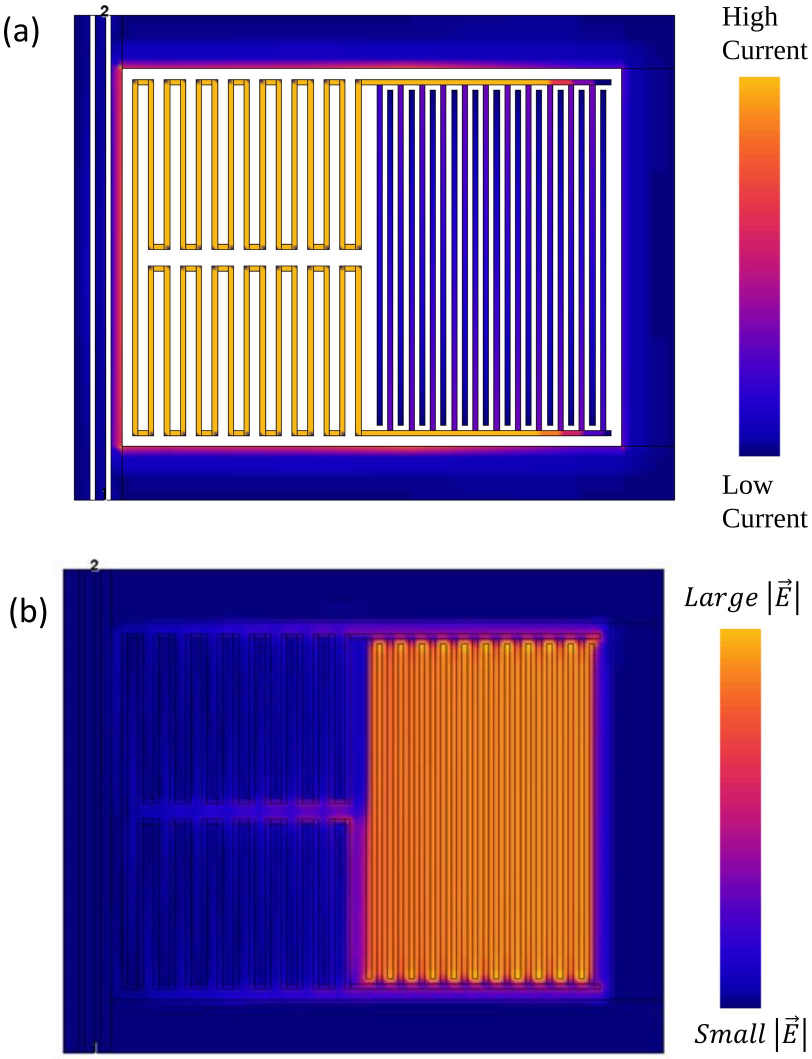

Figure 4.4: (a) Current simulation for the QL resonator on resonance. As expected, most of the current is in the inductor. (b) Electric field simulation for the QL resonator on resonance. As expected, most of the E-field is in the IDC.

device shows a higher order mode at each harmonic while the QL device doesn't show any higher order modes until over 30 GHz, indicating that the device behaves like a lumped element resonator for a large bandwidth.

4.2 Fabrication

I fabricated all of the resonators with 100 nm thick aluminum films (both sputtered and evaporated) on either c-plane sapphire wafers [56] or <1-0-0> undoped 20 kΩ-cm silicon wafers [57]. The aluminum was patterned with positive photoresist and wet etched in an acidic solution.

For the sputtered aluminum the procedure was to first transfer the 3" wafer into the CMS-18 Kurt J. Lesker sputtering chamber and pump to a pressure of 2×10^{-8} torr with a CTI Cryo Torr 8 cryo-pump. I then used a 3 cm argon ion beam source at 300 V beam voltage with 0.3 mT of argon gas to ion mill the surface of the wafer for 30 seconds. This both cleaned the surface and roughened it on an atomic scale to allow for better adhesion of the aluminum. Next I sputtered 100 nm of aluminum with 400 W DC power from a 3" diameter target. The rate of deposition was 4.8 nm/min and was calibrated with a profilometer measurement. I then used a programmable spinner at 3000 RPM for 60 seconds to spin OIR 906-10 photoresist [58] on the aluminum. Next I baked the wafer on a 90 $^{\circ}C$ hot plate for 60 seconds and then exposed it to the device pattern on a mask in the stepper for 0.3 seconds (exposure time depends on UV power output which can vary). With a 3" wafer and a sample size of 6.35×6.35 mm, the stepper independently exposed 88

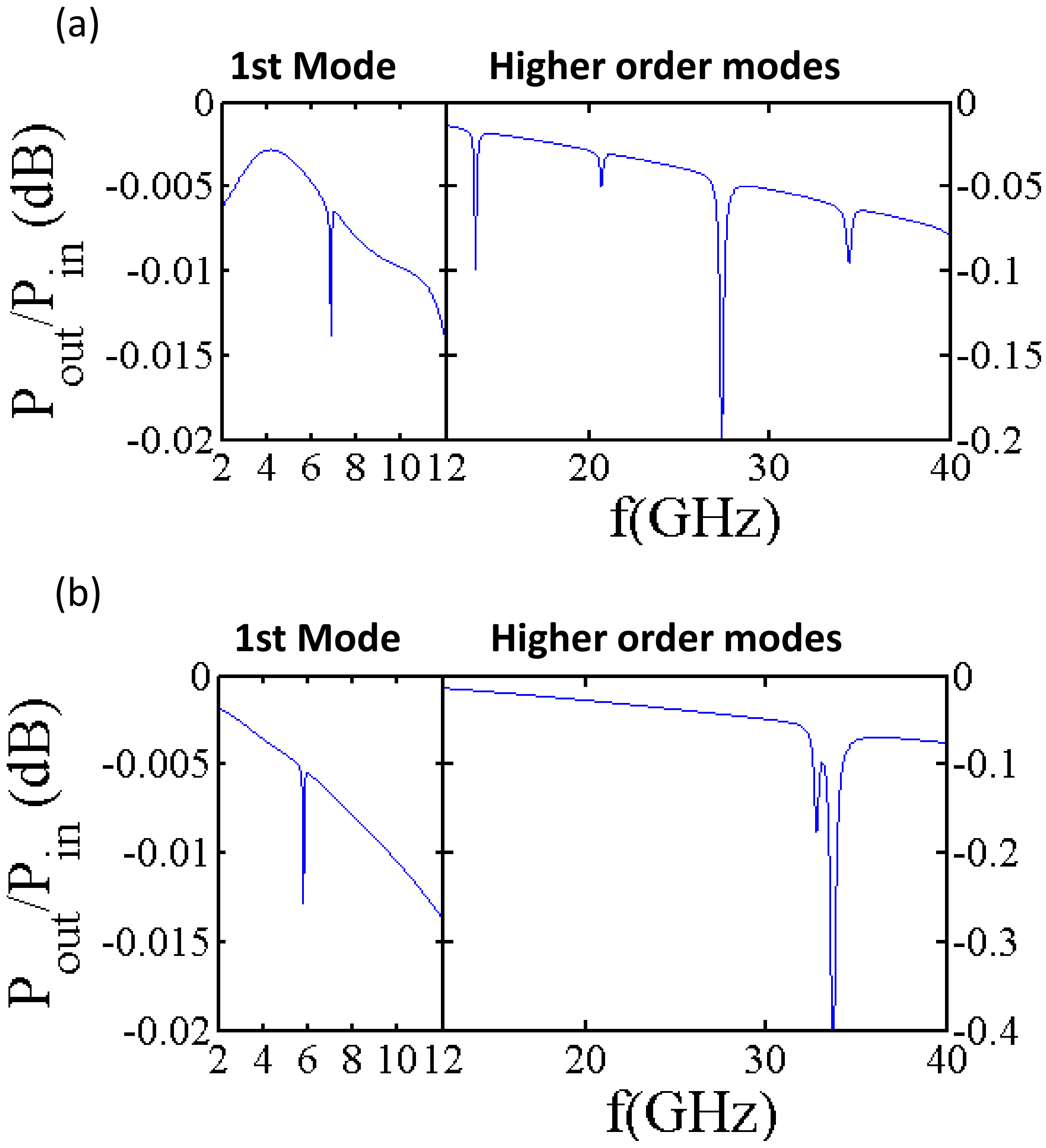

Figure 4.5: (a) Microwave Office simulation for CPS resonator. Higher order harmonics are present every quarter wavelength, as expected for a transmission line resonator. (b) Microwave Office simulation for QL resonator. No higher order modes are present close to the first mode, indicating a quasi-lumped element resonator. The second mode occurs at about 33 GHz.

samples. After exposing the resist, I baked the wafer at 120 $^{\circ}C$ for 60 seconds. Next I developed the exposed photoresist with OPD-4262 developer [58] for 40 seconds. After rinsing with di water, I etched the now exposed aluminum in an aluminum etch solution (Aluminum Etch 80-15-3-2) composed mainly of phosphoric acid. Finally the photoresist was cleaned off with acetone, methanol, and isopropanol.

For the evaporated aluminum I used an e-beam evaporator (CHA Mark 40) and didn't ion mill the wafer before deposition because there was no ion source in the system. After the deposition the procedure was identical to the sputtered aluminum samples.

4.2.1 Dicing

After the aluminum was patterned and the photoresist was removed, I used the spinner to coat the wafer with a layer of FSC-M resist to protect the resonators while dicing the wafer. I then applied tape to the back of the wafer to insure that the samples stay in place after the wafer was diced. After performing a calibration cut on a test wafer (hairline alignment), I mounted the wafer in the dicing saw. After aligning the dicing saw with the pattern on the wafer, I began dicing the wafer first in one direction and then in the other producing 88 6.35 mm × 6.35 mm samples. I used a Disco-DAD 321 dicing saw with a coarse grit resinoid diamond blade (type CX-010-325-080-4) with a rotation speed of 22,000 RPM. The cutting speed for sapphire wafers was 0.75 mm/s and for silicon wafers was 2.0 mm/s. I set the blade height to 0.2 mm to insure that the blade cut through the wafer but not

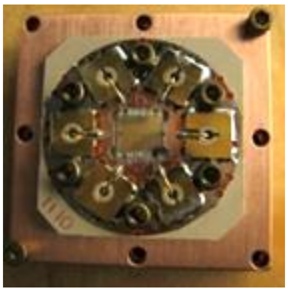

Figure 4.6: Photograph of a sample mounted on a PC board attached to a Cu sample box.

all the way through the tape.

Once the wafer was diced I went back into the clean room to find a good sample (without scratches). I used the microscope to first find a few good candidates. I then cleaned them by first spraying with acetone, then letting them sit in acetone for 10 minutes, and finally rinsing them with methanol and isopropanol. After cleaning I examined the samples in the microscope to confirm that they were indeed clean and selected the best one to mount in the sample box.

4.2.2 Packaging and wire-bonding

The sample chip was mounted to a PC board with GE varnish and the PC board was attached to a copper box. Figure 4.6 shows a photograph of the sample box with a sample mounted in it and Fig. 3.1(a) shows the sample box mounted to the dilution refrigerator. The PC board had wire bond pads that lined up with the CPW launchers of the samples. I connected these pads to the samples' CPW launchers using a West-Bond 7476E-79 wire bonder and aluminum wire.

Transmission through the sample box was tested at room temperatures to ensure that it has no resonance box modes for our group's frequencies of interest (4-8 GHz). The sample box seal is a copper metal-metal seal screwed tight with 2-56 brass screws.

4.3 Solving for resonance voltage waveform

I this section, I discuss solving for the resonance frequency of the four resonator types and in so doing solving for the voltage waveform of the devices on resonance. This allows me extract the voltage across each device despite not being able to use the lumped element approximation Eq. 3.22.

4.3.1 QL resonator

In this part, I solve for the resonance of the QL resonator. This is actually just a specific case of the circuit solved in Chapter 3. Since this device only has inductive coupling, I can model the measurement setup with Fig. 4.7(a), where I've assumed balanced impedances for simplicity and put the loss in series with the LC circuit rather than in parallel because it simplifies the calculation when only inductive coupling is considered.

The input impedance of the resonant circuit is given by

$$Z_{in} = R + i\omega L - \frac{i}{\omega C}. \tag{4.2}$$

Resonance occurs when the impedance $|Z_{in}|$ is minimized, when the inductive and

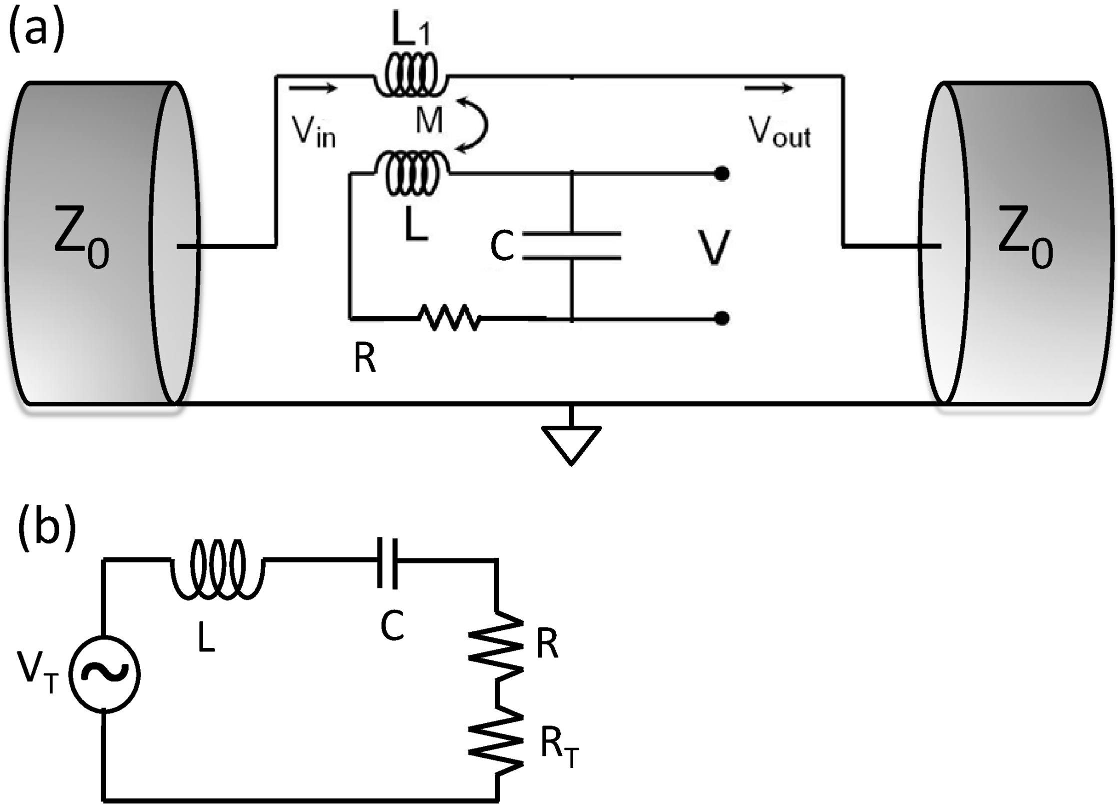

Figure 4.7: (a) Circuit schematic for a QL resonator measurement. A series RLC resonance circuit is assumed because it simplifies the system when only inductive coupling is present. (b) Thevenin equivalent circuit for measurement schematic shown in (a).

capacitive impedances cancel we have

$$\omega_0 = \frac{1}{\sqrt{LC}}. \tag{4.3}$$

Assuming the system is driven close to resonance ($|\omega - \omega_0|/\omega_0 << 1$), the input impedance can be rewritten as

$$Z_{in} \simeq R + 2iL\Delta, \tag{4.4}$$

where $\Delta = \omega - \omega_0$ is the detuning.

Similar to the derivation shown in Chapter 3, by solving Kirchhoff's equations for the circuit in Fig. 4.7(a), it can be shown that it's equivalent to the Thevenin equivalent circuit in Fig. 4.7(b), where

$$R_T = \frac{(\omega_0 M)^2}{2Z_0} \tag{4.5}$$

and

$$V_T = \frac{2i\omega M V_{in}}{2Z_0}, \tag{4.6}$$

depend on the coupling and we've made the approximation that $2Z_0 >> \omega L_1$. Since we know that the impedances of the inductor and the capacitor in Fig. 4.7(b) will cancel on resonance, the current through the circuit on resonance will be simply

$$I_{res} = \frac{V_T}{R_{eff}}, \tag{4.7}$$

where we've defined

$$R_{eff} = R + R_T. \tag{4.8}$$

Solving the circuit in Fig. 4.7(a) for V_{out}, as done in Chapter 3, gives

$$\frac{V_{out}}{V_{in}} = \frac{R}{R_{eff}} \frac{1 + 2i\Delta L/R}{1 + 2i\Delta L/R_{eff}}. \tag{4.9}$$

The quality factors can now be defined in the usual way

$$Q \equiv \frac{1}{\omega_0 R_{eff} C}, \tag{4.10}$$

$$Q_i \equiv \frac{1}{\omega_0 R C}, \tag{4.11}$$

and

$$Q_e \equiv \frac{1}{\omega_0 R_T C}, \tag{4.12}$$

This allows us to rewrite Eq. 4.9 as

$$S_{21} = \frac{V_{out}}{V_{in}} = 1 - \frac{Q/Q_e}{1 + 2Qi\Delta/\omega_0}. \tag{4.13}$$

From Eqs. 4.6 and 4.7 we can calculate the voltage across the capacitor,

$$V_C = \frac{I_{res}}{i\omega C} = \frac{M V_{in}}{Z_0 C R_{eff}}. \tag{4.14}$$

Writing this in terms of the quality factors recovers Eq. 3.22,

$$V_C = \sqrt{\frac{2}{Z_0 \omega_0 C Q_e}} Q V_{in}. \tag{4.15}$$

This is of course to be expected because the QL resonator is simply a lumped element resonator with only inductive coupling (a specific case of the problem we solved in Chapter 3).

4.3.2 CPS resonator

To illustrate the parallels between the QL resonator and the CPS resonator I have redrawn the measurement schematic for the CPS resonator in Fig. 4.8(a). Here Z_{CPS} represents the input impedance of the CPS as the series RLC circuit did

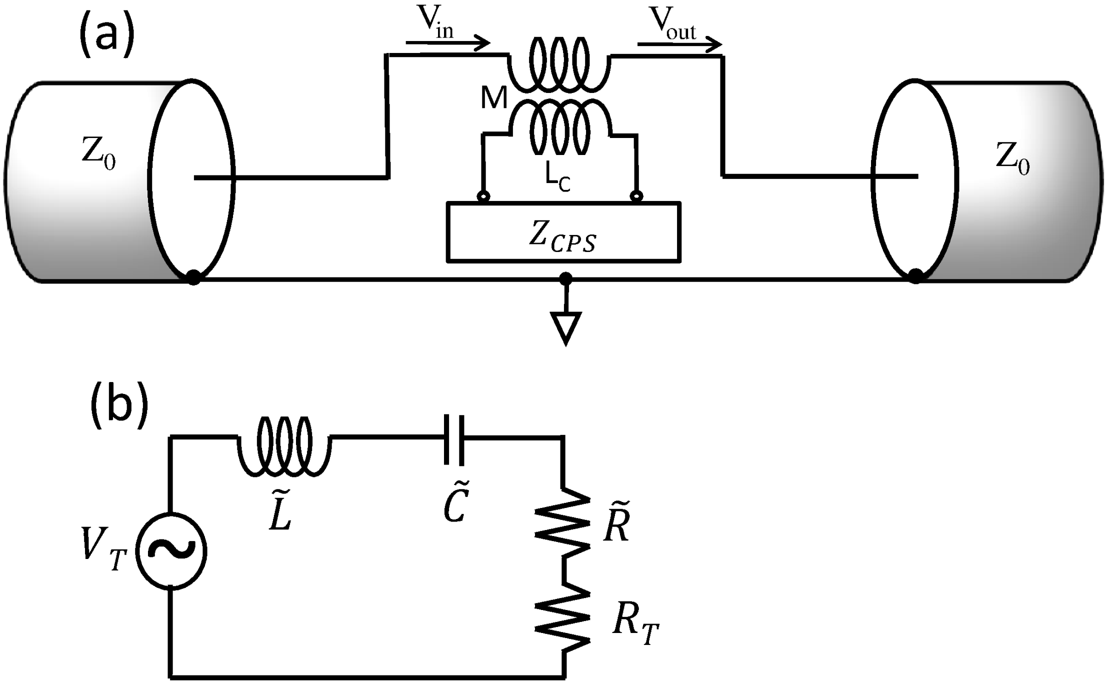

Figure 4.8: (a) Measurement schematic for CPS resonator. (b) Thevenin equivalent circuit for the CPS resonator.

in Fig. 4.7(a). To solve for the voltage across the CPS resonator, we first examine the geometry of the resonance mode. Figure 4.9 shows a representation of the CPS resonator enclosed in a ground plane. Because of the symmetry of the layout, we can assume that the capacitances of either finger to the ground plane are equal i.e. $C_{11} = C_{22}$.

This problem would be easier to solve if we could turn the resonator into a simple transmission line with a single voltage electrode and ground. This is achieved by recognizing that the resonance will excite the odd (antisymmetric) mode of the CPS, which allows us to assume that the middle of the CPS is grounded. To turn this circuit into a simple transmission line we just need to find the total capacitance of one line to ground. That's simply equal to

$$C = C_{11} + 2C_{12}, \tag{4.16}$$

where the factor of 2 in front of the C_{12} comes from the fact that the capacitance between one of the lines and the effective ground plane in the middle is twice the capacitance $C12$ between the two lines. Equation 4.16 can be rewritten as

$$C' = C'_{11} + 2C'_{12}, \tag{4.17}$$

where the primes indicate per unit length, thus $C' = C/l$. And the effective characteristic impedance of this transmission line is

$$Z_C = \frac{1}{vC'}, \tag{4.18}$$

where v is the speed of light on the substrate

$$v = \frac{c}{\sqrt{\epsilon_{re}}}, \tag{4.19}$$

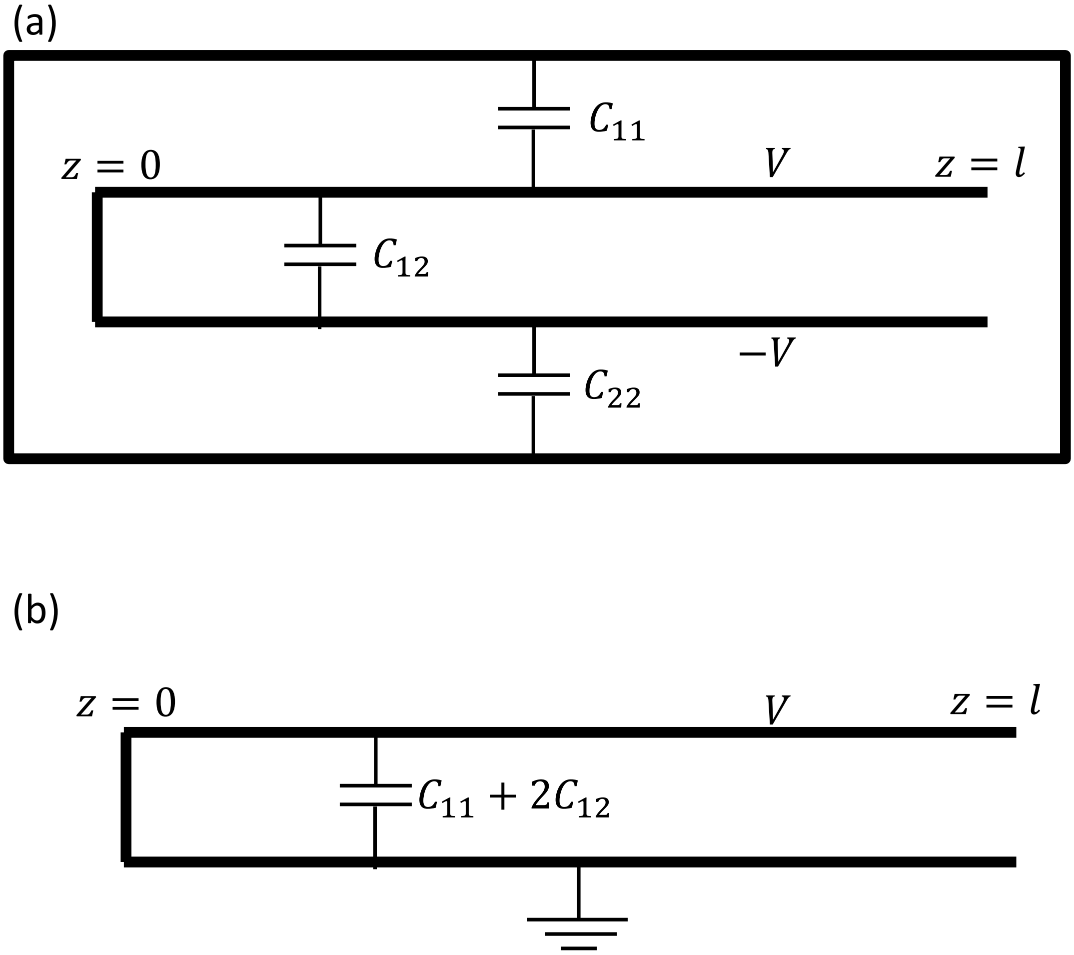

Figure 4.9: (a) Drawing of the CPS resonator inside a ground plane that emphasizes the symmetry of the layout. Note that due to the symmetry, an odd electric mode can be assumed to be grounded down the middle of the resonator. (b) A transformed transmission line resonator created by taking the capacitances between one of the fingers of the CPS to ground, where a ground plane (actually a ground line) is assumed down the middle of the resonator in (a).

and ϵ_{re} is the effective ϵ_r for a coplanar geometry

$$\epsilon_{re} = \frac{\epsilon_r + 1}{2}, \tag{4.20}$$

assuming the substrate has a relative permittivity ϵ_r and the vacuum above has a relative permittivity 1. With the dimensions of the CPS (CPS separation $s = 15\ \mu$m, CPS-ground separation $s_2 = 10\ \mu$m, conductor width $w = 5\ \mu$m, substrate height $h = 430\ \mu$m) I used Ref. [59] to calculate the characteristic odd mode impedance of the device $Z_C = 62\ \Omega$.

The next step is to calculate the input impedance of the CPS transmission line and solve for the resonance. The input impedance Z_{in} of a transmission line open at the end with attenuation constant α and wavenumber $\beta = 2\pi/\lambda$ is [47]:

$$\begin{aligned} Z_{in} &= Z_C \coth[(\alpha + i\beta)l] = Z_C \frac{\cot\beta l + i\alpha l}{\alpha l \cot\beta l + i} \\ &= Z_C \frac{(\alpha l \cot^2\beta l + \alpha l) + ((\alpha l)^2 \cot\beta l - \cot\beta l)i}{1 + (\alpha l)^2 \cot\beta l}. \end{aligned} \tag{4.21}$$

To find the resonance we set the imaginary part of the input impedance to zero giving $\cot\beta l = 0$. This essentially means that on resonance the length l of the transmission line is $\lambda/4$ (i.e. $l = \lambda/4 = (2\pi/\beta_0)/4 \therefore \beta_0 l = \pi/2$). Assuming we're close to resonance ($\cot\beta l << 1$) and have low attenuation ($\alpha l << 1$) Eq. 4.21 becomes

$$Z_{in} \approx Z_C(\alpha l - i\cot\beta l). \tag{4.22}$$

It is more convenient in the experiment to work with frequency than with wavenumber. Using the substitutions $\omega = v\beta$ and $\Delta = \omega - \omega_0$ we have

$$\beta l = \frac{\omega l}{v} = \frac{\omega_0 l}{v} + \frac{\Delta l}{v} = \frac{\pi}{2} + \frac{\Delta}{v}\frac{\pi}{2\beta_0} = \frac{\pi}{2} + \frac{\pi}{2}\frac{\Delta}{\omega_0}, \tag{4.23}$$

thus

$$\cot\beta l = \cot(\frac{\pi}{2}(1+\frac{\Delta}{\omega_0})) \approx -\frac{\pi}{2}\frac{\Delta}{\omega_0}, \tag{4.24}$$

where I have expanded the cot term to first order in Δ/ω_0. Now combining Eq. 4.22 and Eq. 4.24 gives

$$Z_{in} = Z_C(\alpha l + \frac{\pi}{2}\frac{\Delta}{\omega_0}i). \tag{4.25}$$

Now we can see that the input impedance for the CPS, Eq. 4.25, is of the same form as the series RLC input impedance, Eq. 4.4, with the substitutions

$$\tilde{R} = Z_C\alpha l, \tag{4.26}$$

$$\tilde{L} = \frac{\pi}{4}\frac{Z_C}{\omega_0}, \tag{4.27}$$

and

$$\tilde{C} = \frac{4}{\pi Z_C\omega_0}. \tag{4.28}$$

We can now use the input impedance transformation to create the Thevenin equivalent schematic for the CPS geometry (see Fig. 4.8(b)), and as was the case for the QL resonator R_T and V_T are given by Eq. 4.5 and Eq. 4.6 respectively since they only depend on the coupling. Again we set the imaginary part of the impedance to zero to calculate the current on resonance and find

$$I_0 = \frac{\omega_0 M V_{in}}{Z_0\tilde{R}_{eff}}, \tag{4.29}$$

where $\tilde{R}_{eff} \equiv \tilde{R} + R_T$. I've defined the maximum current as I_0 here because it's the current maximum amplitude on the transmission line (at the current anti-node). The maximum voltage amplitude is then:

$$V_0 = Z_C I_0 = Z_c\frac{\omega M V_{in}}{Z_0\tilde{R}_{eff}} = \sqrt{\frac{8Z_C}{\pi Z_0 Q_e}}QV_{in}, \tag{4.30}$$

where Q and Q_e have been defined the same way as they were in the QL case (with $\tilde{C}$ and $\tilde{R}_{eff}$ substituted in for C and R_{eff}). Note however that V_0 in Eq. 4.30 is the voltage amplitude on the transformed transmission lines, which is just one of our CPS fingers to ground. To get the actual voltage from one finger of the CPS to the other we have to double V_0 i.e. $V_{CPS} = 2V_0$.

4.3.3 Quasi-lumped C-CPS resonator

The case of the CPS terminated by an IDC capacitor is slightly more complicated than the previous two cases but the approach used for the CPS can still be used here. Again we can think of the resonator as having an input impedance that's coupled to the CPW. Figure 4.10(a) shows a representation of the resonator enclosed in a ground plane. Again recognizing that we're exciting the odd mode we can assume that the middle of the resonator is grounded and recalculate the capacitances from one of the fingers to ground (see Fig. 4.10(b)). Since the CPS has the same geometry we know from the last section that $Z_C = 62\ \Omega$ and from Ref. [59] we use the dimensions of the IDC (5 μm separation and width, 22 fingers, and 320 μm finger length) to its capacitance $C_{IDC} = 0.30pF$.

Next we find the input impedance of a 62 Ω transmission line of length l ($l = 1.6$ mm for this device) terminated by a $2C_{IDC}$ load. It can be shown that the input impedance is given by

$$\begin{aligned} Z_{CPS,IDC} = {} & Z_C \frac{\alpha l((Z_C + \frac{\tan\beta l}{2\omega C_{IDC}})^2 + (Z_C \tan\beta l - \frac{1}{2\omega C_{IDC}})^2)}{(Z_C + \frac{\tan\beta l}{2\omega C_{IDC}})^2} \\ & + Z_C \frac{(Z_C + \frac{\tan\beta l}{2\omega C_{IDC}})(Z_C \tan\beta l - \frac{1}{2\omega C_{IDC}})i}{(Z_C + \frac{\tan\beta l}{2\omega C_{IDC}})^2}. \end{aligned} \tag{4.31}$$

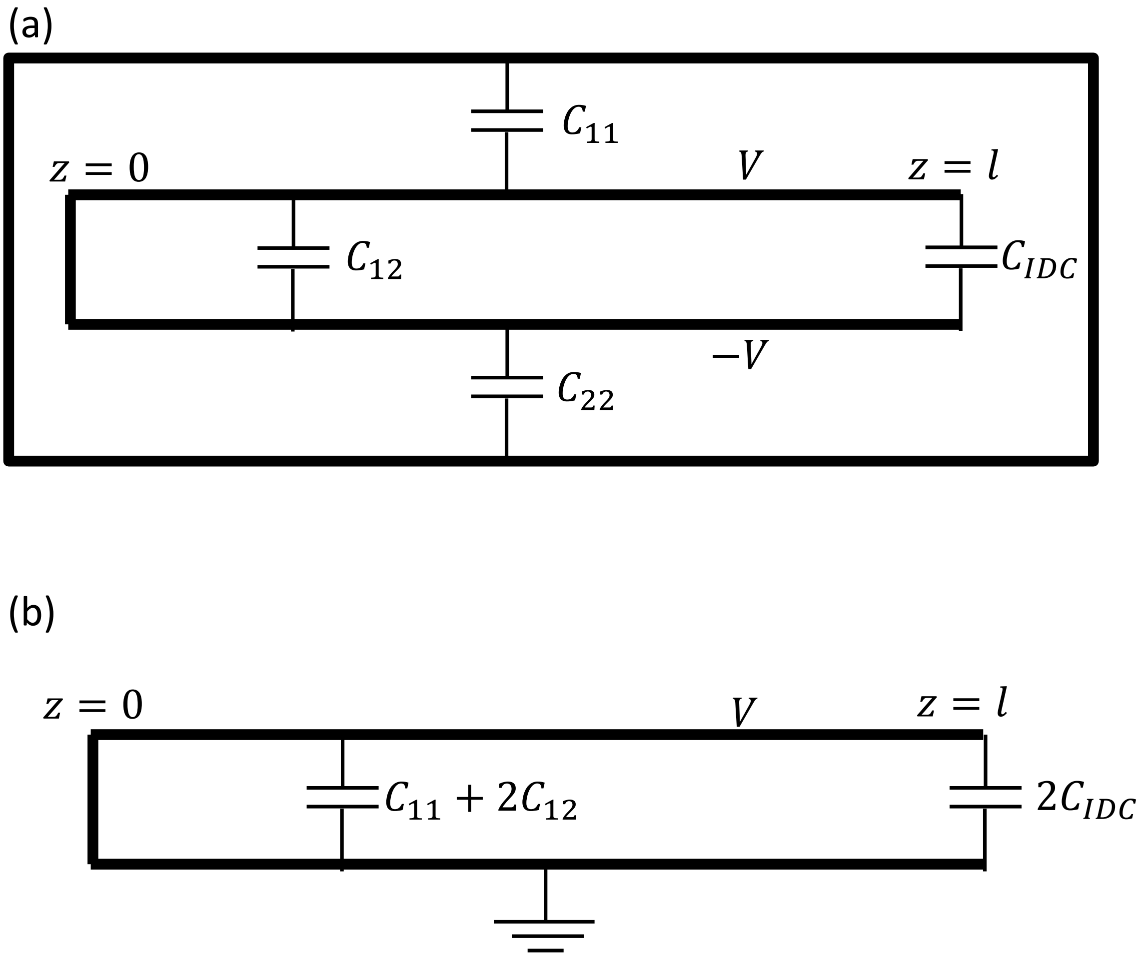

Figure 4.10: (a) Drawing of QLC-CPS resonator inside a ground plane. Note that due to the symmetry, an odd electric mode can be assumed to be grounded down the middle of the resonator. (b) Transformed resonant circuit created by taking the capacitances between one of the fingers of the QLC-CPS resonator to ground, where a ground plane (actually a ground line) is assumed down the middle of the resonator in (a).

To solve for the resonance condition, we make the imaginary part vanish

$$Z_C \tan\beta_0 l - \frac{1}{2\omega_0 C_{IDC}} = 0. \tag{4.32}$$

Using the substitution $\beta = \omega/v$ and expanding around ω_0, it can be shown that the input impedance of the resonator close to resonance is

$$\begin{aligned} Z_{CPS,IDC} \simeq Z_C &\frac{\alpha l((Z_C + \frac{\tan\beta l}{2\omega_0 C_{IDC}})^2 + (Z_C \tan\beta l - \frac{1}{2\omega_0 C_{IDC}})^2)}{(Z_C + \frac{\tan\beta l}{2\omega_0 C_{IDC}})^2} \\ &+ Z_C \frac{(1 + \tan^2(\frac{\omega_0 l}{v})\frac{Z_C l}{v}) + \frac{1}{2C_{IDC}\omega^2}}{Z_C + \frac{\tan(\frac{\omega_0 l}{v})}{2\omega_0 C}} \Delta i. \end{aligned} \tag{4.33}$$

Examination of Eq. 4.33 reveals that the input impedance for this resonator can again be put in the same form as a series RLC resonator (Eq. 4.4) with the substitutions

$$\tilde{L} = Z_C \frac{(1 + \tan^2(\frac{\omega_0 l}{v})\frac{Z_C l}{v}) + \frac{1}{2C_{IDC}\omega^2}}{2(Z_C + \frac{\tan(\frac{\omega_0 l}{v})}{2\omega_0 C})}, \tag{4.34}$$

and

$$\tilde{C} = \frac{1}{\omega_0^2 \tilde{L}}, \tag{4.35}$$

where ω_0 can be solved numerically from Eq. 4.32. These transformations allow us to model this resonator as another Thevenin equivalent circuit. Solving for the current amplitude on resonance we find

$$I_0 = \frac{\omega_0 M V_{in}}{Z_0 \tilde{R}_{eff}} i, \tag{4.36}$$

where once again $Q = 1/(\omega_0 \tilde{C} \tilde{R}_{eff})$.

Note that this case is slightly more complicated than a simple transmission line so to solve for the voltage across the capacitor on resonance we first write the voltage waveform as generally as possible

$$V(z) = V_+ e^{i\beta z} + V_- e^{-i\beta z}, \tag{4.37}$$

where z is distance along the CPS, the boundary value $V(0) = 0$ is known and we're attempting to solve for $V(l) = V_C^*$, where V_C^* is the voltage across the capacitor in this transformed transmission line resonator system. From our boundary condition we know that $V_- = -V_+$, so $V(l)$ becomes

$$V(l) = V_+(e^{i\beta l} - e^{-i\beta l}) = 2iV_+ \sin\beta l = V_0 \sin\beta l = V_C^*, \tag{4.38}$$

where we have defined the voltage amplitude as $V_0 = 2iV_+$. Recognizing that we can solve for the voltage amplitude from the current amplitude ($V_0 = Z_C I_0$) we now find an expression for the voltage waveform of the resonator

$$V(z) = V_0 \sin\beta z = \frac{Z_C \omega_0 M V_{in}}{Z_0 R_{eff}} i \sin\left(\frac{\omega_0}{v} z\right) = \left(\frac{2\tilde{C}\omega_0}{Z_0 Q_e}\right) Z_C Q V_{in} \sin\left(\frac{\omega_0}{v} z\right). \tag{4.39}$$

To solve for the voltage across the capacitor on resonance, we again recognize that this was a transformed system on one of the fingers to ground thus solving for the voltage across the actual capacitor requires a factor of two giving,

$$V_C = 2V_C^* = 2V(l) = 2\left(\frac{2\tilde{C}\omega_0}{Z_0 Q_e}\right) Z_C Q V_{in} \sin\left(\frac{\omega_0}{v} l\right). \tag{4.40}$$

4.3.4 Quasi-lumped L- CPS resonator

Finally we examine the case of the QLL-CPS resonator. Figure 4.11(a) shows a representation of the QLL-CPS resonator enclosed in a ground plane. For this device $l = 3.355$ mm and $L = 2.9$ nH, obtained from the capacitance and the resonance frequency of the QL device. Again, because we're exciting an odd mode we can assume the middle of the resonator is grounded and solve a transformed device of one half of the resonator relative to ground (see Fig. 4.11(b)).

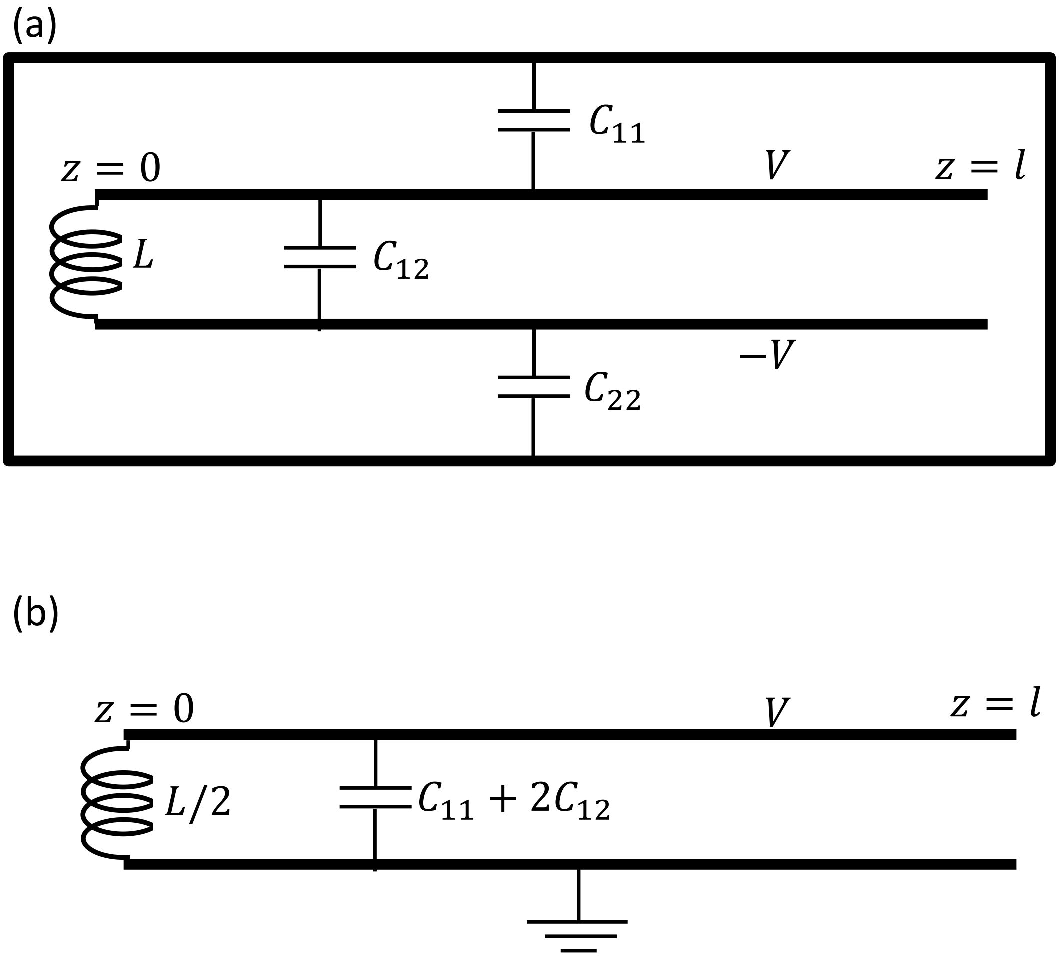

Figure 4.11: (a) Schematic picture of QLL-CPS resonator inside a ground plane. Note that due to the symmetry, an odd electric mode can be assumed to be grounded down the middle of the resonator. (b) Transformed resonant circuit created by cutting the QLL-CPS resonator down the middle and taking the capacitances between one of the fingers to ground, where a ground plane (actually a ground line) is assumed down the middle of the resonator in (a).

Solving for the input impedance of this resonator, we find

$$Z_{L,CPS} = \frac{i\omega L}{2} + Z_C \coth((\alpha + i\beta)l) = Z_C \alpha l(\cot^2 \beta l + 1) + \left(\frac{\omega L}{2} - Z_C \cot \beta l\right) i. \tag{4.41}$$

For the resonance condition, the imaginary part vanishes

$$\frac{\omega_0 L}{2} - Z_C \cot \beta_0 l = 0. \tag{4.42}$$

Solving for the resonance frequency and expanding around it, we find the input impedance on resonance

$$Z_{L,CPS} = \left(\frac{L}{2} + Z_C \left(1 + \cot^2 \left(\frac{\omega_0}{v} l\right)\right) \frac{l}{v}\right) \Delta, \tag{4.43}$$

and again note that it is of the same form as the series RLC input impedance (Eq. 4.4) with the substitutions

$$\tilde{L} = \frac{1}{2} \left(\frac{L}{2} + \left(1 + \cot^2 \left(\frac{\omega_0 l}{v}\right)\right) \frac{l Z_C}{v}\right), \tag{4.44}$$

and

$$\tilde{C} = \frac{1}{\omega_0^2 \tilde{L}}. \tag{4.45}$$

As in the previous geometries, this transformation allows us to model the resonator as a Thevenin equivalent circuit and solve for the current amplitude on resonance

$$I_L = \frac{\omega_0 M V_{in}}{Z_0 \tilde{R}_{eff}} i, \tag{4.46}$$

where I have defined the current amplitude through the inductor as I_L. As with the previous case, we can write the general form of the voltage waveform on the CPS

$$V(z) = V_+ e^{-i\beta z} + V_- e^{i\beta z}. \tag{4.47}$$

Here the boundary condition is

$$V(0) = V_L = \frac{i\omega_0 L I_L}{2} = -\frac{\omega_0^2 L M V_{in}}{2Z_0 \tilde{R}_{eff}}. \tag{4.48}$$

From the transmission line characteristic impedance, we can also write the current waveform

$$I(z) = \frac{V(z)}{Z_C} = \frac{1}{Z_C}(V_+ e^{-i\beta z} + (V_+ - V_L)e^{i\beta z}) \tag{4.49}$$

Since the transmission line is open at the end $z = l$, we also know that the current at the end is zero, i.e.

$$I(l) = \frac{1}{Z_C}(V_+ e^{-i\beta l} + (V_+ - V_L)e^{i\beta l}) = 0. \tag{4.50}$$

Solving for V_+ gives

$$V_+ = \frac{V_L}{e^{-2i\beta l} + 1}. \tag{4.51}$$

And from Eq. 4.47 we then obtain the voltage at the ends of the transmission line

$$V(l) = \frac{V_L e^{-i\beta l}}{e^{-2i\beta l} + 1} + \frac{V_L e^{i\beta l}}{e^{2i\beta l} + 1} = \frac{V_L}{\cos \beta l} = \frac{\left(\frac{\tilde{C}\omega_0^3}{2Z_0 Q_e}\right) L Q V_{in}}{\cos\left(\frac{\omega_0}{v} l\right)}. \tag{4.52}$$

And as in the previous cases, this is the voltage of one of the fingers to ground and it should be doubled to calculate the voltage between the two fingers.

Chapter 5

Coplanar resonator measurements

5.1 Coplanar resonator loss

As discussed in Chapter 2, the loss tangent of a material that is limited by a standard distribution of TLS defects can be described by

$$\tan\delta = \tan\delta_0 \frac{\tanh\left(\hbar\omega/2k_BT\right)}{\sqrt{1+(E/E_c)^2}}, \tag{5.1}$$

where $\tan\delta_0$ is the low-power intrinsic loss tangent, dependent on the frequency distribution and density of the TLSs, E_C is the critical field dependent on the T_1 and T_2 of the TLSs, and E is the applied electric field at the location of the TLSs. In general, the electric field and the loss tangent in a resonator my not be uniform. I that case, the inverse of the internal quality factor of the resonator can be written as a weighted distribution of the loss tangent:

$$\frac{1}{Q_i} = \frac{\int_{LossyMaterial} \tan\delta\epsilon(\vec{r})(\vec{E}(\vec{r}))^2 d^3r}{\int_{All} \epsilon(\vec{r})(\vec{E}(\vec{r}))^2 d^3r}. \tag{5.2}$$

Therefore, in the case of a coplanar resonator, one must consider the electric field distribution for the entire resonator when interpreting the internal quality factor.

5.1.1 Sputtered aluminum resonators on sapphire

I measured coplanar resonators fabricated from several aluminum films, most of which were sputtered films on a sapphire substrate. Here I present measurements

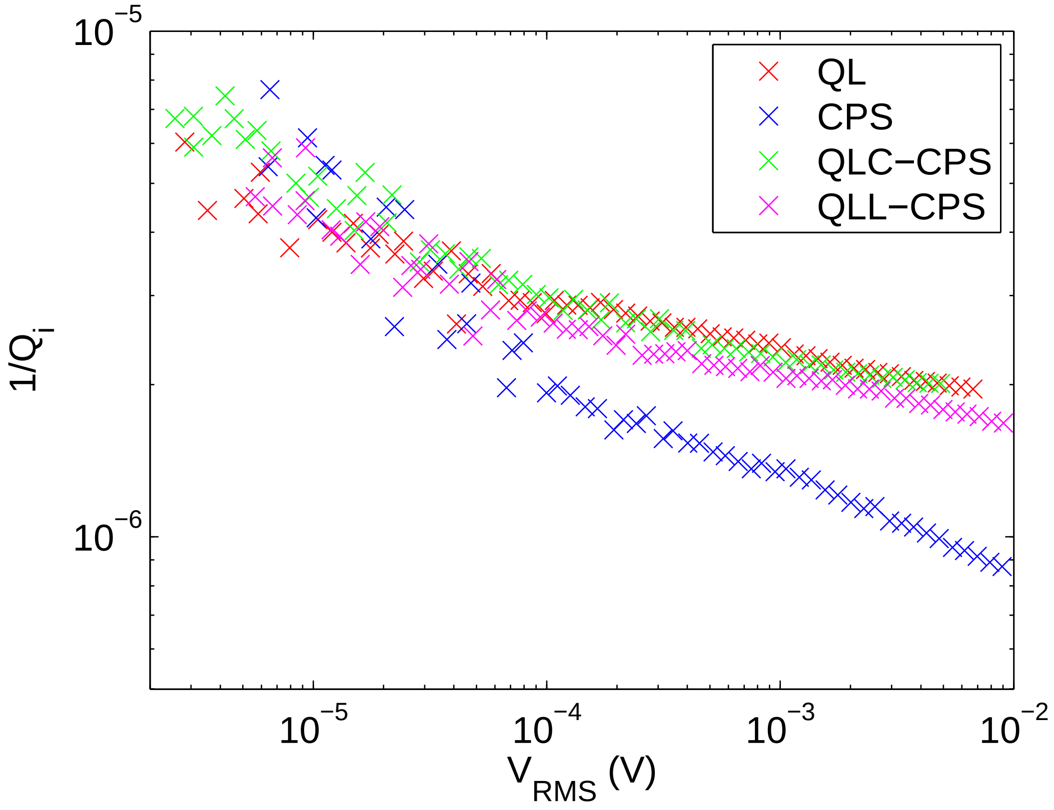

Figure 5.1: The inverse internal quality factor $1/Q_i$ vs. RMS microwave voltage for the four resonators with different geometries from sample sp1.

of resonators from three such chips: two are different chips from the same sputtered film on the same wafer (sp1 and sp1-B) and one is a chip from a different sputtered film with nominally the same film and device parameters (sp2). Figure 5.1 shows a comparison of the $1/Q_i$ for the four coplanar devices, measured on one chip with a single CPW, as a function of the rms excitation voltage. Figure 5.1 indicates that the CPS resonator has a lower loss (higher Q_i) than the other three devices. However, Fig. 5.2 shows that measurements to those on nominally identical devices (sputtered using the same technique and components on the same type of wafer

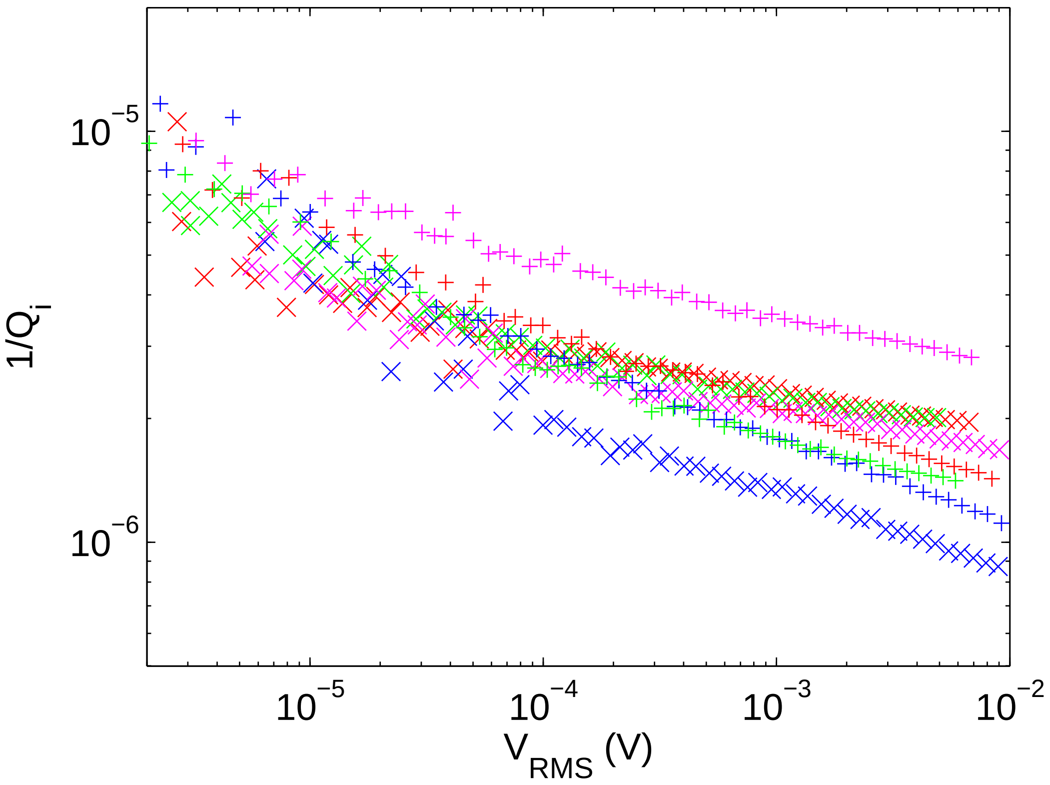

Figure 5.2: plot of the internal loss $1/Q_i$ vs. microwave voltage V_{RMS}, comparing previous measurements from sp1 ($\times$) to measurements of nominally identical resonators from sample sp2 ($+$), using the same device color code as before (QL: red, CPS: blue, QLC-CPS: green, QLL-CPS: magenta).

with nominally the same processing) gives quite different results. In Fig. 5.2 the $\times$ symbols represent measurements from chip sample sp1 as shown in Fig. 5.1, and the $+$ symbols represent the measurements from sp2. Despite being nominally identical, the second set of devices from sp2 have a different distribution of losses with three devices clumped together and the QLL-CPS device showing a distinctly higher loss.

The discrepancy between the two sets of measurements in Fig. 5.2 implies that there is at least one uncontrolled factor that is affecting the loss. To check if this

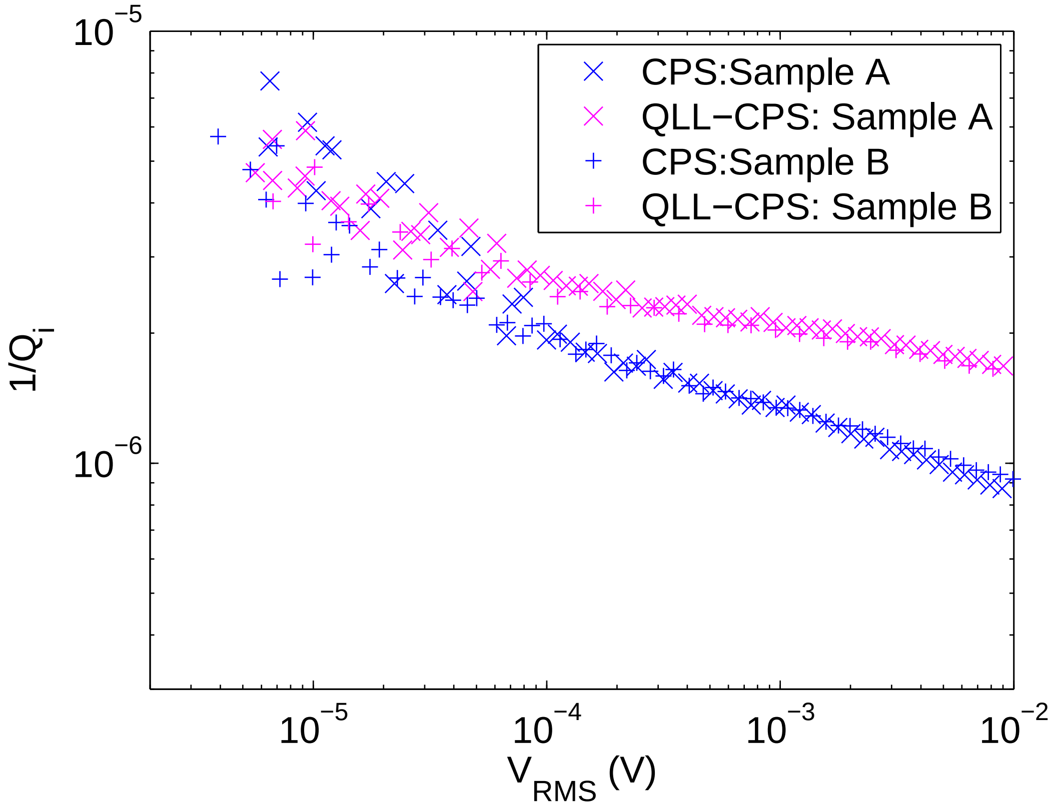

Figure 5.3: Comparing plots of the internal loss $1/Q_i$ vs. microwave voltage V_{RMS} for the CPS (blue) and the QLL-CPS (magenta) resonators from samples sp1 and sp1-B from two different chips from the same film

discrepancy occurs between different samples from the exact same film, I cooled down another chip sp1-B from the same sputtered film as sp1. Figure 5.3 shows two sets of measurements for the CPS and QLL-CPS resonators. As can clearly be seen in Fig. 5.3, the differences between the different resonator geometries are reproducible from sample to sample within the same film. This behavior suggests that significant variations in the resonator qualities are coming from uncontrolled variations in the fabrication process.

5.1.2 Coplanar resonator loss analysis

Taken as a whole, these results suggest that there is little device to device variation due to geometry and no significant loss-based advantages or disadvantages to particular geometry types. However, since the quasi-lumped element resonator does not have harmonic cavity modes, it may still provide an advantage when measuring the lifetime of a coupled qubit.

Another significant characteristic of the data is that the power dependence of the loss is very weak, nowhere near the $\sim 1/V$ dependence predicted by TLS theory in Eq. 9.1. Also, the measured power dependence of $1/Q_i$ seems to vary from device to device in the range from $\sim 1/V^{0.1}$ to $\sim 1/V^{0.2}$, as reported in [39].

Note Eq. 9.1 gives the expected loss tangent and the measurement is only of the device quality factors. It's been found that the loss in these coplanar devices scales with the surfaces [60]. A possible explanation for the weak power dependence is that the loss is occurring at the surface. To model the effects of surface loss, I assumed that the loss is coming from either the native oxide on the aluminum (blue and green in Fig. 5.4), the substrate surface (red in Fig. 5.4), or the substrate metal interface (black in Fig. 5.4). I then used the finite element E&M simulator COMSOL to calculate the electric field at those surfaces as a function of the voltage across the device. Assuming a surface thickness of 5 nm, and an intrinsic loss tangent of 10^{-3}, I used Eq. 7.3 for each surface to find the effective internal loss as a function of the voltage. As Fig. 5.4(b) shows, no matter what lossy surface was assumed, $1/Q_i$ never decreases slower than $1/V$ for more than a decade in voltage. One way

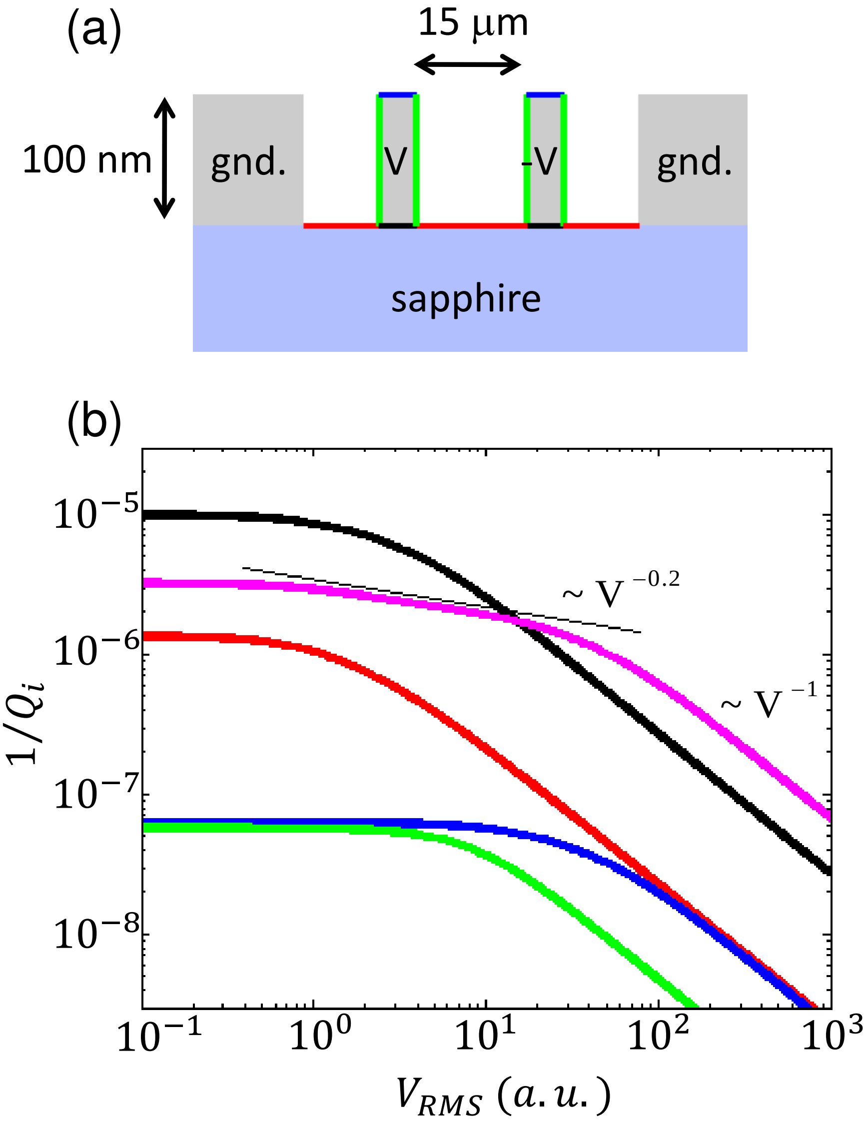

Figure 5.4: (a) Cross sectional diagram of CPS resonator. (b) Calculated $1/Q_i$ for the CPS geometry from simulated fields as a function of the voltage across the resonator assuming the loss is dominated by different possible surfaces (5 nm thicknesses), color coded from (a). Magenta represents the addition of loss from the substrate vacuum interface (red) and the top of electrode surface (blue).

to lower the power dependence was to pathologically consider just the loss from the substrate vacuum interface (red) and the top of electrode surface (blue). But as the magenta curve in Fig. 5.4 shows even that only lowered the power dependence to $1/V^{0.2}$ for less than a decade in voltage. From these simulations it would appear that surface loss is not sufficient to explain the shallow power dependence observed in the coplanar resonators.

5.1.3 Evaporated aluminum resonators on sapphire

As mentioned earlier, I also tested the four resonator geometries using devices made from evaporated aluminum films. Figure 5.5 shows a comparison between the evaporated film ev1 measurements ($\circ$) and the sputtered film measurements sp1 ($+$) (devices color coded as in the previous figures). We see from Fig. 5.5 that the evaporated film tends to have a slightly higher loss than the sputtered film. A possible explanation for this is that the evaporated film is rougher and therefore has more lossy surface area. AFM measurements were performed on the two films (see Fig. 5.6) which confirmed that the evaporated film is in fact rougher with 20-40 nm features compared to the sputtered film's 5-10 nm features. Assuming approximately a factor of 4 increased amplitude and density (in both surface dimensions) of 'bumps' in the evaporated film would mean more than a factor of 3 increase in the total surface area. This of course is not the whole story because surface area topography also affects the electric field, but it's certainly a plausible explanation.

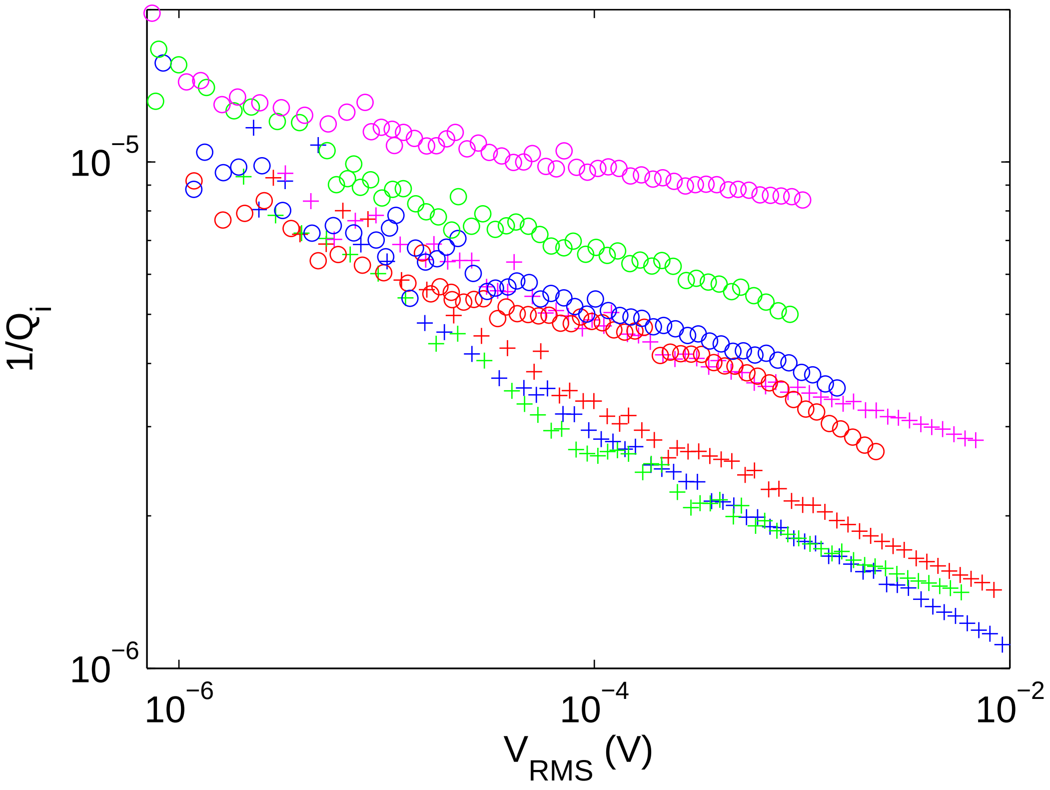

Figure 5.5: plot of the internal loss $1/Q_i$ vs. microwave voltage V_{RMS}, comparing previous measurements from sputtered sample sp1 (+) to evaporated sample ev1 ($\circ$), using the same device color code as before (QL: red, CPS: blue, QLC-CPS: green, QLL-CPS: magenta).

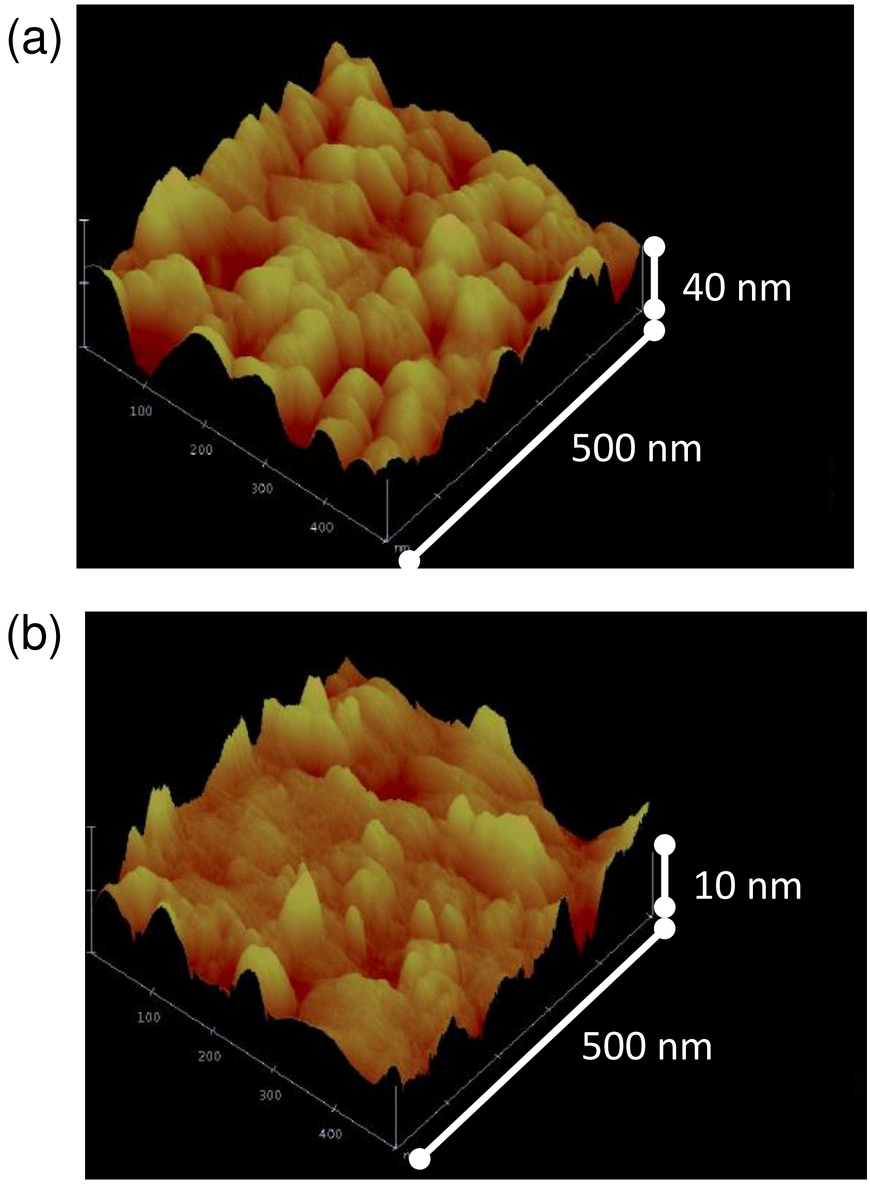

Figure 5.6: (a) AFM measurement of evaporated Al film showing 20-40 nm sized features. (a) AFM measurement of the sputtered Al film showing 5-10 nm sized features.

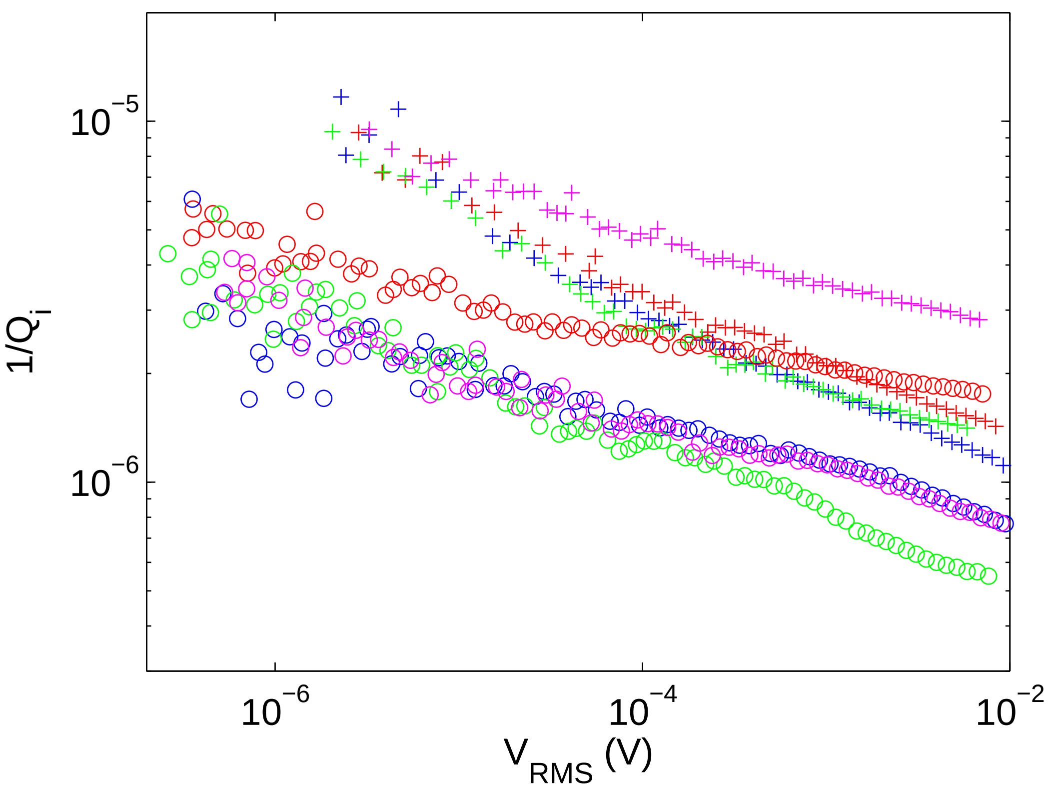

Figure 5.7: plot of the internal loss $1/Q_i$ vs. microwave voltage V_{RMS}, comparing previous measurements from sputtered sample on sapphire sp1 (+) to a sputtered sample on a silicon substrate that was cleaned with HF sp3-Si (∘). The same device color code is used as before (QL: red, CPS: blue, QLC-CPS: green, QLL-CPS: magenta).

5.1.4 Sputtered aluminum resonators on silicon

I also measured sputtered aluminum films on undoped high resistivity silicon wafers sp3-Si. In Fig. 5.7, I compare results from these devices ∘ to results from sp1 + (devices color coded as in the previous figures). The measurements on silicon wafers showed lower loss which is likely due to a cleaner silicon surface as compared to the sapphire surface; I used an HF treatment of the silicon wafers prior to deposition (see Chapter 4).

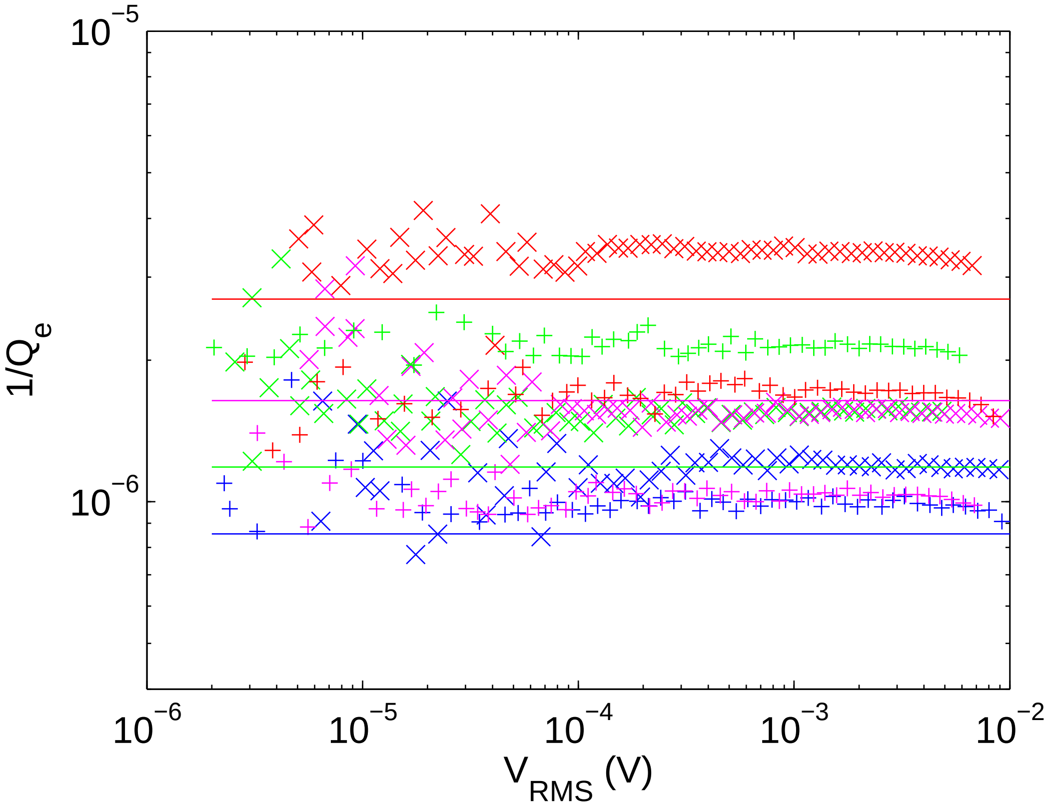

Figure 5.8: Inverse external quality factors $1/Q_i$ (coupling to CPW) vs. RMS microwave voltage for devices from the two sputtered films sp1 and sp2, using the same device color code as before (QL: red, CPS: blue, QLC-CPS: green, QLL-CPS: magenta).

5.2 External quality factor

Another parameter that I monitored during resonator measurements is the external quality factor Q_e. As discussed in Chapter 3, the Q_e is a measure of the coupling of the CPW to the resonator and can be simulated with Microwave Office. Figure 5.8 shows the measured values of $1/Q_e$ for samples sp1 and sp2 along with the four simulated values for the parameter. As Shown in Fig. 5.8, the simulations don't predict the accurate values for Q_e to better than within a factor of two. Also the

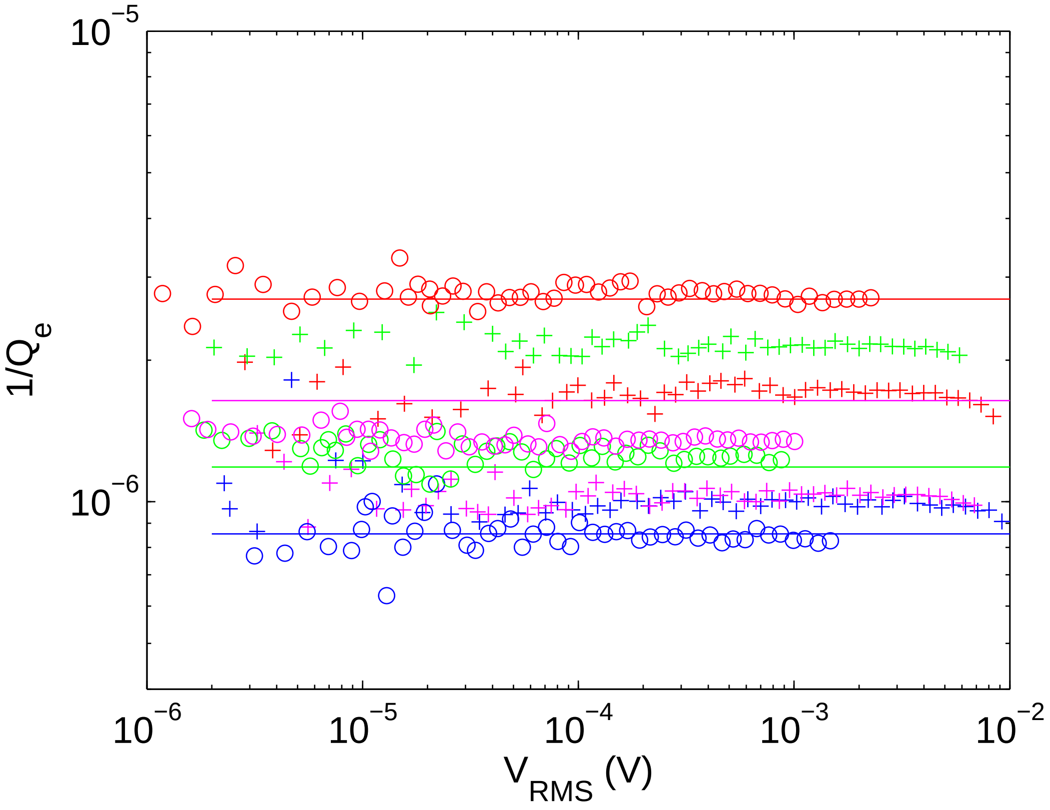

Figure 5.9: Inverse external quality factors $1/Q_i$ (coupling to CPW) vs. RMS microwave voltage for devices from the sputtered sample sp1 (+) and the evaporated sample ev1 (∘), using the same device color code as before (QL: red, CPS: blue, QLC-CPS: green, QLL-CPS: magenta).

difference between the measurements and simulations is not systematic. For example, for the two QL resonators, the measurement of sp1 shows higher coupling than the simulated value and sp2 shows lower. When comparing the Q_e's for the evaporated and sputtered films (see Fig. 5.9) similar deviations are observed, although the predictions appear closer for the evaporated film. It's possible, that while these devices are in nominally identical packaging, small uncontrollable deviations in the packaging can play a large role on the coupling.

5.3 Discussion of likely loss mechanisms

As discussed earlier, a likely loss contributor is the surface native oxide and other surface contaminants. As shown in Fig. 5.4 and discussed in more detail in Ref. [61], the electric field distribution is such that the dominant loss arises from the metal-substrate interface and the substrate-vacuum interface. It's also been found through electric field simulations that the corner at the metal-substrate-vacuum interface is a significant contributor to loss [61]. So a small undercut of the substrate at the corner of the metal would likely go a long way to reducing the loss [62]. Even more evidence for substrate surface limited loss is an experiment where the measured loss in a coplanar resonator was reduced with an 850 ^{o}C O_2 anneal of the sapphire substrate before deposition [63].

Barends *et al.* [64] have found that if the devices aren't properly shielded, stray infrared light can generate quasiparticles that break up Cooper pairs in the superconductor and cause a power independent loss. It's likely that this at least partially limits these measurements because in other measurements of these devices, performed by S. Gladchenko, a steeper power dependence was found when sample box shielding was improved and SiC stycast mixture (see Ref. [64]) was used. However, the microwave line connectors were also changed in that sample box design, so it's possible that other factors caused the change in saturation power dependence.

Thus far I have only discussed electric loss in the capacitor. But it is also possible that these resonators are limited by inductive loss [65]. It's been shown in

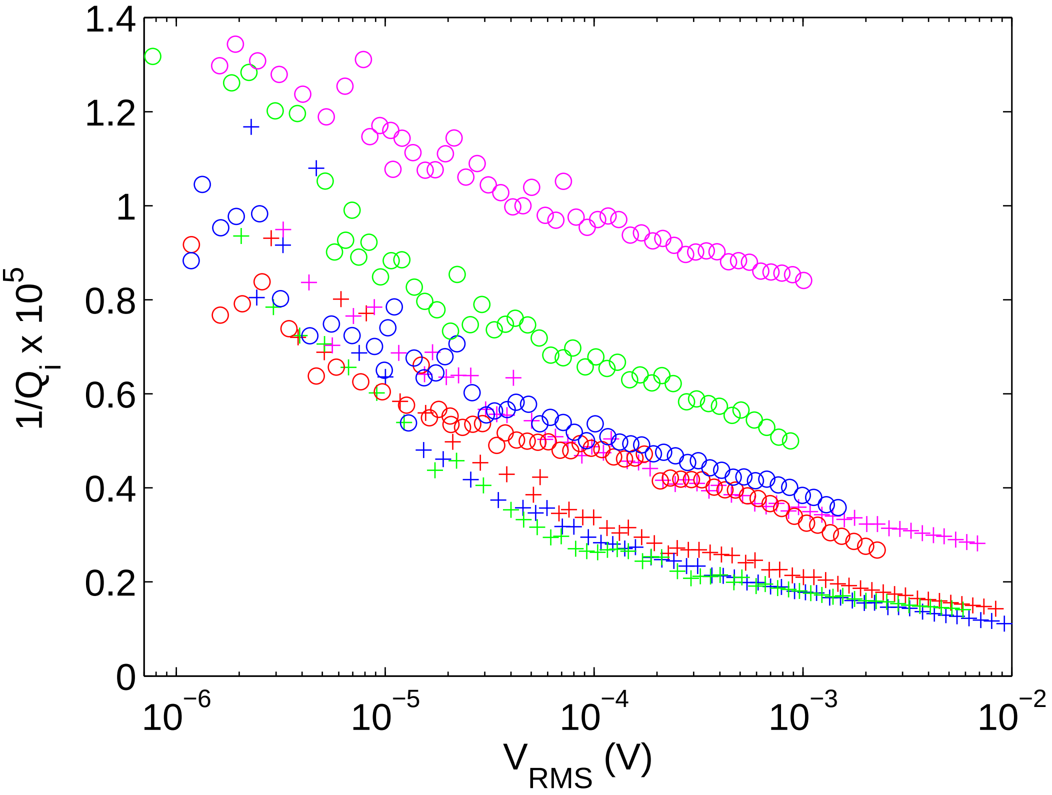

Figure 5.10: Replotted measurements from Fig. 5.5 again with sputtered sample sp1 (+) and evaporated sample ev1 (○) and identical device color code (QL: red, CPS: blue, QLC-CPS: green, QLL-CPS: magenta).

SQUIDs that inductance noise is consistent with surface magnetic spin interactions [66], likely through RKKY interactions [67]. It's plausible that such surface spins are causing inductive loss in these coplanar devices which is convoluted with the capacitive loss resulting in the measured Q_i. Although such magnetic losses would likely still be small in this regime because a comprehensive study of scaling of a quai-lumped resonator based on the QL resonator discussed here found scaling of measured Q_i with the spacing of the IDC fingers and not with the geometry of the meandering inductor [68].

Recently Faoro *et al.* [69] motivated by our results along with others in the community proposed a model where interactions between TLSs confined to resonator surfaces can lead to a shallower loss saturation with electric field. In this model they assumed coherent TLSs with relaxation times longer than their Rabi frequency (saturation time), which they called TLSs, and relatively incoherent TLSs with relaxation times shorter than their Rabi frequency, which they called fluctuators. In their model when a long lived TLS interacts with a short lived fluctuator, its frequency drifts moving it in and out of the resonator's bandwidth. So if a TLS is on resonance and is excited by the resonator, it may shift its frequency through interaction with a fluctuator and dissipate the photon outside the resonator's bandwidth. Thus a photon that could have been returned back to the resonator through stimulated emission has been lost to the system and through this mechanism excess loss can be observed. Faoro *et al.* found that such interactions can lead to a logarithmic TLS loss saturations. In Fig. 5.10 I've replotted the measurements of films sp1 and ev1 from Fig. 5.5 on a semi-log plot. While certainly not conclusive, a logarithmic saturation seems plausible. Note that somewhat coincidently a very similar TLS loss mechanism will be addressed in Chapters 8 and 9.

5.4 Conclusion

In conclusion I measured four types of coplanar devices and they showed similar loss with no clear geometry dependence. This suggests that the four resonator designs are equally appropriate for quantum computing circuits, and there does not seem to be a large advantage for one type of resonator design over another if only considering the fundamental mode. However, since the quasi-lumped element resonator does not have harmonic cavity modes, it may still provide an advantage when measuring the lifetime of a coupled qubit.

I also found that the power dependence of the loss in these resonators is not consistent with a conventional surface distribution of identical TLSs. These measurements, along with other measurements in the quantum computing community indicate that the low power loss tangent is limited by TLS material losses, but that the shallow power dependence may be associated with quasiparticles caused by infrared light absorption. I also observed that evaporated films tended to have higher loss, likely because they were rougher with more native oxide, and that films on HF cleaned high-resistivity silicon substrates showed lower loss, most likely because the silicon surface was cleaner. Finally, I observed variations in the Q_e from simulation predicted values in an unsystematic seemingly random manner.

Chapter 6

Atomic layer deposition

6.1 Atomic layer deposition and its use in trilayer junctions and capacitors

Atomic layer deposition (ALD) is a film deposition technique which alternates the use of two or more gaseous chemical precursors to create a self-limiting layer-by-layer deposition process. Figure 6.1 shows a summary of a generic ALD process. In addition to the self-limiting nature of the process, it also provides atomic level thickness control (see Fig. 6.2) with superb conformality (see Fig. 6.3).

The level of control that ALD provides makes it a potentially attractive choice for Josephson junction preparation. If metal deposition can also be integrated into the ALD chamber, it can allow for *in situ* trilayer fabrication and the potential to produce almost defect-free junctions and capacitors. As with conventional trilayer deposition techniques, the advantage of *in situ* ALD tilayer fabrication is that the deposition of the metal/insulator/metal layers can be done without breaking vacuum, reducing film contamination.

Despite its potential ALD is not without its drawbacks. Incomplete reactions can implant impurities from precursors into the film. Suitable precursors are often limited and for certain materials, research groups have to make their own precursors.

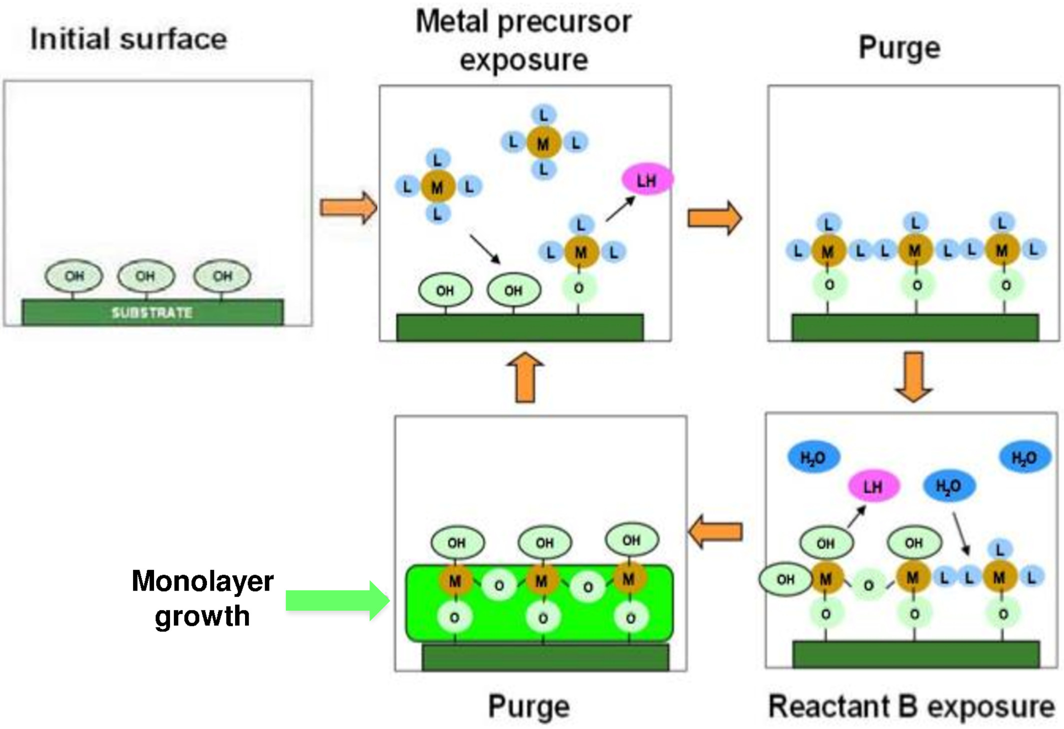

Figure 6.1: ALD cycles exposure and purge of two precursors to grow thin films with monolayer control. In this generic example ML_4 and H_2O are cycled to grow MO_2 [70].

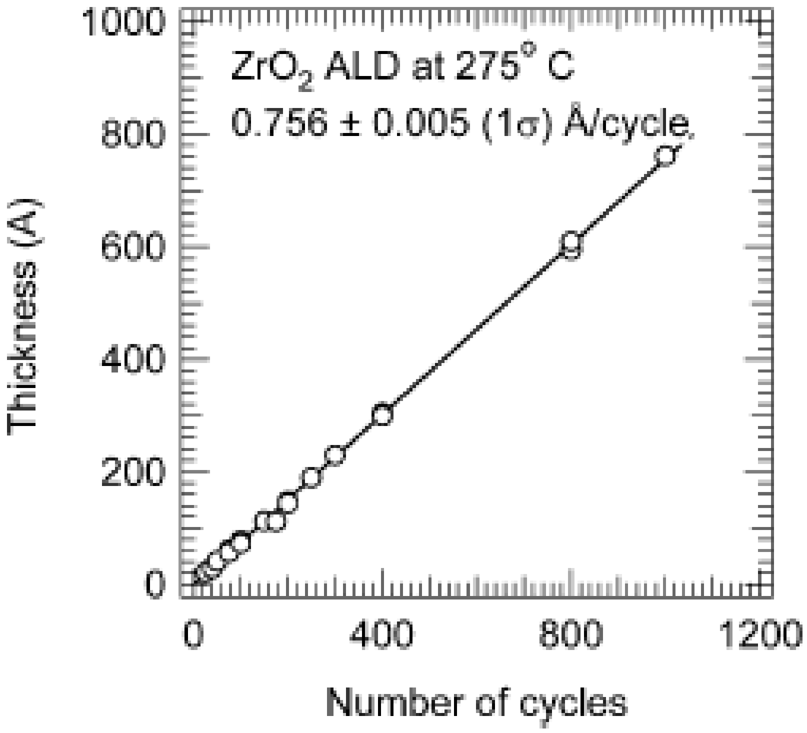

Figure 6.2: A plot of thickness of an ALD grown ZrO_2 as a function of the number of precursor cycles. This shows the level of thickness control that ALD provides [71].

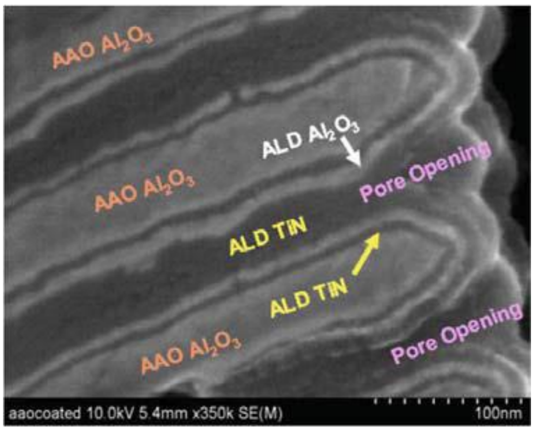

Figure 6.3: ALD MIM nanocapacitor grown on anodized aluminum oxide (AAO) nanopores highlighting the conformality of ALD growth. MIM structure has a thickness of TiN 5.6 nm, AlO_x 6.6 nm, TiN 12.6 nm [70].

And finally, unlike the relatively rapid process of the more common CVD growth, ALD growth tends to have a very low deposition rate.

6.2 Microwave resonator fabrication on ALD materials and field simulations of coplanar geometry

Perhaps the most direct method for measuring the loss of an ALD dielectric at microwave frequencies is to fabricate it into a parallel-plate capacitor as part of a microwave resonator and measure the resonator's Q_i, as described in Chapter 3. Since all of the electric energy would be in the ALD dielectric, and that is by far the limiting source of loss, $1/Q_i$ would be equal to the loss tangent of the material.

If not all of the electric energy is in the ALD dielectric, then one needs to find the filling factor. The filling factor is just the fractional energy stored in a particular part of a resonator,

$$F = \frac{\int_{LossyMaterial} \epsilon(\vec{r})(\vec{E}(\vec{r}))^2 d^3r}{\int_{All} \epsilon(\vec{r})(\vec{E}(\vec{r}))^2 d^3r}, \tag{6.1}$$

Assuming the resonator's quality is limited entirely by the ALD material's loss tangent, the loss tangent of the ALD material can be calculated from the measured Q_i with

$$\tan\delta = \frac{1}{FQ_i}. \tag{6.2}$$

For a parallel-plate capacitor $F = 1$, but the loss tangent can be calculated even if $F \neq 1$ as long as it's known. If the electric field distribution is known, Eq. 7.10 can be calculated and Eq. 6.2 can be used to find the loss tangent of the material after Q_i is measured. This method allowed me to measure the loss tangent of ALD films using simple fabrication techniques that did not require being able to build a parallel-plate capacitor.

In particular, I fabricated coplanar resonators discussed in Chapters 4 and 5 atop ALD dielectrics. I simulated the field distribution of the resonators with the finite element simulator COMSOL and by knowing the thickness of the predeposited ALD dielectric, I was able to calculate Eq. 7.10 for each deposited dielectric.

Figure 6.4 shows a COMSOL simulation of the cross-section of a CPS resonator on top of a thin dielectric film on a substrate. Fig. 6.4(a) shows the electric field in the vacuum and dielectric induced by the CPS fingers and Fig. 6.4(b) shows the electric energy density from said field. In this simulation a difference of 2 mV was placed on the two conductors and the electric field distribution was exported. To find the filling factor I numerically integrated the electric energy stored in the top

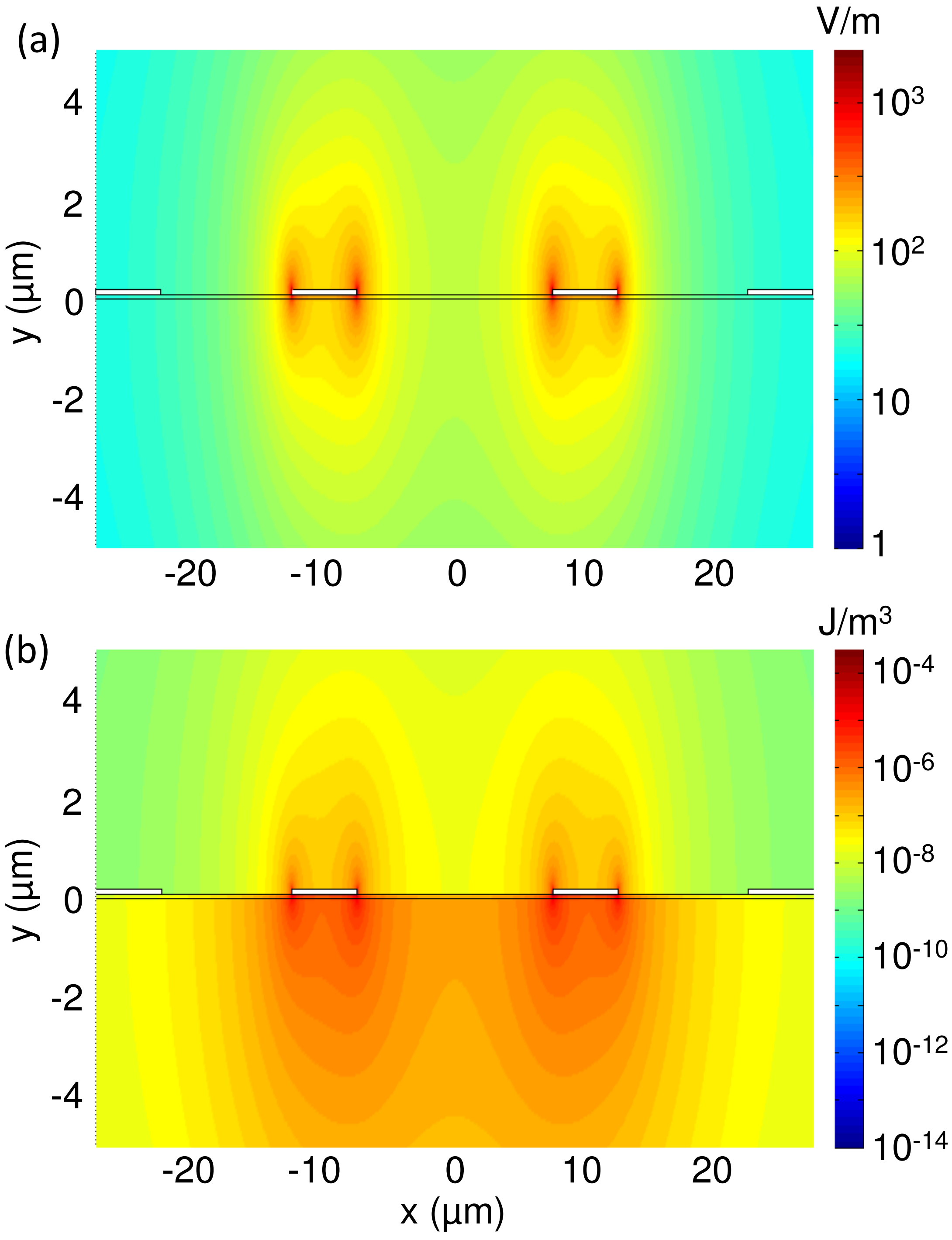

Figure 6.4: (a) Simulated electric field distribution for 100 nm thick CPS resonator (with 2 mV across the CPS electrodes) on 90 nm of ALD grown AlO_x atop a sapphire wafer. (b) Electric energy density distribution of (a).

ALD dielectric, 90 nm thick in this case, as a percentage of the total electric energy of the resonator and assumed that the lossy dielectric was entirely responsible for the resonator's Q_i. There were added complications on the analysis due to the voltage gradient on the resonator, the field dependence of the loss tangent, and as it turns out the non-uniform loss of the ALD material, but these subtleties will be discussed when the data is presented in Chapter 7.

Chapter 7

ALD grown dielectric measurements

In this chapter I summarize my measurements on ALD dielectric films and discuss the implications for future quantum computing studies. As discussed in Chapter 6, the low temperature loss measurements were performed by fabricating coplanar resonators (discussed in Chapters 4 and 5) on top of the ALD dielectrics and measuring their Q_i. In this chapter, I will also discuss the OH defect model, show secondary ion mass spectrometry (SIMS) measurements of ALD dielectrics and discuss their implications.

7.1 Deuterated $\mathrm{AlO_x}$ ALD films

7.1.1 OH defect model

As discussed in Chapter 2, perhaps the most commonly considered TLS micromechanism in oxides is the OH rotor. As early as 1987, Phillips proposed that $\mathrm{OH^-}$ groups could act as TLS defects [26]. It has recently been shown using density functional theory that within particularly O-rich $\mathrm{AlO_x}$, hydrogen is likely to fill cation vacancies and form a significant density of microwave frequency TLSs [34].

Hydrogen is particularly difficult to remove from ALD $\mathrm{AlO_x}$ films because it exists in both the aluminum precursor, trimethylaluminum (TMA), and the oxygen precursor, water. It was not known which precursor contributed most of the hydrogen, nor whether OH^- was really dominating the loss. It was with this in mind that we attempted to substitute deuterium for hydrogen by using deuterated water as a precursor [72]. As calculated by Holder *et al.* [34], the increased mass of deuterium would result in a substantially reduced tunneling rate Δ_0 . Naturally this could move TLS defects into a much lower frequency range and improve the loss tangent of AlO_x at microwave frequencies.

7.1.2 SIMS measurements of AlO_x films

Two 55 nm thick AlO_x films were grown by Alexander Kozen in the Rubloff group at the University of Maryland, one with regular water as the oxygen precursor and the other with 100% deuterated water. To confirm that we were actually substituting deuterium for hydrogen when we were using deuterated water, we had SIMS measurements performed on them [73]. Figures 7.1(a,c) show SIMS results for a non-deuterated film and Figs. 7.1(b,d) show SIMS results for a deuterated film. In Figs. 7.1(a,b), the concentration of hydrogen, deuterium, and carbon are shown as a function of depth in the film (0 is the top and 55 nm is the interface with the sapphire wafer), while in Figs. 7.1(c,d) the integrated concentrations of each impurity are shown. The first feature of note is that using deuterated water does in fact reduce the amount of excess hydrogen and increase the amount of deuterium in the bulk. However, there also appears to be a substantial amount of hydrogen surface contamination at the sapphire-AlO_x interface that doesn't depend on the precursor used. Comparing Fig. 7.1(c) to Fig. 7.1(d), we see that the deuterated film has a total of 4×10^{22} H atoms/cm^2 while the non-deuterated film has a total of 10^{23} Hatoms/cm^2, there is still about a factor of 2 difference between the amount of total hydrogen in the two films. If OH$^-$ defects are a dominant loss contributor we may then expect to see a difference in the loss tangent of the two films. Note that the carbon impurities found in these films come from the aluminum precursor TMA and will be discussed later in the chapter.

7.1.3 Resonator measurements

As mentioned earlier, I used the coplanar resonators discussed in Chapters 4 and 5 to measure the loss of the ALD grown dielectrics. Figure 7.2(a) shows results from the inverse internal quality factor measurement as a function of the RMS microwave voltage across the devices, taken at 80 mK, for two resonators (CPS and QLC-CPS) fabricated on 55 nm of ALD grown $\mathrm{AlO_x}$. Sample dut1 was grown with deuterated water as the oxygen precursor and sample hyd1 was grown with non-deuterated water as the oxygen precursor. All other grown parameters were identical (growth was performed at 250 ^{o}C).

The first thing we notice in Fig. 7.2(a) is that qualitatively this behavior is clearly due to TLS loss, with an intrinsic voltage-independent-loss at low-voltages and a decrease in loss at higher-voltages due to TLS saturation. Next note that there doesn't seem to be a difference in low-voltage Q_i for the same device types between the two films hyd1 and dut1. The non-deuterated film (red symbols) seems to have a higher background loss at high voltages, but that may be due to the measurement

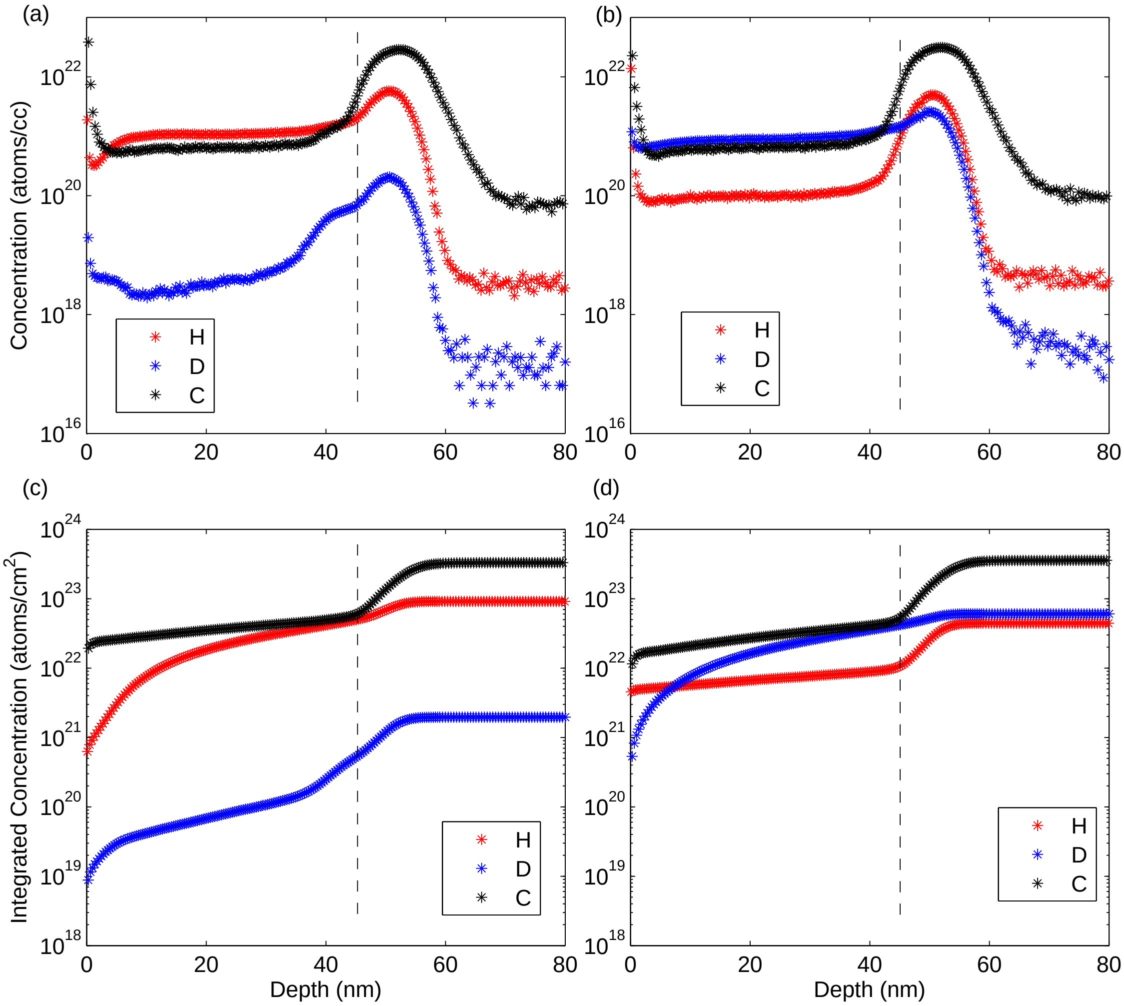

Figure 7.1: (a) SIMS analysis for carbon (black), hydrogen (red), and deuterium (blue) impurities of ALD grown AlO_x. (b) SIMS analysis for carbon, hydrogen, and deuterium impurities of ALD grown AlO_x with deuterated water precursor. (c) Integration of impurities in (a) through the 55 nm film. (d) Integration of impurities in (b) through the 55 nm film. Sapphire-ALD interface is at d=55 nm. The vertical dashed lines indicate the film depth. Dashed lines aren't aligned with the defect peaks because of limitations in the SIMS depth resolution.

setup rather than the TLS defects. The difference between the films is at such a high quality factor that it's likely similar to the discrepancies observed between the coplanar device on bare sapphire in Chapter 5. This result suggests that either the TLSs causing the loss are not hydrogen based or perhaps that there's another factor that compensates for the decreased hydrogen in the deuterated film.

One possibility is that the deuterium substitution worked but that because of their lower tunneling rates and because the TLS distribution is inversely proportional to tunneling rates $\sim 1/\Delta_0$, the deuterium based TLSs ended up having a higher density. To understand this consider an example of a distribution of TLSs with tunneling rates from 100 to 1000 (in arbitrary units). If their tunneling rate is reduced by a factor of 10 then they would be squeezed into having tunneling rates from 10 to 100, thus increasing their density by a factor of 10 as well. So if the distribution of TLSs is sufficiently broad, it can have a negligible effect on the loss. Note that if the TLS well frequency is proportional to the inverse of the square root of the defect mass as one would expect ($\omega^2 \propto 1/m$), we would still expect the deuterated TLS to have a factor of $\sqrt{2}$ less loss, since of course deuterium has twice the mass of hydrogen, but such a difference in loss wasn't resolved.

We also note that the CPS resonators show a lower inverse Q_i than the QLC-CPS resonators. This is because of the electric energy filling factor,

$$F = \frac{\int_{LossyMaterial} \epsilon(\vec{r})(E(\vec{r}))^2 d^3r}{\int_{All} \epsilon(\vec{r})(E(\vec{r}))^2 d^3r}, \tag{7.1}$$

for the lossy ALD grown film is higher for the IDC than it is for the CPS. Simply put, the IDC teeth are closer together than the CPS electrodes are, so more electric energy is stored in the 55 nm directly below the resonator, where the ALD film is. The filling factors for the two devices can be numerically calculated using the COMSOL simulations mentioned in Chapter 6. I found that the IDC filling factor for the 55 nm ALD film is $F_{IDC,55nm} = 0.052$, while the CPS filling factor is $F_{CPS,55nm} = 0.031$. As seen in Fig. 7.2(b) when the $1/Q_i$ measurements for the four resonators are scaled for the different filling factors they lie on top of each other. This is consistent with loss coming uniformly from the ALD film.

7.2 Varying ALD oxides

7.2.1 CPS Q_i measurements and field simulations

To better understand TLSs in amorphous and crystalline ALD oxides, I next measured three different ALD-grown films: crystalline BeO (known to be crystalline from XRD measurements [74]), amorphous $\mathrm{AlO_x}$ [75], and amorphous $\mathrm{LaAlO_x}$[76]. The BeO film from the Banerjee group at UT Austin [74] and was grown at 200 ^{o}C with the beryllium precursor, dimethyl beryllium $\mathrm{Be(CH_3)_2}$, and the oxygen precursor, water. The $\mathrm{AlO_x}$ [75] and $\mathrm{LaAlO_x}$ [76] films from the Gordon group at Harvard were grown at 300 ^{o}C with the aluminum precursor TMA and the lanthanum precursor tris(N,N'-diisopropylacetamidinato)lanthanum ($\mathrm{La(^iPrAMD)_3}$). The BeO film was grown on high-resistivity silicon and the amorphous films were grown on sapphire. The crystalline BeO film is of particular interest because crystalline materials tend not to show TLS loss. Bulk single crystal Al_2O_3 (sapphire) as discussed in Chapter 5, has a low, TLS free, loss tangent, which suggests that either the

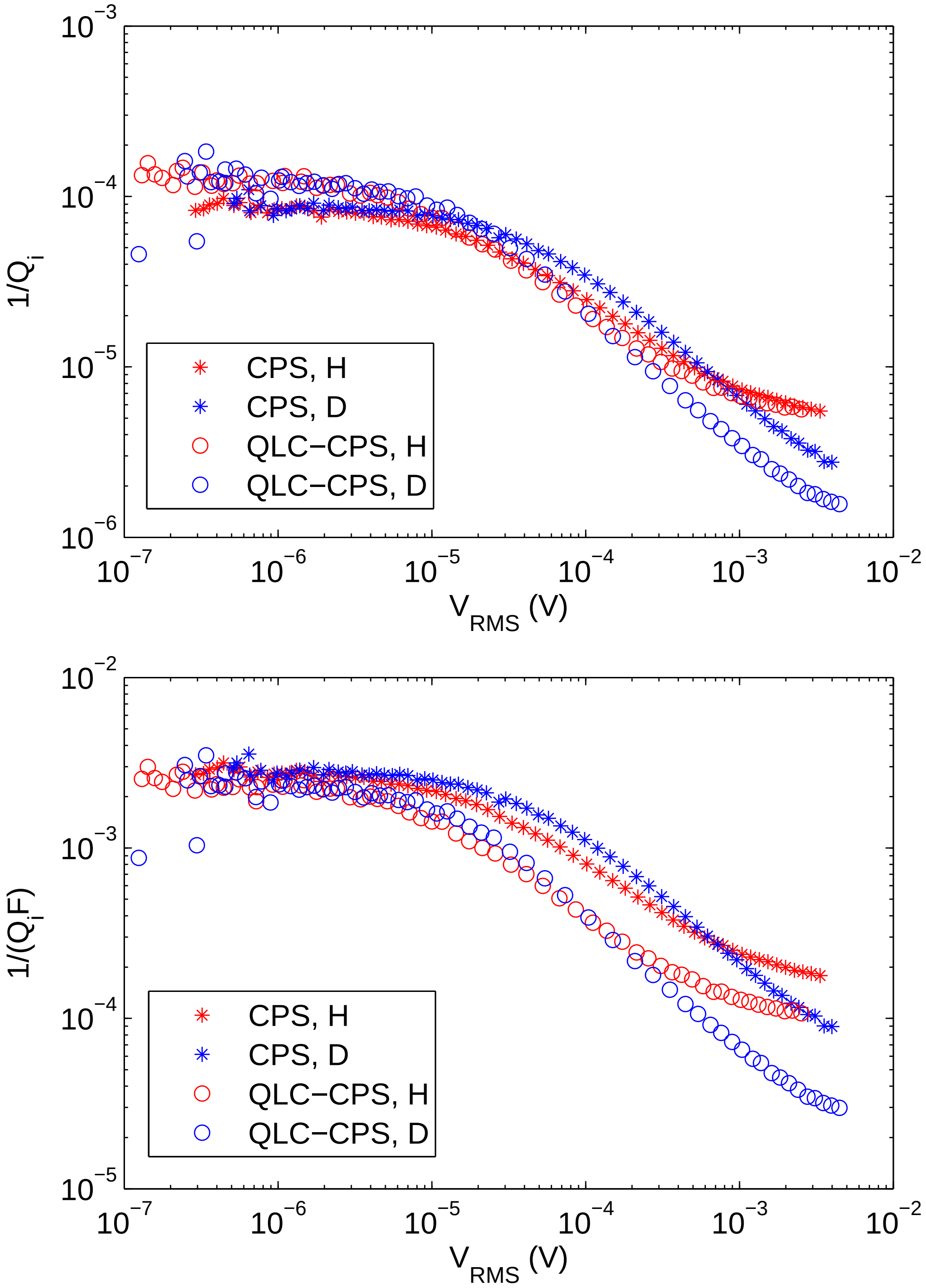

Figure 7.2: (a) Inverse Q_i measurement of CPS ($*$) and QLC-CPS ($\circ$) resonators on a 55 nm ALD grown AlO_x film grown with deuterated (blue) and conventional (red) water. (b) Measurements from (a) divided by the filling factor of the ALD film for the two resonator geometries. At low voltage, this corresponds to the intrinsic voltage-independent loss tangent of the film. Deuterated and undeuterated films show the same level of loss. Data plotted for devices: hyd1-CPS ($*$ in red), dut1-CPS ($*$ in blue), hyd1-QLC-CPS ($\circ$ in red), dut1-QLL-CPS ($\circ$ in blue).

amorphous nature or impurities in the films create additional loss. Also, the high thermal conductivity at low temperature [77] and the low loss tangent near room temperature [78] of crystalline BeO suggests that it [74] may have low loss useful for superconducting devices.

Figure 7.3 shows a plot of the inverse Q_i of the CPS resonators on the three different films taken at 35 mK as a function of the voltage across the CPS electrodes. Immediately we notice that even the crystalline BeO film shows behavior that is clearly consistent with TLS loss. However as discussed earlier, the inverse Q_i only corresponds to the loss tangent when the filling factor of the dielectric is 1, as in a parallel-plate capacitor. Here we must use COMSOL to simulate the field distribution of the CPS geometry using the known permittivity of the oxides ($\epsilon_{r,BeO} = 6.7$, $\epsilon_{r,AlO_x} = 8$, $\epsilon_{r,LaAlO_x} = 16$) and the film thicknesses (78 nm of BeO, 90 nm of $\mathrm{AlO_x}$, and 97 nm of $\mathrm{LaAlO_x}$). For example, Fig. 7.4 shows a COMSOL simulation of the electric field and electric energy distribution for a cross section of the CPS geometry with 2 mV across the electrodes atop a 90 nm ALD $\mathrm{AlO_x}$ film grown on a sapphire wafer. As one would expect, the electric field is symmetric about the vacuum substrate interface, but electric energy of course scales with the permittivity of the substrate. Another factor to consider is that the $\mathrm{LaAlO_x}$ film was also etched by the Aluminum Etch acid used to pattern the aluminum, completely etching away the $\mathrm{LaAlO_x}$ film that was not covered by Al, creating trenches in the $\mathrm{LaAlO_x}$. After this was realized, I adjusted the COMSOL field simulations to account for this (see Fig. 7.5).

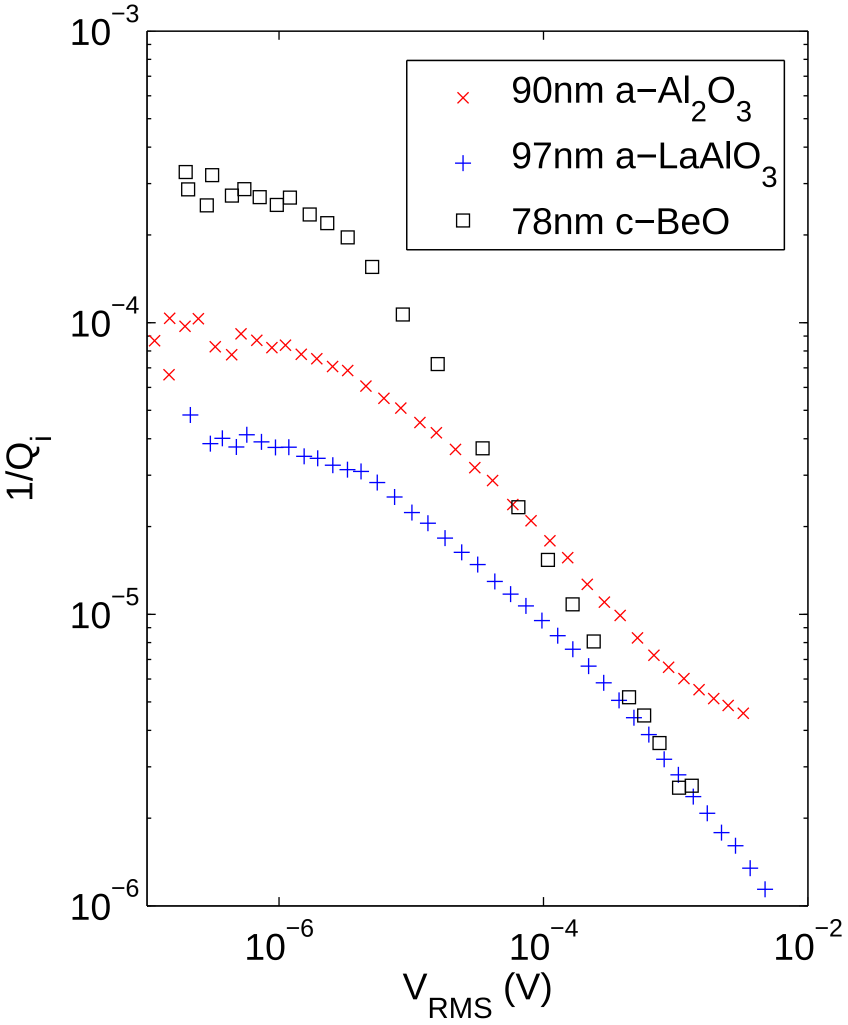

Figure 7.3: Inverse Q_i of coplanar strip resonators on three different ALD grown film types. Data plotted for devices: BeO-CPS, AlO_x-Harv-CPS, and $LaAlO_x$-Harv-CPS.

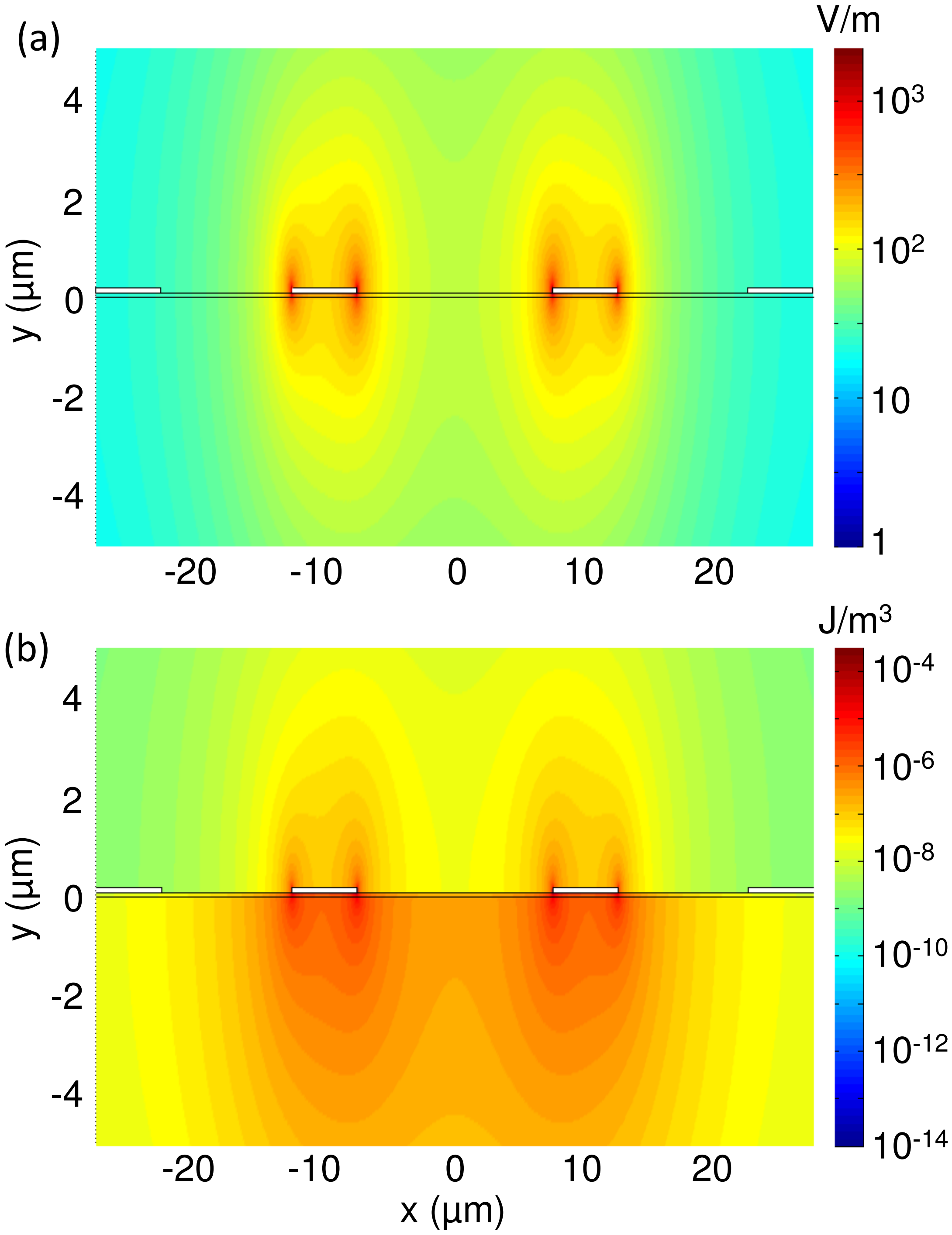

Figure 7.4: (a) COMSOL simulation of electric field distribution for 100 nm thick CPS resonator (with 2 mV across the CPS electrodes) on 90 nm of ALD grown AlO_x atop a sapphire wafer. (b) Electric energy density distribution of (a).

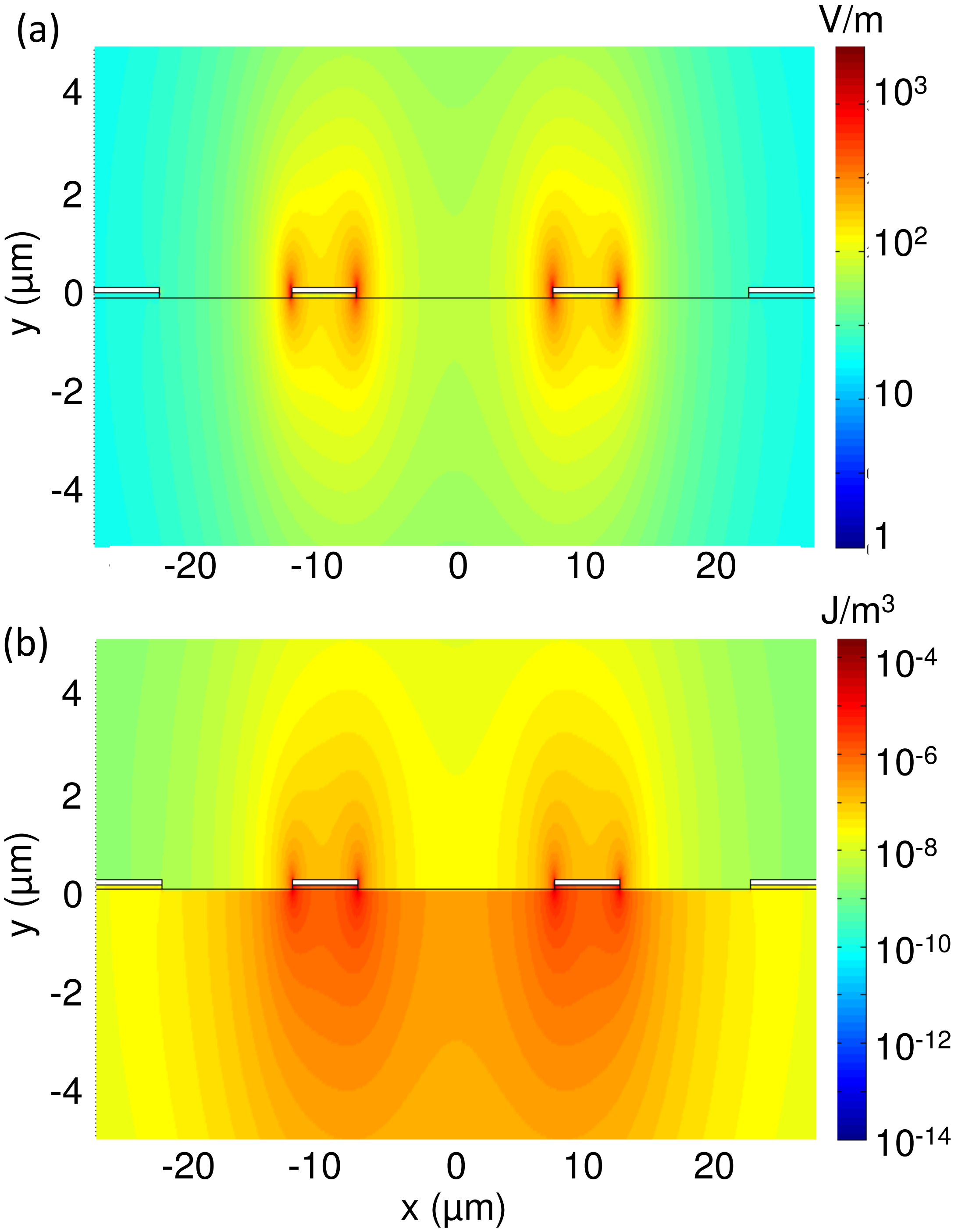

Figure 7.5: (a) COMSOL simulation of electric field distribution for 100 nm thick CPS resonator (with 2 mV across the CPS electrodes) on 97 nm of ALD grown $LaAlO_x$ atop a sapphire wafer. The $LaAlO_x$ is only under the electrodes because elsewhere it was etched away by the aluminum etchant. (b) Electric energy density distribution of (a).

7.2.2 SIMS analysis for ALD dielectrics

Since hydrogen was still the most likely culprit for TLS loss in our ALD films, SIMS measurements were performed on these films to determine the hydrogen impurity concentration. The carbon concentration for the BeO film and the hydrogen concentration for all three film types is plotted as a function of film depth in Fig. 7.6. Examination of the figure shows that there is an 8 times greater concentration in the bulk of the crystalline BeO film than in the amorphous $\mathrm{AlO_x}$ or $\mathrm{LaAlO_x}$ films. In the BeO films the hydrogen is almost uniformly distributed throughout the bulk of the film (although some H diffuses into the Si substrate). In contrast, the amorphous $\mathrm{AlO_x}$ or $\mathrm{LaAlO_x}$ films have a large peak in hydrogen concentration at the surface. This distribution of hydrogen strongly suggests that BeO has incorporated hydrogen during growth with its precursors (dimethyl beryllium and water), while the other oxides have mostly incorporated hydrogen from ambient exposure rather than growth. Figure 7.6 also indicates that there is a high concentration of C impurities in the $\mathrm{c-BeO}$ film, but unlike the hydrogen, it is concentrated on the surface as the impurities in the amorphous films are.

7.2.3 Fitting to CPS Q_i measurements using TLS loss model

Next I discuss fitting the inverse Q_i measurements of the CPS devices using the COMSOL simulated field distributions, SIMS hydrogen impurity measurements, and the TLS loss tangent model,

$$\tan\delta(\vec{r}, E) = \frac{\tan\delta_0 \tanh(\hbar\omega/2k_BT)}{\sqrt{1 + (E(\vec{r})/E_c)^2}}. \tag{7.2}$$

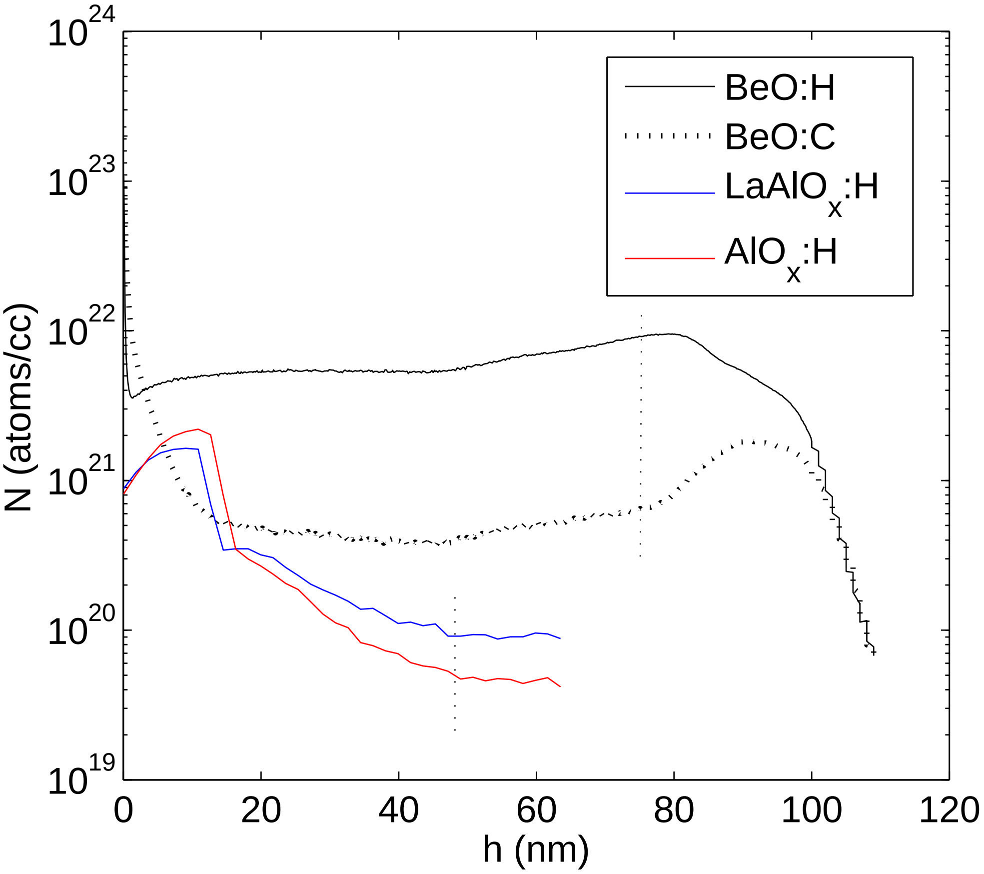

Figure 7.6: Hydrogen impurity concentration measured by SIMS for films with nominally identical parameters to those shown in Fig. 7.3 as well as carbon impurity concentration in BeO film. The crystalline BeO film (75 nm thick) shows a large hydrogen concentration that is nearly uniform throughout the film depth, while the AlO$_x$ and LaAlO$_x$ films (each approximately 48 nm thick) show hydrogen concentrated at the surface of the films. The BeO film also shows a large surface distribution of carbon impurities. Vertical dotted lines indicate film thicknesses.

To do this I started by taking the COMSOL simulated field distribution for the CPS geometry and used the assumption that the field throughout the cross section would scale linearly with the voltage across the electrodes. Knowing the field throughout the resonator geometry I then assumed a $\tan\delta$ and an E_c for the ALD dielectric and that the rest of the volume was lossless . Numerically integrating over the volume for every voltage data point in Fig. 7.3, I could then find:

$$\frac{1}{Q_i(V)} = \frac{\int_{Lossyfilm} \tan\delta(\vec{r}, E)\epsilon_{film}(E(\vec{r}, V))^2 d^3r}{\int_{All} \epsilon(\vec{r})(E(\vec{r}))^2 d^3r}, \tag{7.3}$$

remembering of course to also integrate over the entire length of the CPS (z) with

$$V_{cps}(z) = V_0 \sin(\frac{\pi}{2}\frac{z}{l_{cps}}), \tag{7.4}$$

where $l_{cps} = 4.8$ mm.

Figure 7.7 shows the inverse Q_i data from Fig. 7.3 with loss tangent fits. Not surprisingly when considering the impurity distribution in Fig. 7.6, for the two amorphous films, a single bulk loss term representing the film thickness was insufficient to fit Q_i and an independent surface-loss mechanism was added. I assumed the thickness of the lossy material at the surface was 5 nm. The fit parameters for the curves in Fig. 7.7 are shown in Table 7.1. As expected from the SIMS measurements in Fig. 7.6, I found that the dominant loss occurs in the bulk of the crystalline BeO film and the surface of the amorphous $\mathrm{AlO_x}$ or $\mathrm{LaAlO_x}$ films. A relatively small background loss term was also included in the fit and labeled as the floor in Table 7.1. This power-independent background loss is similar to that discussed earlier and present in coplanar resonator measurements on bare substrate.

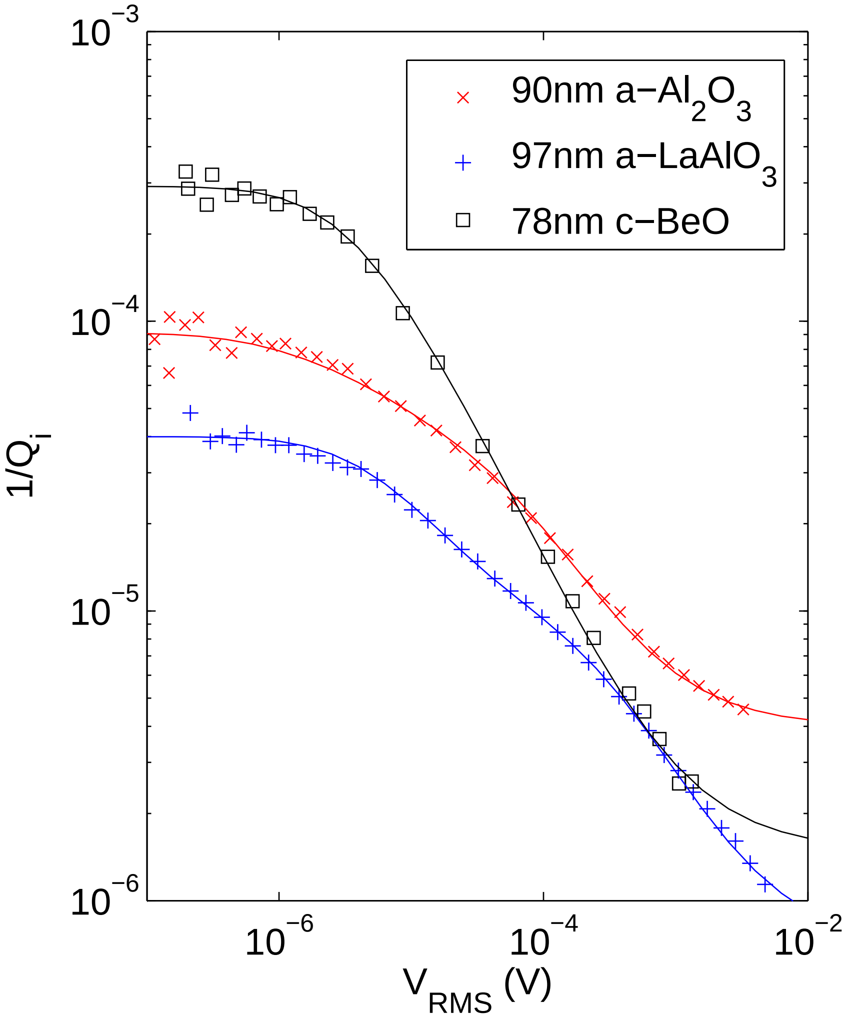

Figure 7.7: Data points same $1/Q_i$ data plotted in Fig. 7.3 solid curves are fits to the TLS loss expression (Eq. 7.2) for the CPS resonator (6.4 GHz) geometry with the fit parameters from Table 7.1. Measurements were taken at 34 mK.

Table 7.1: Fit parameters for the curves in Fig. 7.7. The bold values correspond to the dominant loss terms of the films, in the surface of the amorphous films and the bulk of the crystalline film. All films were fit assuming a bulk loss value, a floor limited by extrinsic effects, and amorphous $\mathrm{AlO_x}$ or $\mathrm{LaAlO_x}$ films were fit with an additional 5 nm thickness of lossy material at the top surface. Films were measured at 34 mK with 6.4 GHz CPS resonator.

Fit parameters	**BeO**	$\mathbf{AlO_x}$	$\mathbf{LaAlO_x}$
$\tan\delta_{0,surface}(\times 10^{-3})$	-	**13.0**	**4.5**
$E_{c,surface}(\mathrm{V/m})$	-	**0.75**	**0.55**
$\tan\delta_{0,bulk}(\times 10^{-3})$	**6.2**	0.70	1.1
$E_{c,bulk}(\mathrm{V/m})$	**0.70**	5.9	60
$\tan\delta_{0,floor}(\times 10^{-6})$	32	4.0	0.68
thickness (nm)	78	90	97

The results from these fits also indicate that despite the high carbon impurity concentration shown in Fig. 7.6, carbon impurities are unlikely to be the cause of TLS loss in the film. This is because unlike the hydrogen impurities in the film, the carbon impurities are concentrated at the surface and so would have resulted in a measureable surface loss term as the amorphous films did.

The BeO loss measurements indicate that TLS defects are not limited to amorphous materials and can in fact have an even greater effect in crystalline materials. This reduces the parameter space available in searching for a TLS micromechanism, perhaps simplifying the task of modeling and identifying it.

7.3 Surface Loss effects in ALD grown AlO_x

To verify that the AlO_x loss tangent was dominated by surface defects, I measured two films that were nominally identical in every way except for their thicknesses. Figure 7.8 shows the inverse Q_i measurement of the resonators on two films with 48 and 90 nm thicknesses measured at 34 mK. The idea is that if the TLS were uniformly distributed in the dielectric, then the Q_i of the resonator would differ by a factor of 1.7, scaling linearly with the electric energy stored in the film thickness. Instead, the quality factor of the resonators matches to within 15% at the low-voltage limit, consistent with loss that is primarily at the surface. I note that the development of *in situ* deposition of dielectrics within MIM trilayer structures would greatly reduce such surface loss [72].

7.4 Hydrogen vs Carbon TLS analysis

One of the most common impurities in ALD films is carbon due to incomplete reaction of the organometallic precursors. In the case of AlO_x the precursor is trimethylaluminum. I therefore had SIMS measurements performed for both carbon and hydrogen impurities in AlO_x films grown in separate ALD chambers in separate labs, but with the same precursors. Figure 7.9 shows the integration of hydrogen and carbon impurities over the thickness of the films. The Lab 1 film from the Rubloff group at the University of Maryland has a much higher (40 times greater) carbon defect concentration than that of Lab 2 from the Gordon group at Harvard. We also measured CPS resonators on these films and found them to have very similar

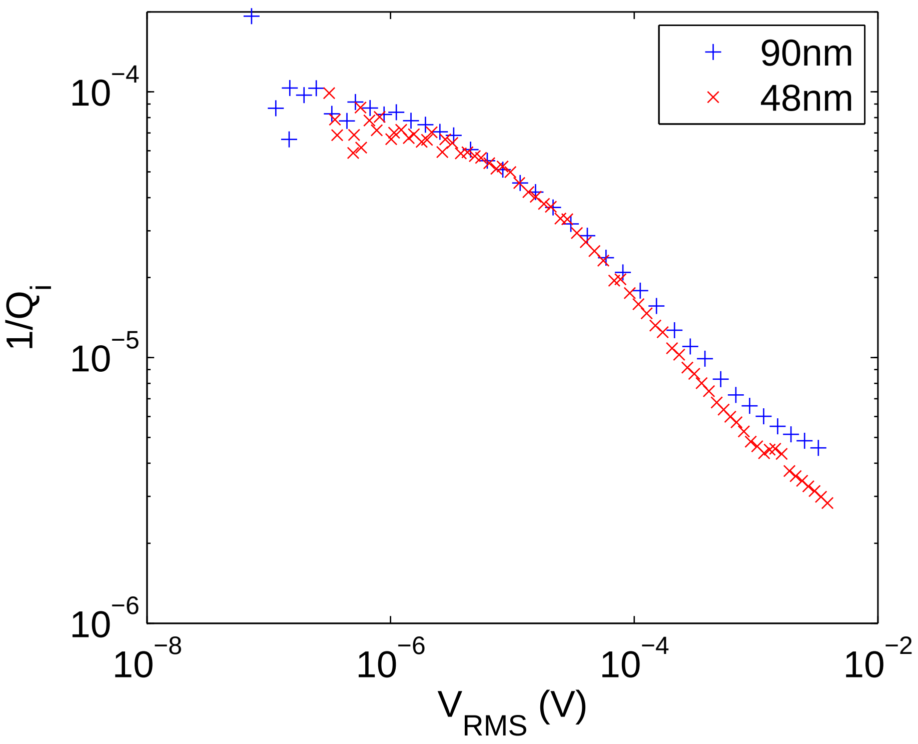

Figure 7.8: plot of $1/Q_i$ vs. voltage of the CPS resonators measured on nominally the same AlO_x films grown in the same chamber but to two different thicknesses. Because the loss is primarily at the surface, the quality factor of the two devices is practically identical and does not scale with the thickness of the film.

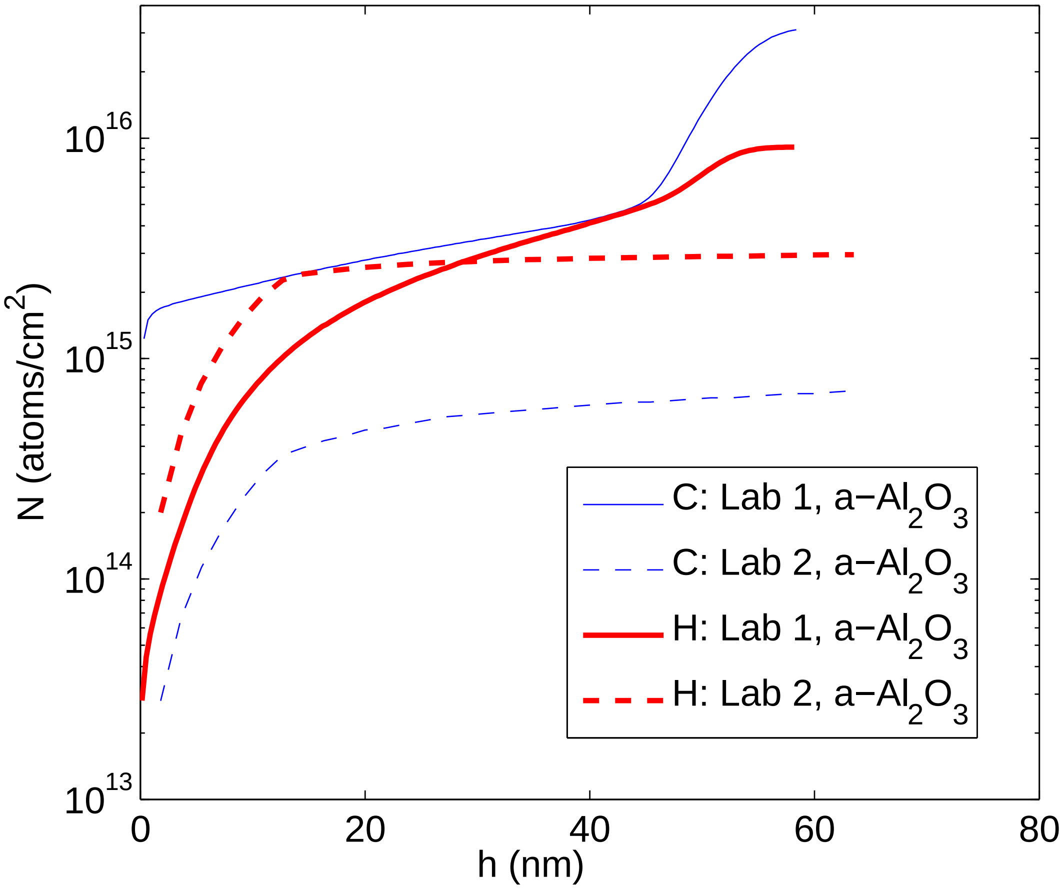

Figure 7.9: Integrated hydrogen and carbon concentration from the surface (0 nm) downward in ALD aluminum oxide films from different labs (Lab 1=Rubloff Lab 2 = Gordon) as measured by SIMS. They show similar hydrogen concentration but the film from Lab 1 shows a much greater carbon concentration. Since the two films have similar loss but very different carbon concentrations, C-based TLSs can be eliminated as a candidate for TLS loss in this regime.

Q_i's, indicating that carbon plays a negligible role in the TLS loss. From Fig. 7.9 we see that hydrogen is a much more viable TLS candidate.

To quantitatively analyze H and C impurities as TLS candidates we assume that the loss tangent for each type of impurity tangent,

$$\tan \delta_{0,x}(\vec{r}) = K_x C_x(\vec{r}), \tag{7.5}$$

is proportional to the impurity concentration $C_x(\vec{r})$ of species x, where K_x is a TLS-loss proportionality constant. Assuming defect x limits the resonator's loss, the low-voltage-amplitude internal quality factor of the film is then

$$\frac{1}{Q_i(V \to 0)} = K_x \langle C_x \rangle F_{film} W_x, \tag{7.6}$$

where $\langle C_x \rangle$ is the average impurity concentration

$$\langle C_x \rangle = \frac{\int_{film} d^3 r C_x(\vec{r})}{\int_{film} d^3 r}, \tag{7.7}$$

F_{film} is the geometric filling factor,

$$F_{film} = \frac{\int_{film} d^3 r \epsilon(\vec{r}) |E(\vec{r})|^2}{\int_{all} d^3 r \epsilon(\vec{r}) |E(\vec{r})|^2}, \tag{7.8}$$

and W_x is impurity weighting coefficient,

$$W_x = \frac{\int_{film} d^3 r \epsilon(\vec{r}) |E(\vec{r})|^2 C_x(\vec{r})}{\langle C_x \rangle \int_{film} d^3 r \epsilon(\vec{r}) |E(\vec{r})|^2}. \tag{7.9}$$

Note that $F_{film} = 1$ for a device with a single dielectric and $W_x = 1$ for a uniform impurity distribution. $W_{H,C}$ can be calculated from the SIMS measurements shown in Fig. 7.9 and F_{film} can be calculated by numerically integrating the energy density of the COMSOL field simulations for the ALD film. Note that instead of defining the

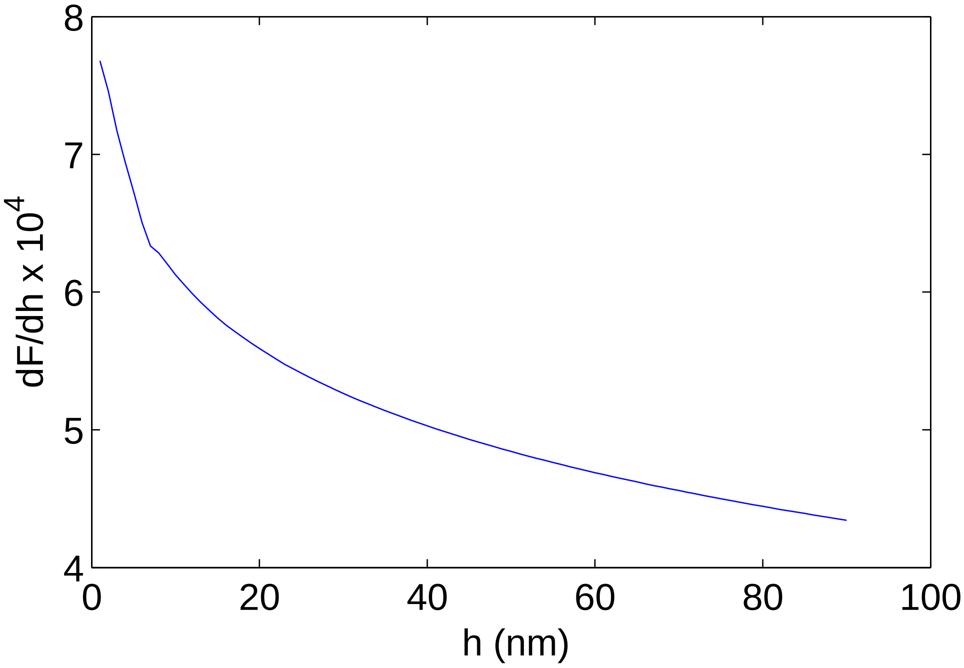

Figure 7.10: Numerically integrated filling factor for each nm depth slice of a 90 nm film of $\mathrm{AlO_x}$ under the CPS resonator geometry as a function of the film depth.

filling factor over the entire film depth, it can instead be defined over any arbitrary thickness of the film, so with that in mind I define

$$F(h) \equiv \frac{\int\int dxdy \int_0^h dh \epsilon(\vec{r})|E(\vec{r})|^2}{\int_{all} d^3r \epsilon(\vec{r})|E(\vec{r})|^2}, \tag{7.10}$$

where $h = 0$ is defined as the surface of the film and h_f is the film thickness, such that $F(h_f) = F_{film}$. In Fig. 7.10 I've plotted the filling factor depth derivative as a function of the depth below the CPS resonator with 1 nm resolution, as calculated by a numerical integration from the COMSOL field simulations.

In Fig. 7.11 I've plotted $1/(Q_i F W_H \langle C_H \rangle)$ and $1/(Q_i F W_C \langle C_C \rangle)$ for the two films as a function of the microwave voltage using the measured values of Q_i (at 80 mK) and C_H/C_C, as well as the simulated field distributions for W_H/W_C and F. If we assume hydrogen impurities are the dominant cause of TLS-loss, at low field values, I've found that the two films from different labs have $K_H = 3 \times 10^{-24}\ cm^3$ to within 50%. However, as made clear by Fig. 7.11, if we instead assume carbon impurities are the dominant cause of TLS-loss, the two films would produce drastically different values for K_H, differing by more than a factor of 30, indicating that carbon is not the dominant source of TLS loss in this experiment. This provides evidence that oxide films can be optimized for low temperature devices by lowering their hydrogen concentration.

7.5 Conclusion

In conclusion, I measured the loss of several ALD grown dielectric oxide films at millikelvin temperatures using the coplanar superconducting resonators discussed in chapter 4. By using deuterated water to grow $\mathrm{AlO_x}$ films, we reduced the amount of hydrogen in the film but were not able to correlate that reduction in hydrogen concentration with a change in low temperature microwave loss, possibly because deuterium also causes TLS loss.

In addition, I found that the TLS loss of the crystalline film, BeO, was higher than that of the amorphous films, $\mathrm{AlO_x}$ and $\mathrm{LaAlO_x}$, despite the fact that BeO is crystalline and has been shown to have low-loss at room temperature with high thermal conductivity at low temperatures. Using SIMS measurements I correlated the low temperature loss with excess hydrogen defects on the surface of the amorphous

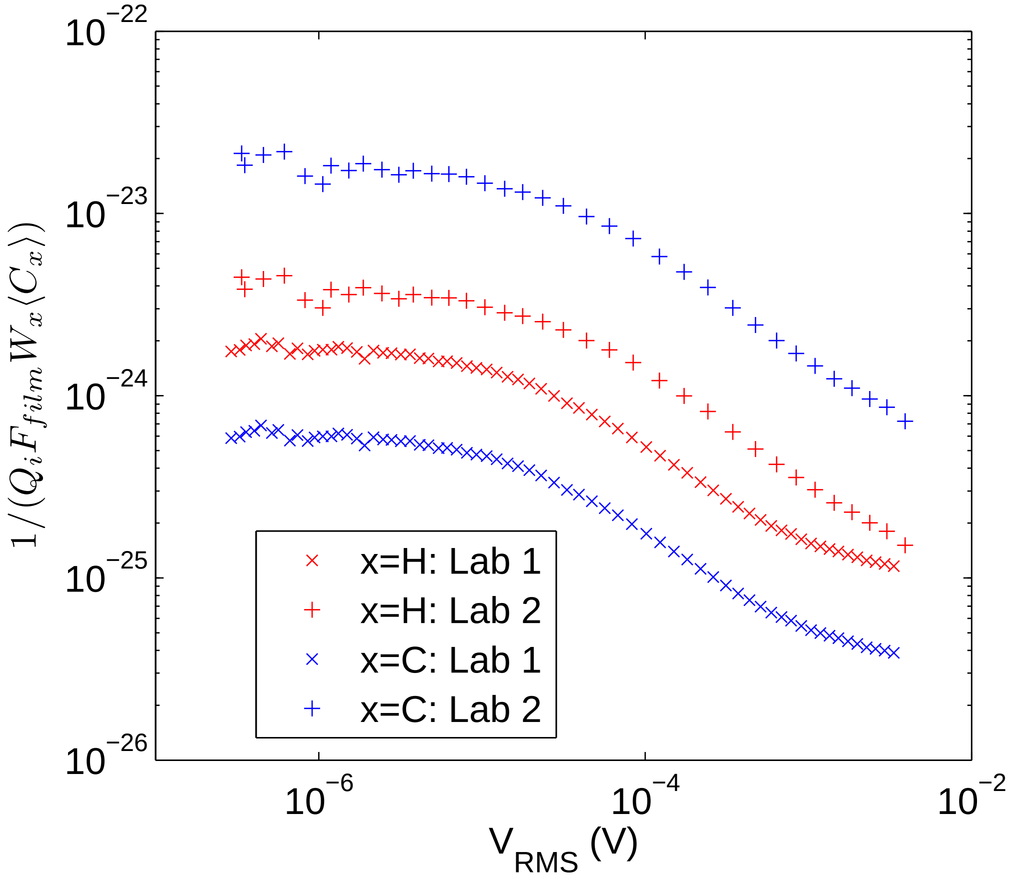

Figure 7.11: Measurements of $1/(Q_i F W_{H,C} \langle C_{H,C} \rangle)$ assuming H or C impurities are the main cause of TLS loss. At low fields this reduces to the proportionality constant of hydrogen impurities to loss tangent, $K_{H,C}$. Since assuming hydrogen impurities are the dominant cause of TLS loss results in consistent K_H between the two labs, it's a much more likely TLS candidate than carbon.

films and in the bulk of the crystalline film. The BeO film had a uniform bulk loss tangent with no excess surface loss consistent with its uniform H impurity concentration and inconsistent with its excess surface C impurity concentration, excluding C as a TLS candidate in BeO. In $\mathrm{AlO_x}$ and $\mathrm{LaAlO_x}$ films, the bulk loss tangent was found to be similar, but the surface loss dominated indicating that the loss tangent was limited by surface impurities, likely hydrogen. A thickness study of $\mathrm{AlO_x}$ films confirmed that the majority of the loss was on the surface. By testing $\mathrm{AlO_x}$ with different carbon concentrations, I found that carbon has a negligible effect on TLS loss. I conclude that various low temperature oxides can be optimized via rapid room temperature measurements of hydrogen.

Chapter 8

Biased resonator

8.1 Biasing TLSs

Once a linear resonator is fabricated, its resonance frequency is determined and is a physical characteristic of the device. In contrast, a Josephson junction acting as a tunable nonlinear inductor allows for tuning of the resonance frequency, such as in the Josephson Junction Defect Spectrometer, but for linear resonators, this cannot be done. However, it is possible is to tune the TLSs that are couple to the resonator, moving them in and out of the resonator's bandwidth. In this chapter, I discuss such an experiment.

As discussed in Chapter 2, the TLS asymmetry energy, Δ, couples to an applied electric field $\vec{E}_{Bias}$ through the TLS's dipole p according to

$$\Delta = \Delta_{E=0} + 2\vec{E}_{Bias} \cdot \vec{p}. \tag{8.1}$$

Since an applied field's effect on the tunneling rate, Δ_0, can generally be neglected we can write the TLS's energy as

$$\mathcal{E} = \sqrt{\Delta_0^2 + |\Delta_{old} + 2\vec{E}_{Bias} \cdot \vec{p}|^2}. \tag{8.2}$$

One implication of Eq. 8.2 is that if we applied an additional bias field to the dielectric, independent of the microwave probe field, we could bias TLSs out of the resonator's bandwidth so they can no longer couple to the resonator, and limit its loss. However, we also know from Chapter 2 that the standard distribution of TLSs is white in Δ:

$$d^2N = \frac{P_0}{\Delta_0} d\Delta d\Delta_0. \tag{8.3}$$

Thus on average the same number of TLSs would be biased into the resonator's bandwidth as were biased out resulting in a similar TLS loss tangent within statistical fluctuations. If a bias field could be applied with a sufficiently high amplitude, such an experiment could act as a check on the limits of the uniformity of the Δ distribution. Similarly, if the distribution is sufficiently narrow, we could polarize most of the TLSs out of the resonator's bandwidth and significantly lower the loss.

8.2 Previous bias measurements

Experiments have previously tried to measure the response of a glassy dielectric in the low-frequency regime ($\hbar\omega \ll k_B T$) after it was driven out of equilibrium. It was found that after the application of either a static electric field or strain field, there was a sudden increase in the permittivity of glassy dielectrics, followed by a subsequent slow logarithmic relaxation back to the equilibrium permittivity [79, 80, 81]. It was also found that there was a persistent change in permittivity at a previously applied bias field value [79]. This memory effect was explained by TLS-TLS interactions causing a pseudogap which decreased the density of TLSs at energies bellow 20 GHz [82, 83]. The sudden increase in permittivity was attributed to the biasing of TLSs by the dc field and closing of the pseudogap, thus increasing the density of low-frequency TLSs, while the subsequent relaxation was explained by the reforming of the gap via long-range TLS-TLS interactions. This led to a better understanding of TLSs and amorphous dielectrics in general. More recently the biasing of individual TLSs with strain has been observed in Josephson junctions [84].

8.3 Swept bias

After performing the experiments described in the next chapter, Professor A. Burin derived the theory I discuss next to explain the data [85].

As mentioned earlier, if the TLS distribution is completely white in the asymmetry energy, then a change in the bias field would have no effect on the resonator's loss because on average the same number of TLSs would remain in the resonator. However, even without a change in the TLS density, if a swept bias field is used, a change in the measured loss tangent of a material should be expected. Qualitatively this is because if the TLSs are biased fast enough, they can take energy away from the resonator not only through their own relaxation but also through the bias.

To understand this quantitatively, we first define the energy of a TLS that is being swept through the resonator's frequency,

$$\mathcal{E}(t) = \hbar\omega_0 + \hbar\nu(t - t_0) \tag{8.4}$$

where ν is the energy bias rate of the TLS and t_0 is the time when the TLS passes the resonator's frequency ω_0. Expanding Eq. 8.2 around small shifts in Δ (because we're only interested in TLSs close to resonance) gives the energy bias rate

$$\nu = 2\sqrt{1 - \left(\frac{\Delta_0^2}{\hbar\omega}\right)^2}\frac{p}{\hbar}\frac{dE_{bias}}{dt}\cos\theta = \nu_0\sqrt{1 - \left(\frac{\Delta_0^2}{\hbar\omega}\right)^2}\cos\theta \tag{8.5}$$

where θ is the angle between the dipole moment and the field and ν_0 is the ensemble TLS energy bias rate

$$\nu_0 = 2\frac{p}{\hbar}\frac{dE_{bias}}{dt}. \tag{8.6}$$

Note that ν has dimensions of frequency squared or more intuitively frequency per second because it's effectively the velocity at which the TLS's energy is biased.

Schrodinger's equation for a TLS in a resonant field with states $\psi = (c_1, c_2)$ can be written as

$$\begin{aligned} \frac{dc_1}{dt} &= -i\mathcal{E}(t)c_1/2 - i\Omega_R\cos(\omega t)c_2, \\ \frac{dc_2}{dt} &= i\mathcal{E}(t)c_2/2 - i\Omega_R\cos(\omega t)c_1, \end{aligned} \tag{8.7}$$

where, Ω_R is the Rabi frequency of the TLS

$$\Omega_R = \frac{pE_{ac}}{\hbar}\cos\theta\frac{\Delta_0}{\mathcal{E}} = \Omega_{R0}\cos\theta\frac{\Delta_0}{\mathcal{E}}, \tag{8.8}$$

Ω_{R0} is the ensemble TLS Rabi frequency, and c_1 (c_2) is the amplitude of being in the ground (excited) state of the TLS. If we make a transformation into a new basis $(a_1, a_2) = (c_1e^{i\omega t}, c_2e^{i\omega t})$, Eq. 8.7 becomes

$$\begin{aligned} \frac{da_1}{dt} &= -i\left(\mathcal{E}(t) - \hbar\omega\right)\frac{a_1}{2} - i\frac{\Omega_R}{2}a_2 - i\frac{\Omega_R}{2}a_2e^{2i\omega t}, \\ \frac{da_2}{dt} &= i\left(\mathcal{E}(t) - \hbar\omega\right)\frac{a_2}{2} - i\frac{\Omega_R}{2}a_1 - i\frac{\Omega_R}{2}a_1e^{2i\omega t}. \end{aligned} \tag{8.9}$$

Using the rotating wave approximation, we can neglect the last term because it's oscillating much faster than the rest of the expression. Thus Eq. 8.9 becomes

$$\begin{aligned} \frac{da_1}{dt} &= -i\frac{\nu(t-t_0)}{2}a_1 - i\frac{\Omega_R}{2}a_2, \\ \frac{da_2}{dt} &= i\frac{\nu(t-t_0)}{2}a_2 - i\frac{\Omega_R}{2}a_1, \end{aligned} \tag{8.10}$$

where I've also substituted in Eq. 8.4.

Here we can recognize that Eq. 8.10 is identical to the equation for a Landau-Zener transition of a two-level quantum system (see Fig. 8.1) [86, 87]. We know from the Landau-Zener problem that if at $t = -\infty$, only the ground state is populated $|a_1|^2 = 1$, $|a_2|^2 = 0$ then long after the TLS crossing, $t = \infty$, we have

$$\begin{aligned} |a_1|^2 &= \exp(-\frac{\pi\Omega_R^2}{2\nu}), \\ |a_2|^2 &= 1 - \exp(-\frac{\pi\Omega_R^2}{2\nu}). \end{aligned} \tag{8.11}$$

Thus for fast bias ($\nu \gg \Omega_R^2$) the TLS crosses the resonance while staying it its ground state (green to blue in Fig. 8.1) and for slow bias the TLS transitions into its excited state (green to red in Fig. 8.1), following the bottom path in Fig. 8.1.

Using Eq. 8.11 for the probability of making a Landau-Zener transition we can derive an expression for the bias rate induced loss. We first define the tunneling rate as $\Delta_0 = x\hbar\omega$, allowing us to write the Rabi frequency as $\Omega_R = xpE_{ac}\cos(\theta)/\hbar$ and the bias rate as $\nu = 2p\dot{E}_{bias}\cos(\theta)\sqrt{1-x^2}$, where θ is the angle between the dipole moment and the external field. We know from the Landau-Zener formula that the probability of a TLS excitation is $P_{ex} = 1 - e^{-\gamma}$, where $\gamma = \pi\Omega_R^2/(2\nu)$ is the dimensionless Landau-Zener parameter from Eq. 8.11. So the energy lost from the bias integrated over the entire volume of the dielectric is

$$dE = \hbar\omega \int d^3r \int dN P_{ex}, \tag{8.12}$$

where the $\hbar\omega$ comes from the fact that that's the amount of energy lost every time a TLS is excited when crossing the resonance bandwidth and the integral over dN

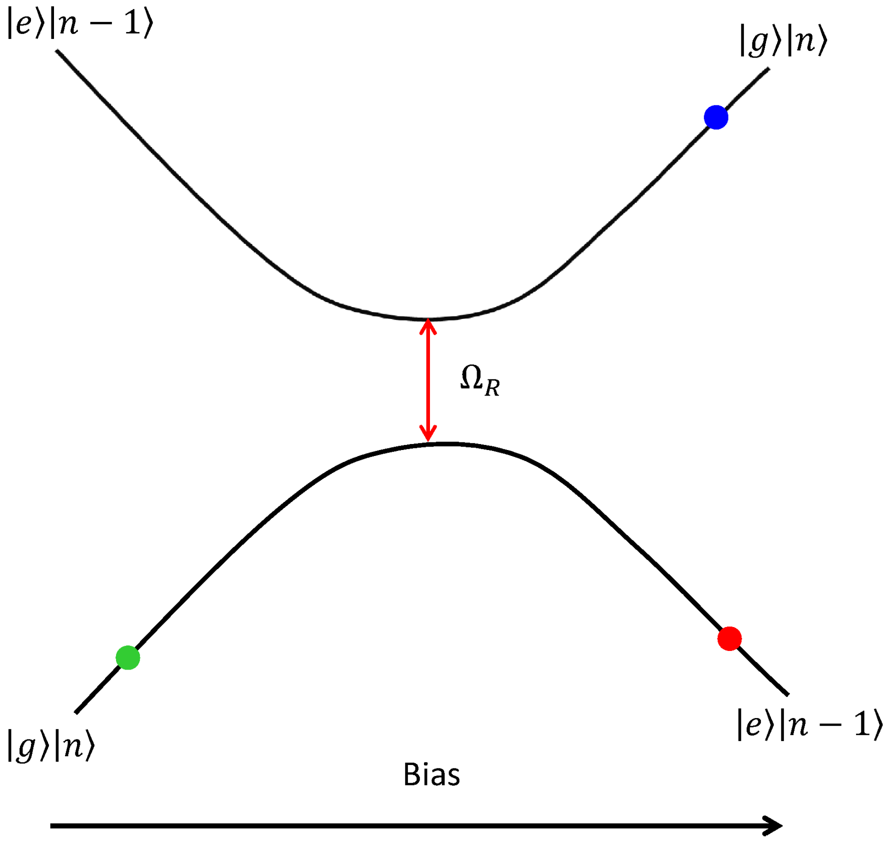

Figure 8.1: TLS-resonator energy spectrum as the TLS is biased across the resonance frequency of the resonator. If biased quickly it is likely to stay in the ground state not coupling to the resonator (green to blue TLS). If biased slowly enough it's likely to couple to the resonator and be pumped up to its excited state, taking a photon away from the resonator, thus $|n\rangle \rightarrow |n-1\rangle$ (green to red TLS).

is only preformed over the TLSs that cross the resonance frequency. Expanding the integral over the TLSs in Eq. 8.12, we have

$$dE = \hbar\omega P_0 \mathrm{V} \int_0^1 d\cos(\theta) \int\int (1-e^{-\gamma}) \frac{d\Delta d\Delta_0}{\Delta_0}, \tag{8.13}$$

where we are integrating over dipole angles θ in addition to the asymmetry energies Δ and tunneling rates Δ_0, and the d^3r integral over volume (V) has been performed. Next it is convenient to convert the integral of Δ into an integral over TLS energy $\mathcal{E} = \sqrt{\Delta^2 + \Delta_0^2}$ in order to more easily set a limit on the TLSs crossing the resonance,

$$dE = \hbar\omega P_0 \mathrm{V} \int_0^1 d\cos(\theta) \int_0^{\hbar\omega} d\Delta_0 \int_{\hbar\omega - \hbar\nu dt}^{\hbar\omega + \hbar\nu dt} d\mathcal{E} \frac{(1-e^{-\gamma})\mathcal{E}}{\Delta_0\sqrt{\mathcal{E}^2 - \Delta_0^2}}, \tag{8.14}$$

where the bias is assumed to be on for a time period dt only TLSs with energies $\hbar\nu dt$ away from the resonance frequency will cross it. The integral over $\mathcal{E}$ can be evaluated as a Dirac delta function at $\hbar\omega$ with magnitude $2\hbar\nu dt$

$$dE = \hbar\omega P_0 \mathrm{V} \int_0^1 d\cos(\theta) \int_0^{\hbar\omega} 2\hbar\nu dt (1-e^{-\gamma}) \frac{\hbar\omega d\Delta_0}{\Delta_0\sqrt{(\hbar\omega)^2 - \Delta_0^2}}. \tag{8.15}$$

Next substituting $x\hbar\omega$ in for Δ_0 we have

$$\frac{dE}{dt} = 2\hbar^2\omega P_0 \mathrm{V} \int_0^1 d\cos(\theta) \int_0^1 \nu(1-e^{-\gamma}) \frac{dx}{x\sqrt{1-x^2}}. \tag{8.16}$$

Expressing the bias rate $\nu = 2p\dot{E}_{bias}\cos(\theta)\sqrt{1-x^2}$ in terms of the dimensionless Landau-Zener parameter γ gives

$$\begin{aligned} \frac{dE}{dt} &= 2\hbar^2\omega P_0 \mathrm{V} \int_0^1 d\cos(\theta) \int_0^1 \frac{\pi\Omega_R^2}{2\gamma}(1-e^{-\gamma}) \frac{dx}{x\sqrt{1-x^2}} \\ &= \pi\omega E_{ac}^2 P_0 p^2 \mathrm{V} \int_0^1 d\cos(\theta)\cos^2(\theta) \int_0^1 \frac{(1-e^{-\gamma})}{\gamma} \frac{x dx}{\sqrt{1-x^2}}. \end{aligned} \tag{8.17}$$

Next using the definition of loss tangent (or quality factor) I can define the loss tangent in terms of dE/dt

$$\tan\delta = \frac{\text{Power loss rate}}{\omega(\text{Energy stored in resonator})} = \frac{dE/dt}{\omega\epsilon E_{ac}^2 \mathrm{V}}. \tag{8.18}$$

Combining Eq. 8.17 and Eq. 8.18 gives

$$\tan\delta = \frac{\pi P_0 p^2}{\epsilon}\int_0^1 d\cos(\theta)\cos^2(\theta)\int_0^1 \frac{(1-e^{-\gamma})}{\gamma}\frac{xdx}{\sqrt{1-x^2}}. \tag{8.19}$$

Here we recognize from previous discussions of TLS loss that Eq. 8.19 can be rewritten as

$$\tan\delta = 3\tan\delta_0\int_0^1 d\cos(\theta)\cos^2(\theta)\int_0^1 \frac{(1-e^{-\gamma})}{\gamma}\frac{xdx}{\sqrt{1-x^2}}, \tag{8.20}$$

where $\tan\delta_0 = \pi P_0 p^2/(3\epsilon)$ is the intrinsic TLS loss without electric field or thermal saturation. Here it's useful to also remind ourselves of the electric field saturated TLS loss tangent

$$\tan(\delta) = \tan\delta_0 \frac{\tanh(\hbar\omega/2k_BT)}{\sqrt{1+(E_{ac}/E_c)^2}}. \tag{8.21}$$

In the limit of fast bias ($\nu \gg \Omega_R^2$) we can use the approximation $e^{-\gamma} \simeq 1-\gamma$ which simplifies Eq. 8.20 and makes its evaluation trivial

$$\tan\delta = 3\tan\delta_0\int_0^1 d\cos(\theta)\cos^2(\theta)\int_0^1 \frac{xdx}{\sqrt{1-x^2}} = \tan\delta_0, \tag{8.22}$$

thus reducing the loss tangent to its intrinsic low E_{ac} value as given by Eq. 9.1. This is obviously not a coincidence. A qualitative way to understand this is that in this limit, almost all of the TLSs passing through resonance remain in their ground state so the resonator effectively sees a bath of ground state TLSs ready to absorb a photon as in the low ac field limit. A slightly more comprehensive explanation for this phenomena is that as the bias rate increases, proportionally more TLSs are being swept through the Landau-Zener region in each unit of time. Since the TLSs are in the ground state they are all capable of absorbing power. However, the higher the bias rate, the faster a given TLS will cross through the Landau-Zener transition region, and the smaller the probability of the TLS absorbing energy from the resonator and being left in its excited state. These two effects conspire to yield the intrinsic low ac field loss tangent.

We note here that we've neglected TLS relaxation for this derivation ($T_1 = T_2 = \infty$). So the loss calculated thus far comes entirely from energy lost to the system through the bias and does not include the possibility that an excited TLS can lose energy and be available to absorb more from the resonator. This assumption will of course fail for sufficiently fast TLS relaxation. The crossover occurs when a TLS is likely to decohere during the time it takes it to pass through the resonance i.e. for $\nu \sim \Omega_R/\tau$, where $\tau \approx \sqrt{T_{1,min}T_2}$ is a characteristic TLS lifetime. Thus for sufficiently slow biases, TLS relaxation dominates and the loss tangent reduces to the steady state value given by Eq. 9.1.

In the regime where the bias is sufficiently fast $\nu \gg \Omega_R/\tau$ such that the loss limited by the bias rate, Eq. 8.20 can be evaluated numerically. The numerical solution is plotted in Fig. 8.2 as a function of the dimensionless bias rate

$$\xi = \frac{2\nu_0}{\pi\Omega_{R0}^2}. \tag{8.23}$$

As discussed earlier the blue curve in Fig. 8.2 is only applicable at high bias rates and will fail at lower bias rates where the loss is limited by TLS relaxation.

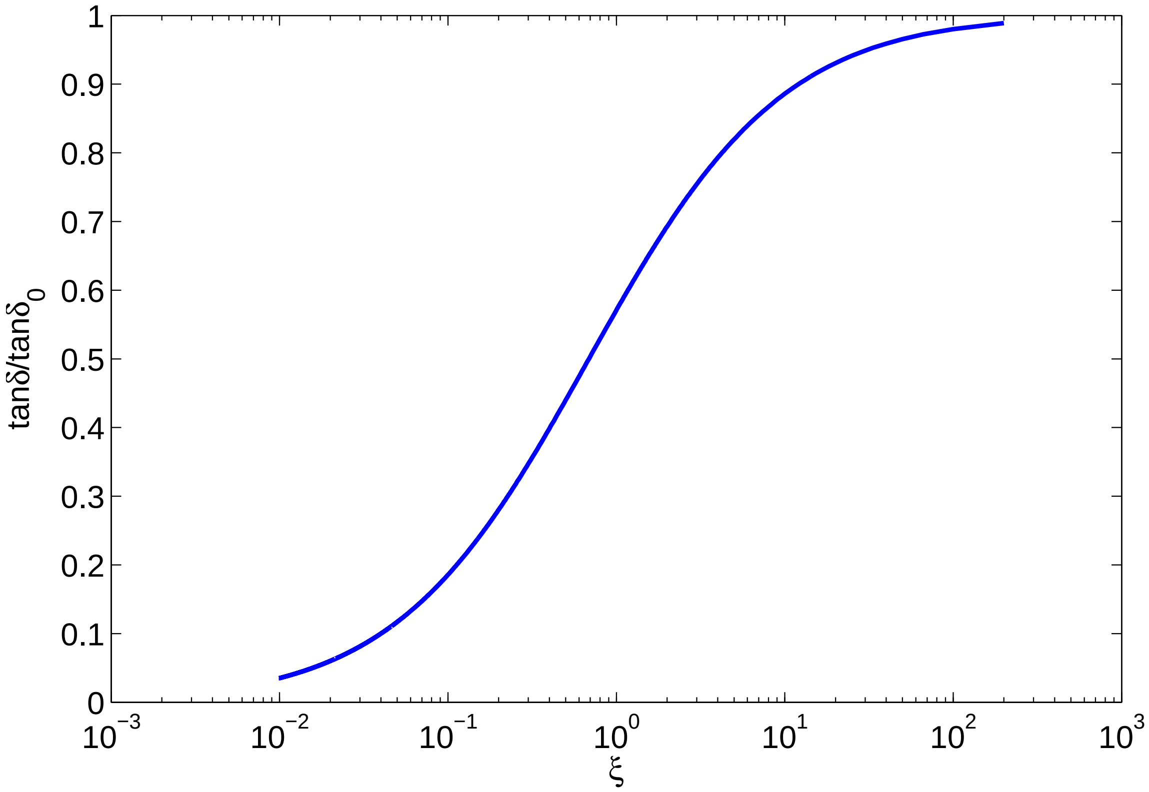

Figure 8.2: Plot of $\tan\delta/\tan\delta_0$ as a function of the dimensionless bias rate $\xi = 2\nu_0/(\pi\Omega^2_{R0})$ found by evaluating Eq. 8.20 numerically.

The crossover at low bias sweep rate is dependent on the Rabi frequency and the TLS lifetime $\nu_0 \sim \Omega_{R0}/\tau$. Thus given a Rabi frequency and a TLS lifetime, we can calculate the characteristic dimensionless bias rate $\xi_c = 1/(\Omega_{R0}\tau)$ below which TLS relaxations dominate and the blue curve in Fig. 8.2 is no longer applicable.

8.4 Monte Carlo simulations

One way to address the behavior of a random distribution of TLSs coupled to a cavity is through a Monte Carlo simulation. It involves choosing a set of TLSs with the right distribution, turning on a field similar that which exists in the cavity and calculating the coupling of the TLSs to the field. Some advantages of this approach are that it allows me to include T_1 and T_2 effects, and examine statistical fluctuations resulting from using a finite number of TLSs.

8.4.1 Theory for Monte Carlo simulations

As discussed in Chapter 2, the Hamiltonian of a single TLS in an electric field can be split into the Hamiltonian of the TLS in its eigenbasis

$$\mathcal{H}_0 = \frac{1}{2}\begin{pmatrix} \mathcal{E} & 0 \\ 0 & -\mathcal{E} \end{pmatrix}, \tag{8.24}$$

and the perturbation Hamiltonian due to interaction with the applied electric field

$$\mathcal{H}_S = \frac{1}{\mathcal{E}}\begin{pmatrix} \Delta & \Delta_0 \\ \Delta_0 & -\Delta \end{pmatrix}(\vec{p}\cdot\vec{E}). \tag{8.25}$$

The total Hamiltonian is then

$$\mathcal{H} = \mathcal{H}_0 + \mathcal{H}_S. \tag{8.26}$$

We know from the Heisenberg equation of motion that

$$i\hbar\dot{\rho} = [\mathcal{H}, \rho], \tag{8.27}$$

where ρ is the TLS density matrix. By combining Eqs. 8.24-8.27 for a single TLS we can write the set of equations

$$\begin{aligned}
i\hbar\dot{\rho}_{00} &= (\rho_{01} - \rho_{10})\frac{\Delta_0}{\mathcal{E}}\vec{p}\cdot\vec{E} \\
i\hbar\dot{\rho}_{01} &= \rho_{00}\frac{\Delta_0}{\mathcal{E}}\vec{p}\cdot\vec{E} + \rho_{01}\left(\mathcal{E} + 2\frac{\Delta}{\mathcal{E}}\vec{p}\cdot\vec{E}\right) - \rho_{11}\frac{\Delta_0}{\mathcal{E}}\vec{p}\cdot\vec{E} \\
i\hbar\dot{\rho}_{10} &= -\rho_{00}\frac{\Delta_0}{\mathcal{E}}\vec{p}\cdot\vec{E} - \rho_{10}\left(\mathcal{E} + 2\frac{\Delta}{\mathcal{E}}\vec{p}\cdot\vec{E}\right) + \rho_{11}\frac{\Delta_0}{\mathcal{E}}\vec{p}\cdot\vec{E} \\
i\hbar\dot{\rho}_{11} &= (\rho_{10} - \rho_{01})\frac{\Delta_0}{\mathcal{E}}\vec{p}\cdot\vec{E}
\end{aligned} \tag{8.28}$$

for the TLS density matrix.

Note that Eq. 8.28 does not include dissipation. We add dissipation and decoherence to the equations of the density matrix in an *ad hoc* manner [88] and arrive at

$$\begin{aligned}
i\hbar\dot{\rho}_{00} &= (\rho_{01} - \rho_{10})\frac{\Delta_0}{\mathcal{E}}\vec{p}\cdot\vec{E} + i\hbar\frac{\rho_{11}}{T_1} \\
i\hbar\dot{\rho}_{01} &= \rho_{00}\frac{\Delta_0}{\mathcal{E}}\vec{p}\cdot\vec{E} + \rho_{01}\left(\mathcal{E} + 2\frac{\Delta}{\mathcal{E}}\vec{p}\cdot\vec{E}\right) - \rho_{11}\frac{\Delta_0}{\mathcal{E}}\vec{p}\cdot\vec{E} - i\hbar\frac{\rho_{01}}{T_2} \\
i\hbar\dot{\rho}_{10} &= -\rho_{00}\frac{\Delta_0}{\mathcal{E}}\vec{p}\cdot\vec{E} - \rho_{10}\left(\mathcal{E} + 2\frac{\Delta}{\mathcal{E}}\vec{p}\cdot\vec{E}\right) + \rho_{11}\frac{\Delta_0}{\mathcal{E}}\vec{p}\cdot\vec{E} - i\hbar\frac{\rho_{10}}{T_2} \\
i\hbar\dot{\rho}_{11} &= (\rho_{10} - \rho_{01})\frac{\Delta_0}{\mathcal{E}}\vec{p}\cdot\vec{E} - i\hbar\frac{\rho_{11}}{T_1}.
\end{aligned} \tag{8.29}$$

Equation 8.29 can be rewritten as a matrix equation

$$\begin{pmatrix} \dot{\rho_{00}} \\ \dot{\rho_{01}} \\ \dot{\rho_{10}} \\ \dot{\rho_{11}} \end{pmatrix} = \mathcal{M} \begin{pmatrix} \rho_{00} \\ \rho_{01} \\ \rho_{10} \\ \rho_{11} \end{pmatrix}, \tag{8.30}$$

where

$$\mathcal{M} = \frac{1}{i\hbar} \begin{pmatrix} 0 & \frac{\Delta_0}{\mathcal{E}}\vec{p}\cdot\vec{E} & -\frac{\Delta_0}{\mathcal{E}}\vec{p}\cdot\vec{E} & \frac{i\hbar}{T_1} \\ \frac{\Delta_0}{\mathcal{E}}\vec{p}\cdot\vec{E} & \mathcal{E} + 2\frac{\Delta}{\mathcal{E}}\vec{p}\cdot\vec{E} - \frac{i\hbar}{T_2} & 0 & -\frac{\Delta_0}{\mathcal{E}}\vec{p}\cdot\vec{E} \\ -\frac{\Delta_0}{\mathcal{E}}\vec{p}\cdot\vec{E} & 0 & -\left(\mathcal{E} + 2\frac{\Delta}{\mathcal{E}}\vec{p}\cdot\vec{E} - \frac{i\hbar}{T_2}\right) & \frac{\Delta_0}{\mathcal{E}}\vec{p}\cdot\vec{E} \\ 0 & -\frac{\Delta_0}{\mathcal{E}}\vec{p}\cdot\vec{E} & \frac{\Delta_0}{\mathcal{E}}\vec{p}\cdot\vec{E} & -\frac{i\hbar}{T_1} \end{pmatrix}. \tag{8.31}$$

To solve Eq. 8.30 we use the ansatz

$$\begin{pmatrix} \rho_{00}(t) \\ \rho_{01}(t) \\ \rho_{10}(t) \\ \rho_{11}(t) \end{pmatrix} = e^{t\mathcal{M}} \begin{pmatrix} C_1 \\ C_2 \\ C_3 \\ C_4 \end{pmatrix}, \tag{8.32}$$

where we know that $\mathcal{M}$ is in general time dependent ($\mathcal{M} = \mathcal{M}(t)$) since it's a function of the applied field and we have the initial conditions

$$\begin{pmatrix} \rho_{00}(0) \\ \rho_{01}(0) \\ \rho_{10}(0) \\ \rho_{11}(0) \end{pmatrix} = \begin{pmatrix} 1 \\ 0 \\ 0 \\ 0 \end{pmatrix}. \tag{8.33}$$

To solve for $\rho(t)$ we can take short iterative time steps where we assume $\mathcal{M}(t)$ is a constant. This is effectively an induction proof, we know $\rho(0)$, so let's assume we know $\rho(t_0)$ and try to calculate $\rho(t_0 + \Delta t)$, thus proving that we can solve for $\rho(t)$ iteratively. First we know the solution around $t = t_0$ to be

$$\begin{pmatrix} \rho_{00}(t) \\ \rho_{01}(t) \\ \rho_{10}(t) \\ \rho_{11}(t) \end{pmatrix} = e^{t\mathcal{M}(t_0)} \begin{pmatrix} C_1(t_0) \\ C_2(t_0) \\ C_3(t_0) \\ C_4(t_0) \end{pmatrix}, \tag{8.34}$$

since we're assuming $\mathcal{M}(t)$ and by extension $C(t)$ are constant over small time steps. We can now calculate the constant matrix $C(t_0)$ from our initial conditions

$$\begin{pmatrix} \rho_{00}(t_0) \\ \rho_{01}(t_0) \\ \rho_{10}(t_0) \\ \rho_{11}(t_0) \end{pmatrix} = e^{t_0\mathcal{M}(t_0)} \begin{pmatrix} C_1(t_0) \\ C_2(t_0) \\ C_3(t_0) \\ C_4(t_0) \end{pmatrix} \therefore \begin{pmatrix} C_1(t_0) \\ C_2(t_0) \\ C_3(t_0) \\ C_4(t_0) \end{pmatrix} = \left[e^{t_0\mathcal{M}(t_0)}\right]^{-1} \begin{pmatrix} \rho_{00}(t_0) \\ \rho_{01}(t_0) \\ \rho_{10}(t_0) \\ \rho_{11}(t_0) \end{pmatrix}, \tag{8.35}$$

and with Eq. 8.36 calculate $\rho(t_0 + \Delta t)$

$$\begin{pmatrix} \rho_{00}(t_0 + \Delta t) \\ \rho_{01}(t_0 + \Delta t) \\ \rho_{10}(t_0 + \Delta t) \\ \rho_{11}(t_0 + \Delta t) \end{pmatrix} = e^{(t_0+\Delta t)\mathcal{M}(t_0)} \begin{pmatrix} C_1(t_0) \\ C_2(t_0) \\ C_3(t_0) \\ C_4(t_0) \end{pmatrix}. \tag{8.36}$$

By using this method we can choose a Monte Carlo distribution of TLSs and an arbitrary electric field bias to shift the asymmetry energies Δ and propagate the density matrix for each of the TLSs in time. What we are interested in is to

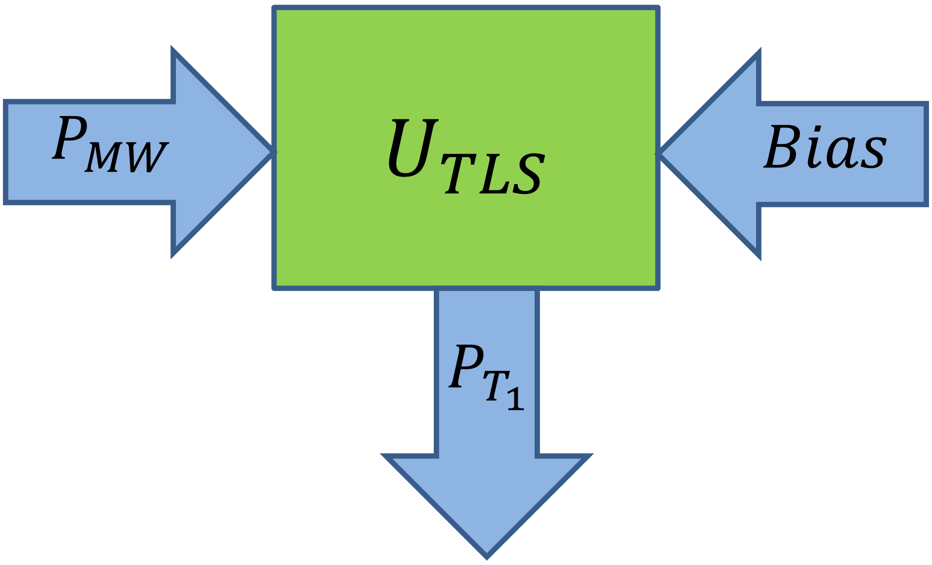

Figure 8.3: A cartoon illustrating how the TLS energy U_{TLS} is affected by the microwave drive P_{Bias}, the bias, and the TLS relaxation P_{T_1}

calculate the loss to the microwave field caused by the TLSs. Figure 8.3 illustrates that the TLS energy is effected by: the microwave field excitations, the bias field biasing TLSs, and T_1 relaxation. Writing this as a conservation of energy equation gives

$$\frac{dU}{dt} = P_{MW} + P_{Bias} - P_{T_1}. \tag{8.37}$$

Since we're interested in the loss to the microwave field we simply solve for the microwave field

$$P_{MW} = \sum_{TLS} \hbar\omega_{TLS}\dot{\rho}_{11} - \sum_{TLS} \hbar\omega_{TLS}\frac{\rho_{11}}{T_1}. \tag{8.38}$$

where we've evaluated the TLS energy as $dU/dt = \sum_{TLS} \hbar\omega_{TLS}\dot{\rho}_{11} + \sum_{TLS} \hbar\dot{\omega}_{TLS}\rho_{11}$, the bias caused energy change as $P_{Bias} = \sum_{TLS} \hbar\dot{\omega}_{TLS}\rho_{11}$, and the T_1 relaxation caused energy change as $P_{T_1} = \sum_{TLS} \hbar\omega_{TLS}\rho_{11}/T_1$.

We can now assume that the total energy in the system is

$$U = \text{Volume} \times \epsilon \times |\vec{E}|^2, \tag{8.39}$$

making the loss tangent of the system

$$\tan\delta = \frac{P_{MW}}{\omega_c U}, \tag{8.40}$$

where ω_c is the resonance frequency and is the frequency of the applied ac field in the simulation.

Note that if we break up the sums in Eq. 8.38 when solving Eq. 8.40 we can get the loss tangent contribution from each individual TLS. Also note that I have not quantized the resonator for this result. Rather I've treated it as a classical externally applied field. This is an approximation that ignores some details of the behavior of the solution and treating the Jaynes-Cummings Hamiltonian is required to solve the full quantum mechanical problem.

8.4.2 Monte Carlo steady state-results

In this section I discuss the results from the Monte Carlo simulation when no bias is turned on and show that we can reproduce the well-known steady-state loss tangent response. Figure 8.4 shows the TLS distribution used to evaluate the loss. A $T_{1,min}$ of 10 ns was assumed for this simulation with the T_1 distribution described in Chapter 2

$$\frac{1}{T_1} = \left(\frac{\Delta_0}{\mathcal{E}}\right)^2 \frac{1}{T_{1,min}}. \tag{8.41}$$

I assumed that there was no pure dephasing and set $T_2 = 2T_1$. Iterative steps of $\Delta t = 0.1$ ns were used to solve for the density matrix. All TLSs were assumed

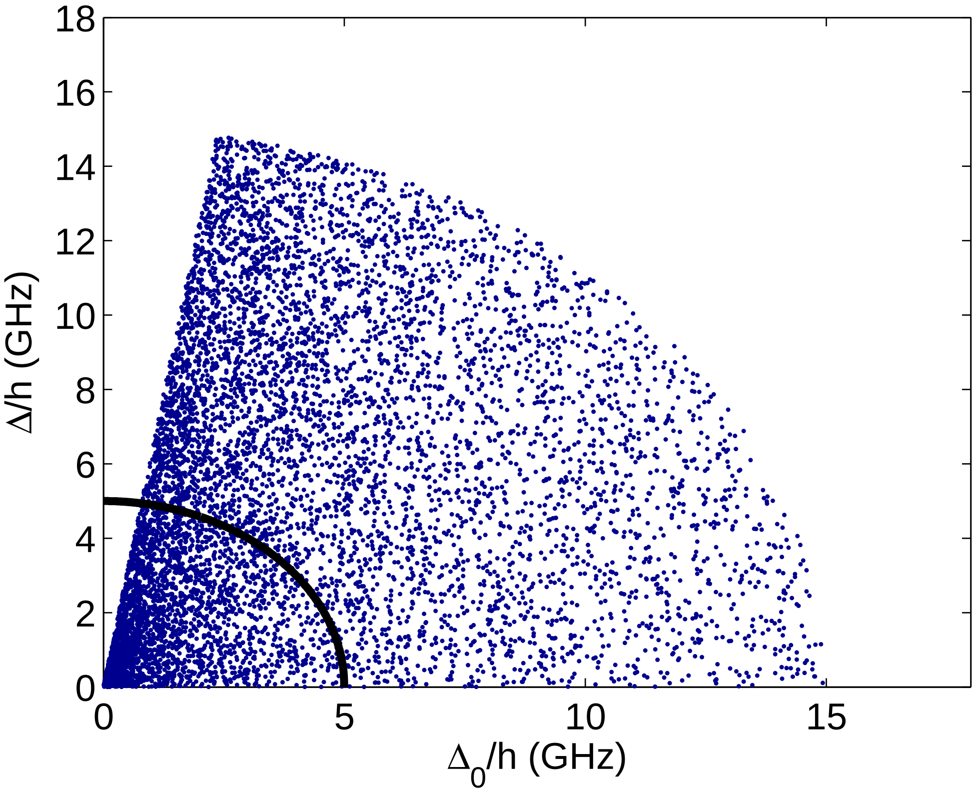

Figure 8.4: The Monte Carlo TLS distribution used for the simulation. The black curve represents the resonance frequency of the cavity. The limits set on the TLS distribution were 0.01 GHz $< \mathcal{E}_{TLS}/h <$ 15 GHz and $0 < \arctan(\Delta/\Delta_0) < 9\pi/20$.

to have the same dipole moment $p = 1\ D$ and the TLS density used was $P_0 = 1.28 \times 10^{42}\mathrm{J}^{-1}\mathrm{m}^{-3}$, calculated from the number of TLSs (8000), the distribution bandwidth (14.99 GHz), and the maximum angle used for the TLS distribution $(\arctan(\Delta_0/\Delta)_{max} = 9\pi/20)$

$$N_{TLS} = \int d^3r \int \frac{P_0 d\Delta d\Delta_0}{\Delta_0} = VP_0 \int_0^{9\pi/20} \frac{d\theta}{\cos\theta} \int_{BW} d\mathcal{E}$$
$$= V \times P_0 \times BW \times 2.54 \therefore P_0 = N_{TLS}/(V \times BW \times 2.54). \tag{8.42}$$

I also set the volume to $V = 100$ nm $\times$ $50\ \mu$m $\times$ $50\ \mu$m and the resonance frequency to $f = 5$ GHz. Figure 8.4 shows and example of a distribution of 8000 TLSs and the black curve represents the resonance frequency used.

The loss tangent was calculated using Eq. 8.40 after 100 ns of propagation, averaged for 100 time steps (10 ns). Figure 8.5 shows the loss tangent calculated for these conditions with several E_{ac} drive fields. The dashed line is a $1/E$ reference slope, the vertical black line at 2.2×10^3 V/m represents the expected characteristic saturation field with these parameters calculated from $E_c = \hbar/(\sqrt{T_{1,min}T_2}p)$ and the horizontal black line at 8×10^{-8} represents the expected intrinsic loss tangent from the parameters calculated by $P_0p^2/(3\epsilon)$. The value for E_c matches well with the simulated loss tangent, reaffirming the integrity of the simulation and the assumptions used. Figure 8.5 shows a variation of about a factor of two between the simulated intrinsic loss and the analytically calculated value (horizontal line) but statistical fluctuations in the simulation are on that scale.

Next I look at the transients of the loss tangent to see how the steady state loss in Fig. 8.5 is reached, both at low ac fields for the intrinsic loss (see Fig. 8.6(a))

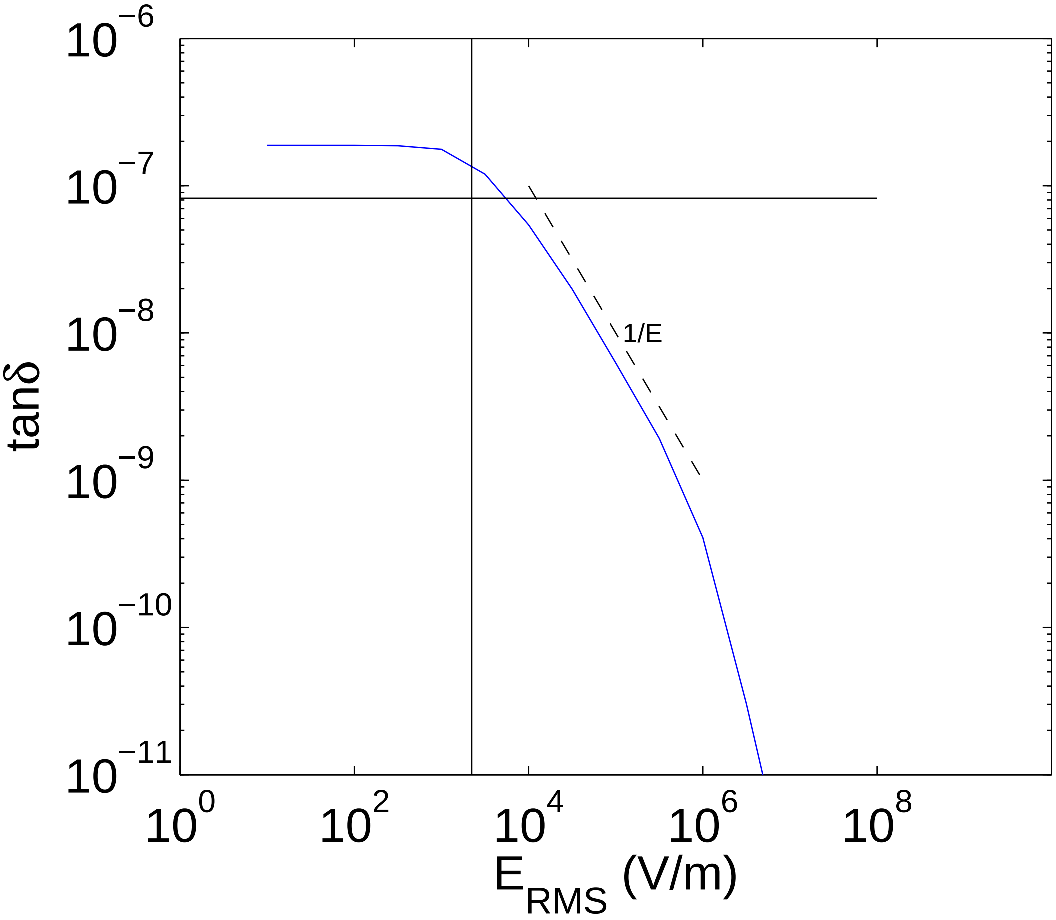

Figure 8.5: Calculated loss tangent vs. applied electric field from the Monte Carlo TLS simulation with Eq. 8.40 averaged for the last 100 time steps (10 ns) of the simulation. The dashed line is a $1/E$ reference slope. The simulation reproduces the expected TLS loss with a field independent low field loss and an onset of $\sim 1/E$ loss tangent behavior. The steepening to a $1/E^2$ response comes from hitting limits to the TLS distribution in the simulation. The vertical black line at 2.2×10^3 V/m represents the expected characteristic saturation field $E_c = \hbar/(\sqrt{T_{1,min}T_2}p)$ and the horizontal black line at 8×10^{-8} represents the expected intrinsic loss tangent $P_0p^2/(3\epsilon)$. The deviation between the simulated intrinsic loss tangent and the horizontal black line is due to statistical fluctuations in the number of TLSs near resonance in the simulation.

and at high ac fields (see Fig. 8.6(b)). As seen in Fig. 8.6, the loss starts at around the same value for both high and low ac field drives. This happens because initially all the TLSs are in their ground state and will absorb photons proportional to the drive field energy. For low drive (Fig. 8.6(a)) the TLSs aren't excited very much and the loss response stays around the same with roughly 10% fluctuations in $\tan\delta$. In contrast for high drive (Fig. 8.6(b)) the TLSs are saturated and their loss contribution decreases after sufficient time (determined by their Rabi frequency and relaxation time).

8.4.3 A closer look at the response of the TLS distribution

Figure 8.7 shows the TLS excitation response as ac drive is increased. In this figure, each point represents a TLS with its color scale representing its excitation probability (blue being ground state and red being excited state). For each simulation the same TLS distribution is used but with a different electric field drive. Figure 8.7(d) with the highest electric field drive shows that this method also simulates two and three photon processes (10 and 15 GHz). Figure 8.7(d) also shows that at these relatively large ac fields the simulation starts being limited by the TLS distribution used. This is why at high fields in Fig. 8.5 the loss response changes from what is expected for a broad distribution of, $\sim 1/E$, to the expected response from a single TLS, $\sim 1/E^2$.

The loss tangent contribution of individual TLSs with 10^5 V/m ac field drive is plotted in Fig. 8.8. As can be seen in Fig. 8.8 the loss contribution of TLSs is

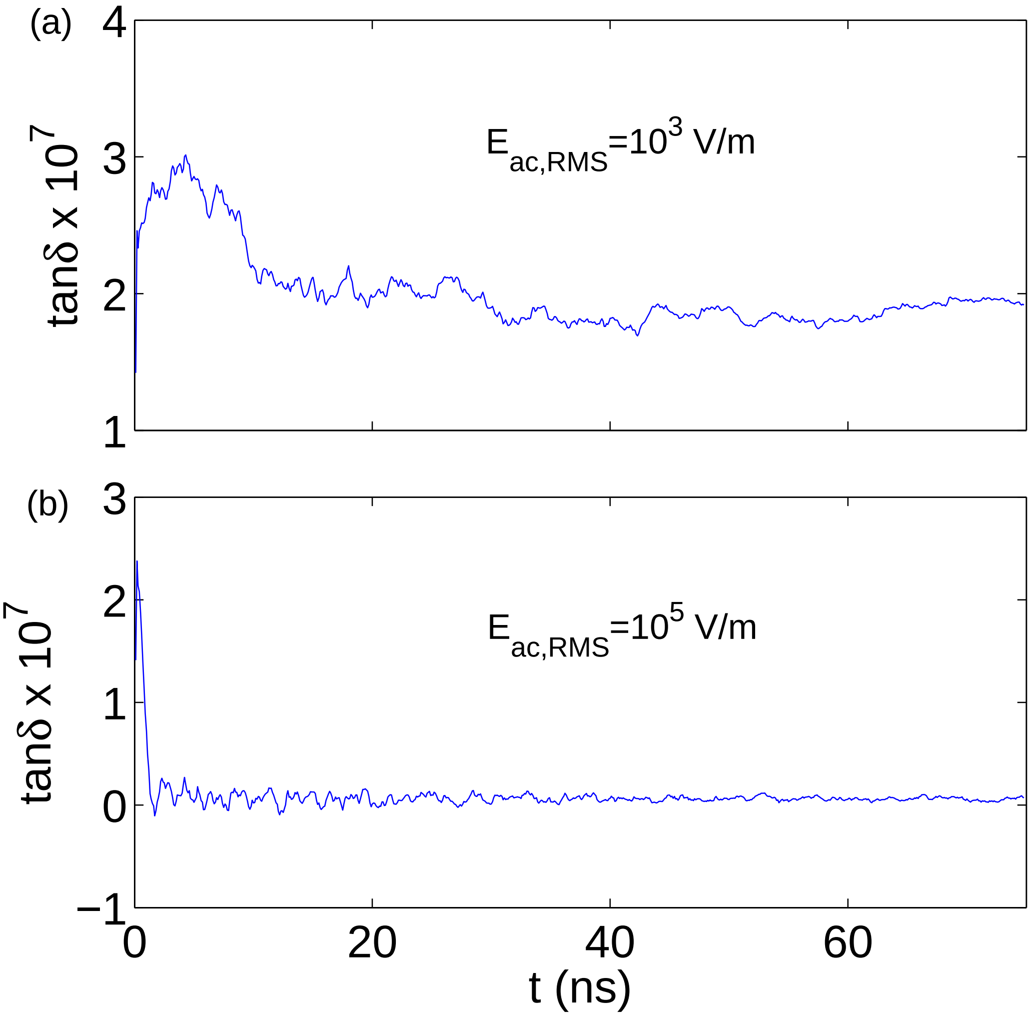

Figure 8.6: (a) Simulated loss as a function of time with an ac drive field of 10^3 V/m, near the intrinsic loss low field limit. Initially the loss is higher because all the TLSs are in their ground state. (b) Simulated loss as a function of time with an ac drive field of 10^5 V/m, above the TLS saturation knee in Fig. 8.5. Initially the loss is high because all the TLSs are in their ground state but, after a short period determined by the ac drive field, the TLSs are saturated and the loss decreases to the value found in Fig. 8.5 at $E_{RMS} = 10^5$ V/m.

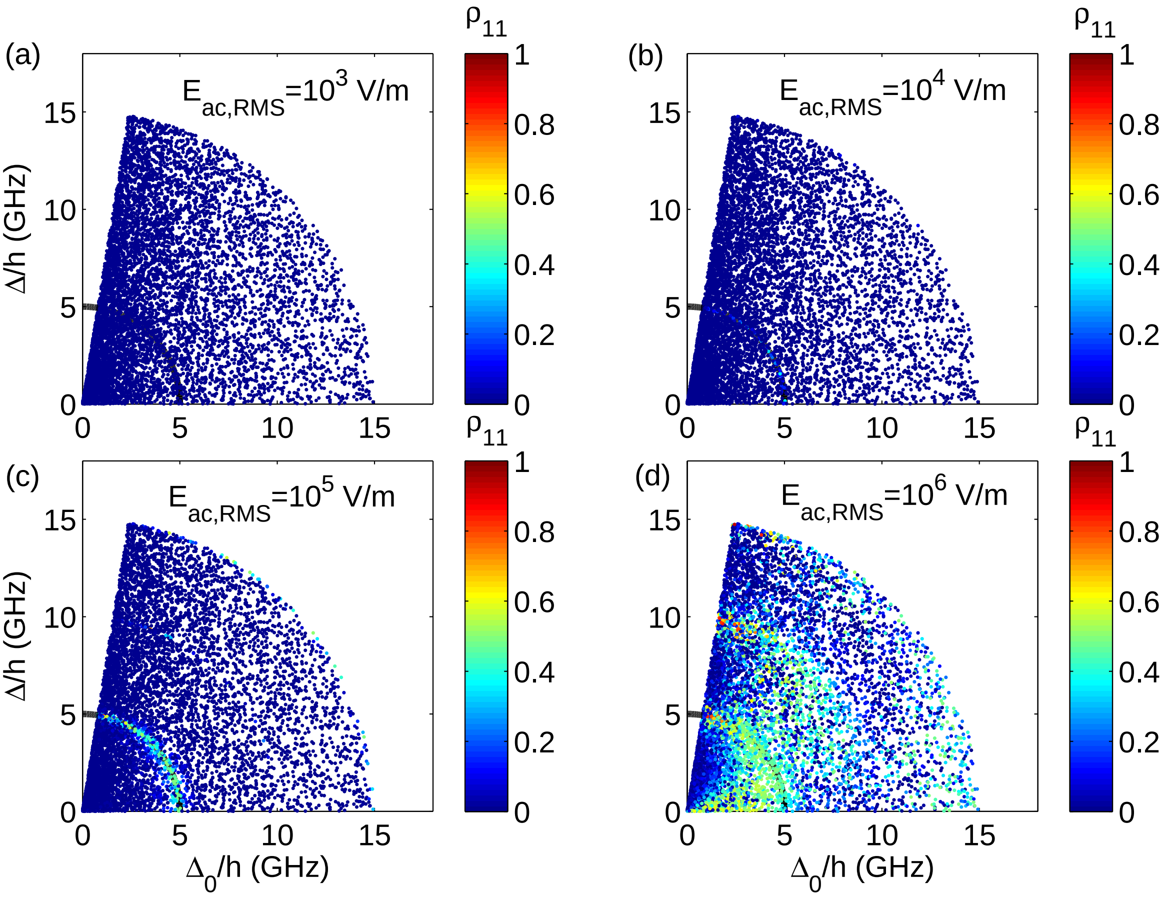

Figure 8.7: The TLS distribution excited state probability (ρ) after equilibrium was reached with a 5 GHz drive field of 10^3 V/m (a) 10^4 V/m (b) 10^5 V/m (c) 10^6 V/m (d). As the drive field was increased the TLSs on resonance (as well as at higher modes of the resonance) began to saturate. As shown by Fig. 8.5, at higher fields the simulation became less accurate and (d) strongly suggests that this is due to the limits in the TLS distribution used.

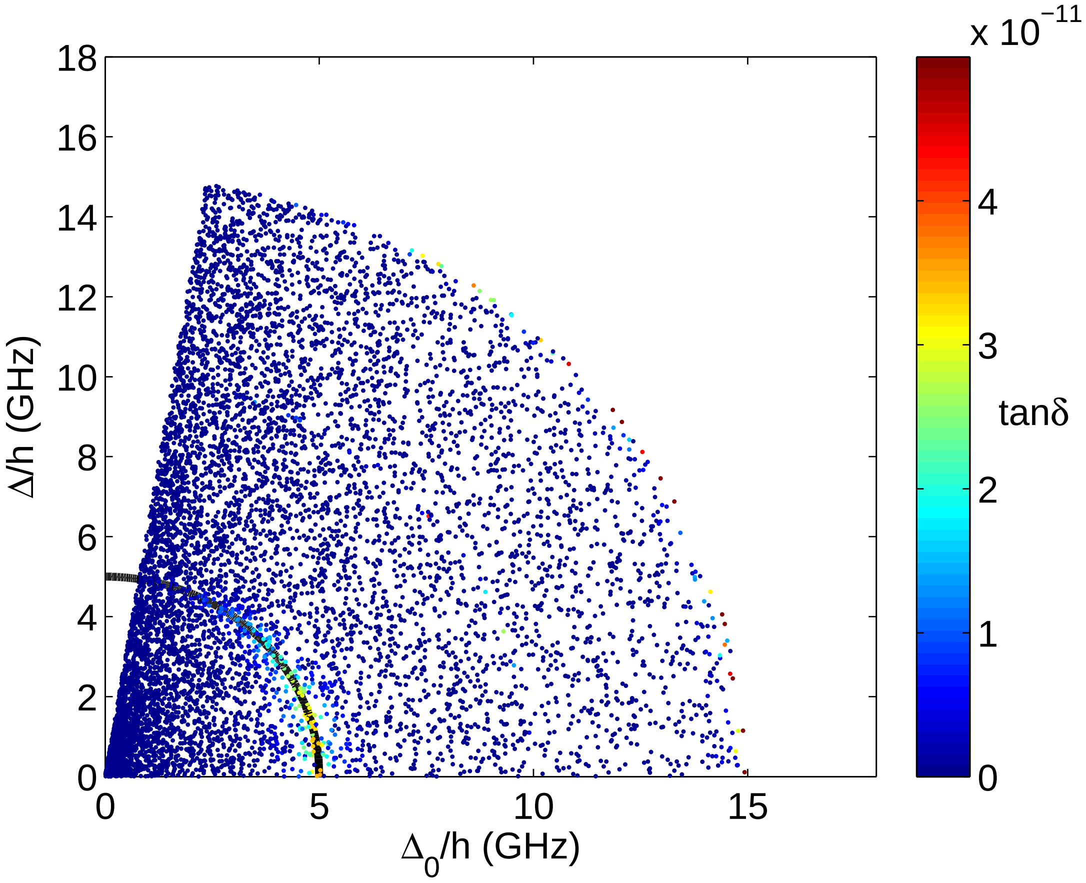

Figure 8.8: Loss contribution from each TLS after equilibrium was reached with 10^5 V/m ac field drive.

higher for TLSs with higher tunneling rates. This is both because it's easier to drive transitions with higher tunneling rates (as indicated by the $\Delta_0/\mathcal{E}$ terms in Eq. 8.29) and because TLSs with higher tunneling rates have shorter lifetimes (Eq. 8.41).

8.4.4 Individual TLS response

To gain a better understanding of the TLS loss I examined the loss contribution for individual planted TLSs in the simulation as a function of ac field drive. I chose nine TLSs at 4, 5, and 6 GHz with $\arctan(\Delta/\Delta_0) = \pi/6,\ \pi/4,\ \pi/3$ (see Fig. 8.9

inset). The loss from each of the TLSs as a function of the applied ac field is plotted in Fig. 8.9. As expected 4 and 6 GHz TLSs (dotted and solid lines respectively) contribute much lower loss than the resonant 5 GHz TLSs (dashed lines). And also as expected, as the tunneling rate to TLS energy ratio $\Delta_0/\mathcal{E}$ is decreased (red to green to blue in Fig. 8.9) the TLS loss contribution decreases. As can be seen from the field dependence in Fig. 8.9, an individual TLS's loss response goes as $1/E^2$. It's the sum of an ensemble of TLSs that gives the $1/E$ response.

Figure 8.10 shows a plot of the excited state probability ρ_{11} for TLS number 2 in Fig. 8.9 with increasing ac drive field. For low applied fields the TLS ρ_{11} increases to a steady state value (see Fig. 8.10(a,b)). For sufficiently high fields the TLS begins to show Rabi oscillations (see Fig. 8.10(c,d)).

8.4.5 Monte Carlo simulation with a bias field

Once convinced of the Monte Carlo's integrity in simulating individual TLS loss I returned to the distribution of 8000 TLSs from Fig. 8.4 and turned on a bias field sweep that varied the asymmetry of each TLS by $2\vec{p} \cdot \vec{E}_{Bias}$. I simulated the TLS response for 200 ns and, as shown in Fig. 8.11(a), with the bias field increasing from 0 to 500 kV/m between 75 and 125 ns resulting in $\dot{E}_{Bias} = 10^{13}$ V/m/s. For this bias ramp Fig. 8.11(b) shows the corresponding loss response at 10^4 V/m ac field drive and Fig. 8.11(c) shows the response at 10^5 V/m. As predicted by the theory discussed in section 8.3, the loss tangent increased when the bias is swept. In Fig. 8.11(b), with the lower ac field drive, the loss increases to close to the same

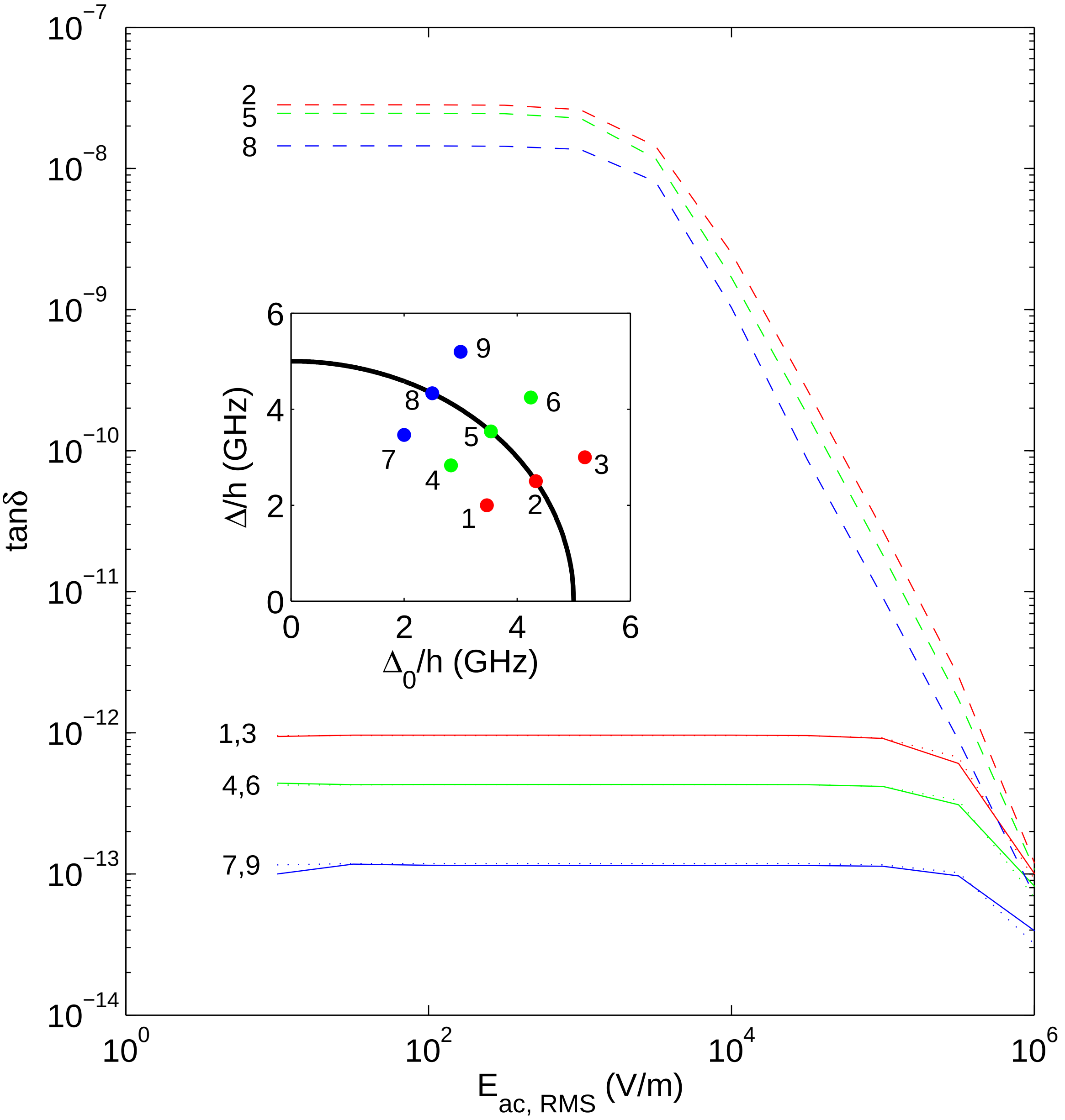

Figure 8.9: The loss contribution from each of 9 TLSs that were simulated at 4 (dotted line), 5 (dashed line), and 6 (solid line) GHz with $\arctan(\Delta/\Delta_0) = \pi/6$ (red), $\pi/4$ (green), $\pi/3$ (blue).

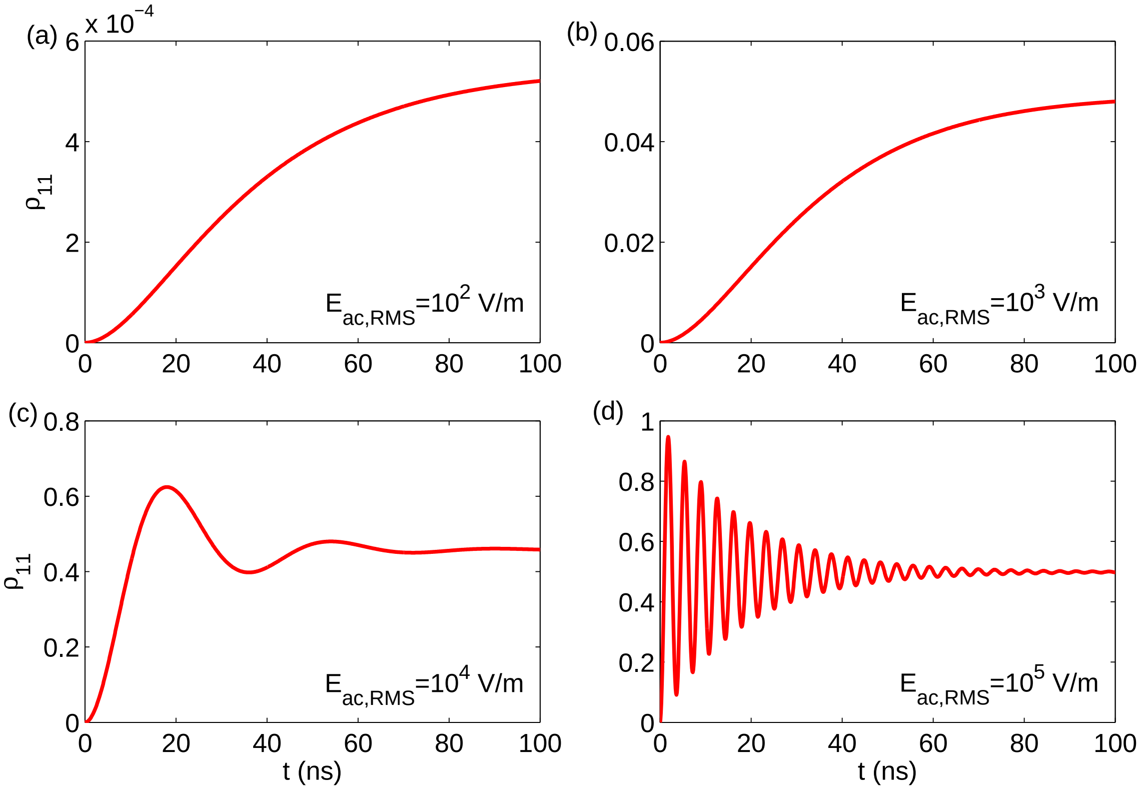

Figure 8.10: Simulated excited state probability ρ_{11} for TLS number 2 from Fig. 8.9 with an ac drive of (a) 10^2 V/m (b) 10^3 V/m (c) 10^4 V/m and (d) 10^5 V/m.

value it started with (t=0). In Fig. 8.11(c) when the ac field is relatively high and therefore the TLS Rabi frequency is high, there's only a small increase in the loss tangent response during the sweep.

In Fig. 8.12 I increased the field ramp sweep rate by a factor of 10 resulting in $\dot{E}_{Bias} = 10^{14}$ V/m/s. Here again Fig. 8.12(b) shows an increase in loss to close to the initial (t=0) loss value, but because of the increased bias rate Fig. 8.12(c) shows a much greater increase in the loss.

8.4.6 Monte Carlo simulation of TLS dynamics and adiabatic rapid passage

In this section I examine the excited state probability response of a single TLS in a swept bias field. As discussed in section 8.3, a TLS crossing the resonance frequency of the cavity can experience a Landau-Zener transition. If the bias is sufficiently fast, as in Fig. 8.13(a) where $\dot{E}_{Bias} = 9.88 \times 10^{14}$ V/m/s, then the TLS is likely to stay in the ground state, as shown in Fig. 8.13(b). But if the bias is sufficiently slow, as in Fig. 8.14(a) where $\dot{E}_{Bias} = 1.32 \times 10^{13}$ V/m/s, then the TLS experiences adiabatic rapid passage and is likely to be excited as shown in Fig. 8.14(b). The insets in Fig. 8.13 and Fig. 8.14 show the TLS before and after it was biased. In both simulations the Rabi frequency for the TLS is higher after the bias and that's because as shown by the insets the TLS is further detuned from the resonance frequency after the bias. The lifetime used for this TLS was $T_1 = T_2/2 = 83$ ns and the ac drive was 10^5 V/m.

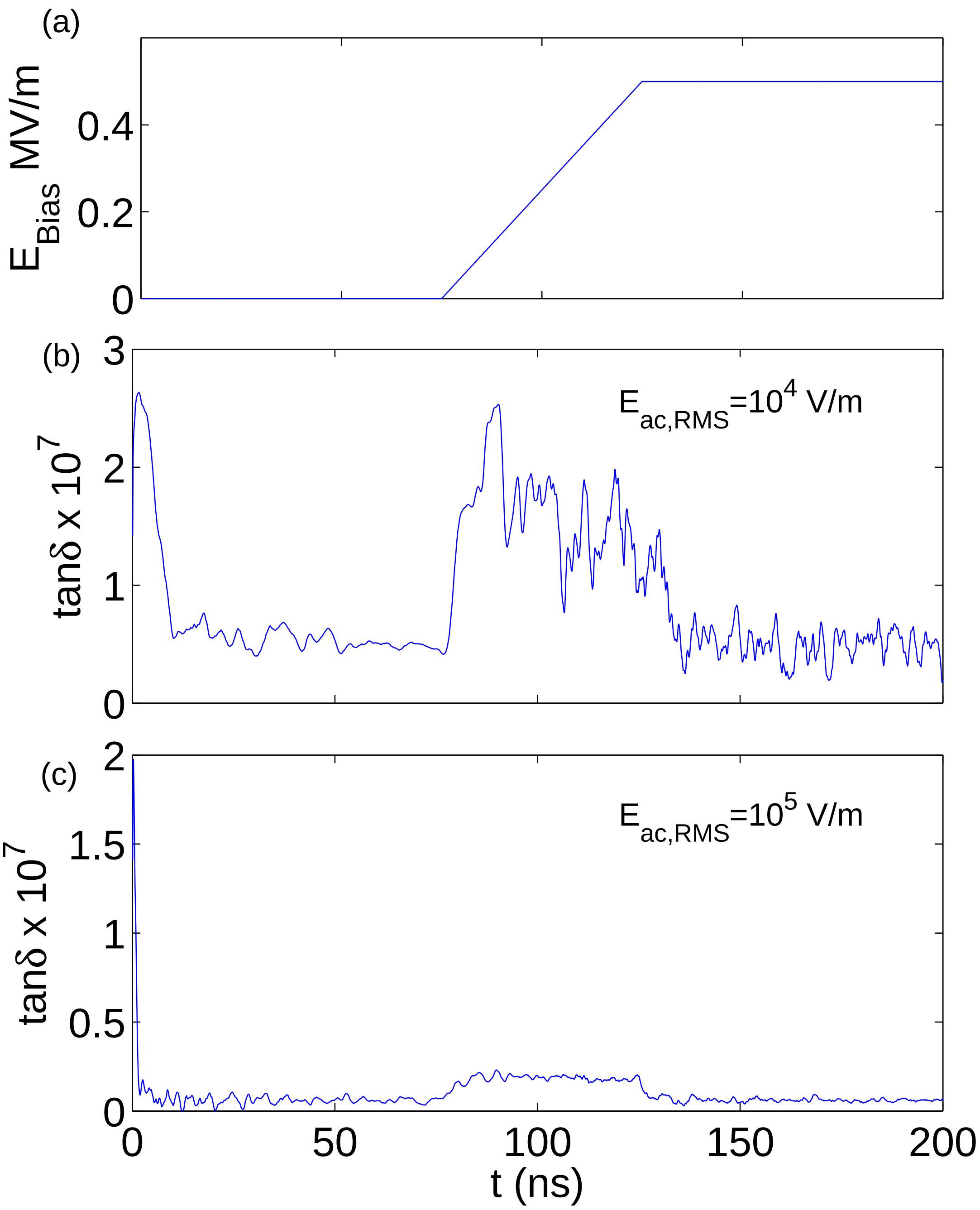

Figure 8.11: (a) Bias field used in Monte Carlo simulation of distribution in Fig. 8.4 to sweep the asymmetry energy Δ. (b) The loss tangent with 10^4 V/m ac drive starts high then reaches an equilibrium after TLSs are saturated then when the bias is turned on and new TLSs are moved into the resonator's bandwidth, the loss increases again. (c) The loss tangent with 10^5 V/m ac drive doesn't increase as much as (b) when the bias is swept because the Rabi frequency of the TLSs is higher.

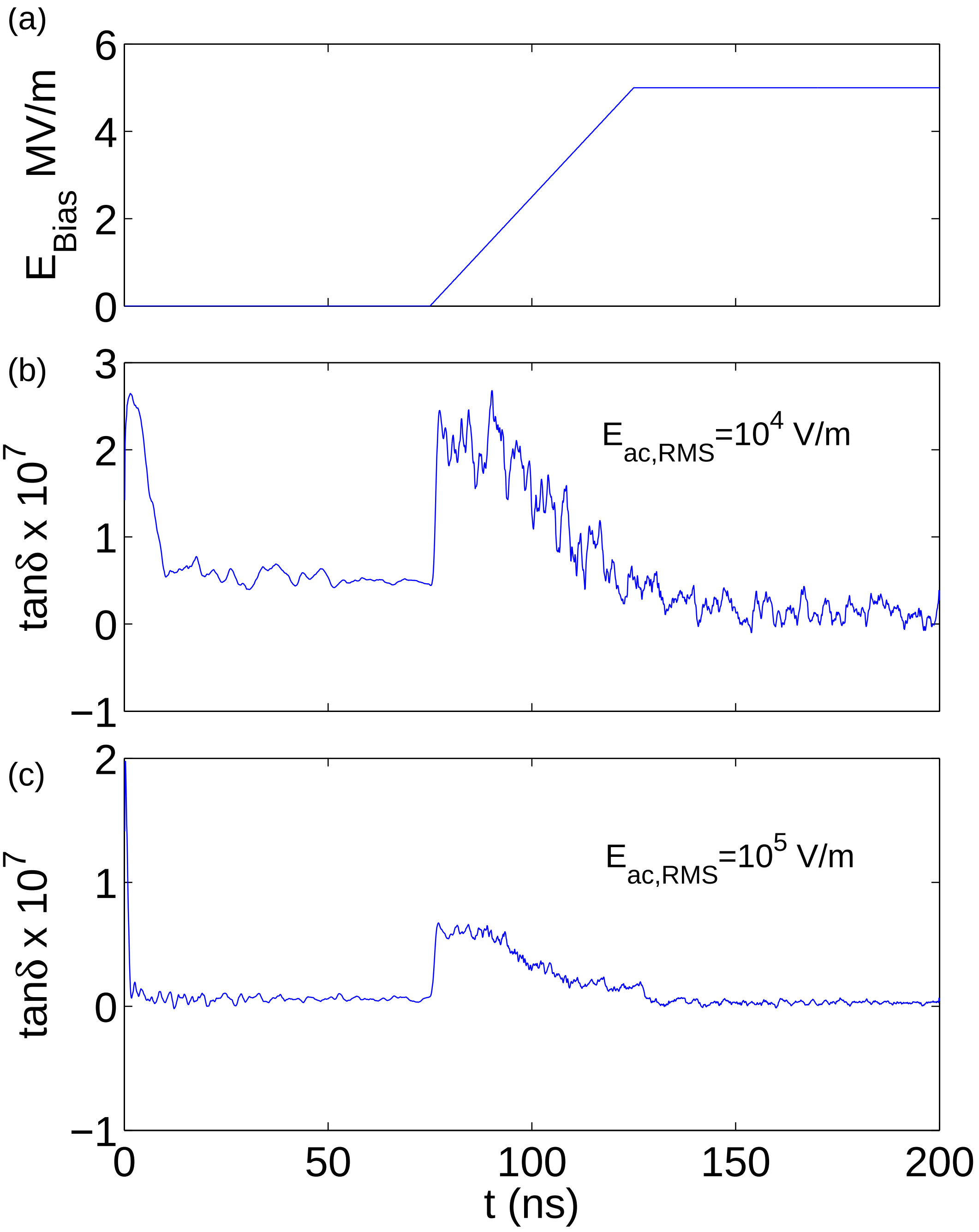

Figure 8.12: (a) Bias field used in Monte Carlo simulation with a sweep rate 10 times greater than Fig. 8.11. (b) The loss tangent with 10^4 V/m ac drive starts high then reaches an equilibrium after TLSs are saturated then the loss increases again when the bias is turned on and new TLSs are moved into the resonator's bandwidth. (c) Loss tangent with 10^5 V/m ac drive, as in Fig. 8.11, the loss doesn't increase as much as in (b) when the bias is swept because the Rabi frequency of the TLSs is higher but increases more than it did in Fig. 8.11(c) because the bias sweep rate is higher.

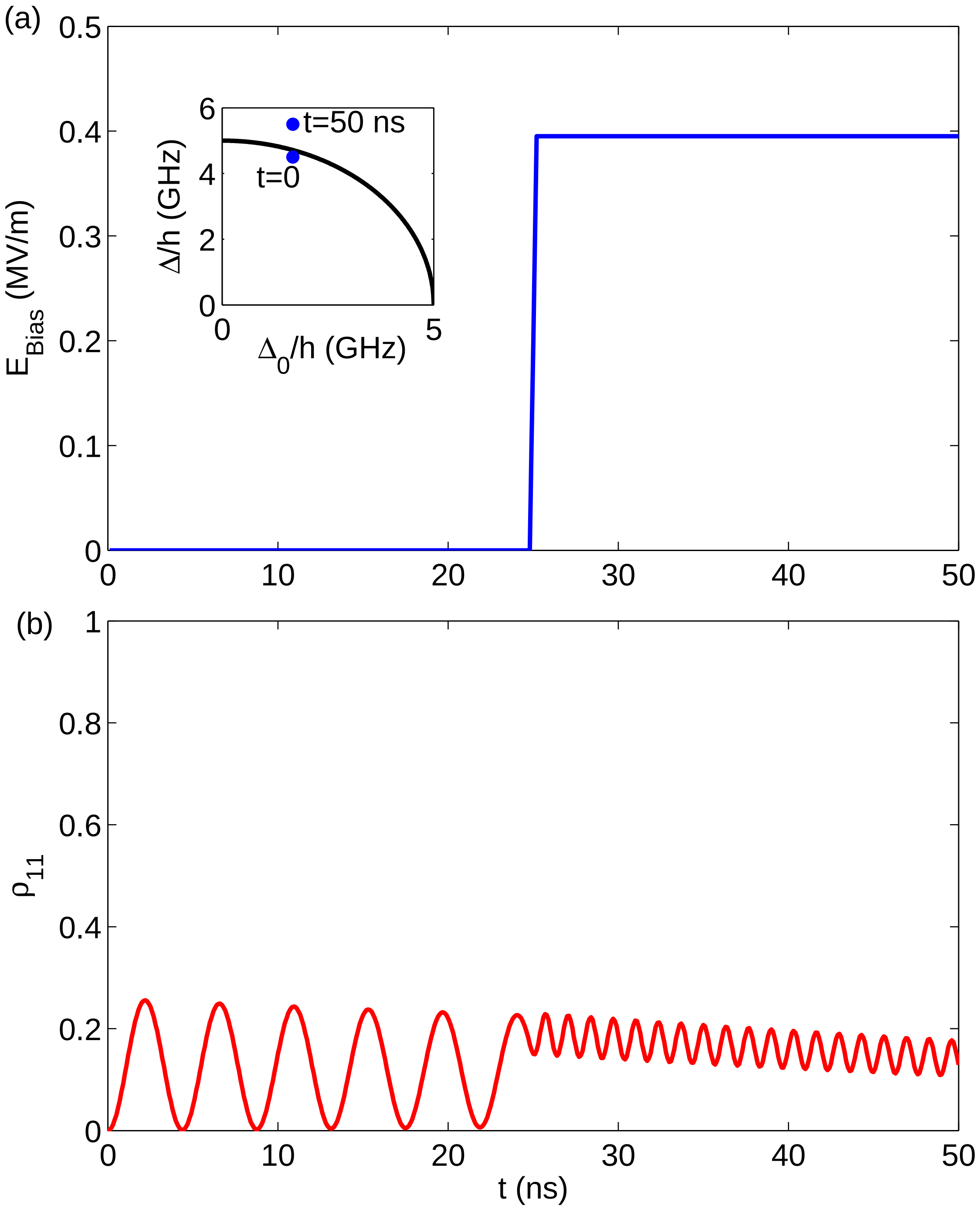

Figure 8.13: (a) Bias field vs. time for a fast sweep (9.88×10^{14} V/m/s) of a single TLS. (b) Simulation of excited state probability ρ_{11} vs. time for the bias in (a). Because the bias was very fast compared to the Rabi frequency, the TLS stayed in its ground state. Inset shows asymmetry Δ vs. tunneling Δ_0 for the TLS as the start and end of the sweep and the black curve represents the resonance frequency.

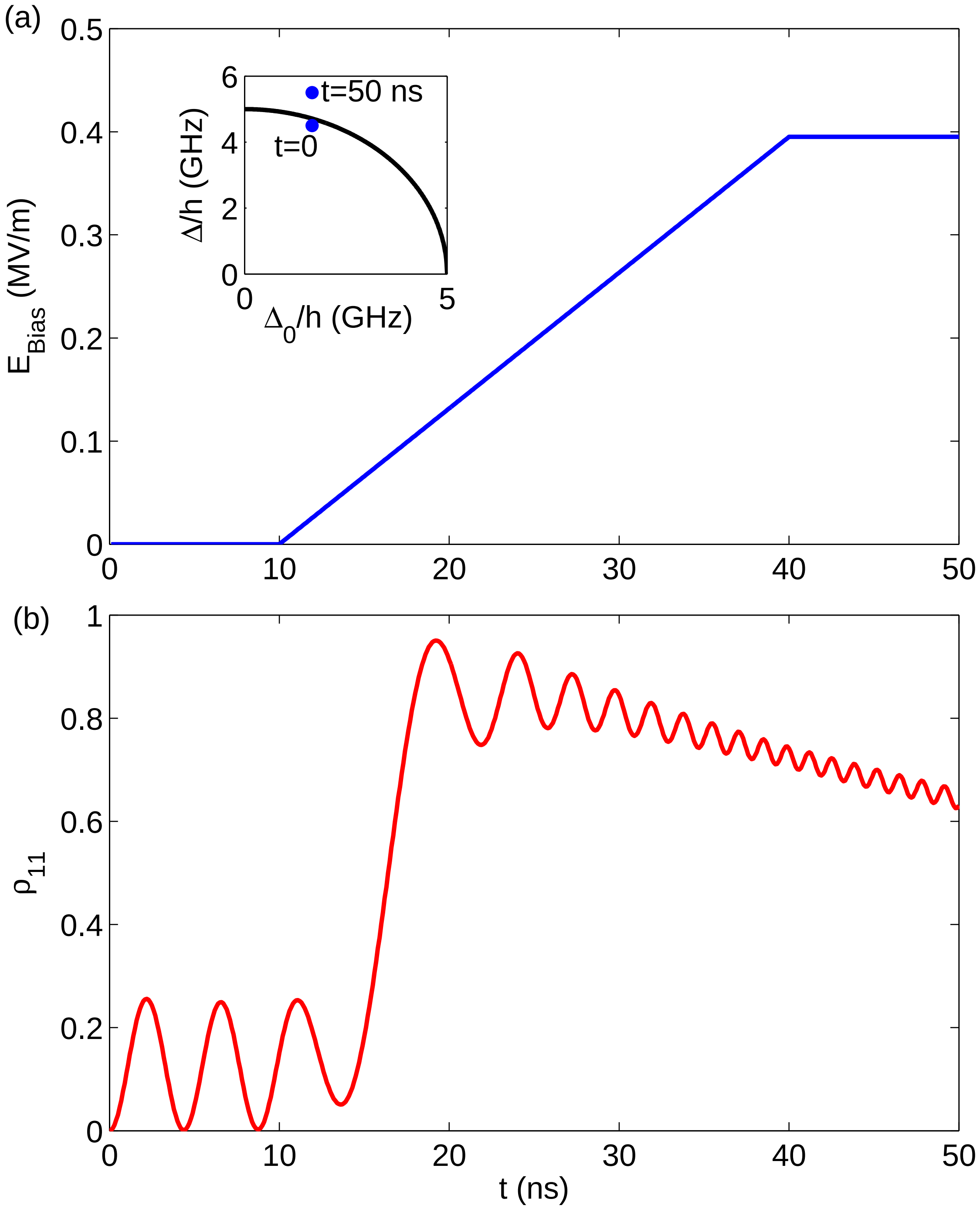

Figure 8.14: (a) Bias field vs. time for a slow sweep (1.32×10^{13} V/m/s) of a single TLS. (b) Simulation of excited state probability ρ_{11} vs. time for the bias in (a). Because the bias was slow compared to the Rabi frequency, The TLS underwent adiabatic rapid passage and was pumped to the excited state with a high probability. Inset shows asymmetry Δ vs. tunneling Δ_0 for the TLS as the start and end of the sweep and the black curve represents the resonance frequency.

8.5 Conclusion

In conclusion, I've discussed biasing TLSs with a field while probing and exciting them with an independent microwave (ac) field. It can be shown analytically that a TLS biased across the resonance frequency can experience a Landau-Zener transition. One consequence of this is that if the bias is sufficiently fast the loss tangent response of the TLSs at high ac fields approaches the unsaturated linear response at low ac fields [85]. I've also demonstrated a method for simulating the TLS loss response both with and without a swept bias field. Using this method I simulated the steady state TLS loss response, including the onset of TLS saturation as the ac field is increased. By simulating the system with a swept bias field, I also showed the predicted loss increases as the bias sweep rate increases. I also simulated the behavior of a TLS at two bias sweep rates and showed that for the fast bias sweep rate a TLS is likely to stay in the ground state as it crosses the resonance frequency while for a slower bias sweep rate the TLS experienced adiabatic rapid passage and is likely to be excited by the resonator.

Chapter 9

Biased resonator results

In this chapter I discuss the experimental setup I used for measuring the effects of a swept bias on a resonator and I compare the results from the experiment to the theory discussed in Chapter 8.

9.1 Biased resonators

9.1.1 The resonator

For these experiments I designed (most of the design was done with my advisor Kevin Osborn who suggested this experiment) and fabricated a resonator with capacitors that can be biased independently from the microwave (ac) resonant field. Figure 9.1(a) shows an optical image of a devices that is nominally identical to the one measured (from the same wafer) and Fig. 9.1(b) shows a schematic of the resonator design. The resonator was composed of a meandering inductor and four 250 nm thick amorphous $\mathrm{SiN_x}$-dielectric parallel-plate capacitors. As shown by Fig. 9.1, the resonator capacitance was broken up into four nominally equivalent capacitors with capacitance $C = 1.8$ pF in a bridge design, such that the equivalent resonator capacitance was C. One side of the capacitance bridge was grounded and the other was connected to a bias line with an applied bias voltage V_{bias} creating a bias of $V_{bias}/2$ across each capacitor. As with previously discussed resonators, the reso-

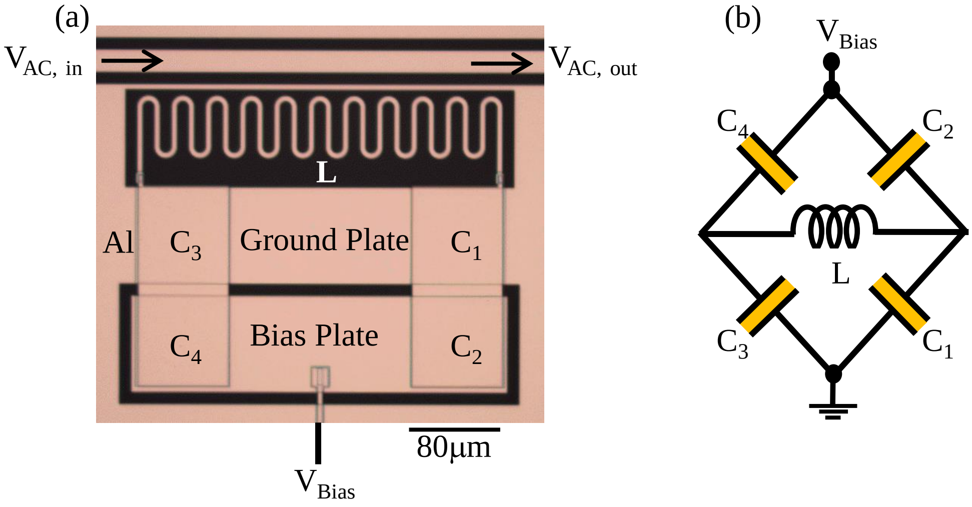

Figure 9.1: (a) Optical image of the thin-film superconducting aluminum resonator (nominally identical to devices *bias1-4.7GHz-A* and *bias1-4.7GHz-B*) comprised of a meandering inductor and four equal amorphous SiN_x parallel-plate capacitors. C_1 and C_3 are connected to the ground plane while C_2 and C_4 are connected to a bias plate. The resonator is inductively coupled to a CPW which is probed at microwave frequencies. (b) Circuit schematic of the resonator highlighting the bridge nature of the capacitors and their bias.

nance is driven through coupling to a CPW transmission line, creating a notch filter. As will be shown in the next section, the bias line is not coupled to the fundamental microwave resonance so as not to limit the resonance quality factor. The reason the coupling to the bias line is so weak on resonance is because at the location on the bias plate where the bias line is connects there is very little voltage and current from the fundamental microwave resonance mode.

9.1.2 Resonator simulations

Figure 9.2(a) shows the resonator design used for the Microwave Office simulation. A third port was added to simulate the bias line. As in the experiment, the bias line was separated from the ground plane by 250 nm of $\mathrm{SiN_x}$ dielectric. As shown by the transmission simulations in Fig. 9.2(b), port 3 (bias port) has less than -40 dB coupling to port 1 even on resonance. This corresponds to limiting the internal quality factor of the device to about $Q_i < 2 \times 10^6$, much higher than the expected quality of the dielectric used ($\mathrm{SiN_x}$), indicating that port 3 can be assumed to be isolated from the resonant circuit and will not affect its quality factor.

9.1.3 Resonator fab

Fabrication of this multi-layer resonator is more complicated than the fabrication of the coplanar resonators discussed in Chapter 4. For the bottom layer–comprised of the meandering inductor, the bottom plate of the capacitors and the ground plane–aluminum was sputtered, patterned and etched in exactly the same way that was discussed for the coplanar resonators in chapter 4. Next 250 nm of $\mathrm{SiN_x}$ was deposited with an Oxford high density plasma enhanced chemical vapor deposition (HD-PECVD) system. Nitrogen (N_2) and silane (SiH_4) precursor gasses were used with flow rates of 11 sccm and 10 sccm, respectively. The depositions rate was calibrated by first depositing SiH_4 on a silicon wafer and then measuring the thickness with an n&k diffraction measurement system [89]. Next I spun the same OIR 906-10 photoresist [58] that was used for the bottom layer in the same manner. The photoresist was patterned with a stepper and developed with OPD-4262 developer [58] again using the same technique discussed for the bottom aluminum layer in chapter 4. Next I exposed the bottom aluminum layer by etching vias in

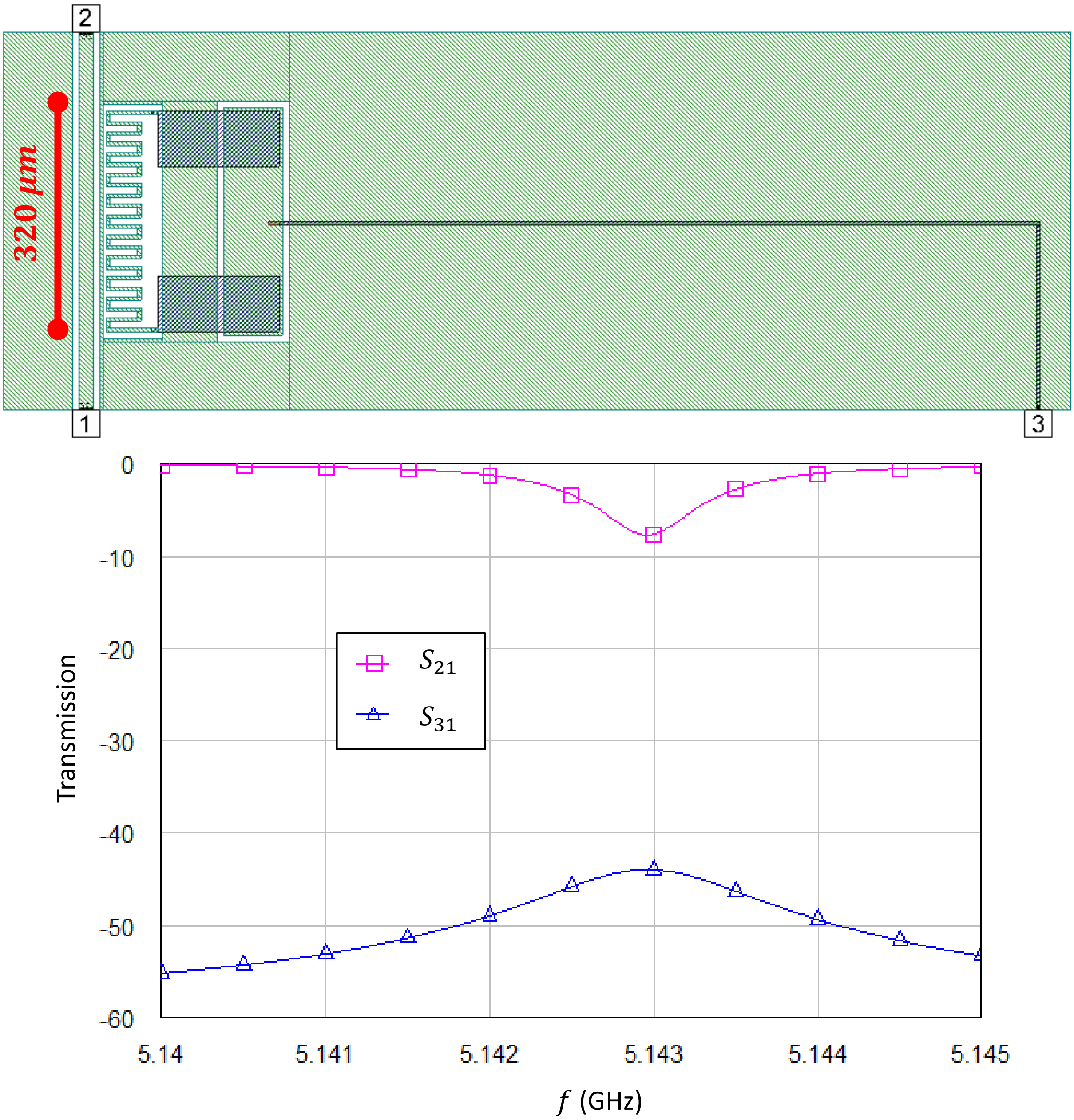

Figure 9.2: (a) Layout of 4-capacitor bridge resonator used for Microwave Office simulations. (b) Simulated transmission from port 1 to ports 2 (magenta) and 3 (blue). The coupling between ports 1 and 3 is very low at the resonant frequency (less than -40 dB) thus the bias line will not limit the resonator's loss.

the $\mathrm{SiN_x}$ were etched using a sulfur hexafluoride ($\mathrm{SF_6}$) reactive ion etching (RIE) process. After cleaning the photoresist, in the same manner discussed earlier, the wafer was again put in the sputtering chamber where it was ion milled with argon at 800 V beam voltage for 60 seconds in order to ensure that the native oxide on the bottom aluminum layer was entirely etched for good electrical contact. Next, the top aluminum layer (200 nm) was sputtered, patterned, and etched leaving only the top plates of the capacitors, the vias connecting the capacitors to the inductor, and the bias line connecting to the bias plate. Finally the excess $\mathrm{Si3N_4}$ was patterned and etched away (using the same RIE process) everywhere except where it was required to support a top aluminum layer (the capacitors and the bias line). Once the fabrication process was complete the wafer was diced (in the same manner discussed for the coplanar devices in Chapter 4) and mounted in a copper box similar to that shown in Fig. 4.6. The devices was wire bonded to in the same manner discussed in Chapter 4 with the simple addition of also wire bonding to the bias line.

9.2 Dependence on loss on a static (DC) bias voltage

The first measurement I made on these devices was to bias the resonator with a static (DC) electric field and see if the TLS loss was affected. Figure 9.3 shows measurements of the loss tangent taken at 30 mK for device *bias1-4.7GHz-A*. The presence of a DC bias field did not have a significant effect on the TLS loss even with a bias field of 200 V/m, corresponding to a shift of 2.0 THz for the asymmetry energy (Δ/h) of a TLS assuming a 1 Debye dipole moment aligned with the field.

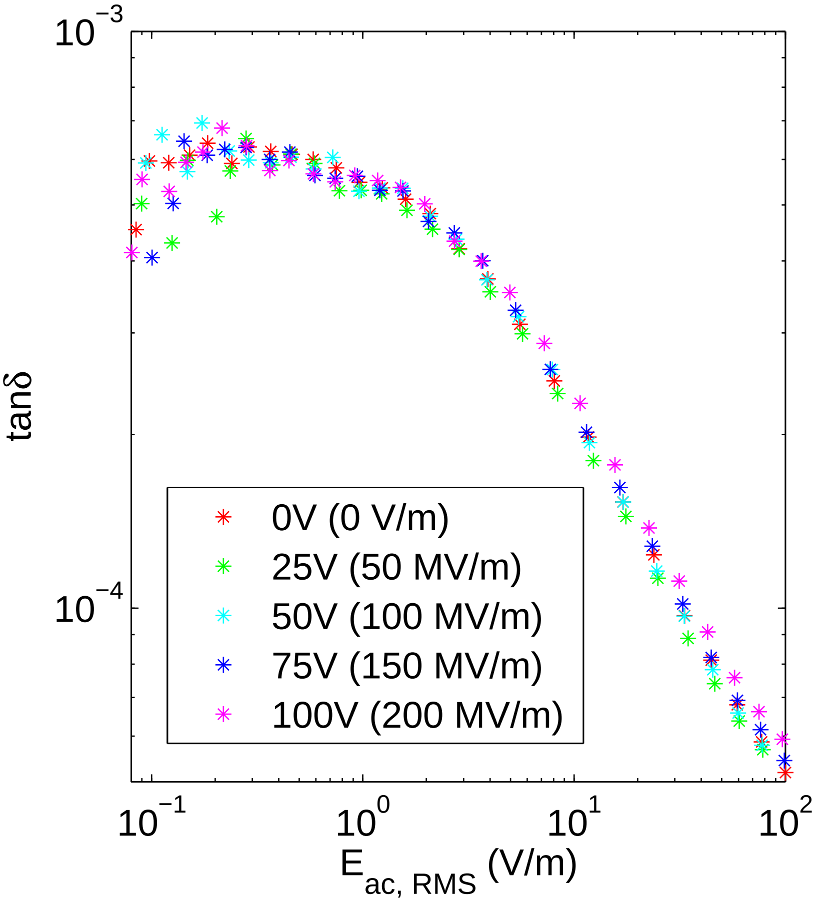

Figure 9.3: Loss tangent measurements of resonator *bias1-4.7GHz-A* at 30 mK as a function of the microwave excitation field taken with various DC bias fields. The DC bias fields showed no substantial effect on the loss.

For higher biases the SiN_x broke down, and thus I can only conclude that the TLS asymmetry energy distribution is flat in the 0-2 THz range.

As mentioned in Chapter 8, even if a systematic shift in loss tangent as a function of bias field is not measured, the measurement of random shifts in loss tangent due to the discrete nature of the TLSs is still possible. Figure 9.4 shows measurements where such texture in both loss (Fig. 9.4(b)) and dielectric constant (Fig. 9.4(c)) is resolved by varying the bias field (Fig. 9.4(a)). As shown in Fig. 9.4

when a bias field is applied, the shifts in loss and dielectric constant (capacitance) are random, as expected. It was somewhat surprising however to see the loss and permittivity systematically return to the same value when the bias is turned off. This suggests that the TLSs are not rearranging themselves in some irreversible, glassy manner when the bias field changes. Note that these measurements were taken over a period of several hours which seems like a relatively long timescale for the stability of atomic systems. We can also use the scale of these TLS induced loss tangent jumps to estimate the number of TLSs in the resonator's bandwidth. The loss tangent jumps are on the scale of about $\Delta \tan\delta / \tan\delta \sim 0.02$, and since the loss tangent scales with the number of TLS in the resonator, we can say $1/\sqrt{N} \sim 0.02$. Thus the number of TLSs in the bandwidth of the resonator is approximately $N \sim 2500$, which for the capacitor volume of $V = 4 \times 80\ \mu\text{m} \times 80\ \mu\text{m} \times 250$ nm, a resonator bandwidth of about 1 MHz, and a TLS linewidth of about 1 MHz corresponds to a TLS spectral spatial density of about $P_0 \sim 10^{43}$, which as I will show later in this chapter comparable to another measurement I preform in this system.

9.3 Loss with swept bias

9.3.1 Pulsed bias effect

As discussed in the previous section, the changes in TLS loss due to a DC bias were typically only a few percent. I next discuss results from measurements of the loss tangent response with a rapidly swept bias field. Figure 9.5(a) shows a bias pulse of 40 MV/m with a rise and fall time of 8.5 ms. The color scale in

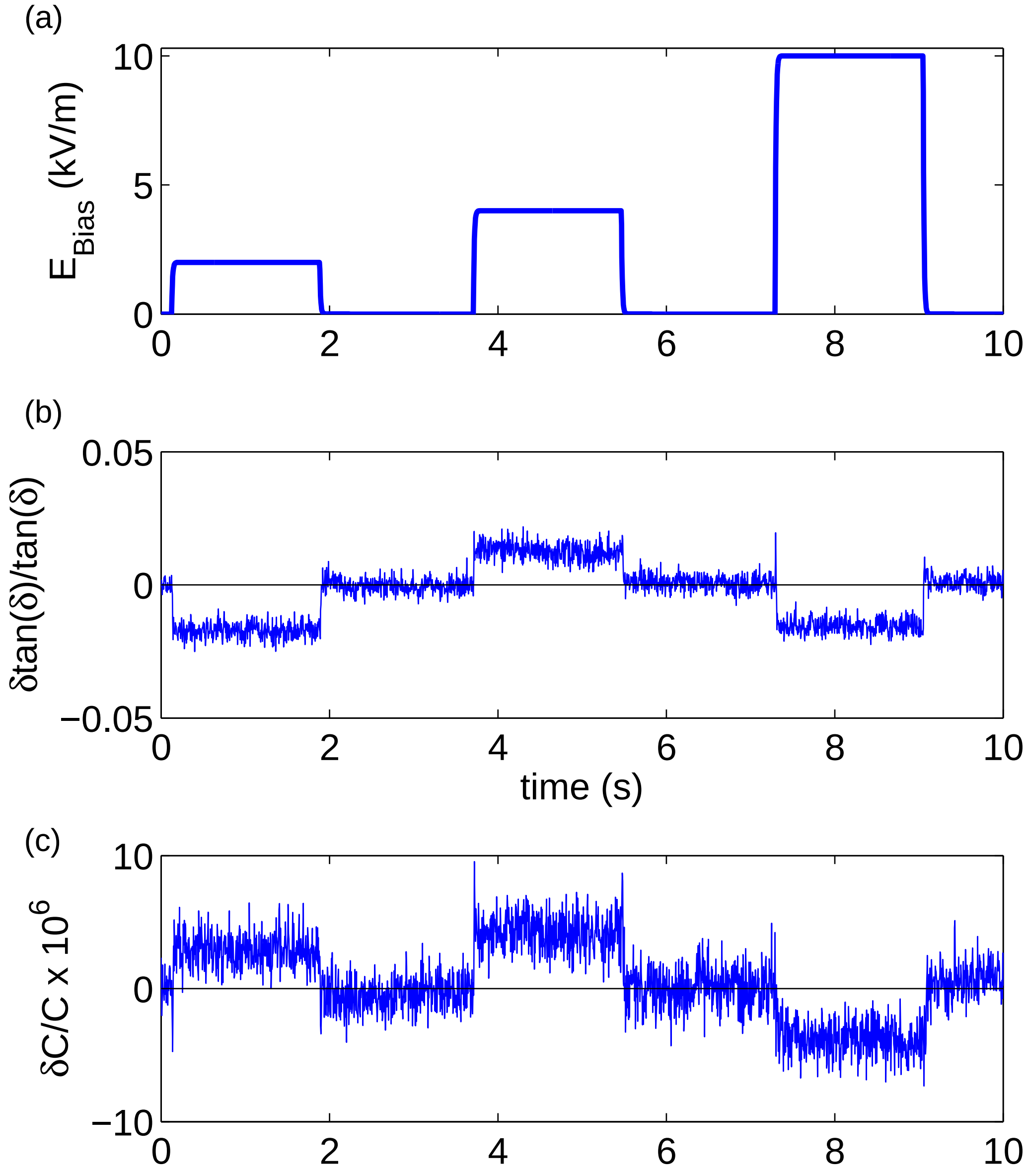

Figure 9.4: (a) Three bias field pulses applied sequentially. (b) The corresponding fractional change in loss tangent from the value at zero bias field in device *bias1-4.7GHz-B*. The shifts are due to the random and discrete nature of the TLSs. (c) Similar (but smaller) random shifts are also observed in the capacitance, also caused by small changes in the TLS distribution.

Fig. 9.5(b) shows the transmission through the CPW of device *bias1-6.5GHz-A* at the resonance frequency. Before the bias ramp start up (step up) the resonance line shape is constant, but once the bias step occurs, the resonance line shape becomes wider and shallower indicating a decrease in the quality factor. After some time at the constant bias field of 40 MV/m, the resonance line shape returned to its original value. When the bias ramp down occurred, the resonator responded again in the same manner, with a lower quality factor that eventually returns back to its original value.

Each of the time slices in Fig. 9.5(b) were fit to a resonance line shape and the extracted loss tangents are plotted in Fig. 9.5(c). Examination of Fig. 9.5(c) makes it clear that the loss jumps to the same value at both the step up and down of the bias field and returns to this same value once the bias field stabilizes. As discussed in Chapter 8, this behavior is caused by TLSs being swept through the resonance frequency and taking energy from the microwaves not only by relaxing but also by moving outside the resonator's bandwidth. It is also worth remarking that these effects were observed experimentally before the phenomenon was explained theoretically, and it was this peculiar behavior which motivated the theoretical effort.

9.3.2 Biased and steady state losses

Based on the model discussed in chapter 8 [85], for a sufficiently fast bias rate, the loss tangent can be expected to increase to its intrinsic unsaturated value. Figure 9.6(a) shows the steady state loss tangent measurements for the resonator at

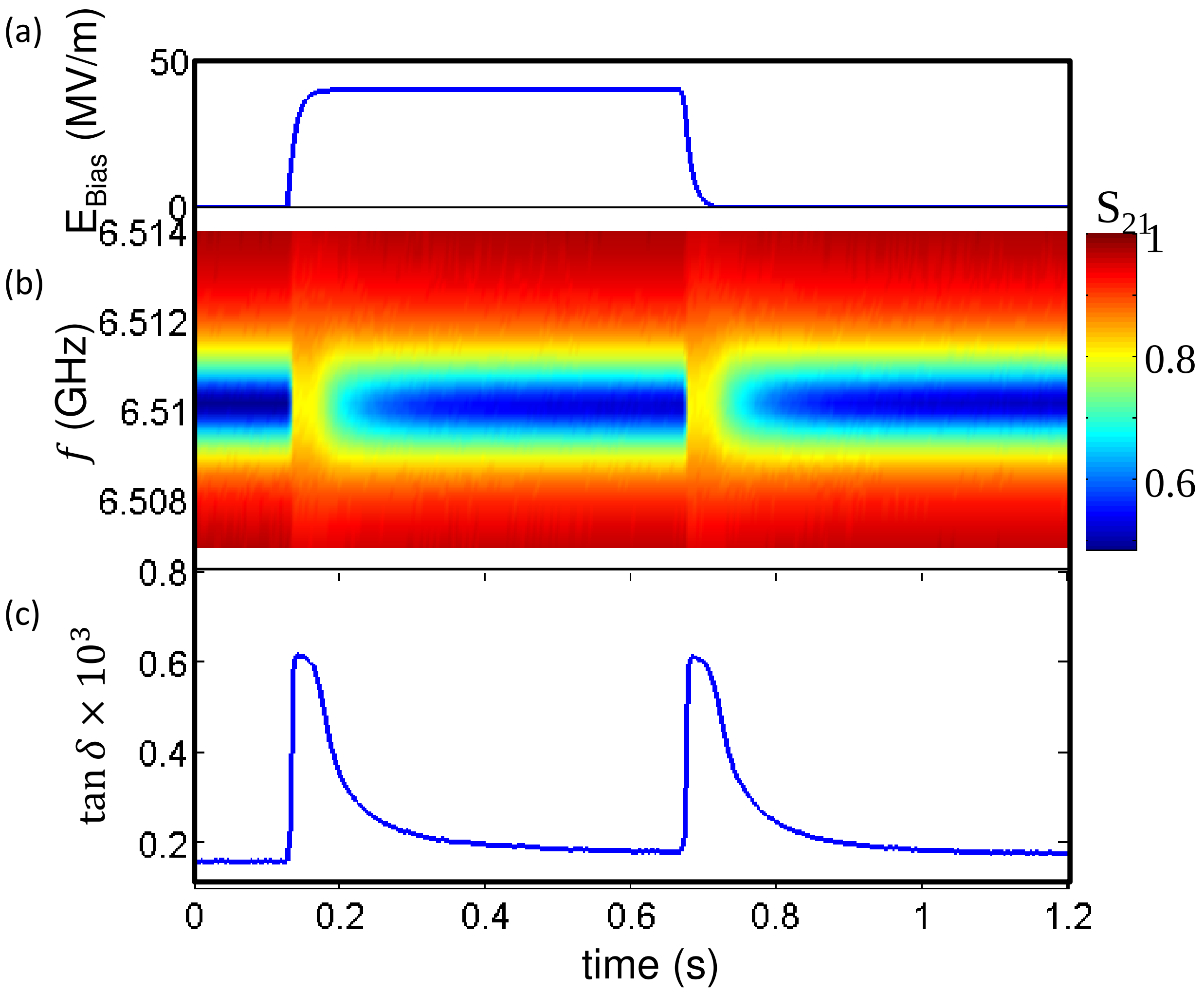

Figure 9.5: (a) Bias electric field pulse applied with a rise and fall time of 8.5 ms resulting in a maximum bias rate of $\dot{E}_{Bias} = 4.7$ GV/m/s. (b) Transmission of CPW showing the resonance line shape as the bias is applied. Both at the rise and fall of the pulse the resonance line shape becomes shallower and broader indicating an increase in the loss. (c) Each time slice in (b) is fit to a resonance line shape and the extracted loss tangent is plotted. The loss tangent initially increases as the bias field is swept up or down and then relaxes back to its steady state value. This measurement was performed on device *bias1-6.5GHz-A*.

33 and 200 mK as a function of the magnitude of the ac resonant field. Figure 9.6(b) shows the loss tangent response at those same temperatures while exciting with a single ac drive field as the bias is ramped (see inset). Comparing Fig. 9.6(a) to Fig. 9.6(b), we see that the loss tangent does in fact increase to the intrinsic unsaturated value at both temperatures.

In Fig. 9.6(c) the intrinsic loss tangent at low ac field with no bias (black triangles) is compared to the maximum loss tangent jump height with a ramped bias field (blue circles). The loss for a ramped bias field show an approximately 5% greater loss than the linear-response loss tangent at the lowest temperatures. Assuming this non-equilibrium loss should exactly equal the linear response loss, it is possible that the small systematic difference may be due to slow TLS interactions, which move TLSs towards the global ground state that creates a slightly different loss tangent [83]. The solid curve in Fig. 9.6(c) is a fit to $\tan\delta_0 \tanh(\hbar\omega/2k_BT)$, which describes the thermal saturation of the loss tangent in the conventional theory. I find good agreement with this fit.

9.4 Varying bias rate

As discussed in chapter 8, the loss tangent is dependent on the bias ramp rate and the Rabi frequency (ac field amplitude). At low bias ramp rates we expect to be in the steady state limit, resulting in a loss tangent that is dependent on the ac field amplitude according to the conventional tunneling model:

$$\tan(\delta) = \tan\delta_0 \frac{\tanh(\hbar\omega/2k_BT)}{\sqrt{1+(E_{ac}/E_c)^2}}. \tag{9.1}$$

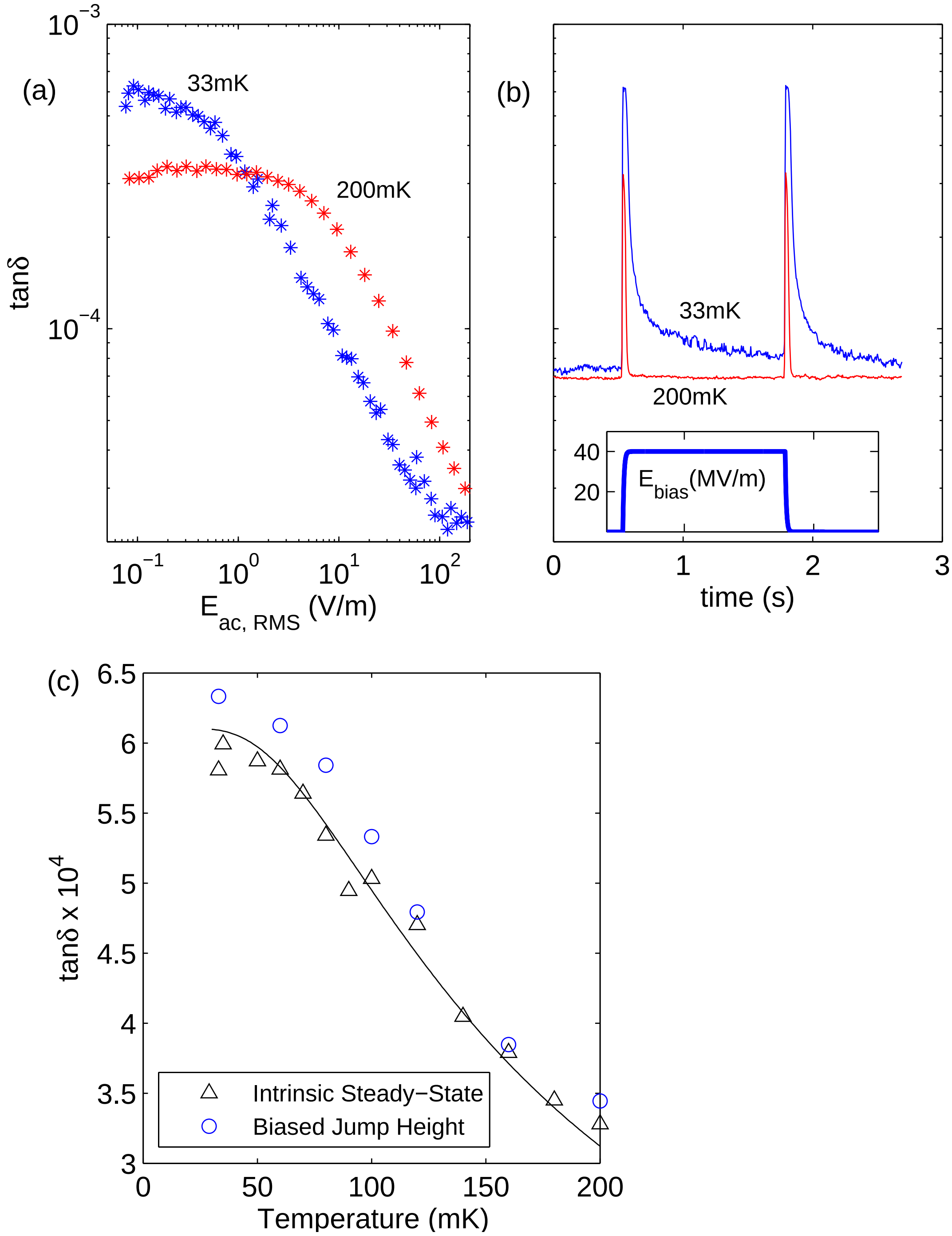

Figure 9.6: (a) Steady-state loss tangent, measured in device *bias1-4.7GHz-B* as a function of the microwave field at temperatures of 33 (blue) and 200 (red) mK. (b) Corresponding time-dependent loss tangent measured (main panel) with an electric field bias that sweeps up (down) at 0.53 s (1.78 s) (inset). (c) Comparison of steady state intrinsic unsaturated loss tangent (blue circles) to the maximum loss tangent reached with a swept bias (black triangles) as a function of temperature. The solid curve shows a fit of the conventional theory of thermally saturated TLS, $\tan\delta_0 \tanh(\hbar\omega/2k_BT)$, to the steady state data.

At high bias rates, as seen in Fig. 9.6, the model in Chapter 8 predicts a loss tangent equal to the intrinsic unsaturated value for the material. In between, the same model predicts a loss tangent that is dependent on the dimensionless bias rate

$$\xi = \frac{2\nu_0}{\pi \Omega_{R0}^2}, \tag{9.2}$$

where, as discussed in chapter 8,

$$\nu_0 = 2\frac{p}{\hbar}\frac{dE_{bias}}{dt}, \tag{9.3}$$

and

$$\Omega_{R0} = \frac{pE_{ac}}{\hbar}. \tag{9.4}$$

Here I'll discuss measurements of loss tangent as a function of the bias rate and show that I get a good fit to the model discussed in Chapter 8 and in Ref. [85].

9.4.1 Methods for varying bias rate

To vary the bias rate, I used a voltage supply with a constant rise time and varied the amplitude of the bias. I used a Stanford Research Systems SIM928 Isolated Voltage Source with a characteristic rise/fall time of 8.5 ms. I varied the bias pulse amplitude (see Fig. 9.7(a)) which resulted in varying loss tangent responses (see Fig. 9.7(b)). Figure 9.7(c) shows the resulting plot of loss tangent as a function of bias rate bound by taking the maximum loss tangent jump height from each pulse and plotting it against the maximum bias rate. The maximum bias rate was calculated by dividing the pulse amplitude by the characteristic rise and fall time of the pulse.

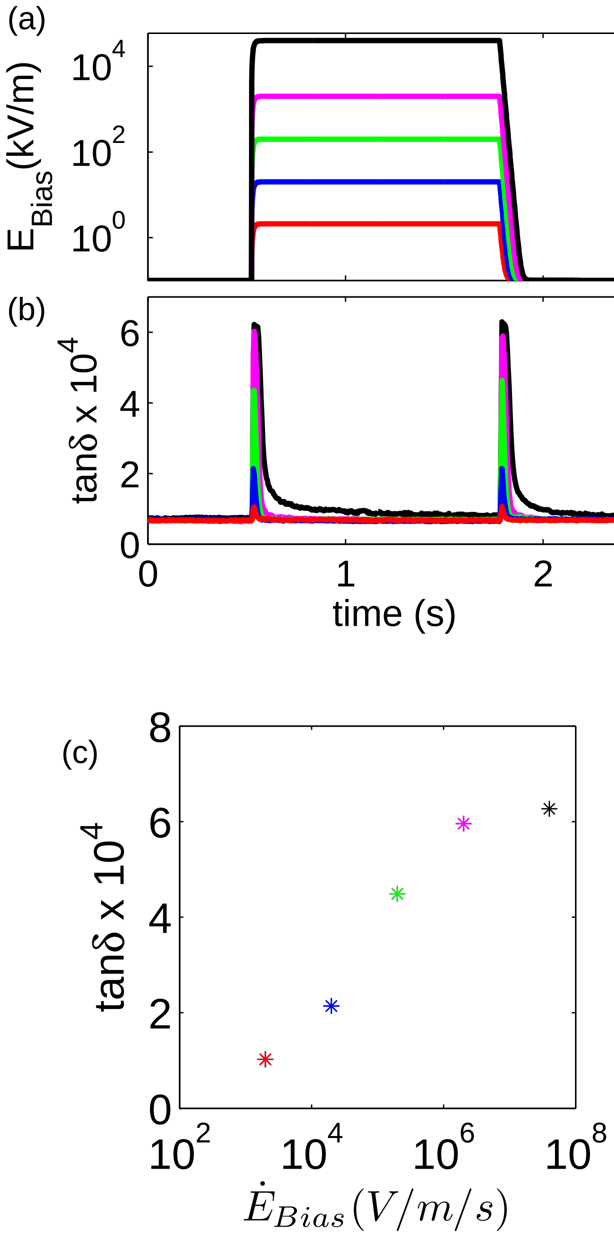

Figure 9.7: (a) Various bias pulse amplitudes with the same rise and fall time of 8.5 ms resulting in various bias sweep rates. (b) Loss tangent as response for the various bias pulses. (c) Plotting the maximum loss tangents reached from (b) against the corresponding maximum bias rate from (a).

Another technique used see how the loss tangent depends on the bias rate is to add a low pass filter to the voltage supply, slowing the characteristic rise and fall time of the voltage bias to 50 ms (see Fig. 9.8(a)). The resulting response of the loss tangent (see Fig. 9.8(b)) can be monitored as the time derivative of the voltage bias changes in time. Thus in Fig. 9.8(c) I plotted the loss tangents from Fig. 9.8(b) against the color coded instantaneous bias field time derivative (bias rates) from Fig. 9.8(a). With this technique I was able to get the entire loss tangent vs. bias rate S-curve with a single pulse.

Figure 9.9 shows my results for device *bias1-4.7GHz-B* from both techniques showing that they produce the same loss vs. bias rate S-curve. When plotting the instantaneous loss tangent against the instantaneous bias rate I used both the step up (blue) and the step down (red). The dashed curve in Fig. 9.9 is the numerical evaluation of Eq. 8.18 which was also plotted in Fig. 8.2. In Fig. 8.2 the loss tangent is plotted as a function of the dimensionless bias rate

$$\xi = \frac{2\nu_0}{\pi\Omega_{R0}^2} = \frac{4\hbar\dot{E}_{Bias}}{pE_{ac}^2}, \tag{9.5}$$

were the ac field across the resonator on resonance, E_{ac}, is known. However, the dipole moment p of the TLSs is unknown. The dashed curve in Fig. 9.9 is a fit of the model to the data by using the dipole moment as a free parameter. Using this method I extracted a dipole moment of 7.9 ± 0.5 Debye. It is noteworthy that this technique allows for determination of the TLS dipole moment.

Examining the dashed curve in Fig. 9.9, we see however that the fit only catches the top of the S-curve. This is because, as discussed in chapter 8, when

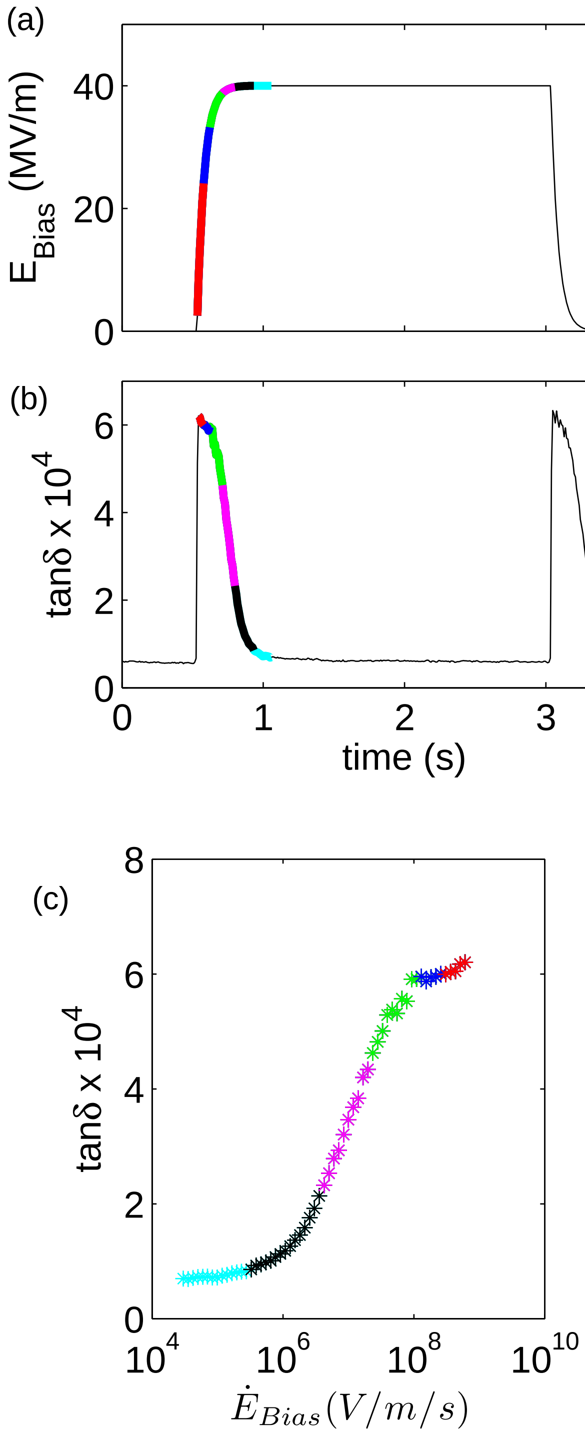

Figure 9.8: (a) Applied bias pulse with a rise and fall time of 50 ms. (b) Loss tangent response to the applied bias. (c) The instantaneous loss tangent response from (b) as a function of the instantaneous time derivative of the applied bias from (b) (the bias rate).

deriving Eq. 8.18 we neglected TLS decoherence ($T_1 = T_2 = \infty$) and assumed all of the loss comes from the Landau-Zener process produced by biasing the TLSs. Thus it is not surprising that the calculation fails when the bias is so slow that the loss due to TLS decoherence cannot be ignored ($\nu \sim \Omega_R/\sqrt{T_{1,min}T_2}$).

The solid curve in Fig. 9.9 is a fit to the data using a Monte Carlo averaged solution of the TLS density matrix similar to that discussed in Chapter 8. Note that this Monte Carlo simulation was performed with code written by Professor Alex Burin from Tulane University and is more streamlined than the Monte Carlo simulations I created and discussed in Chapter 8 (i.e. only TLSs near resonance were considered). The solution assumed a T_1 limited T_2 ($T_2 = 2T_1$) and that there was a loss tangent background of $\tan\delta_{floor} = 1.8 \times 10^{-5}$, as found from steady-state saturation measurements. From this fit we extract the same average TLS dipole moment of $p = 7.9$ Debye, and a TLS relaxation time of $T_1 = 3.0\ \mu s$. This value of p is comparable to that found for TLSs in an amorphous $\mathrm{Al_2O_3}$ Josephson junction tunneling barrier [15] and OH in alkali halides [90]. However, unlike previous measurements our ramped bias technique does not require fabrication of a Josephson junction and allows for TLS dipole measurements in any insulating film thickness. From the dipole moment and the intrinsic loss tangent, I can calculate a value of $P_0 = 4.9 \times 10^{43}\mathrm{J^{-1}m^{-3}}$ for the TLS spectral spatial population density using the relation $\tan\delta_0 = p^2 P_0/(3\epsilon)$.

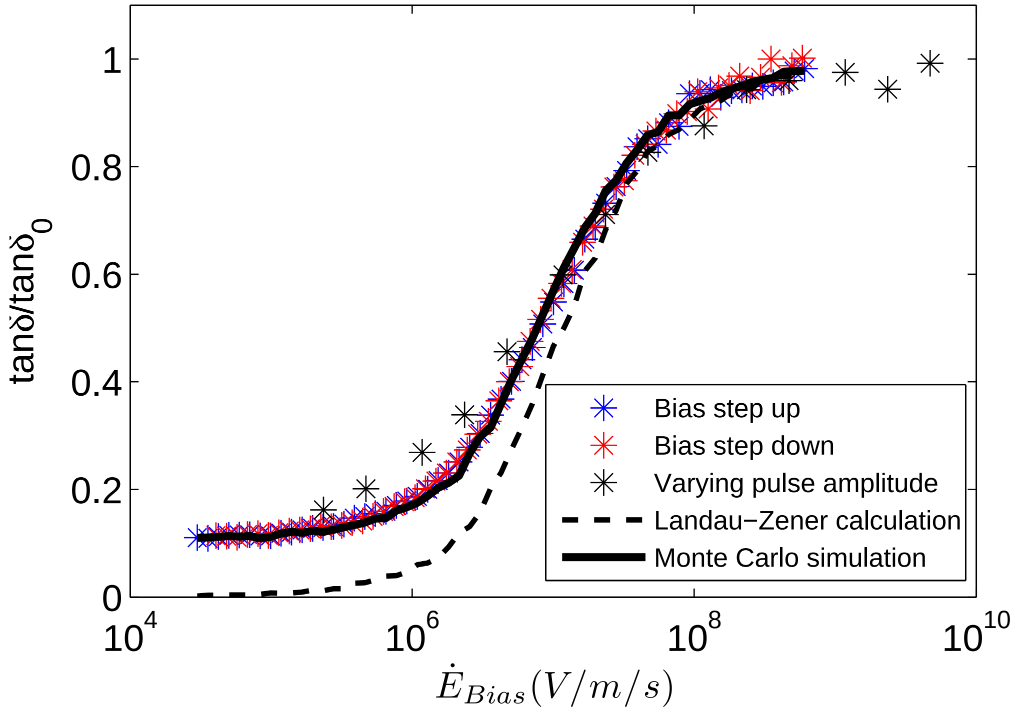

Figure 9.9: Loss tangent as a function of bias rate in device *bias1-4.7GHz-B* taken with different techniques. The blue (red) symbols show the loss tangent during the 50 ms rise (fall) time step up (down) of a bias pulse. The black symbols show data taken by varying the bias step amplitude and using the maximum loss tangent measured. The dashed curve is a fit based on the theory discussed in chapter 8 which assumes TLSs with infinite relaxation times experience a Landau-Zener transition as they're biased through the resonator's bandwidth. It therefore fails at low bias rates where the loss becomes limited by TLS relaxation instead of the bias. The solid curve is a fit using a Monte Carlo averaged solution of the TLS density matrix (see section 9.4.1).

9.4.2 Fitting S curve for different microwave (ac) powers and extracting the TLS dipole moment

The next measurement I made on device *bias1-4.7GHz-B* was a bias field measurement with different ac drive strengths (see Fig. 9.10). Note that while the amplitude of the input ac field is constant for any given curve, as the loss tangent varies it also changes the ac field across the capacitors; the low sweep rate (steady-state) ac field is given for each curve in Fig. 3A. The ac field for the middle curve (blue) varies from $E_{ac} = 4.55$ V/m at the highest bias rate to $E_{ac} = 15.52$ V/m at the lowest bias rate (the steady-state regime). To calculate E_{ac} for a given bias, I first measure the quality factor of the resonator, as discussed earlier, and then use Eq. 3.22 along with the microwave line calibrations. As expected, the different ac field measurements approach the same intrinsic loss tangent limit for fast bias rates and they saturate at different steady state loss tangents, based on their ac field drive.

A qualitative way to understand the shifts in bias rate between the different ac field curves in Fig. 9.10 is that the ac field is proportional to the Rabi frequency of the TLSs and, as discussed earlier, the Rabi frequency is what you need to compare the bias rate to decide if the bias was fast enough for the TLS to Landau-Zener transition and remain in the ground state. The key quantity is the dimensionless bias rate $\xi = 2\nu_0/(\pi\Omega_{R0}^2)$.

In Fig. 9.11(a) the solid curves are fits of the data from Fig. 9.10 for different ac fields to the same Monte Carlo solution discussed earlier (see section 9.4.1).

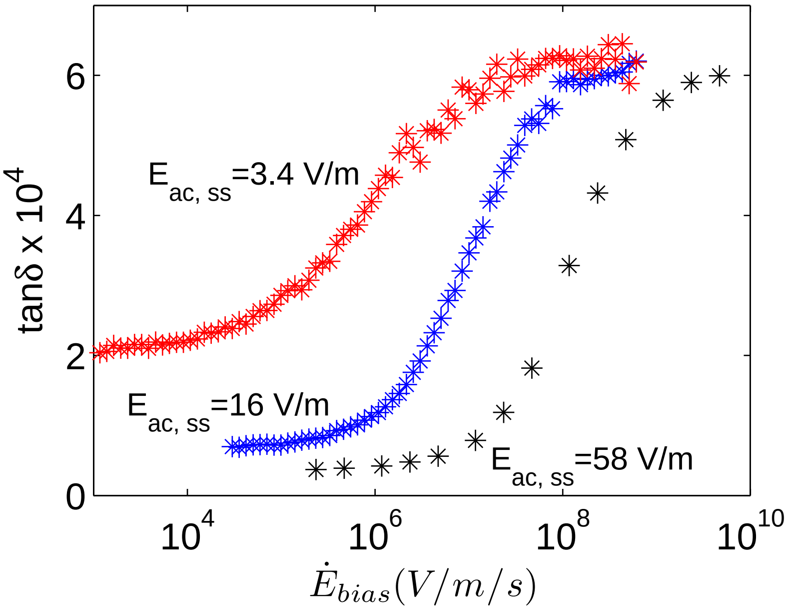

Figure 9.10: Loss tangent vs. bias field ramp rate in device *bias1-4.7GHz-B* for three different input ac fields.

The fits show excellent agreement especially considering that a single value for the dipole moment was assumed. The curves in Fig. 9.11(a) are rescaled in Fig. 9.11(b) by plotting them against the dimensionless bias rate ξ, using the extracted dipole moment $p = 7.9$ D. I find a good collapse to a single curve at high bias rates where the loss is limited by the bias rate ($\nu > \Omega_R/\sqrt{T_{1,min}T_2}$), but the curves don't collapse at low bias rates since there the loss is limited by TLS relaxations which the model neglected.

Figure 9.12 shows another version of the data from Fig. 9.11. Here I also rescaled y-axis by subtracting the zero bias rate steady-state loss tangent value ($\tan\delta_{ss}$) for each of the three sets of ac field amplitudes to account for the varying steady-state losses. This procedure is *ad hoc* and not predicted by theory, but is

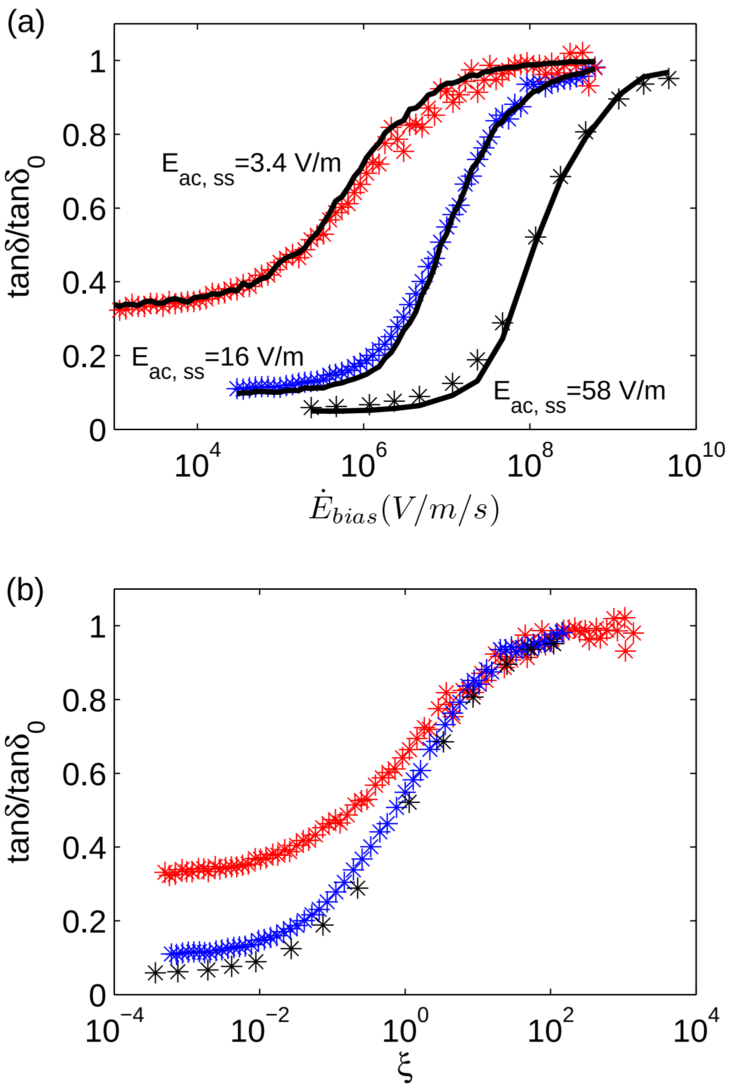

Figure 9.11: (a) The loss tangents from Fig. 9.10 normalized by the intrinsic zero field loss. The solid curves are fits from a Monte Carlo averaged solution of the TLS density matrix where the same dipole moment was assumed ($p = 7.9$ D) for all three fits (i.e. no additional free parameters). (b) The bias rate from (a) rescaling by the dimensionless bias rate ξ. The three curves converge at high bias rates where the loss is limited by the bias rate and not by TLS relaxation.

done to emphasize the agreement in the scaling. From Fig. 9.12 it's even clearer that rescaling by the dimensionless bias rate ξ collapses the data onto one curve.

9.5 S curves at 100 mK

All of the swept bias rate measurements discussed thus far in this chapter have been taken at 33 mK on device *bias1-4.7GHz-B*. In Fig. 9.13 I show similar measurements on the same device taken at 100 mK. Figure 9.13(b) shows the corresponding plot of the loss vs. dimensionless bias rate ξ. Again, we see good collapse onto one curve at high ramp rates but poor collapse as they approach the steady state regime where the loss is limited by TLS relaxation. The solid curve in Figure 9.13(b) shows a fit to the numerical evaluation of Eq. 8.18 discussed in chapter 8 and plotted in Fig. 8.2. The three horizontal lines indicate the known loss tangent values of the three data sets measured in the steady state regime. These fits yield a TLS dipole moment of $p = 8.0$ Debye, close to that extracted from the 33 mK data.

9.6 Conclusion

In conclusion, with help from my advisor Kevin Osborn, I designed, fabricated, and measured a parallel-plate thin-film microwave (ac) resonator which due to its bridge design allowed for electric field biasing of the capacitors independent of the ac field drive. This biased the asymmetry energy Δ of the TLSs in the $\mathrm{SiN_x}$ dielectric, shifting their energies in and out of the resonator's bandwidth. Consistent with a flat distribution of the TLS asymmetry energies, only small random changes of a

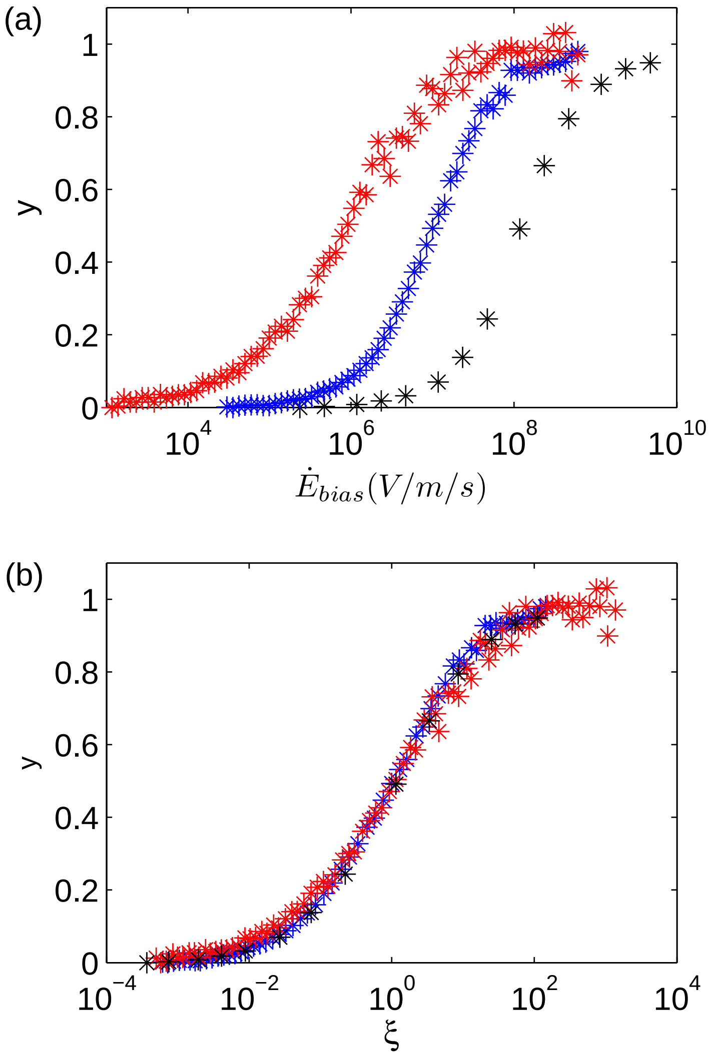

Figure 9.12: (a) Plot of the quantity $y = (\tan\delta - \tan\delta_{ss})/(\tan\delta_0 - \tan\delta_{ss})$ vs. bias rate. This is rescaling Fig. 9.12 by subtracting the zero bias rate steady-state loss tangent value ($\tan\delta_{ss}$), effectively pinning the data to zero at low bias rates. (b) Data from (a) with x-axis rescaled by the dimensionless bias rate ξ. The rescaling collapses the three curves on top of each other.

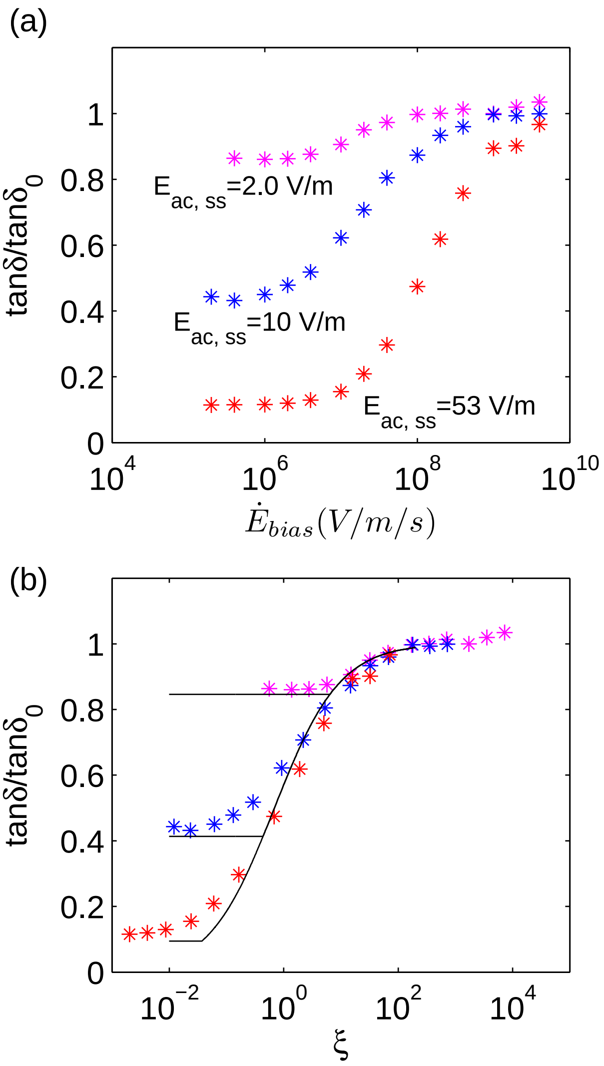

Figure 9.13: (a) Normalized loss tangent as a function of the bias rate sweep rate for three different input ac fields taken at 100 mK. (b) Rescaling the bias rate from (a) to the dimensionless bias rate ξ and collapsing the three curves at high bias rates where the loss is limited by the bias rate and not by TLS relaxation. Solid curve shows a fit based on the theory discussed in chapter 8 assuming a TLS Landau-Zener transition. The horizontal lines indicate the low bias limit loss tangent measured in the steady state regime.

few percent were observed in the TLS loss tangent.

In contrast, when the bias was swept, an increase in loss tangent was observed. For a sufficiently fast bias rate the loss approached the intrinsic unsaturated loss tangent of the material, consistent with the theory discussed in Chapter 8. This behavior was seen for temperatures spanning 30 to 200 mK. The loss tangent increased with the bias rate, from its low bias steady state limit to its high bias intrinsic loss tangent value. The variation of loss tangent with bias rate was fit to a calculation based on the TLSs making Landau-Zener transitions as they crossed the resonance field. This model did not capture the loss caused by TLS relaxation, so a Monte Carlo simulation of the TLS density matrix was used to fit the data for the full bias rate range. This analysis allowed me to deconvolute the TLS dipole moment p from the TLS spectral density P_0 which cannot be done in the corresponding steady-state measurement.

Chapter 10

Conclusion

10.1 Summary of key results

10.1.1 Diameter correction method for extracting Q_i

In chapter 3 I analyzed the transmission through a non-ideal resonant circuit and it was found that the empirically measured resonance line shape asymmetry can be modeled analytically. I also found that the conventional method used for extracting Q_i from an asymmetric resonance line shape (ϕRM) systematically overestimated Q_i and proposed a novel method (DCM) for correctly extracting Q_i from an asymmetric resonance line shape.

10.1.2 ALD dielectric results

In chapter 7 I discussed my measurements of loss in several ALD grown dielectrics by fabricating and measuring coplanar aluminum resonators on top of the ALD grown films. By comparing low temperature microwave measurements to room temperature SIMS measurements of the dielectrics, I was able to correlate excess hydrogen impurities to low temperature microwave loss. I also found that the amorphous dielectrics ($\mathrm{AlO_x}$ and $\mathrm{LaAlO_x}$) showed excess surface hydrogen impurities and this was associated with greater surface loss than bulk loss. While the crystalline dielectric (BeO) showed excess carbon impurities at the surface it had a uniform hydrogen impurity concentration and the data could be explained by a single bulk loss tangent. This suggested that hydrogen impurities were the source of TLS loss in BeO film.

I also described measurements in which I compared two ALD grown $\mathrm{AlO_x}$ films deposited in different labs with nominally the same precursors. The films showed drastically different quantities of carbon impurities but similar hydrogen impurity levels. The two films had similar loss, consistent with hydrogen based TLSs. By comparing low temperature microwave loss measurements on $\mathrm{AlO_x}$ to SIMS impurity analysis of the films, I found a low field loss tangent (intrinsic loss tangent) per hydrogen concentration of $K_H = 3 \times 10^{-24}$ cm^3.

10.1.3 Biased resonator results

In Chapter 9, I described my work on electric field biased resonators. I fabricated and measured a biased bridge superconducting resonator designed to bias TLSs in the $\mathrm{SiN_x}$ parallel-plate capacitors in and out of the resonator's bandwidth. By applying several DC biases, I was able to observe small (a few percent) reproducible fluctuations in the TLS distribution but due to the wideband white distribution of TLS asymmetry energies Δ the loss did not vary monotonically with the bias.

In contrast, if I swept the bias sufficiently rapidly I observed an increase in loss tangent due to the biasing of unsaturated (ground state) TLSs into the resonator's bandwidth and the biasing of excited TLSs out of the resonator's bandwidth. When measuring with a high (saturating) microwave field, I found that a sufficiently high bias rate increased the loss tangent to the unsaturated intrinsic loss tangent of the material. This result motivated work on a theory in which TLSs undergo Landau-Zener transitions as they are biased across the resonator's bandwidth. Using this model I fit my bias rate loss tangent data and was able to extract an average dipole moment of $p = 7.9$ Debye and a spectral spatial density of $P_0 = 4.9 \times 10^{43}$ J^{-1}m^{-3} for the TLSs in an amorphous film of Si_3N_4.

10.2 Future work

10.2.1 Trilayer resonator fabrication

In chapter 7, I showed that in some cases dielectric loss can be limited by surface impurities that are likely introduced when the surface is exposed to the ambient atmosphere during processing. This suggests that the loss can be reduced by adopting trilayer fabrication techniques where the dielectric is grown *in situ* with the metal on top of it. Such an approach would be especially useful after optimizing the dielectric growth to minimize impurities introduced during the growth process, as discussed in chapter 7. Trilayer processes can also be useful for junction fabrication. For example such trilayer fabrication has recently been developed to improve phase qubits [91] and is currently being developed by B. Sarabi in Kevin Osborn's group.

10.2.2 Biasing TLSs in coplanar resonator

As I discussed in Chapters 8 and 9, the ability to bias TLSs in a resonator can reveal much about their properties and their energy distribution. A possible extension of the bias experiments is to attempt TLS biasing for coplanar resonators with interdigital capacitors as discussed in chapters 4 and 5. A similar capacitor bridge design can be used but with IDCs instead of parallel-plate capacitors. This will allow for biasing of TLSs in resonators fabricated on low-loss wafers which can lead to a better understanding of loss mechanisms in such geometries. Work along these lines is now being pursued by K. Voigt *et al.* [92].

10.2.3 Lasing and loss reduction with biased resonator

While not discussed in Chapters 8 and 9, one implication of the swept bias analysis is that the TLSs biased across a resonator's bandwidth can undergo population inversion, and in principle this might allow which can theoretically be used for lasing. Attempts at measuring this phenomenon in the same device used for this thesis are already underway by Y. Rosen in Kevin Osborn's group.

A possible technique for taking advantage of TLS biasing to achieve is to fabricate a resonator with multiple modes that share the same parallel-plate capacitors. This would allow TLSs to be excited in one resonance mode and then biased into another resonance mode where they can be measured through lasing. A variation on this would be to have three modes in total: Two side modes excited with high microwave power to excite TLSs, and a middle mode for the TLSs to emit into by stimulated emission (lase). The reason for two side modes is to allow TLSs with a dipole in one direction to be excited by one side mode and TLSs with a dipole in the other direction to be excited by the other side mode.

If this device with multiple modes is used, in addition to lasing, it can also be used to reduce the loss tangent of a material at low microwave fields. The idea is to continually saturate TLSs by applying power at the side modes and then biasing them into the central mode which is being probed with single photon energies in the unsaturated regime.

10.3 Concluding remarks

This field has progressed so much in the brief six years that I have been fortunate to observe it. If you had asked me six years ago what I thought the first quantum computer (as determined by a reasonable person) would look like, I would have said a bunch of atoms with lasers everywhere. Today I believe it will be a superconducting circuit at the bottom of a dilution refrigerator. Part of that of course was my naivety at the time, but much of it is to the credit of the accomplishments of the superconducting quantum computing community in such a short time period. If we continue the two pronged approach of improving device performance empirically while not forgetting to hone a better understanding of decoherence mechanisms, I have little doubt that a quantum computer is achievable within my lifetime. Actually I think (also hope) my lifetime is a very conservative estimate, but it seems like an appropriate timescale to reference.

Bibliography

[1] Richard P. Feynman. Simulating physics with computers. *International Journal of Theoretical Physics*, 21(6-7):467–488, June 1982.

[2] Alejandro Perdomo-Ortiz, Neil Dickson, Marshall Drew-Brook, Geordie Rose, and Alán Aspuru-Guzik. Finding low-energy conformations of lattice protein models by quantum annealing. *Scientific reports*, 2:571, January 2012.

[3] A. Church. An Unsolvable Problem of Elementary Number Theory. *American Journal of Mathematics*, 58(2):345–363, 1936.

[4] A. M. Turing. On Computable Numbers, with an Application to the Entscheidungsproblem. *Proceedings of the London Mathematical Society*, s2-42(1):230–265, January 1937.

[5] D. Deutsch. Quantum theory, the Church-Turing principle and the universal quantum computer. *Proceedings of the Royal Society of London A*, 400:97–117, 1985.

[6] D. Deutsch and R. Jozsa. Rapid Solution of Problems by Quantum Computation. *Proceedings of the Royal Society A: Mathematical, Physical and Engineering Sciences*, 439(1907):553–558, December 1992.

[7] P.W. Shor. Algorithms for quantum computation: discrete logarithms and factoring. In *Proceedings 35th Annual Symposium on Foundations of Computer Science*, pages 124–134. IEEE Comput. Soc. Press.

[8] Lov K. Grover. A fast quantum mechanical algorithm for database search. page 8, May 1996.

[9] B. Apolloni, C. Carvalho, and D. de Falco. Quantum stochastic optimization. *Stochastic Processes and their Applications*, 33(2):233–244, December 1989.

[10] C. Monroe, D. Meekhof, B. King, W. Itano, and D. Wineland. Demonstration of a Fundamental Quantum Logic Gate. *Phys. Rev. Lett.*, 75(25):4714–4717, December 1995.

[11] David G. Cory, Mark D. Price, and Timothy F. Havel. Nuclear magnetic resonance spectroscopy: An experimentally accessible paradigm for quantum computing. *Physica D: Nonlinear Phenomena*, 120(1-2):82–101, September 1998.

[12] B.D. Josephson. Possible new effects in superconductive tunnelling. *Phys. Lett.*, 1(7):251–253, 1962.

[13] Y. Nakamura, Yu. A. Pashkin, and J. S. Tsai. Coherent control of macroscopic quantum states in a single-Cooper-pair box. 398(6730):786–788, April 1999.

[14] M. Nielsen and I. Chuang. *Quantum Computation and Quantum Information.* Cambridge University Press, 2000.

[15] John Martinis, K. Cooper, R. McDermott, Matthias Steffen, Markus Ansmann, K. Osborn, K. Cicak, Seongshik Oh, D. Pappas, R. Simmonds, and Clare Yu. Decoherence in Josephson Qubits from Dielectric Loss. *Phys. Rev. Lett.*, 95(21):1–4, November 2005.

[16] A Wallraff, D I Schuster, A Blais, L Frunzio, R-S Huang, J Majer, S Kumar, S M Girvin, and R J Schoelkopf. Strong coupling of a single photon to a superconducting qubit using circuit quantum electrodynamics. *Nature*, 431(7005):162–7, September 2004.

[17] Hanhee Paik, D. Schuster, Lev Bishop, G. Kirchmair, G. Catelani, A. Sears, B. Johnson, M. Reagor, L. Frunzio, L. Glazman, S. Girvin, M. Devoret, and R. Schoelkopf. Observation of High Coherence in Josephson Junction Qubits Measured in a Three-Dimensional Circuit QED Architecture. *Phys. Rev. Lett.*, 107(24):1–5, December 2011.

[18] Peter K Day, Henry G Leduc, Benjamin A Mazin, Anastasios Vayonakis, and Jonas Zmuidzinas. A broadband superconducting detector suitable for use in large arrays. *Nature*, 425(October):12–14, 2003.

[19] H. Padamsee. The science and technology of superconducting cavities for accelerators. *Supercond. Sci. Technol.*, 28:R28–R15, 2001.

[20] R.W. Simon, R.B. Hammond, S.J. Berkowitz, and B.a. Willemsen. Superconducting microwave filter systems for cellular telephone base stations. *Proceedings of the IEEE*, 92(10):1585–1596, October 2004.

[21] C. A. Regal, J. D. Teufel, and K. W. Lehnert. Measuring nanomechanical motion with a microwave cavity interferometer. *Nature Physics*, 4(7):555–560, May 2008.

[22] R. C. Zeller and R. O. Pohl. Thermal Conductivity and Specific Heat of Noncrystalline Solids. *Phys. Rev. B*, 4(6):2029–2041, September 1971.

[23] W. A. Phillips. Tunneling states in amorphous solids. *Jour. of Low Temp. Phys.*, 7(3-4):351–360, May 1972.

[24] P. W. Anderson, B. I. Halperin, and c. M. Varma. Anomalous low-temperature thermal properties of glasses and spin glasses. *Phil. Mag.*, 25(1):1–9, January 1972.

[25] C. Enss and S. Hunklinger. *Low-Temperature Physics.* Springer, 2005.

[26] W A Phillips. Two-level states in glasses. *Rep. Prog. Phys.*, 50:1657–1708, 1987.

[27] Jiansong Gao. The Physics of Superconducting Microwave Resonators Thesis by. *The Physics of Superconducting Microwave Resonators, Doctoral Dissertation, California Institute of Technology.*, 2008.

[28] S. Hunklinger and W. Arnold. Ultrasonic Properties on Flasses at Low Temperatures. *Physical Acoustics*, 12:155, 1976.

[29] F. Bloch. Nuclear Induction. *Phys. Rev.*, 70(7-8):460–474, October 1946.

[30] M Vonschickfus and S Hunklinger. Saturation of the dielectric absorption of vitreous silica at low temperatures. *Phys. Rev. Lett.*, 64(1):144–146, November 1977.

[31] R. Simmonds, K. Lang, D. Hite, S. Nam, D. Pappas, and John Martinis. Decoherence in Josephson Phase Qubits from Junction Resonators. *Phys. Rev. Lett.*, 93(7):077003, August 2004.

[32] Z. Kim, V. Zaretskey, Y. Yoon, J. Schneiderman, M. Shaw, P. Echternach, F. Wellstood, and B. Palmer. Anomalous avoided level crossings in a Cooper-pair box spectrum. *Physical Review B*, 78(14):1–6, October 2008.

[33] M. J. A. Stoutimore, M. S. Khalil, C. J. Lobb, and K. D. Osborn. A Josephson junction defect spectrometer for measuring two-level systems. *App. Phys. Lett.*, 101(6):062602, 2012.

[34] Aaron M. Holder, Kevin D. Osborn, C. J. Lobb, and Charles B. Musgrave. Bulk and Surface Tunneling Hydrogen Defects in Alumina. *arXiv:1303.6713*, March 2013.

[35] Hanhee Paik and Kevin D. Osborn. Reducing quantum-regime dielectric loss of silicon nitride for superconducting quantum circuits. *App. Phys. Lett.*, 96(7):072505, 2010.

[36] Weinreb Radiometer Group at Caltech, http://radiometer.caltech.edu/.

[37] Aaron D. OConnell, M. Ansmann, R. C. Bialczak, M. Hofheinz, N. Katz, Erik Lucero, C. McKenney, M. Neeley, H. Wang, E. M. Weig, a. N. Cleland, and J. M. Martinis. Microwave dielectric loss at single photon energies and millikelvin temperatures. *Appl. Phys. Lett.*, 92(11):112903, 2008.

[38] David S. Wisbey, Jiansong Gao, Michael R. Vissers, Fabio C. S. da Silva, Jeffrey S. Kline, Leila Vale, and David P. Pappas. Effect of metal/substrate interfaces on radio-frequency loss in superconducting coplanar waveguides. *Jour. of Appl. Phys.*, 108(9):093918, 2010.

[39] Moe S. Khalil, F. C. Wellstood, and Kevin D. Osborn. Loss Dependence on Geometry and Applied Power in Superconducting Coplanar Resonators. *IEEE Trans. on Appl. Supercond.*, 21(3):879–882, June 2011.

[40] M.V. Klein and J. Kruse. Mode coupling in superconducting parallel plate resonator in a cavity with outer conductive enclosure. *IEEE Trans. on Micr. Theory and Techn.*, 44(6):944–952, June 1996.

[41] M. S. Khalil, M. J. a. Stoutimore, F. C. Wellstood, and K. D. Osborn. An analysis method for asymmetric resonator transmission applied to superconducting devices. *Jour. of App. Phys.*, 111(5):054510, 2012.

[42] A. Khanna and Y. Garault. Determination of Loaded, Unloaded, and External Quality Factors of a Dielectric Resonator Coupled to a Microstrip Line. *IEEE Trans. on Micr. Theory and Techn.*, 31(3):261–264, 1983.

[43] D. Kajfez and E.J. Hwan. Q-Factor Measurement with Network Analyzer. *IEEE Trans. on Micr. Theory and Techn.*, 32(7):666–670, July 1984.

[44] D. Kajfez. Q-factor measurement with a scalar network analyser. *IEEE Proceedings - Micr.s, Ant. and Propagation*, 142(5):369, 1995.

[45] K. Leong and J. Mazierska. Precise measurements of the Q factor of dielectric resonators in the transmission mode-accounting for noise, crosstalk, delay of uncalibrated lines, coupling loss, and coupling reactance. *IEEE Trans. on Micr. Theory and Techn.*, 50(9):2115–2127, September 2002.

[46] Paul J. Petersan and Steven M. Anlage. Measurement of resonant frequency and quality factor of microwave resonators: Comparison of methods. *Jour. of Appl. Phys.*, 84(6):3392, 1998.

[47] David Pozar. *Microwave Engineering.* John Willey & Sons, New York, 3rd ed. edition, 2005.

[48] Chunqing Deng, Martin Otto, and Adrian Lupascu. An analysis method for transmission measurements of superconducting resonators with applications to quantum-regime dielectric-loss measurements. *Jour. of App. Phys.*, 114(5):054504, August 2013.

[49] Mika a Sillanpää, Jae I Park, and Raymond W Simmonds. Coherent quantum state storage and transfer between two phase qubits via a resonant cavity. *Nature*, 449(7161):438–42, September 2007.

[50] Max Hofheinz, H Wang, M Ansmann, Radoslaw C Bialczak, Erik Lucero, M Neeley, a D O'Connell, D Sank, J Wenner, John M Martinis, and a N Cleland. Synthesizing arbitrary quantum states in a superconducting resonator. *Nature*, 459(7246):546–9, May 2009.

[51] John Martinis, S. Nam, J. Aumentado, and C. Urbina. Rabi Oscillations in a Large Josephson-Junction Qubit. *Physical Review Letters*, 89(11):9–12, August 2002.

[52] Anthony J. Przybysz, H Kwon, R Budoyo, B. K. Cooper, E Crowe, A. J. Dragt, J. R. Anderson, C. J. Lobb, and F. C. Wellstood. Identifying Sources of Decoherence in a dc SQUID Phase Qubit With a Sub- Junction and Interdigitated Capacitor. *IEEE Trans on Applied Supercond.*, 21(3), 2011.

[53] K. D. Osborn, J. A. Strong, A. J. Sirois, and R. W. Simmonds. Frequency-Tunable Josephson Junction Resonator for Quantum Computing. *IEEE Trans on Applied Supercond.*, 17(2), 2007.

[54] A. Houck, J. Schreier, B. Johnson, J. Chow, Jens Koch, J. Gambetta, D. Schuster, L. Frunzio, M. Devoret, S. Girvin, and R. Schoelkopf. Controlling the Spontaneous Emission of a Superconducting Transmon Qubit. *Phys. Rev. Lett.*, 101(8):1–4, August 2008.

[55] Matthias Steffen, Frederico Brito, David DiVincenzo, Shwetank Kumar, and Mark Ketchen. Decoherence of floating qubits due to capacitive coupling. *New Journal of Physics*, 11(3):4, 2009.

[56] Kyocera, http://global.kyocera.com/prdct/fc/product/category/sapphire/sapphire002.html.

[57] Silicon Quest International Inc, http://www.siliconquest.com/.

[58] Fujifilm, http://www.fujifilmusa.com/products/.

[59] K. C. Gupta. *Microstrip Line and Slotlines.* Artech House, Inc., Norwood, MA, 2rd ed. edition, 1996.

[60] Jiansong Gao, Miguel Daal, Anastasios Vayonakis, Shwetank Kumar, Jonas Zmuidzinas, Bernard Sadoulet, Benjamin a. Mazin, Peter K. Day, and Henry G. Leduc. Experimental evidence for a surface distribution of two-level systems in superconducting lithographed microwave resonators. *Appl. Phys. Lett.*, 92(15):152505, 2008.

[61] J. Wenner, R. Barends, R. C. Bialczak, Yu Chen, J. Kelly, Erik Lucero, Matteo Mariantoni, A. Megrant, P. J. J. OMalley, D. Sank, A. Vainsencher, H. Wang, T. C. White, Y. Yin, J. Zhao, A. N. Cleland, and John M. Martinis. Surface loss simulations of superconducting coplanar waveguide resonators. *App. Phys. Lett.*, 99(11):113513, September 2011.

[62] R. Barends, N. Vercruyssen, A. Endo, P. J. de Visser, T. Zijlstra, T. M. Klapwijk, P. Diener, S. J. C. Yates, and J. J. A. Baselmans. Minimal resonator loss for circuit quantum electrodynamics. *App. Phys. Lett.*, 97(2):023508, July 2010.

[63] A. Megrant, C. Neill, R. Barends, B. Chiaro, Yu Chen, L. Feigl, J. Kelly, Erik Lucero, Matteo Mariantoni, P. J. J. OMalley, D. Sank, A. Vainsencher, J. Wenner, T. C. White, Y. Yin, J. Zhao, C. J. Palmstrom, John M. Martinis,

and A. N. Cleland. Planar superconducting resonators with internal quality factors above one million. *App. Phys. Lett.*, 100(11):113510, March 2012.

[64] R. Barends, J. Wenner, M. Lenander, Y. Chen, R. C. Bialczak, J. Kelly, E. Lucero, P. OMalley, M. Mariantoni, D. Sank, H. Wang, T. C. White, Y. Yin, J. Zhao, A. N. Cleland, John M. Martinis, and J. J. A. Baselmans. Minimizing quasiparticle generation from stray infrared light in superconducting quantum circuits. *App. Phys. Lett.*, 99(11):113507, September 2011.

[65] Michael R. Vissers, Martin P. Weides, Jeffrey S. Kline, Martin Sandberg, and David P. Pappas. Identifying capacitive and inductive loss in lumped element superconducting hybrid titanium nitride/aluminum resonators. *App. Phys. Lett.*, 101(2):022601, July 2012.

[66] S. Sendelbach, D. Hover, M. Mück, and R. McDermott. Complex Inductance, Excess Noise, and Surface Magnetism in dc SQUIDs. *Phys. Rev. Lett.*, 103(11):11–14, September 2009.

[67] Lara Faoro and Lev Ioffe. Microscopic Origin of Low-Frequency Flux Noise in Josephson Circuits. *Phys. Rev. Lett.*, 100(22):227005, June 2008.

[68] K. Geerlings, S. Shankar, E. Edwards, L. Frunzio, R. J. Schoelkopf, and M. H. Devoret. Improving the quality factor of microwave compact resonators by optimizing their geometrical parameters. *App. Phys. Lett.*, 100(19):192601, 2012.

[69] Lara Faoro and Lev B. Ioffe. Internal Loss of Superconducting Resonators Induced by Interacting Two-Level Systems. *Phys. Rev. Lett.*, 109(15):157005, October 2012.

[70] Conventional and ALD dielectric film studies for improved Josephson phase qubits, White Paper, 2009.

[71] A. Kozen, private communication.

[72] Alexander C. Kozen, Marshall A. Schroeder, Kevin D. Osborn, C. J. Lobb, and Gary W. Rubloff. Examining the role of hydrogen in the electrical performance of in situ fabricated metal-insulator-metal trilayers using an atomic layer deposited Al2O3 dielectric. *App. Phys. Lett.*, 102(17):173501, April 2013.

[73] Evans Analytical Group LLC, http://www.eag.com/.

[74] J.H. Yum, T. Akyol, M. Lei, D.a. Ferrer, Todd.W. Hudnall, M. Downer, C.W. Bielawski, G. Bersuker, J.C. Lee, and S.K. Banerjee. Electrical and physical characteristics for crystalline atomic layer deposited beryllium oxide thin film on Si and GaAs substrates. *Thin Solid Films*, 520(7):3091–3095, January 2012.

[75] R. Matero, A. Rahtu, M. Ritala, M. Leskela, and T. Sajavaara. Effect of water dose on the atomic layer deposition rate of oxide thin films. *Thin Solid Films*, 368(1):1–7, 2000.

[76] Booyong S. Lim, Antti Rahtu, Philippe de Rouffignac, and Roy G. Gordon. Atomic layer deposition of lanthanum aluminum oxide nano-laminates for electrical applications. *App. Phys. Lett.*, 84(20):3957, 2004.

[77] Glen A. Slack. Thermal Conductivity of BeO Single Crystals. *J. of App. Phys.*, 42(12):4713, November 1971.

[78] William C. Daywitt. Complex Permittivity of Beryllium Oxide between 100 and 300 K at 9.3 GHz. *IEEE Trans. on Inst. and Meas.*, 34(1):98–99, 1985.

[79] D. Salvino, S. Rogge, B. Tigner, and D. Osheroff. Low Temperature ac Dielectric Response of Glasses to High dc Electric Fields. *Phys. Rev. Lett.*, 73(2):268–271, July 1994.

[80] S Rogge, D Natelson, and D Osheroff. Evidence for the importance of interactions between active defects in glasses. *Phys. Rev. Lett.*, 76(17):3136–3139, April 1996.

[81] Douglas Natelson, Danna Rosenberg, and D. Osheroff. Evidence for Growth of Collective Excitations in Glasses at Low Temperatures. *Phys. Rev. Lett.*, 80(21):4689–4692, May 1998.

[82] Hervé M. Carruzzo, Eric R. Grannan, Clare C. Yu. Nonequilibrium dielectric behavior in glasses at low temperatures: Evidence for interacting defects. *Phys. Rev. B*, 50(10):6685–6695, 1994.

[83] Alexander L. Burin. Dipole gap effects in low energy excitation spectrum of amorphous solids. Theory for dielectric relaxation. *Jour. of Low Temp. Phys.*, 100(3-4):309–337, August 1995.

[84] Grigorij J Grabovskij, Torben Peichl, Jürgen Lisenfeld, Georg Weiss, and Alexey V Ustinov. Strain tuning of individual atomic tunneling systems detected by a superconducting qubit. *Science*, 338(6104):232–4, October 2012.

[85] Alexander L. Burin, Moe S. Khalil, and Kevin D. Osborn. Universal Dielectric Loss in Glass from Simultaneous Bias and Microwave Fields. *Phys. Rev. Lett.*, 110(15):157002, April 2013.

[86] Lev. Landau. Zur Theorie der Energieubertragung. II. *Physics of the Soviet Union*, 1932.

[87] C. Zener. Non-adiabatic Crossing of Energy Levels. II. *Proceedings of the Royal Society of London A*, 1932.

[88] Claude Cohen-Tannoudii, Jacques Dupont-Roc, and Gilbert Gryberg. *Atom-Photon Interactions: Basic Processes and Applications.* Wiley, 1992.

[89] n&k Technology, http://www.nandk.com/.

[90] J. De Yoreo, W. Knaak, M. Meissner, and R. Pohl. Low-temperature properties of crystalline (KBr)_{1-x}(KCN)_{x}: A model glass. *Phys. Rev. B*, 34(12):8828–8842, December 1986.

[91] M Weides, R C Bialczak, M Lenander, E Lucero, Matteo Mariantoni, M Neeley, A D OConnell, D Sank, H Wang, J Wenner, T Yamamoto, Y Yin, A N Cleland, and J Martinis. Phase qubits fabricated with trilayer junctions. *Superconductor Science and Technology*, 24(5):055005, May 2011.

[92] K. Voigt, private communication.